

Université catholique de Louvain
–
Institute of Mechanics, Materials and Civil Engineering
and
Institute of Condensed Matter and Nanosciences

Predicting and compensating distortions of composite parts

Benoît Wucher

Thèse présentée en vue de l'obtention du grade
de Docteur en Sciences de l'Ingénieur

Jury:

Prof Thomas Pardoen (Promoteur)	Université catholique de Louvain, Belgique
Prof Christian Bailly (Promoteur)	Université catholique de Louvain, Belgique
Prof Laurent Delannay (Président)	Université catholique de Louvain, Belgique
Prof Issam Doghri	Université catholique de Louvain, Belgique
Prof Stepan Lomov	KU Leuven, Belgique
Dr Olivier Pierard	Cenaero, Belgique
Dr Frédéric Lani	Any-Shape, Belgique
Mr Sjoerd van der Veen	Airbus, France

7 décembre 2016

Abstract

Thermoset-based composite materials exhibit distortions as a result of the manufacturing process. The shape of a composite part deviates slightly between the beginning and the end of the cure, owing to several irreversible phenomena. If these distortions are not anticipated, the assembling of several components together may require unacceptable forces or lead to internal stresses detrimental to the in-service behavior of the structure.

Despite numerous studies about cure-induced distortions, the literature still lacks tried-and-tested methodologies for their reduction. The increasing complexity of the designs makes rules of thumb obsolete, while relying on experimental trial-and-error sequences results in prohibitive additional costs and delays. The present thesis focuses on the development of numerical tools capable of predicting the shape of the mold which minimizes the deviations with respect to the target design. The use of numerical simulation enables to bypass expensive experimental studies. Three complementary methods are proposed, focusing on their applicability to complex geometries in an industrial context.

In another contribution, the thesis improves the feasibility and accuracy of the curing simulation methodology by answering to the deep need for material properties. Instead of relying on material characterization at the composite level, homogenization is used to predict the properties of the multi-phase material based on those of the constituents. The novelty of the approach resides in making finite element homogenization applicable to coarsely-modeled woven textiles, for which the geometrical representation of the yarns usually overlaps. Instead of spending resources on suppressing the penetrations, the latter are accommodated by using non-conformal meshes and a procedure to reallocate the fiber volume within the overlapping regions.

In a final stage, the homogenization and mold compensation methodologies are put into practice to manufacture composite parts in Cenaero's laboratory. The non-compensated and compensated parts are compared to confirm that the distortions are largely reduced by the developed techniques.

Acknowledgments

Completing a doctorate is a combination of planting seeds which hopefully blossom into interesting ideas and concrete results, and a few sleepless nights to bring those ideas to life and to put them on paper. Since I can only take credit for the latter, I must acknowledge the support of all the seed-planters who have accompanied me through this almost 5-year long journey.

I cannot express enough gratitude to my dear supervisors, Prof Thomas Pardoen and Prof Christian Bailly, who have guided me, from afar, through my research. Although I did not see them as often as I should – which I take full responsibility for – they always found simple and elegant solutions to help me go forward. Working with such eminent yet simple persons has been a humbling experience.

I am grateful to the members of my jury for agreeing to my request and taking the time to read my humble contribution to the field: Prof Issam Doghri, Prof Stepan Lomov, Dr Olivier Pierard and Mr Sjoerd van der Veen. I do not forget Prof Laurent Delannay, whom I thank for accepting to preside this jury. I hope this manuscript will meet your expectations and I look forward to discussing with you about potential improvements.

I am warmly and equally grateful to my three successive team leaders at Cenaero. First, Dr Frédéric Lani, who is also in my jury, is the person who trusted and hired me, and, most of all, single-handedly built this project and fought to secure my financing. He has also had a great influence on the technical content of this work, giving me merciless feedback and key ideas which I have always appreciated to the fullest. Second is Dr Philippe Martiny, who took me in when I was a clueless student back in 2009, for an internship which will remain the foundation of my desire to work at Cenaero. He also carried me through the first two years of my research, with his exceptional vision and unique human skills. Moreover, Philippe will learn by reading these words that his experience has been most inspiring when the time came to wrap up this manuscript. As hard as it is to complete a PhD as a Cenaero employee, it cannot be one hundredth as hard as for a married Cenaero team leader with two kids. Bien joué chef. Finally, I give praise to David Dumas, who took me to the finish line with his eternal good spirit, gave me great freedom and has always answered to my desperate cries for help, selflessly, when needed. I also acknowledge the support of other Cenaero members who have volunteered to read this thesis, Éric and Benoît, providing a fresh point of view and insightful advice to improve it.

I send my friendliest regards to Prof Stefan Hallström, who had the kindness to welcome me for three months in KTH in the fall of 2013. Stefan planted one of those seeds in my mind which literally grew into a full chapter of this manuscript. Thank you for that.

I would like to thank Cenaero's management team for making this company a unique workplace where human qualities and technical expertise are at their best. Thank you also for giving me the time I needed to complete this project, and for trusting me for the new and exciting journey which I am ready to embark on. Of course, I could not have completed this PhD without my colleagues of the former CSP team. Special greetings to Antoine, whose leak detection skills surely deserve some kind of Nobel Prize, and Arnaud, who, by machining a much nicer mold than the original supplier, played a great role in my success in the compensation area. LaTeX lovers will also be grateful to Antoine, who made me switch, for good reasons, in a 20-hour frenzy. I will dearly miss everything about this team, except vacuuming the lab at two o'clock in the morning.

I sincerely thank the interns who have crossed my path during the last four years, Théo Baumard, Benoît Bracquart and Nicolas Pautet. Although their work is not necessarily reflected in this PhD, they all helped me advance in my projects and grow as a person. I was glad to hear that at least two of them started a PhD, although I am sort of relieved to finish mine before them.

This work has been made possible by the financial support of the Walloon Region, through the First DoCA OPTIMOLD project (grant number ECV320 600FD012F / 1117310).

I could not have accomplished this work without my parents, who have done everything to give me a good education and have always supported me and my life choices. Finally, I salute my beloved brother, my rock, my role model, my star. I am lucky to have you beside me.

Acronyms

2D / 3D	Two- or three-dimensional
CAD	Computer aided design
CFRP	Continuous fiber reinforced polymer
CHILE	Cure-hardening instantaneous linear elastic
CPM	Control points method
CPU	Computational
CTE	Coefficient of thermal expansion
DMM	Distortion modes method
DOE	Design of experiments
DMA	Dynamic mechanical analysis
DSC	Differential scanning calorimetry
FE	Finite Elements
FEM	Finite Element Method
HPC	High performance computing
LOO	Leave-one-out
PBCs	Periodic boundary conditions
RTM	Resin transfer molding
RVE	Representative volume element
SBO	Surrogate-based optimization
SQRTM	Same qualified resin transfer molding
UD	Unidirectional
VARTM	Vacuum assisted resin transfer molding

Generic notations

E	Young's modulus
G	Shear modulus
ν	Poisson's ratio
ε	Strain tensor
σ	Stress tensor
C	Stiffness tensor
α	Coefficient of thermal expansion
β	Coefficient of chemical shrinkage
k_f	Fiber volume fraction
ρ	Density
δ_{ij}	Kronecker delta
X	Degree of cure
T	Temperature
T_g	Glass transition temperature

Contents

1 Introduction **1**
- 1.1 Industrial context . . . 1
- 1.2 Objective of the thesis . . . 2
- 1.3 Structure of the thesis . . . 5

2 Scientific background **7**
- 2.1 Composite manufacturing processes . . . 7
  - 2.1.1 The autoclave process . . . 7
  - 2.1.2 The RTM process . . . 8
  - 2.1.3 The VARTM process . . . 8
- 2.2 Manufacturing-induced distortions . . . 9
  - 2.2.1 Cure development . . . 9
  - 2.2.2 Origins of the distortions . . . 10
- 2.3 Process modeling – an overview . . . 15
  - 2.3.1 Preamble . . . 15
  - 2.3.2 Cure kinetics . . . 15
  - 2.3.3 Glass transition temperature . . . 16
  - 2.3.4 Chemical shrinkage and thermal expansion . . . 17
  - 2.3.5 Heat transfer in thermoset composites . . . 18
  - 2.3.6 Mechanical behavior of thermosets during cure . . . 20
  - 2.3.7 Modeling strategies and existing software . . . 22
- 2.4 Conclusion . . . 24

3 Non-conformal mesh finite element homogenization **25**
- 3.1 Introduction . . . 25
  - 3.1.1 Scope . . . 25
  - 3.1.2 Objective and outline . . . 26
- 3.2 The theory of homogenization in a nutshell . . . 28
  - 3.2.1 The homogenization problem . . . 28
  - 3.2.2 Resolution by the finite element method . . . 29
  - 3.2.3 Micromechanics-based model . . . 32
- 3.3 Homogenization of textile composites: literature review . . . 34
  - 3.3.1 Textile modeling . . . 34
  - 3.3.2 Homogenization methods for woven textiles . . . 35
  - 3.3.3 Motivation for the development of a new methodology . . . 37
- 3.4 An unstructured non-conformal meshing approach . . . 38

3.4.1 Principle . . . 38
3.4.2 Distance computation and meshing . . . 40
3.4.3 Convergence studies and comparison to the voxel approach 44
3.5 Homogenization of penetrating textiles . . . 51
3.5.1 A strategy to compensate for textile penetrations . . . 51
3.5.2 Sensitivity analyses . . . 55
3.6 Comparison to textiles studied in the literature . . . 59
3.6.1 Case 1: A 3D-woven textile with high penetrations . . . 59
3.6.2 Cases 2 to 6: 3D-woven textiles without penetrations . . . 62
3.7 Discussion about computational times . . . 64
3.8 Conclusion . . . 66

4 Mold compensation strategies **69**
4.1 Objective and literature review . . . 69
4.2 Development of mold compensation methods . . . 71
4.2.1 CAD-based versus mesh-based methods . . . 71
4.2.2 CAD-based methods . . . 71
4.2.3 A mesh-based method . . . 76
4.3 Numerical applications . . . 77
4.3.1 Hypotheses and numerical model . . . 77
4.3.2 Curved C-spar . . . 79
4.3.3 Other applications . . . 88
4.4 Discussion and conclusion . . . 92

5 Experimental validation **97**
5.1 Introduction . . . 97
5.2 Test case definition . . . 98
5.3 Manufacturing of nominal parts . . . 98
5.3.1 VARTM setup . . . 98
5.3.2 Processing conditions . . . 99
5.3.3 Measurements . . . 100
5.4 Curing model and material properties . . . 101
5.4.1 Constitutive model . . . 101
5.4.2 Properties of the epoxy resin RTM6 . . . 102
5.4.3 Properties of the carbon fibers . . . 103
5.5 Homogenization . . . 103
5.5.1 Fiber volume fraction measurement . . . 103
5.5.2 Yarn arrangement measurement . . . 106
5.5.3 Homogenized properties . . . 108
5.6 Simulation of nominal parts and compensation . . . 108
5.6.1 Comparison simulation/experiments for the nominal parts 108
5.6.2 Sensitivity analysis: material properties . . . 114
5.6.3 Numerical compensation . . . 115
5.7 Manufacturing of the compensated parts . . . 118
5.8 Discussion about the twist . . . 124
5.9 Conclusion . . . 125

6 Conclusions and perspectives **127**
6.1 Main results and conclusions 127
6.1.1 The global context 127
6.1.2 Mold compensation 128
6.1.3 Homogenization 129
6.2 Perspectives for future work 130
6.2.1 Mold compensation 130
6.2.2 Homogenization 132

Appendices **135**

A Periodic boundary conditions for FE homogenization **137**

B Detailed comparison unstructured/voxel meshing **147**

C Textile geometrical description **163**

D Best-fit algorithm **167**

E Detailed experimental results **173**

List of publications **183**

Bibliography **185**

Chapter 1

Introduction

1.1 Industrial context

The benefits of composite materials with respect to stiffness and strength expressed per unit mass are widely recognized. Reduction of fuel consumption, environmental impact in the context of increasing demand for international travel, constitute strong arguments in favor of weight reduction of aircraft structures.

Flying lightweight structures is crucial to save cost on fuel consumption. More importantly, over the longer term, global fuel shortage will most likely drive research towards less powerful alternative energy sources. From this point of view, the Solar Impulse 2, a 72-meter wide, 2,300 kg carbon fiber prototype, is an inspiring accomplishment. In the industry, the last decade has been a cornerstone for the full accomplishment of the transition to massive use of composites, with the advent of Boeing's Dreamliner 787 and Airbus' A350 XWB. Their airframes exceeded for the first time the symbolic threshold of 50 % of composites content in terms of weight [1]. Other industries have started to develop composite structures in order to save weight as well. Composites have made their way towards the automotive industry, with different challenges – mainly in terms of rate production and cost optimization [2]. The wind turbine industry is now able to produce large-scale wind turbine blades made out of composites [3], with the complication of setting up a reliable process at such scales and respecting tolerances in terms of aerodynamic profiles.

However, designing and manufacturing composite structures involves many challenges. From the designer's point of view, the heterogeneous, anisotropic nature of composites calls for a detailed understanding, at different scales, of various complex mechanisms and interactions. On the manufacturing side, micro- or mesoscopic defects, such as fiber misalignment, delaminations, internal stresses, resin-rich zones, porosity, are constant concerns. There are also macroscopic "defects". The present thesis focuses on one of the most prominent macroscopic issues: cure-induced distortions.

Cure-induced distortions are the deviations exhibited by a polymer-based composite material when it is removed from its mold. They are the result

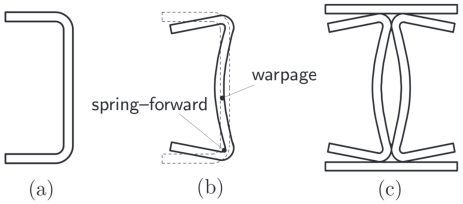


Figure 1.1: Typical distortions of a C-shaped part: (a) intended geometry, (b) distorted geometry and (c) potential assembling problem [4].

of multiple phenomena, such as thermal and chemical shrinkage, material anisotropy, temperature heterogeneity, tool/part interaction or unsuitable process conditions, for instance. The distortions are most commonly experienced in the form of spring-in (or spring-forward), meaning that angles in curved regions tend to close up after cure, and warpage, which is the curvature or twist of initially flat regions. Typical distortions of a curved panel are shown in Figure 1.1. The deformations create a series of problems for the manufacturer or for the end user. For instance:

- The high stiffness of the composite structures can complicate or even make impossible the assembling steps, since the efforts required for matching two parts together may lead to complete failure.
- Even when assembling requires acceptable forces, internal stresses are generated, which are to be subtracted to the in-service stresses that the structure will be able to support. Kappel et al. [5] summarizes the problem of internal stresses in Figure 1.2.
- The current trend is to manufacture more complex parts with integrated stiffeners [6]. While these stiffeners help reduce the amount of distortions, they also make the distortion modes more complex and harder to anticipate and to compensate based on rules of thumb. Moreover, stiffer parts are more difficult to assemble.
- Other complications related to shape non-conformities, such as aerodynamic issues.

1.2 Objective of the thesis

This thesis is a step towards the production of defect-free composite structures, taking advantage of computational methods to accelerate and optimize the design and the processing steps into a one-step high quality manufacturing chain. Since this is a task involving many different aspects, the present work will focus on developing a generic framework to generate composite parts within the targeted geometrical tolerances. More specifically, a series of tools are developed to predict numerically the shape of the mold that enables to produce parts within the manufacturing tolerances, avoiding expensive experimental trials

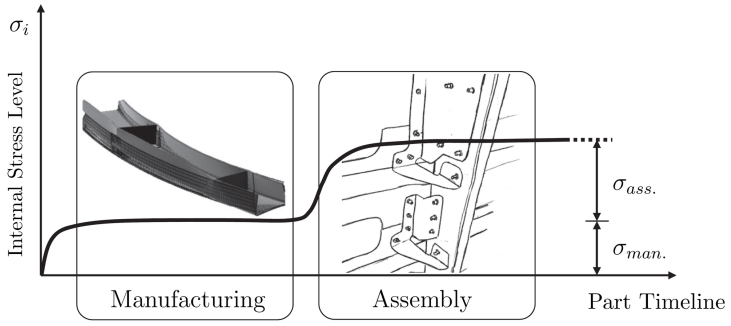


Figure 1.2: The problem of cure- and assembly-induced internal stresses [5].

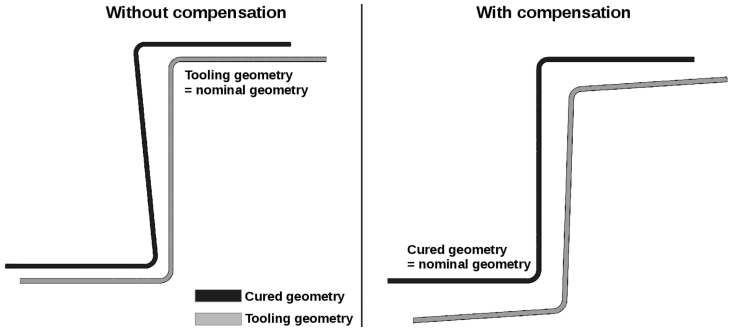


Figure 1.3: Principle of mold compensation.

and tooling design iterations. From now on, this concept is referred to as mold compensation, illustrated in Figure 1.3, where the "nominal geometry" designates the target design. A hypothetical perfect mold compensation numerical framework would require:

- A perfect numerical model of the manufacturing process. Here, "perfect" means that the model is able to predict flawlessly the distortions of any baseline geometry, with any material and any stacking sequence, manufactured using any kind of process. Process modeling is an ongoing research topic at the research center Cenaero [7, 8], where most of this research has been performed, and has received extensive interest from other researchers in the past. Consequently, this thesis does not aim at developing an entirely new modeling chain, and will rely on existing models. Nevertheless, a constant obstacle with all models is the considerable amount of material data, typically several dozens, of different importance [8], needed to obtain reliable numerical predictions. Indeed, the curing process of polymers is a coupled chemical-thermal-mechanical multi-material problem, during which the resin goes through three material states under various curing cycles and mechanical boundary conditions. Ideally, the ad hoc material properties should be characterized by specific material

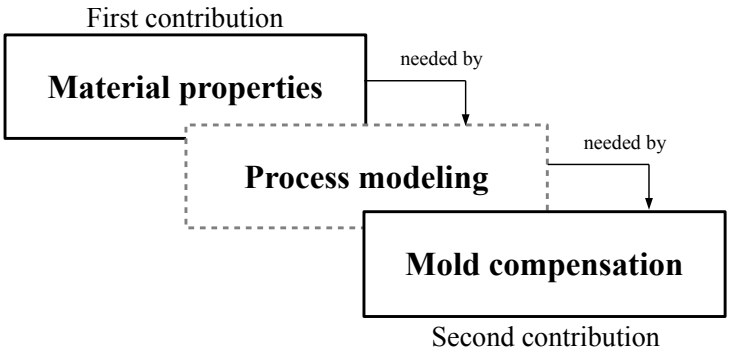


Figure 1.4: Summary of the thesis' contributions and position with respect to process modeling.

testing, in the three directions of orthotropy of the composite and in all material states. This is technically challenging and unrealistically expensive. It is more convenient to use homogenization techniques to predict the properties of the composites based on the intrinsic properties of the constituents (resin and fibers). A first major contribution of this thesis is the development of a generic finite element (FE) procedure to predict the thermo-elastic properties of a wide range of textile composites, including highly-compacted ones. While various analytical approaches are efficient in that respect, the use of FE-based approaches keeps a window open towards non-linear aspects, which require accurate stress-strain states within the composite. The developed approach handles complex textiles with very limited geometrical modeling effort, whereas they often need cumbersome and non-generic developments with other FE-based approaches.

- A perfect mold compensation strategy. Here, "perfect" means that the output of the methodology is the tooling shape that leads to a final composite part with zero deviation with respect to the nominal design. Contrary to process modeling, this line of research is rarely tackled in the literature, focusing only on very simple cases (e.g. [9, 10]). The second major contribution of this thesis is the development of generic mold compensation techniques, suitable to complex geometries and various manufacturing processes and constraints.

Keeping in mind that perfection is not a relevant target, if only due to the manufacturing variability, the purpose of the thesis is more accurately to improve the industrial know-how and to increase the efficiency of tooling design, providing almost turn-key solutions to anticipate and keep shape distortions of composite parts within the manufacturing tolerances. The contributions of the thesis and their position with respect to process modeling are summarized by Figure 1.4.

The generic nature of both contributions is essential. The concepts developed throughout the thesis are influenced by two important precepts:

- The use of this work by an industrial stakeholder for its specific applications must not require more than little additional developments. The tools are, a priori, readily suited to a wide range of geometries and materials. In addition, both the homogenization and the mold compensation procedures are thought as computational chains where software dependency is reduced to a minimum, and open-source software is used when possible. Where FE computations are necessary, the user can choose to employ either Abaqus [11] or Samcef [12], two commonly used commercial FE software, and the extension to other software necessitates limited developments.
- The tools can serve as a basis for further considerations. The focus in this thesis is set on shape optimization, but the window is open towards the study and optimization of a wide range of phenomena related to the manufacturing process, such as residual stresses, energy consumption, or cure-induced microscopic damage.

1.3 Structure of the thesis

The thesis is structured as follows. Chapter 2 provides an overview of the scientific background needed to understand the concepts used throughout the next chapters, for which the thesis does not contribute in terms of research. In particular, this thesis does not contribute to the field of process modeling, but since it is nonetheless an important ingredient of mold compensation, this chapter describes the physical mechanisms leading to cure-induced distortions and the available numerical solutions to solve this problem. Moreover, the manufacturing processes that lie within the scope of the thesis are briefly explained. Chapter 3 is devoted to the development of the FE homogenization procedure fulfilling the objective described previously. First, the existing homogenization solutions for the evaluation of the linear thermo-elastic properties of 2D and 3D woven textiles are reviewed, highlighting why the new methodology is a relevant alternative. Next, the developed approach is presented, consisting in two separate steps allowing the application of FE homogenization to penetrating textiles: a non-conformal distance-based mesh adaptation technique, and a method to correct penetrations based on yarn material properties. The latter is the most original contribution of this chapter. Then, sensitivity and mesh convergence studies are conducted, before comparing the results obtained with this new methodology to experimental results drawn from the literature. Chapter 4 steps into the mold compensation problem. After reviewing the various attempts that have been made in the literature, three compensation techniques are proposed and tested on several numerical test cases. The three methods are complementary and each one has its strengths and weaknesses. The choice of the method is mainly a balance between computation time and manufacturing constraints. Chapter 5 presents the experimental campaign which is undertaken to validate the developments conducted in the previous chapters. To begin with, the test case geometry and materials are described. A doubly-curved geometry is chosen to ensure non-trivial mold compensation, namely a curved

C-spar. The nominal geometry, i.e. without compensation, is manufactured to check the validity of the process simulation. Next, the numerical mold compensation approach is applied, with help of homogenization to determine the material parameters for the simulation. This results in a compensated tooling shape, which is then machined, allowing the production of compensated parts. The final step is to measure the different parts to check that the distortions are indeed considerably reduced. This chapter represents the third major contribution of the project, since such an experimental study cannot be found in the existing literature, at least not with transparent methodologies and results. Finally, Chapter 6 concludes the work by highlighting the key achievements of this thesis, and by proposing a series of interesting topics which could be investigated to improve and extend the capabilities of the developed tools.

Chapter 2

Scientific background

2.1 Composite manufacturing processes

Proper appraisal of the different manufacturing techniques is essential for the development of modeling strategies involving suitable underlying hypotheses. A non-exhaustive review is proposed in this section, focusing on low- to medium-volume production of medium-sized high-performance continuous fibers thermoset based composite parts.

There are numerous manufacturing techniques suitable to composite processing, each with its advantages and constraints. Laminate quality, structural requirements, part dimensions and shape, production rate, economical context, materials at hand, are, among others, elements that will drive the choice of one technique over the others [13]. However, a few common points serve as a basis for all manufacturing processes [14]:

- Some form of molding to shape the composite part is always involved. The mold material and complexity depend on the manufacturing process itself and more importantly on the cost. The tooling can be made of aluminum, steel, invar, or even of composite or solid resin [13].
- At the end of the process, a curing cycle is performed to consolidate the resin from its liquid or viscous state to a solid state.

The fibers can be placed by hand or by an automated process, such as automated fiber placement. At this stage, they can be dry or already pre-impregnated with resin, in which case the material is referred to as prepreg.

2.1.1 The autoclave process

Prepreg processing usually requires the application of a high compacting pressure to increase the fiber volume fraction and to reduce the porosity [15]. The autoclave [16] is a chamber that can withstand this pressure, see Figure 2.1. The temperature of the composite is regulated owing to convective heat exchange with circulating hot air, following the pre-determined curing cycle. Confinement of the composite material is secured by a vacuum bag sealed

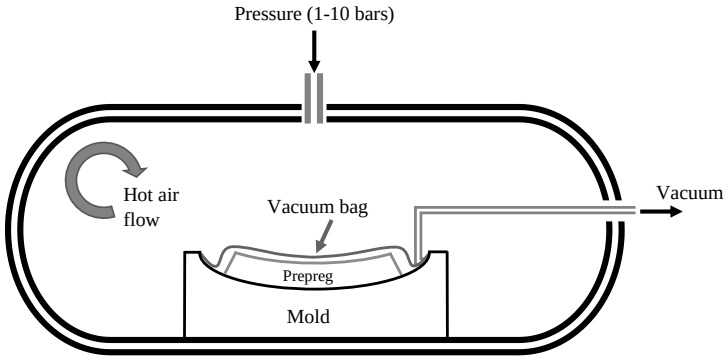


Figure 2.1: Schematic of the autoclave process.

at the periphery of the part. On the one hand, the resulting part quality is very high and only a lower mold is necessary. On the other hand, the structure of the autoclave has the disadvantages of being very expensive and limited in size, typically a few meters long. This drives research towards out-of-autoclave prepreg processing, whose main challenge is to counter the presence of porosity due to low compacting pressure [17–19]. Moreover, the composite part has only one "A-surface", i.e. one surface with smooth surface finish, and prepregs must be stored at low temperatures.

2.1.2 The RTM process

The resin transfer molding (RTM) process [20] is an alternative to produce high quality, near-net shaped parts. Dry fabric is placed into a closed mold, see Figure 2.2. The two half molds are sealed together by a clamping force, exerted either by a press or by another mechanical device. If the mold is not self-heating, the press has to play this role. Low viscosity resin is then injected at high pressure, allowing full and relatively fast impregnation of the fibers. The cure is performed inside the mold. The dry preforms and resins are generally less expensive than prepregs and may sometimes be stored at room temperature. Furthermore, a smooth surface finish is achieved on all exposed surfaces, and a low void conten is expected [21]. On the down side, self-heating molds are expensive, and the alternative of using a press limits the size of the parts. A variant is the SQRTM process [22], where the dry fabric is replaced by prepregs and where the injected resin serves only as in-mold compaction pressure.

2.1.3 The VARTM process

The vacuum-assisted resin transfer molding (VARTM) process (Figure 2.3) is a low-cost alternative to the RTM process, where the resin flow is driven by the atmospheric pressure instead of a piston-induced pressure [23]. This drastically reduces the impregnation speed, and a flow-facilitating medium is generally needed on top of the fabric, which prevents the use of an upper mold. The

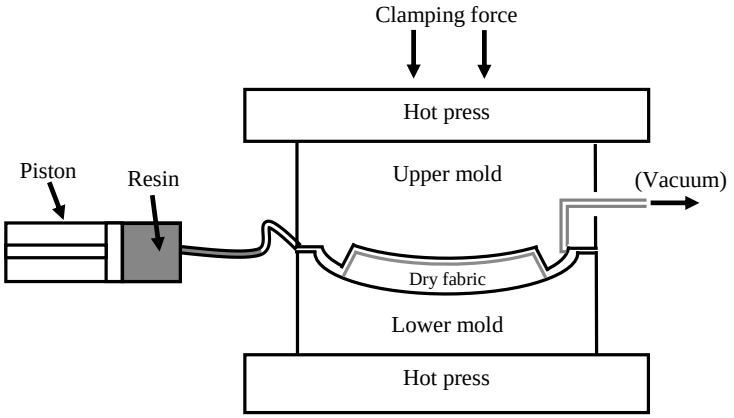


Figure 2.2: Schematic of the RTM process.

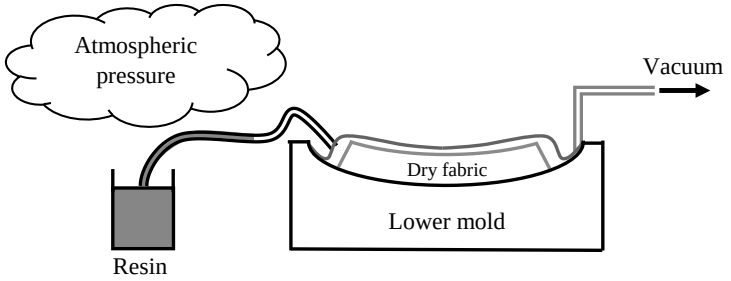


Figure 2.3: Schematic of the VARTM process.

lower pressure also results in a higher void content, although using a double bag technique helps improve this aspect [24]. Contrary to the aforementioned processes, the part size is, in theory, not limited, which is why the VARTM process finds applications in the naval [25] or wind turbine [3] industries. This process is not used for high performance applications, but it is still part of this review because it has been used in the experimental validation section of this thesis, Chapter 5.

2.2 Manufacturing-induced distortions

2.2.1 Cure development

In order to understand the cure-induced distortions, it is necessary to grasp what a curing mechanism implies. The curing of a composite material is actually that of the matrix, i.e. the thermoset resin. After the molding process, the curing step aims to give the composite its final structural performance by transforming the liquid or viscous resin into a solid material. The solidification of the resin stems from the cross-linking of the polymer chains, an irreversible process. It is a heat-activated auto-catalytic exothermic chemical reaction. The

temperature required to activate the reaction ranges from room temperature for low-cost resins to about 180°C for the high performance epoxy resins such as the ones studied in the present work, namely the 8552 and RTM6 resins by Hexcel, and typical processing time is a few hours [26, 27]. Figure 2.4 shows the manufacturer's recommended curing cycle for the 8552 epoxy resin [27], and the corresponding cure development. The degree of cure X, which represents the advancement of the curing reaction, is the most fundamental quantity to understand the curing process of a composite and its distortions. It drives the dramatic change in the resin stiffness, its thermal expansion and its chemical shrinkage, as will be discussed further on. The resin is liquid until X reaches a certain level X_{gel}, called the gel point. This value is assumed to be a constant, characteristic of the resin. After this point, the resin is in the so-called rubbery state, and it can withstand some stresses with a very low stiffness [28]. As the cure progresses, the glass transition temperature T_g increases. T_g is the temperature at which the material transitions between the glassy (or solid) and rubbery states. The glassy state is reached when T_g becomes higher than the temperature of the material. From this point on, the mobility of the polymer chains drops drastically: the reaction becomes diffusion-controlled [29], as opposed to chemically-controlled, the cure slows down and eventually stagnates. Full curing is not necessarily reached, depending on the cure temperature. A higher final degree of cure can then be reached by increasing the cure temperature or by performing a post-cure step, leading to improved material properties [30]. A first temperature dwell at a lower temperature (here 120°C) is commonly applied to limit the amount of exothermic heat [31] and to lower the viscosity of the resin in order to degas it more easily. Then the material is heated and maintained at the cure temperature until a desired degree of cure is reached. This hold is generally long enough for the resin to reach the glassy state, by increasing of the glass transition temperature. Typical heating and cooling rates are 1 to 3°C/min for epoxy resins.

2.2.2 Origins of the distortions

This section presents the main phenomena responsible for the development of cure-induced distortions and residual stresses.

Thermal and chemical shrinkage, curing cycle

A prominent effect is the development of non-reversible dilatational strain during the cure, dependent on the temperature curing cycle. On the one hand, chemical shrinkage is due to the increasing density of thermoset resins as curing progresses, as a result of the conversion of secondary bonds between monomer molecules into covalent bonds [33], the latter being shorter than the former. Since cure is an irreversible process, the change in density is permanent and significant, typically around 5 % for a completely cured neat epoxy resin [34, 35]. Whether or not the reduction in volume plays a significant role in the residual stresses and shape distortions seems to depend on the material. For instance, White and Hahn [36] have observed for the material system IM6/3100 that the majority of chemical shrinkage occurs while the material is highly viscoelastic

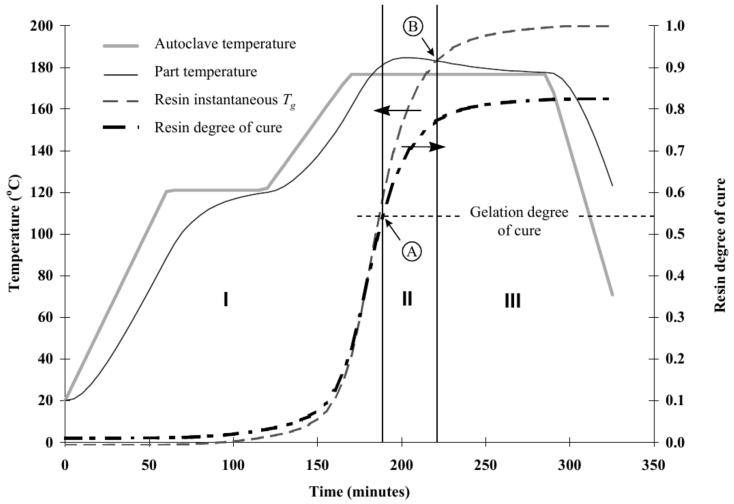


Figure 2.4: Typical curing cycle and cure development for a high performance epoxy. Point A is gelation, point B is vitrification. Phases I to III refer to liquid, rubbery and glassy states, respectively [32].

and the stresses are released very quickly. To the contrary, Ochi et al. [37] have studied several Epikote epoxy resins and, for some of them, measured substantial levels of shrinkage when the material is elastic, generating important internal stresses.

On the other hand, thermal shrinkage is caused by the different behaviors of the resin during the evolution through three material states. During the heating phase of the curing cycle, the resin is in a liquid or rubbery state and undergoes a certain thermal expansion. Only the expansion experienced in the rubbery state results in the creation of residual stresses and subsequent shape distortions, since, in the liquid state, the resin just flows through the fibers. During the cooling phase, the resin has already transitioned to the glassy state, in which the coefficient of thermal expansion (CTE) is smaller than in the rubbery state. Consequently, the thermal expansion experienced during the heating phase is not necessarily canceled out by the thermal contraction during the cooling phase. The latter is usually higher than the former, hence the term "thermal shrinkage". Figure 2.5 schematically depicts the development of the dilatational strain ε^E, to which the chemical and thermal shrinkage contribute.

In addition to the combination of shrinkage with anisotropy leading to shape distortions, as described in the next paragraph, an important consequence of dilatational strain is the influence of the temperature cycle. Indeed, it can be deduced from Figure 2.5 that reaching gelation at a lower temperature leads to larger thermal expansion in the rubbery phase, which could balance out the subsequent chemical shrinkage and thermal contraction, thus minimizing the distortions. This has been confirmed experimentally by White and Hahn [38] and Albert and Fernlund [39], who have observed reduced residual stresses and shape distortions when using a two-dwell curing cycle compared to a one-dwell

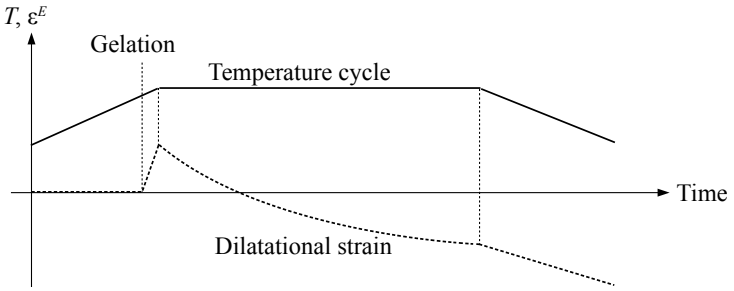


Figure 2.5: Development of dilatational strain resulting in residual stresses.

cycle. White and Hahn [38] have also evidenced reductions in distortions by decreasing the cure temperature or the dwell time, owing to reduced chemical shrinkage, albeit with degraded material properties due to a lower final degree of cure. Finally, a lower cooling rate seems to produce less distortions [38, 40]. This effect is attributed to increased stress relaxation allowed by the lower cooling rate, but these results have been obtained with non-standard cooling rates (0.56 K/min and 5.6 K/min for White and Hahn [38]; 0.56 K/min and 4.2 K/min for Sarrazin et al. [40]). A numerical study by Brauner [41] shows no influence of the cooling rate when realistic values are used.

Anisotropy and stacking sequence

Since the fibers are chemically inert and exhibit a much lower CTE than epoxy resins, thermoset composite materials are highly anisotropic, which is the reason why dilatational strain results in spring-in. Indeed, it can be shown [4] that an L-shaped bracket initially forming an angle θ (Figure 2.6), when subjected to orthotropic strains, undergoes a change of angle $\Delta\theta$ which amounts to:

$$\Delta\theta = \theta\frac{\varepsilon_t - \varepsilon_r}{1 + \varepsilon_r}, \tag{2.1}$$

where ε_r and ε_t are the strains in the radial (through-thickness) and tangential directions, respectively. Since the tangential strain is constrained by the fibers (i.e. virtually zero) and the radial strain is negative, $\Delta\theta$ is positive, hence the spring-in effect. Eq. 2.1 can give a reasonably good approximation of the spring-in angle, provided that all the other effects are negligible [42]. Another well-known effect of anisotropy is the warpage of asymmetric layups, an academic example of which is a flat plate made of 0-degree unidirectional plies topped by 90-degree plies. Since both series of plies tend to shrink in orthogonal directions with respect to one another, a mismatch occurs and the plate distorts into a saddle shape, as shown in Figure 2.7. While this layup is not good practice and would not be found in an industrial application, asymmetry is not uncommon and the same mechanisms come into play, albeit to a less exaggerated extent.

The in-plane anisotropy also influences the distortions. For instance, Albert and Fernlund [39] have observed experimentally that angled composite parts

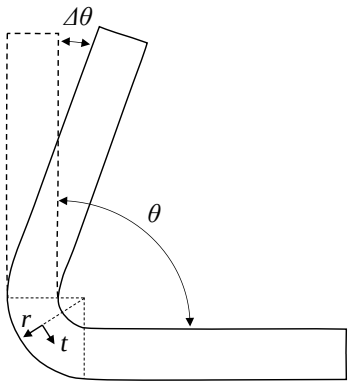


Figure 2.6: Spring-in resulting from anisotropic strain.

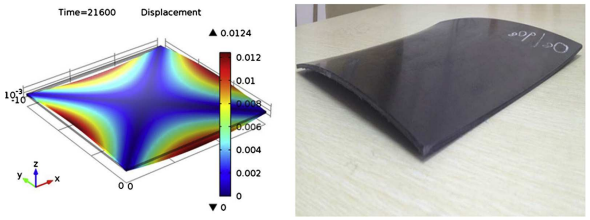


Figure 2.7: Distortion of an asymmetric flat plate composed with a layup $[0_8/90_8]$ [43].

exhibit less spring-in when the degree of in-plane anisotropy is higher (unidirectional laminates compared to quasi-isotropic laminates). It is explained by an associated decrease of the through-thickness contraction, due to Poisson's effect.

Tool-part interaction

A vast research topic is the study of the influence of the tool on the shape distortions of the composite part. The main factor is the traction applied by the tool to the layup due to the CTE mismatch between these two materials. The effect is thus much higher in the case of steel [44] or aluminum [45] tooling compared to Invar [46], whose CTE is virtually zero, but this advantage comes with a higher price. This issue is more sensitive when dealing with autoclave processing, since the one-sided tool applies asymmetric in-plane forces to the layup, and the high pressure increases the friction between the metal and the composite. Several mechanisms have been proposed to account for this effect, including inter-ply slippage (Figure 2.8) or fiber volume fraction gradients due to resin bleeding [47]. The phenomenon can be mitigated by decreasing the friction between the tool and the composite, for instance with the insertion of Mylar or propylene sheets at the interface [39, 45, 48]. In the case of the RTM process, the pressure is distributed uniformly on the part, and friction between the mold and the composite is more easily neglected [41].

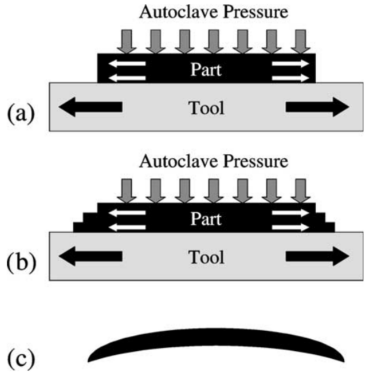


Figure 2.8: Proposed mechanism for warpage due to the tool-part interaction: (a) tool expands when heating to prepreg cure temperature. Friction/bonding at interface induces tensile stresses in lay-up; (b) inter-ply slippage relieves fiber stresses preferentially in layers furthest from tool face. Stress gradient is locked in when prepreg cures; (c) Laminate bows away from tool face [46].

Inhomogeneities and variability

To the aforementioned sources of residual stresses must be added their combination with effects that deviate from the idealized process, whether they are inherent to the process, such as temperature gradients in massive metal molds, or the result of imperfections. Temperature gradients create inhomogeneities in the course of the curing and, consequently, an imbalance in the residual stresses which can result in warpage [32]. In particular, through-thickness gradients can lead to a strain mismatch between the plies, similar to what is observed for asymmetric layups. Thermal gradients can be caused for instance by asymmetric thermal contact conditions, thermal inertia of the mold, thermal gradient in the autoclave, or heterogeneous mold heating conditions, to name a few.

Potter [49] has established a list of about 60 sources of variability for the autoclave and RTM processes, related to the materials, to the molding process and to the post-molding process (e.g. machining, non-destructive testing). It is not possible to evaluate the influence of each source on the distortions. This list is used as a way to enhance process control and develop potential routes to develop zero defect design. Since the physical mechanisms that drive shape distortions are known, it is fundamental to understand how the process and its variability are related to those mechanisms. For instance, it has already been stated that anisotropy is a prominent cause of shape distortions. Since the fiber content is directly linked to anisotropy, fiber volume fraction gradients are likely to have an impact on shape distortions. Other sensitive variability sources are fiber misalignment, corner thickening or void content, among others.

2.3 Process modeling – an overview

2.3.1 Preamble

The numerical prediction of the cure-induced distortions necessitates models to predict, at any point in space and in time, the following quantities:

- the degree of cure X, to know the advancement of the reaction;
- the glass transition temperature T_g;
- the coefficients of thermal expansion and of chemical shrinkage, since they are the main source of distortions;
- the temperature T;
- the mechanical properties of the composite.

The present section describes the most commonly used models for each of these quantities.

2.3.2 Cure kinetics

Cure kinetics pertain to the evolution of the degree of cure X during the hardening of polymer materials. There exist two modeling alternatives: mechanistic or phenomenological models. While the former describe the chemical reactions that actually take place within the epoxy resin [50, 51], phenomenological models are heavily favored in the literature. They are simpler, and no microscopic information is generally needed about the concentrations of the different compounds, when modeling cure-induced distortions of composite parts. The degree of cure X relates to the advancement of the curing reaction. It is defined as the ratio between the heat released by the cure reaction and the maximum possible heat per unit mass released by the reaction H_T (i.e. for a fully-cured sample):

$$X(t) = X_0 + \frac{1}{H_T} \int_0^t \frac{\mathrm{d}H}{\mathrm{d}\tau} \, \mathrm{d}\tau, \tag{2.2}$$

where X_0 is the degree of cure at the beginning of the experiment (usually zero), and $\mathrm{d}H/\mathrm{d}\tau$ is the instantaneous heat flux per unit mass released by the reaction. X is a dimensionless value varying between 0 and 1. The vast majority of phenomenological models assume that the cure rate is solely a function of the degree of cure and of the temperature:

$$\frac{\mathrm{d}X}{\mathrm{d}t} = f(X, T). \tag{2.3}$$

Numerous models are available in the literature (e.g. [52, 53]). Listing them here is not relevant, the only objective being to find a function f that matches as close as possible the experimental measurements. The models that perform the best are the ones that account for the auto-catalytic nature of the reaction and for the diffusion effect which limits the cure rate in the glassy state [50], and several models are suitable for that purpose. The most commonly used model is the one developed by Sourour and Kamal [54], in Eq. 2.4, corrected

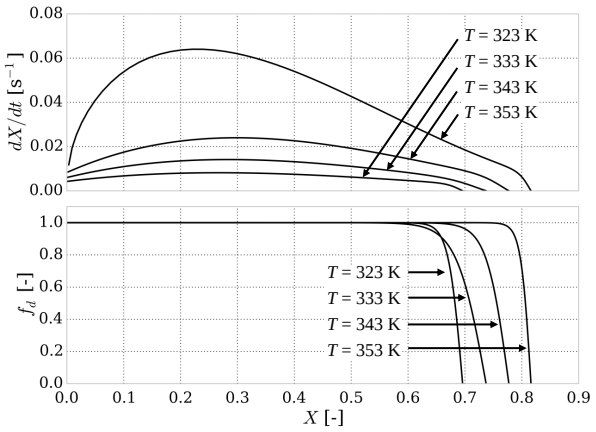


Figure 2.9: Typical cure kinetics model and diffusion factor f_d. The curves are reconstructed from [55] for the DGEBA-PACM thermoset system.

by a diffusion function f_d which tends to zero when the low mobility of the polymer chains prevent further cure:

$$\frac{\mathrm{d}X}{\mathrm{d}t} = (k_1 + k_2 X^m)(1 - X)^n f_d(X), \tag{2.4}$$

where k_1 and k_2 are rates that follow Arrhenius relationships: $k_i = A_i e^{-E_i/RT}$, where T is in Kelvin. The term X^m guides the aforementioned auto-catalytic aspect. A popular diffusion function has been defined by Fournier et al. [55] with Eq. 2.5, where X_f is a logarithmic function of temperature and can be directly interpreted as the maximum degree of cure attainable for a given cure temperature. An example of this model is shown in Figure 2.9.

$$f_d(X) = \frac{2}{1 + \mathrm{e}^{(X - X_f(T))/b}} - 1. \tag{2.5}$$

The parameters of a kinetic model are most commonly fitted from Differential Scanning Calorimetry (DSC) measurements, monitoring the heat flux released during curing reactions. Other researchers [56] choose to use direct interpolation of DSC data, instead of trying to fit to an analytical model.

2.3.3 Glass transition temperature

The glass transition temperature T_g is an increasing function of X. Several models have been proposed [57–59]. As for cure kinetics, they are different ways of fitting experimental data. The most commonly used model has been proposed by DiBenedetto [57]:

$$T_g(X) = T_{g0} + (T_{g\infty} - T_{g0}) \frac{\lambda X}{1 - (1 - \lambda)X}, \tag{2.6}$$

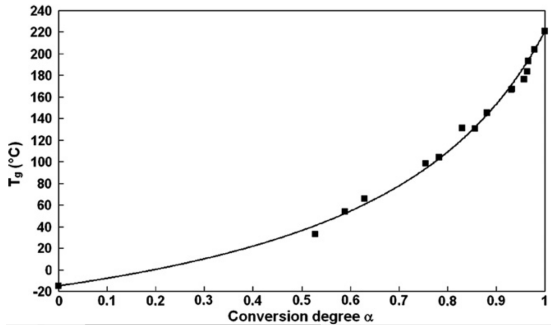


Figure 2.10: DiBenedetto equation: comparison between experiments and model for the RTM6 resin (here, α is the degree of cure) [61].

where T_{g0} is the T_g of an uncured sample, $T_{g\infty}$ the T_g of a fully-cured sample, and λ is a fitting parameter. An example of such a model is illustrated in Figure 2.10 for the RTM6 epoxy resin. The glass transition temperature can be measured by DSC or dynamic mechanical analysis (DMA), for instance [60].

2.3.4 Chemical shrinkage and thermal expansion

Thermal expansion

As explained previously, the CTE of thermoset resins changes dramatically during the curing process. An example of this variation is provided in Figure 2.11. It is common practice (e.g. [62, 63]) to use separate values for the rubbery state and for the glassy state, the CTE being constant within each state. Zarrelli et al. [64] have measured the CTE of an epoxy resin, concluding that it is 1.8 times higher in the rubbery state than in the glassy state. It is possible to further tune the model by measuring the variation of the CTE within the glassy state [41, 65]. The CTE can be measured by thermo-mechanical analysis (TMA) [41] or optical measurements [66], for instance.

Chemical shrinkage

A widely spread observation is that the chemical shrinkage of neat resin, i.e. the volumetric shrinkage related to the curing reaction, is directly correlated to the degree of cure. A common assumption [4, 62, 68] is that the chemical shrinkage is proportional to the degree of cure. This has been confirmed by experimental results for "a proprietary thermoplastic-modified epoxy resin" [64]. Other researchers find the shrinkage to be bi-linear with an inflexion point at gelation. Li et al. [35] have measured bi-linear shrinkage for the MY750 epoxy resin by a gravimetric method. In that case, the slope was higher before the gel point, whereas Khoun and Hubert [69] have used the same method and found a higher slope after gelation for the CYCOM 890RTM epoxy resin. They have also measured shrinkage by rheology, with consistent results, although this method does not permit to measure volumetric changes before the gel point. Rheology has

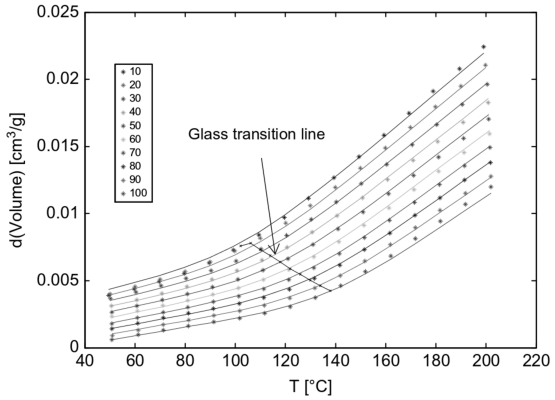


Figure 2.11: Volume change of a filled epoxy resin with various contents of filler [67]. Below the glass transition, the material exhibits a smaller CTE.

also been used by Haider et al. [70], who have found linear shrinkage with respect to the degree of cure for a polyester resin, with a plateau after about 80 % of cure.

In addition, a few non-linear models have been proposed. White and Hahn [36] have used the following model for the transverse shrinkage of the epoxy prepreg IM6/3100:

$$\varepsilon_{ch}^{T} = \begin{cases} \beta_1 10^{\beta_2 X} & \text{if } X \leq X_c \\ \varepsilon_{ch,final}^{T} & \text{if } X > X_c \end{cases}, \tag{2.7}$$

but very poor correlation with their experimental results has been obtained. Finding a degraded fit with the linear model in the late stages of cure, Hill et al. [71] have proposed to relate the chemical shrinkage of an unsaturated polyester resin to the radical concentrations:

$$\varepsilon_{ch} = S_f \frac{c\bar{R}^n}{1 + c\bar{R}^n}, \tag{2.8a}$$

$$\bar{R} = \frac{R}{R_f - R}, \tag{2.8b}$$

where R is the radical concentration, R_f its final value, and S_f the final value of the chemical shrinkage.

Finally, Tai and Chou [72] combine the CTE and the coefficient of chemical shrinkage into one coefficient, but it does not seem natural to combine two phenomena (thermal expansion and chemical shrinkage) when one is reversible and the other one is not. Such a model is likely to be correct for only one curing cycle.

2.3.5 Heat transfer in thermoset composites

Heat transfer is an important aspect of process modeling when it comes to thermoset composites for two main reasons:

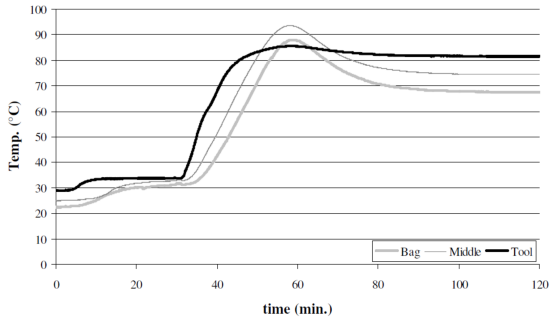


Figure 2.12: Illustration of the exothermic nature of the curing reaction by temperature measurements during the cure of a 12.5 mm thick part [58].

- The temperature distribution drives the cure reaction, which in turn is the source of the distortions, as it has been already detailed. This distribution can be heterogeneous in some cases. For instance, if a large mold with high thermal inertia is used, or when the heating technique itself is not homogeneous [73–75].
- The cure reaction is an exothermic reaction, which means that it releases heat. This phenomenon is proportional to the cure rate and it is thus more intense between the gel point and the glass transition. An illustration is proposed in Figure 2.12, where the temperature in the middle of a 12.5 mm thick composite part reaches a peak higher by 5 to 10°C compared to the temperature on its external faces. This exothermic peak can be much higher for other resins, for instance the RTM6 [76].

For thin composite parts, heat transfer may sometimes be disregarded, as the temperature distribution is less likely to be heterogeneous, and the exothermic heat is dissipated much faster. In that case, the temperature field is considered as homogeneous, which has the double advantage of reducing the computational time and of suppressing the need for additional material data, such as thermal conductivity. However, understanding the underlying physics remains important to be able to assess the validity of this hypothesis.

The evolution of the temperature over time at a given point of a composite part is governed by the transient Fourier anisotropic heat conduction equation, where a source term is added to account for the heat released by the curing reaction [32]:

$$\frac{\partial}{\partial t}(\rho C_p T) = \nabla \cdot (\overline{\overline{\lambda}} \nabla T) + q(X,T), \tag{2.9}$$

where ρ is the density of the composite, C_p its specific heat, $\overline{\overline{\lambda}}$ its thermal conductivity tensor, and ∇ denotes the gradient operator. $q(X,T)$ is the energy per unit time released by the curing reaction of a unit volume of composite material. Given the definition of the degree of cure X, and taking into account the fact that Eq. 2.9 deals with a composite and not a pure epoxy, follows

directly the expression of q:

$$q(X,T) = \rho_r(1-k_f)H_T\frac{\mathrm{d}X}{\mathrm{d}t}, \tag{2.10}$$

where ρ_r is the density of the resin, and k_f the fiber volume fraction within the composite.

2.3.6 Mechanical behavior of thermosets during cure

Modeling the mechanical behavior of thermoset materials during the curing process is complex and a variety of models have been proposed over the years. They can be classified in two groups: cure-hardening instantaneous linear elastic (CHILE) models and viscoelastic models. The latter account for time-dependent stress relaxation but require very cumbersome material characterization [77]. The former are more computationally efficient but lack the physical faithfulness of the viscoelastic models, especially in the vicinity of the glass transition. Brockman et al. [78] have studied the different models and show that commercially available CHILE models perform well, except when a post-cure step is imposed to the composite part. This is likely due to the fact that the matrix undergoes a slower glass transition during post-cure than during cure, and viscoelastic effects would have more time to develop. Zobeiry et al. [79] and Bracquart [80] have implemented both types of models and observed no significant difference, but post-cure has not been studied. The viscoelastic approach may also be useful when a very accurate prediction of the mesoscopic stresses inside the composite is required. For instance, when a machining simulation is performed after the curing simulation. Since this is not the case in the present thesis, and since post-cure is also not studied, only CHILE-based models are used. An example of viscoelastic model is given below for the sake of completeness.

Viscoelastic models

Viscoelastic approaches are referred to by Zobeiry et al. [79] as the "gold standard" for cure modeling of thermoset materials. Based on the following assumptions:

- the resin is isotropic, linearly viscoelastic and exhibits a thermorheologically simple behavior;
- the time-temperature-conversion superposition principle is invoked, meaning that an increment of time at fixed temperature and fixed degree of cure has the same effect as an increment of temperature at fixed time and fixed degree of cure, and as a (negative) increment of degree of cure at fixed time and fixed temperature;

the corresponding constitutive equation is:

$$\sigma_{ij}(t) = \int_0^t C_{ijkl}(\xi(t)-\xi(\tau))\frac{\partial(\varepsilon_{kl}-\varepsilon_{kl}^E)}{\partial\tau}\mathrm{d}\tau, \tag{2.11}$$

where C is the stress relaxation tensor, σ is the stress, ε is the total strain and ε^E the dilatational strain resulting from thermal expansion and chemical shrinkage. ξ is called the reduced time, given by:

$$\xi(t) = \int_0^t \frac{1}{a_T} \mathrm{d}\tau, \tag{2.12}$$

where a_T is the shift factor that enables to derive the behavior of the material at any temperature and degree of cure from the behavior at a reference temperature and a reference degree of cure (the so-called "master curve").

Eqs. 2.11 and 2.12 provide the framework for the description of the viscoelastic behavior of thermosets. Additional models are required to represent the relaxation modulus and the shift factor. Among other works, let us cite the model by Simon et al. [77], who describe the isotropic shear relaxation modulus G as a sum of n Maxwell elements and the shift factor with the Williams-Landel-Ferry equation, for the 8551-7 epoxy resin:

$$G(t) = G_r + (G_g - G_r) \sum_{i=1}^{n} g_i \mathrm{e}^{-t/a_T \tau_i}, \tag{2.13}$$

$$\log a_T = \left(\frac{b}{T - T_\infty} - \frac{b}{T_{ref} - T_\infty} \right) - \left(\frac{b}{T_g(X) - T_\infty} - \frac{b}{T_g(X_{ref}) - T_\infty} \right), \tag{2.14}$$

where T_{ref} and X_{ref} are the reference temperature and the reference degree of cure for the master curve, respectively, G_r is the completely relaxed modulus, G_g is the unrelaxed modulus, τ_i are relaxation times, T_g is the glass transition temperature (given for instance by Eq. 2.6) and the other values are fitted parameters. Using such a model requires extensive material characterization, such as relaxation tests or DMA at various degrees of cure and temperatures.

CHILE models

CHILE models (for Cure Hardening Instantaneous Linear Elastic) neglect relaxation effects and consider the material as linear elastic at every point in time [32], considering an evolution of the elastic modulus during the curing cycle:

$$\sigma_{ij}(t) = \int_0^t C_{ijkl}(\tau) \frac{\partial(\varepsilon_{kl} - \varepsilon_{kl}^E)}{\partial \tau} \mathrm{d}\tau. \tag{2.15}$$

where C is the elastic tensor. Once again, a model is needed to describe the evolution of C during the curing cycle, transitioning from a very low modulus in the rubbery state to a high modulus in the glassy state. Several models have been proposed for the Young's modulus of curing epoxies, gathered in Figure 2.13.

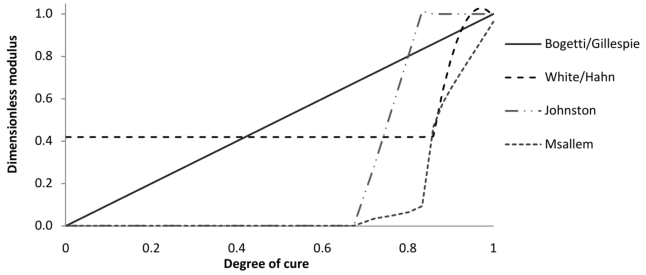


Figure 2.13: Several models for the development of the elastic modulus during cure [41].

Starting from a viscoelastic model, Svanberg and Holmberg [62] formulate a new CHILE-based approach to take into account the so-called "frozen-in deformations", which are due to the dramatic increase of relaxation times during the vitrification. The incremental formulation of their model is the following:

$$S_{ij}(t+\Delta t) = \begin{cases} 0 & T \geq T_g(X) \\ S_{ij}(t) + (C^g_{ijkl} - C^r_{ijkl})\Delta(\varepsilon_{kl} - \varepsilon^E_{kl}) & T < T_g(X) \end{cases}, \quad (2.16a)$$

$$\Delta\sigma_{ij}(t) = \begin{cases} C^r_{ijkl}\Delta(\varepsilon_{kl} - \varepsilon^E_{kl}) - S_{ij}(t) & T \geq T_g(X) \\ C^g_{ijkl}\Delta(\varepsilon_{kl} - \varepsilon^E_{kl}) & T < T_g(X) \end{cases}, \quad (2.16b)$$

where C^r and C^g are the elastic tensors in the rubbery and glassy states, respectively (summation over repeated indices is implicit). One of the main assumptions of this model is that these matrices are constant, i.e. the material properties do not evolve during the curing except at the glass transition. The underlying hypothesis is the immediate relaxation exhibited by the material in the rubbery state, and the absence of relaxation in the glassy state. In Eq. 2.16, the term $S_{ij}(t)$ is not zero only when the material transitions from the glassy to the rubbery state, which usually happens only if a post-cure step is performed. This term differentiates Svanberg's model from classical CHILE models, forming a more general framework. It is the approach followed in the present thesis for the numerical prediction of cure-induced distortions.

2.3.7 Modeling strategies and existing software

Once the physics of the problem are understood and each phenomenon is modeled adequately, an algorithm is needed to solve the equations. Figure 2.14 schematically summarizes the generally used procedure: starting from an initial state, the heat equation is solved in conjunction with the chosen kinetics model. This results in a distribution of temperature, degree of cure and glass transition temperature over the structure. These three fields determine the coefficients of chemical shrinkage and thermal expansion, as well as the mechanical properties, which are transmitted to the mechanical simulation to solve the constitutive equation. The thermo-mechanical coupling can either be weak, staggered or strong. In the first case, the entire thermal simulation is

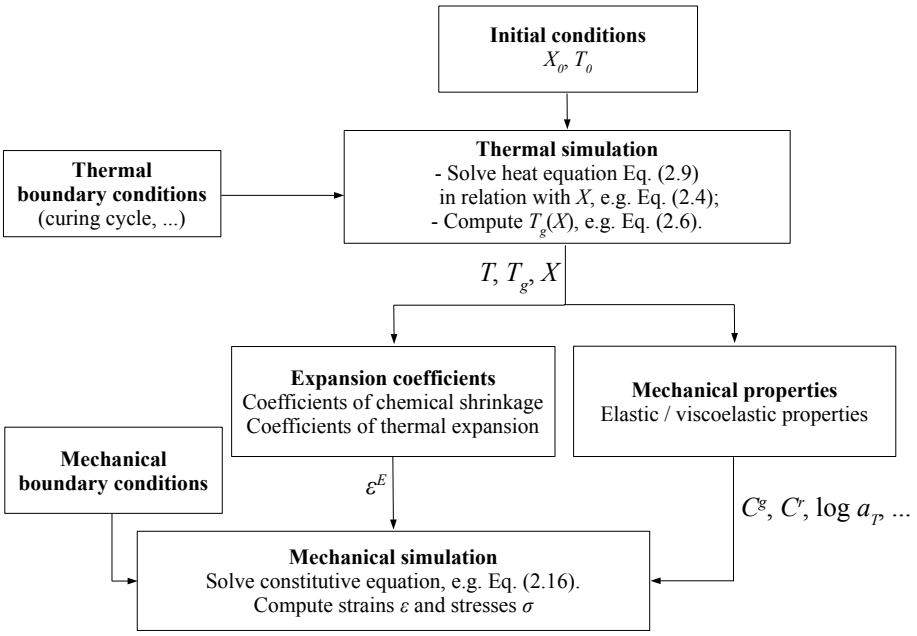


Figure 2.14: Schematic of the resolution of a curing model.

performed and used as an input to the mechanical simulation. In the second case, this communication is performed at every time step. In the case of strong coupling, all the equations are solved simultaneously at each time step. Since the mechanical behavior has no influence on the thermal behavior, except for some second-order effects (e.g. distortions leading to a loss of thermal contact), the choice of the coupling method has almost no influence on the solution. However, depending on the software, it may be more practical and/or more efficient to choose one or the other method.

General-purpose finite element packages, such as Abaqus [11] or Samcef [12], provide the possibility to implement the cure modeling via user subroutines [7, 41, 62]. Wijskamp [4] has developed a modified classical laminate theory formulation accounting for shape distortions and has implemented it in the in-house FE software DiekA. Other researchers choose to develop software specific to cure modeling. For instance, the work of Johnston [32] has given birth to the COMPRO software, which is now commercially available. The PRECIMOULD project has lead to the development of the Lusas HPM software [81], which now seems abandoned. Samcef and ESI PAM-Distortion [82] encapsulate built-in capabilities for the prediction of cure-induced distortions.

2.4 Conclusion

This chapter has given an overview of the main driving forces which can lead to distortions of composite structures, and of the modeling strategies which can be put into place to reproduce those phenomena. Any consistent process model must account for:

- the development of the curing reaction, via the degree of cure X, the glass transition temperature T_g and the change of state of the resin. Phenomenological models which monitor the reaction by the heat generated by the reaction provide sound and simple implementations of these quantities;
- the dilatational strain, which comprises thermal and chemical strains. Most researchers consider a piecewise evolution, with inflexion points at gelation and at the glass transition;
- the evolution of the stiffness of the composite material throughout the curing cycle. CHILE and viscoelastic models are the most widely used, the former being much simpler than the latter. Viscoelastic models can be interesting in case of non-standard curing cycles (e.g. with fast heating or cooling ramps), in the presence of a post-curing step, or if a very detailed prediction of the internal stresses is required.

The temperature may be considered as uniform (following the curing cycle) if the composite is thin enough and if the manufacturing process is appropriate. Otherwise, a transient thermal simulation must be considered to predict the temperature field, possibly accounting for the heat generated by the reaction. In any case, complicating the simulation increases the need for material data. The curing simulations performed in Chapters 4 and 5 follow the simpler route by implementing a CHILE model and assuming a homogeneous temperature, as well as small strains and rotations. This is however not a limitation of the methodology, but a way to speed up the computations and simplify the material characterization. The procedures developed in the thesis are also applicable to more advanced process modeling strategies.

Chapter 3

Non-conformal mesh finite element homogenization

3.1 Introduction

3.1.1 Scope

The aim of this chapter[1] is to provide a generic framework for the determination of the thermo-elastic properties of continuous fiber reinforced polymers (CFRP). The focus is placed on highly-compacted textiles, since their modeling and homogenization give rise to a series of problems. The scope of this chapter, and therefore of the homogenization facet in this thesis, is limited to the following aspects:

- The study is restricted to the linear elastic regime. As explained in Chapter 2, the viscoelastic behavior of the polymers may be ignored under the usual processing conditions. Non-linear phenomena, such as cure-induced damage, delamination or failure, are not considered.
- The main objective is the determination of the thermo-mechanical properties required to perform a coupled chemical-mechanical curing simulation, i.e. the elastic moduli, the CTEs and the coefficients of chemical shrinkage in the different directions of anisotropy. In the cases studied in the subsequent chapters, the temperature is assumed to be homogeneous and thermal properties such as thermal conductivity or specific heat, are not needed.
- Only textile composites are considered. They consist of tows, or yarns, which are interlaced together following a certain periodic pattern, as illustrated in Figure 3.1. Each yarn is composed of several thousands of fibers, thus creating a new intermediate scale between the microscopic

[1] *Reproduced in part from:* B. Wucher, S. Hallström, D. Dumas, T. Pardoen, C. Bailly, Ph. Martiny, F. Lani (2016). Nonconformal mesh-based finite element strategy for 3D textile composites. *Journal of Composite Materials*, first published on September 20, 2016, *doi:10.1177/0021998316669875.*

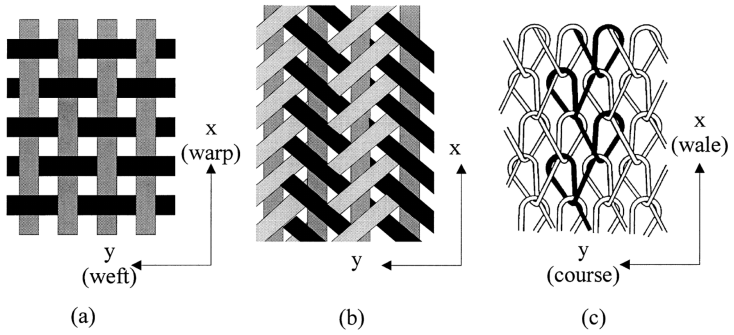


Figure 3.1: (a) Plain-woven fabric, (b) triaxially-braided fabric and (c) warp-knitted fabric [84].

and the macroscopic scales. Figure 3.2 provides an overview of the different scales involved in the multi-scale analysis of textile composites. Homogenization consists in predicting the behavior of the material at the macroscopic scale from the properties of the constituents: the fibers and the resin. In this chapter, the transition from the microscopic scale to the mesoscopic scale (i.e. the prediction of the behavior of the yarn) is performed with the help of a micromechanics-based model. This is based on the assumption that the yarn can be considered as unidirectional (UD) material. The transition from the mesoscopic scale to the macroscopic scale is the subject of the methodology which is developed throughout the chapter.

- This work focuses on 2D- and 3D-woven textiles, but the use of the homogenization procedure for braided textiles does not create new challenges. In principle, knitted fabrics can also be considered, although the small size of the yarns in this case is likely to lead to unusually heavy finite elements (FE) meshes.

The hypotheses listed above fit well within the study of the curing process of composite materials, and they are sufficient to pursue the objective of Chapter 5, which is the experimental validation of the compensation of a curved C-spar. This scope has been extended by student projects throughout the duration of the thesis. In particular, Bracquart [80] has adapted the homogenization chain to viscoelasticity for unidirectional materials, and Pautet [83] has studied the effect of non-uniform shear angles on the homogenized properties and on the resulting cure-induced distortions. However, these works are exploratory and are not presented here. They belong to the perspectives discussed in Chapter 6.

3.1.2 Objective and outline

Setting up a generic framework for the homogenization of textile composites raises a series of challenges. The term generic implies that the procedure can be applied quickly to any textile without fine-tuning or additional develop-

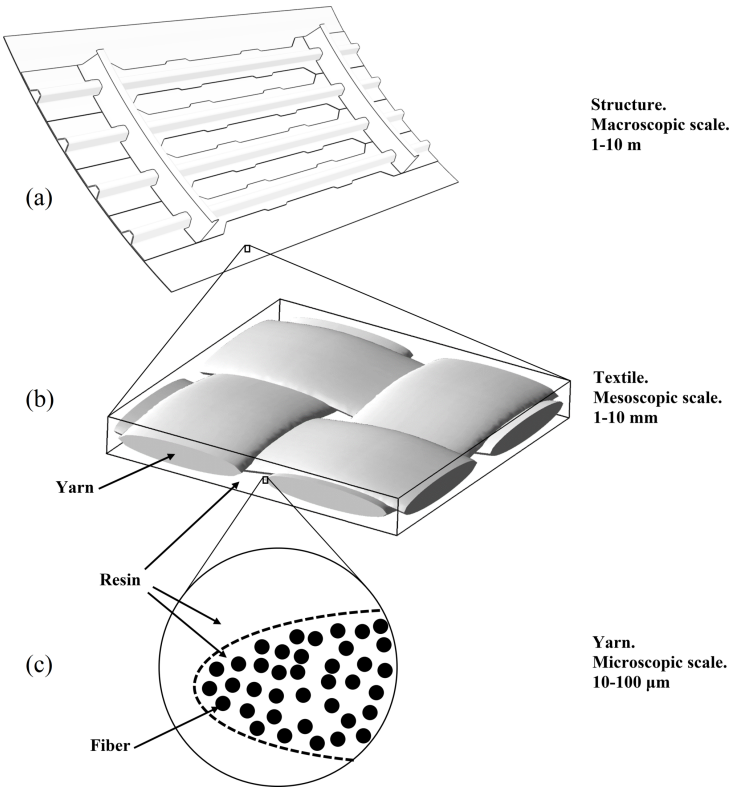


Figure 3.2: The different scales in a textile composite structure.

ments. In particular, the time spent on the generation of the geometry of the microstructure (Figure 3.2(b)) must be minimal. For complex or highly-compacted textiles, this can lead to overlapping between the different yarns. In the rest of this chapter, this overlapping is referred to as textile penetrations. Although the scope of the chapter is limited to linear elasticity, flexibility and openness to more advanced aspects must be ensured for future work. Specifically, the accurate description of the microscopic stresses will be of interest when studying the effects of cure-induced damage, for instance. The use of the FE Method is thus favored in this thesis, as they are more likely to provide accurate microscopic stress-strain fields. This is discussed in Section 3.3.

The outline of this chapter is as follows. Section 3.2 establishes succinctly the theory of homogenization and its concrete application with the FE method. Then, Section 3.3 presents a brief literature review of the different modeling techniques (in the geometrical sense) of textile composites, and also of the homogenization methods which can be considered for those materials. Sections 3.4 and 3.5 describe the newly developed methodology, which can be broken down into two complementary aspects. In Section 3.4, a non-conformal meshing approach is developed and applied to textile composites which contain penetrations. A mesh convergence study demonstrates the benefits of the approach

compared the widely-used voxel mesh. In Section 3.5, a procedure is proposed to adapt the mechanical properties of the yarns to virtually compensate for the textile penetrations. The combination of those two approaches enables the FE homogenization of textile which are coarsely modeled and which involve small or large yarn overlapping. Finally, the results obtained within this framework are compared to experimental measurements from the literature in Section 3.6.

3.2 The theory of homogenization in a nutshell

3.2.1 The homogenization problem

Let us consider the heterogeneous material in Figure 3.3(a). Understanding that it can be represented by a periodic repetition of a representative volume element (RVE), this RVE can be studied separately, see Figure 3.3(b), and its behavior is identical to that of the whole structure. It is assumed that the material in each point of the RVE behaves orthotropically in a local coordinate system (1,2,3). An orthotropic material has three mutually perpendicular symmetry planes, and its elastic behavior can be described by 9 independent constants [85]. In linear elasticity, the constitutive equation which defines the behavior in each point of the RVE is [85],

$$\sigma^*_{ij} = C^*_{ijkl}(\varepsilon^*_{kl} - \alpha^*_{kl}\Delta T), \quad \forall(i,j) = 1\dots3, \tag{3.1}$$

where the asterisk denotes a quantity in the local coordinate system of the considered material point. σ is the stress tensor and ε is the strain tensor. C and α are the stiffness and CTE tensors at this particular point, respectively. Summation over repeated indices is implicit.

In a nutshell, the theory of homogenization aims to determine the properties $\bar{C}$ and $\bar{\alpha}$ of an equivalent homogeneous material which has an identical behavior, on average, to that of the material contained within the heterogeneous RVE. The homogeneous material is also assumed to be orthotropic in the global coordinate system of the RVE (x,y,z). For instance, when both RVEs of Figure 3.3(b) and (c) are subjected, on their respective boundary, to displacements corresponding to a strain tensor $\bar{\varepsilon}$, then the average of the strain over the heterogeneous RVE is equal to $\bar{\varepsilon}$ [86] and the average stress therein is equal to $\bar{\sigma}$, which is also the linear elastic response of the homogeneous material under the same load:

$$\bar{\sigma}_{ij} = \bar{C}_{ijkl}(\bar{\varepsilon}_{kl} - \bar{\alpha}_{kl}\Delta T), \quad \forall(i,j) = 1\dots3. \tag{3.2}$$

The averages of the microscopic tensors are given by,

$$\bar{\sigma} = \frac{1}{V}\int_\omega \sigma dV \text{ and } \bar{\varepsilon} = \frac{1}{V}\int_\omega \varepsilon dV, \tag{3.3}$$

where σ and ε are expressed in the global coordinate system and V is the volume of the RVE ω. The transition between the local and global coordinate systems is performed as follows:

$$\sigma_{ij} = Q_{ki}Q_{lj}\sigma^*_{kl}, \tag{3.4}$$

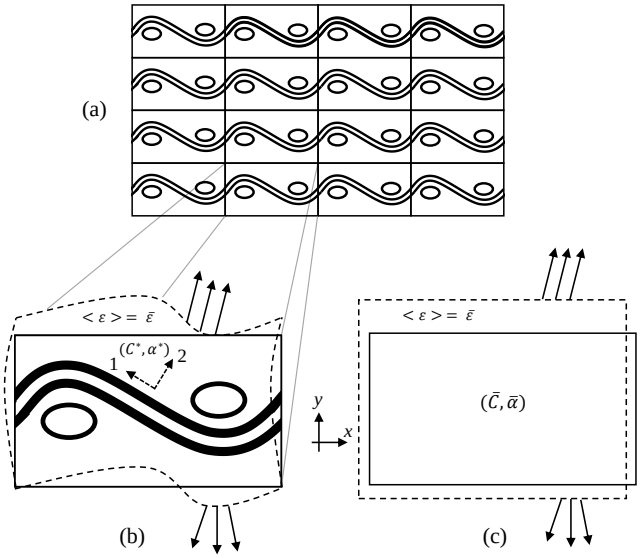


Figure 3.3: (a) Extraction of a RVE from a periodic microstructure. Correspondence between (b) the RVE; and (c) the equivalent homogeneous material.

where Q is the rotation matrix between the global and local coordinate systems. The k-th row of Q contains the components in the global coordinate system of the k-th vector of the local coordinate system [86].

There are a number of methodologies for the resolution of the homogenization problem, i.e. the determination of $\bar{C}$ and $\bar{\alpha}$. Among them, one can cite mean-field approaches [87–89], asymptotic expansion homogenization [90–92], the generalized method of cells [93] and its higher-order extension [94], and FE-based approaches [95, 96]. A brief review, focused on textile composites, is provided in Section 3.3. However, to ensure the continuity of the theoretical aspects in this chapter, the resolution by the finite element method is provided in detail below, since it is the methodology which is used throughout the thesis.

3.2.2 Resolution by the finite element method

The components of $\bar{C}$ can be determined as follows. Let a and b be two integers between 1 and 3, and μ an arbitrary scalar. An average strain tensor $\bar{\varepsilon}$ is imposed to the heterogeneous RVE such that [97]:

$$\bar{\varepsilon}_{kl} = \frac{\mu}{2}\left(\delta_{ak}\delta_{bl} + \delta_{bk}\delta_{al}\right) \quad \forall (k,l) = 1\ldots 3, \tag{3.5}$$

where δ_{kl} is the Kronecker delta. Eq. 3.2, at constant temperature ($\Delta T = 0$), thus becomes,

$$\begin{aligned}\bar{\sigma}_{ij} &= \bar{C}_{ijkl}\frac{\mu}{2}\left(\delta_{ak}\delta_{bl} + \delta_{bk}\delta_{al}\right) \quad \forall(i,j) = 1\dots3 \\ &= \bar{C}_{ijab}\frac{\mu}{2} + \bar{C}_{ijba}\frac{\mu}{2} \\ &= \bar{C}_{ijab}\mu. \end{aligned} \tag{3.6}$$

The last equality is true owing to the symmetry of $\bar{C}$ ($\bar{C}_{ijab} = \bar{C}_{ijba}\ \forall a,b,i,j$ [86]). Eq. 3.6 implies that the components of $\bar{C}$ can be calculated by imposing a well-chosen average strain and computing the resulting average stresses. The entirety of these components can be obtained by considering all the possible couples (a,b), i.e. 6 different couples considering the aforementioned symmetry. Then, the homogenized elastic properties are deduced from the components of $\bar{C}$. In the case of an orthotropic material [85]:

$$\begin{aligned}\bar{E}_1 = \frac{1}{\bar{C}_{2222}\bar{C}_{3333} - \bar{C}_{2233}^2}\Big(&\bar{C}_{1111}\bar{C}_{2222}\bar{C}_{3333} + 2\bar{C}_{2233}\bar{C}_{1122}\bar{C}_{1133} \\ &- \bar{C}_{1111}\bar{C}_{2233}^2 - \bar{C}_{2222}\bar{C}_{1133}^2 - \bar{C}_{3333}\bar{C}_{1122}^2\Big),\end{aligned} \tag{3.7a}$$

$$\begin{aligned}\bar{E}_2 = \frac{1}{\bar{C}_{1111}\bar{C}_{3333} - \bar{C}_{1133}^2}\Big(&\bar{C}_{1111}\bar{C}_{2222}\bar{C}_{3333} + 2\bar{C}_{2233}\bar{C}_{1122}\bar{C}_{1133} \\ &- \bar{C}_{1111}\bar{C}_{2233}^2 - \bar{C}_{2222}\bar{C}_{1133}^2 - \bar{C}_{3333}\bar{C}_{1122}^2\Big),\end{aligned} \tag{3.7b}$$

$$\begin{aligned}\bar{E}_3 = \frac{1}{\bar{C}_{1111}\bar{C}_{2222} - \bar{C}_{1122}^2}\Big(&\bar{C}_{1111}\bar{C}_{2222}\bar{C}_{3333} + 2\bar{C}_{2233}\bar{C}_{1122}\bar{C}_{1133} \\ &- \bar{C}_{1111}\bar{C}_{2233}^2 - \bar{C}_{2222}\bar{C}_{1133}^2 - \bar{C}_{3333}\bar{C}_{1122}^2\Big),\end{aligned} \tag{3.7c}$$

$$\bar{\nu}_{12} = \frac{\bar{C}_{1122}\bar{C}_{3333} - \bar{C}_{1133}\bar{C}_{2233}}{\bar{C}_{2222}\bar{C}_{3333} - \bar{C}_{2233}^2}, \tag{3.7d}$$

$$\bar{\nu}_{13} = \frac{\bar{C}_{2222}\bar{C}_{1133} - \bar{C}_{1122}\bar{C}_{2233}}{\bar{C}_{2222}\bar{C}_{3333} - \bar{C}_{2233}^2}, \tag{3.7e}$$

$$\bar{\nu}_{23} = \frac{\bar{C}_{1111}\bar{C}_{2233} - \bar{C}_{1122}\bar{C}_{1133}}{\bar{C}_{1111}\bar{C}_{3333} - \bar{C}_{1133}^2}, \tag{3.7f}$$

$$\bar{G}_{12} = \frac{\bar{C}_{1212}}{2}, \tag{3.7g}$$

$$\bar{G}_{13} = \frac{\bar{C}_{1313}}{2}, \tag{3.7h}$$

$$\bar{G}_{23} = \frac{\bar{C}_{2323}}{2}. \tag{3.7i}$$

To determine the homogenized CTE $\bar{\alpha}$, a temperature increment ΔT is imposed to the RVE and, in the absence of external loads, Eq. 3.2 becomes,

$$\bar{\sigma}_{ij} = 0 = \bar{C}_{ijkl}(\bar{\varepsilon}_{kl} - \bar{\alpha}_{kl}\Delta T) \quad \forall(i,j) = 1\dots3, \tag{3.8}$$

or, in other words, computing the average strain leads to the value of $\bar{\alpha}$ [98]. Within the FE framework, the computation of the averages of the stress and

strain tensors (Eq. 3.3) becomes,

$$\bar{\sigma} = \frac{1}{V}\sum_i \sigma_i V_i \text{ and } \bar{\varepsilon} = \frac{1}{V}\sum_i \varepsilon_i V_i \tag{3.9}$$

where σ_i and ε_i are the stress and strains at the centroid of a finite element i of volume V_i, expressed in the global coordinate system.

The thermo-mechanical boundary conditions imposing $\bar{\varepsilon}$ or ΔT to the RVE are enforced via periodic boundary conditions under the form of multi-point constraints detailed in Appendix A [97]. These constraints ensure that (i) the shape and orientation in space of two opposite edges are and remain identical during the deformation process, and (ii) the stress vectors acting on opposite sides are opposite in direction (in order to have stress continuity across the boundaries of the RVE) [99]. This periodicity is schematically depicted in Figure 3.3(b). In addition, the displacement of one node close to the middle of the RVE is blocked, to suppress the rigid body motions [100].

To conclude, the homogenization of an orthotropic RVE by the FE method involves the computation of seven different boundary value problems (BVP). These BVPs are summarized in Table 3.1, along with the associated names which will be used in the rest of the chapter. The number of computations may be reduced, depending on the symmetry of the microstructure (e.g. four different BVPs for a transversely isotropic material, i.e. an orthotropic material which contains a plane of isotropy). The values of the imposed average strain μ and temperature increment ΔT do not influence the predictions of the homogenization procedure, as long as the small perturbation hypothesis still holds. In practice, values of 10^{-6} and 10^{-6}°C are used, respectively. Figure 3.4 shows the displacement fields obtained for all boundary conditions applied to a typical plain-weave textile. Assuming that the architecture of the textile is uniform throughout the structure, this procedure needs to be performed only once per material.

Name of the BVP	Imposed boundary conditions	Extracted result
Traction X	$\bar{\varepsilon}_{kl} = \mu\delta_{1k}\delta_{1l}$, $\Delta T = 0$	$\bar{C}_{ij11} = \bar{\sigma}_{ij}/\mu$
Traction Y	$\bar{\varepsilon}_{kl} = \mu\delta_{2k}\delta_{2l}$, $\Delta T = 0$	$\bar{C}_{ij22} = \bar{\sigma}_{ij}/\mu$
Traction Z	$\bar{\varepsilon}_{kl} = \mu\delta_{3k}\delta_{3l}$, $\Delta T = 0$	$\bar{C}_{ij33} = \bar{\sigma}_{ij}/\mu$
Shear YZ	$\bar{\varepsilon}_{kl} = \frac{\mu}{2}(\delta_{2k}\delta_{3l} + \delta_{3k}\delta_{2l})$, $\Delta T = 0$	$\bar{C}_{ij23} = \bar{\sigma}_{ij}/\mu$
Shear XZ	$\bar{\varepsilon}_{kl} = \frac{\mu}{2}(\delta_{1k}\delta_{3l} + \delta_{3k}\delta_{1l})$, $\Delta T = 0$	$\bar{C}_{ij13} = \bar{\sigma}_{ij}/\mu$
Shear XY	$\bar{\varepsilon}_{kl} = \frac{\mu}{2}(\delta_{1k}\delta_{2l} + \delta_{2k}\delta_{1l})$, $\Delta T = 0$	$\bar{C}_{ij12} = \bar{\sigma}_{ij}/\mu$
Thermal	$\Delta T \neq 0$	$\bar{\alpha}_{ij} = \bar{\varepsilon}_{ij}/\Delta T$

Table 3.1: Names and boundary conditions for the periodic FE homogenization procedure. The imposed boundary conditions ensure implicitly the periodicity of the RVE, see Appendix A.

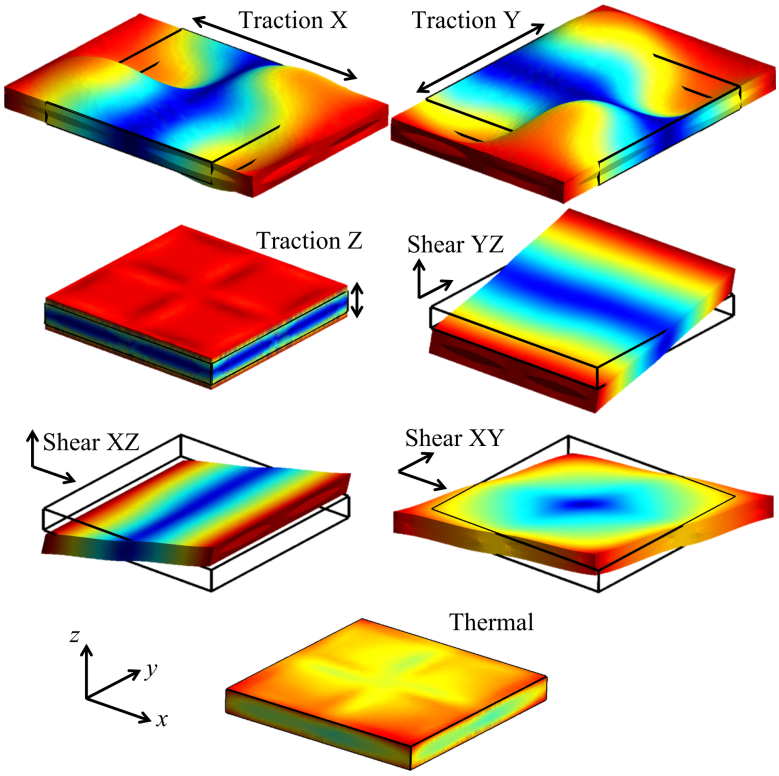


Figure 3.4: Displacement fields obtained by solving the BVPs of Table 3.1 for a typical plain-weave textile.

3.2.3 Micromechanics-based model

As mentioned previously, the homogenization of textile composites is actually a two-step homogenization, since there are three scales at stake: microscopic, mesoscopic, macroscopic (Figure 3.2). The transition between the microscopic and mesoscopic scales calls for the homogenization of the behavior of the impregnated yarns. In this case, there is no need to use a costly FE procedure, since micromechanics-based models are very efficient [101]. The set of equations used in this thesis is introduced by Eq. 3.10. The equations for the mechanical properties have been established by Chamis [102]. The formulations for the longitudinal and transverse CTEs have been proposed by Schapery [103] and Hyer [104], respectively. The subscripts L and T refer to the longitudinal and transverse directions of the yarn, respectively. The subscripts y, f and r designate the properties of the yarn, fibers and resin, respectively. k_f is the fiber volume fraction inside the yarn. In [102], Chamis does not consider the yarns to be transversely isotropic, whereas this would be a reasonable assumption. As a matter of fact, this model performs better versus a reference FE model compared to a set of equations which assumes transverse isotropy of the UD material, also by Chamis [105]. This comparison is displayed in Figure 3.5.

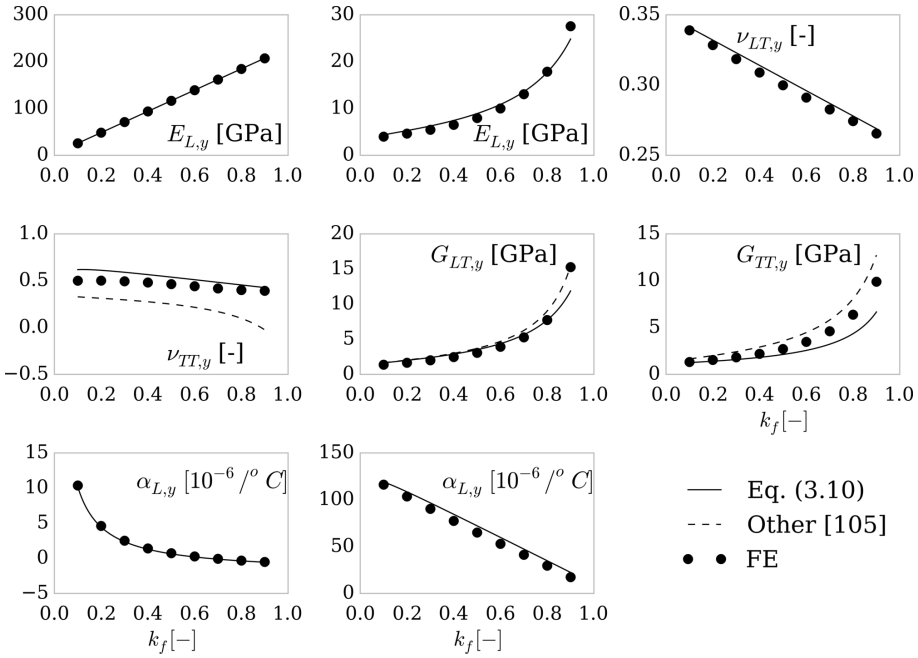


Figure 3.5: A 3D-woven textile modeled in TexGen [106].

Transverse isotropy implies that the Poisson's ratio in the plane of isotropy $\nu_{TT,y}$ is predicted as $E_{T,y}/(2G_{TT,y}) - 1$. It is clear from Figure 3.5 that $\nu_{TT,y}$ is better predicted with Eq. 3.10, even when the carbon fibers are transversely isotropic. The interested reader will find the properties used for Figure 3.5 in Table 5.1 for the carbon fibers and in Table C.1 for the resin.

$$E_{L,y} = k_f E_{L,f} + (1 - k_f) E_r \tag{3.10a}$$

$$E_{T,y} = \frac{E_r}{1 - \sqrt{k_f}(1 - E_r/E_{T,f})} \tag{3.10b}$$

$$G_{LT,y} = \frac{G_r}{1 - \sqrt{k_f}(1 - G_r/G_{LT,f})} \tag{3.10c}$$

$$G_{TT,y} = \frac{G_r}{1 - k_f(1 - G_r/G_{TT,f})} \tag{3.10d}$$

$$\nu_{LT,y} = k_f \nu_{LT,f} + (1 - k_f)\nu_r \tag{3.10e}$$

$$\nu_{TT,y} = k_f \nu_{TT,f} + (1 - k_f)(2\nu_r - \frac{E_{T,y}}{E_{L,y}}\nu_{LT,y}) \tag{3.10f}$$

$$\alpha_{L,y} = \frac{\alpha_{L,f} k_f E_{L,f} + \alpha_r (1 - k_f) E_r}{E_{L,y}} \tag{3.10g}$$

$$\begin{aligned} \alpha_{T,y} = {} & \alpha_r + (\alpha_{T,f} - \alpha_r) k_f \\ & + \frac{\nu_r E_{L,f} - \nu_{LT,f} E_r}{E_{L,y}} (\alpha_r - \alpha_{L,f})(1 - k_f) k_f \end{aligned} \tag{3.10h}$$

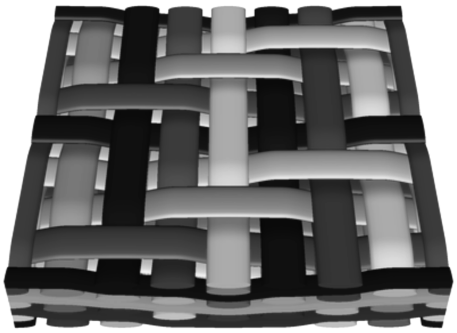


Figure 3.6: A 3D-woven textile modeled in TexGen [106].

3.3 Homogenization of textile composites: literature review

The multi-scale analysis of textile composites is the combination of a geometrical representation of the microstructure (i.e. the creation of the RVE), and of a homogenization technique to determine the effective properties of the RVE. A brief literature survey of both aspects is performed in the present section, followed by a discussion motivating the choices made to meet the objective of this chapter.

3.3.1 Textile modeling

When it comes to the modeling of the microstructure of a textile composite, general-purpose textile modeling software must be distinguished from very detailed, less generic approaches. In the first category, the most commonly used solutions are WiseTex [101, 107–109] and TexGen [106, 110], which provide user interfaces to generate a wide range of textiles with minimum effort. Figure 3.6 presents an example. WiseTex also provides capabilities to homogenize a wide range of textiles with analytical [107] or FE tools [101] for permeability [109] or mechanical analysis. TexGen is limited to geometrical aspects, but it is open-source and data can be transferred to commercial FE software packages. With a user-friendly interface, textiles can be generated in a few minutes.

On the other hand, researchers have explored very fine textile modeling approaches for specific applications. Straumit et al. [111] generate a very precise voxel model of textile architectures from X-ray computed tomography (micro-CT) data. They have then used this technique for the computation of permeability [112], for which an accurate geometrical representation is important. Textile compacting FE analyses are another alternative [113, 114]. Mahadik and Hallett [113] model the yarns as bundles of one-dimensional beams, which are put under tension and compressed by the explicit simulation of a drop in temperature and of the compaction between two rigid plates. General contact must be enforced between all the beams. Miao et al. [115] and Green et al. [114, 116] (Figure 3.7) use the same kind of approach. The latter au-

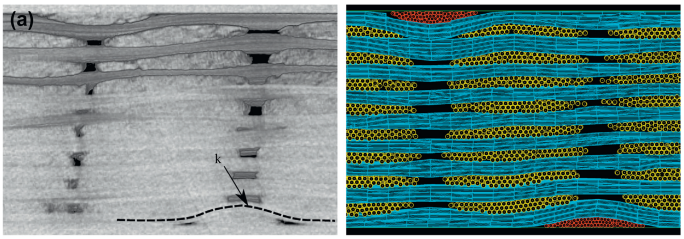


Figure 3.7: Left: Microscopic image of a 3D-woven textile. Right: textile generated by a compaction FE analysis of bundles of 1D beams, representing the yarns [114].

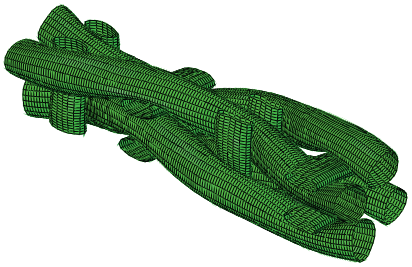


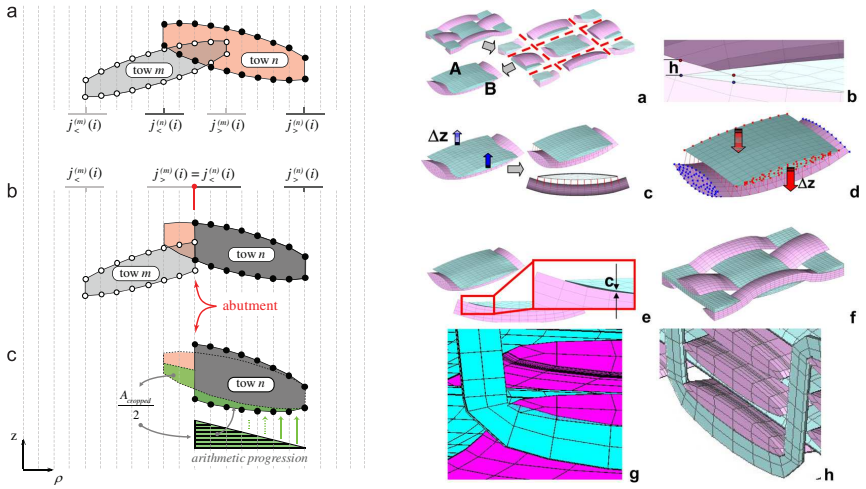
Figure 3.8: A RVE generated by yarn inflation [117].

thors announce very large computational times to generate the architecture (72 hours). Stig and Hallström [117] take the opposite direction and perform a yarn inflation analysis, starting from small tubes and expanding them through an explicit FE simulation until a pre-defined yarn volume fraction is reached (Figure 3.8). All of these techniques rely on heavy calculations, and are sometimes degraded by the obligation to use a voxel mesh [111, 116]. In any case, in the frame of linear elasticity, modeling one RVE of the composite very finely (as with micro-CT) is not necessarily more relevant than modeling a simplified idealized RVE based on averaged measurements over the entire composite [118].

One of the main purposes of refined textile modeling is to avoid material overlap, also referred to as penetrations. One strategy is to start from a simplified geometrical model of the yarns, and to remove regions with penetrations a posteriori, either by geometrical considerations [108, 119, 120] or by FE analysis [101]. Figure 3.9 provides two examples. These solutions are however usually not very generic or are suitable to small penetrations only. TexGen does provide fine-tuning capabilities which enable the modeling of complex textiles without penetrations, at the cost of very significant scripting [121], or limited to very small penetrations [118].

3.3.2 Homogenization methods for woven textiles

Pioneering works in homogenization of woven textile composites include that of Ishikawa and Chou [122], namely the mosaic, bridging and fiber undulation models to predict in-plane properties of woven textiles. These models are based



(a) Geometry-based [119] (b) FE-based [101]

Figure 3.9: Textile penetration suppression methods

on classical laminate theory and are thus based on the simple iso-strain assumptions. Other analytical or semi-analytical schemes rely on the complementary variational principle, like the approach proposed by Vandeurzen et al. [123, 124] or the generalized method of cells [93, 94]. The latter is quite universal and has been exploited for advanced phenomena, such as failure modeling of 3D-woven textiles by Prodromou et al. [125]. Mean-field techniques such as the Mori-Tanaka method are efficient for predicting homogenized properties [84, 126]. In that case the yarns are replaced by a set of ellipsoids with circular or elliptical cross-section. However, most analytical solutions, even with rich kinematics and high order representation of the geometry, generally lead to rather poor predictions of the magnitude of the local or per-phase average fields.

The advent of high performance computing has made possible the use of FE-based approaches for complex architectures, which can provide reference solutions as a basis for the assessment of the aforementioned analytical methods. FE techniques can be further divided into two categories:

- Classical approaches use either conformal meshes of yarns and of the resin rich domains, or non-conformal meshes that do not align element edges with yarn boundaries, of which a typical example is voxel meshing. Although conformal meshes provide better means for modeling detailed microscopic stress states inside the RVE, modeling and meshing properly the geometry of the thin resin layers appearing where the yarns come into contact can be difficult. Among other techniques, an artificial resin layer between the yarns can be added [101, 117]. Voxel approaches [111, 116, 118, 127–131] describe the textile as a grid of uniformly-sized hexahedra. In essence, the irregularity of the yarn boundaries then leads to spurious stress concentrations but the approach is nevertheless widely used in linear elastic homogenization, and even in

the context of failure analysis [116, 131], especially when generating conformal meshes becomes complicated.

- Other approaches consist in modifying the FE formulation to take into account the presence of the yarns inside the matrix. Independent mesh methods [132], mesh superposition [133–135], or the binary model of Cox et al. [136] are examples of such approaches.

Homogenization capabilities are readily available in specialized commercial software, like Digimat [137, 138]. It offers a wide range of solutions to model not only textile composites but also short-fiber reinforced plastics and discontinuous fiber composites both with FE-based and mean-field methods.

3.3.3 Motivation for the development of a new methodology

The present work investigates an alternative approach, based on the following questions:

- How can complex highly-compacted textiles, such as the one in Figure 3.8, be modeled with minimal effort?
- How can this simplified model be used in a classical finite element homogenization framework (i.e. without modifying the FE formulation)?

The answer brought to the first question is to use a general-purpose modeling software like TexGen. However, this brings unresolved issues when dealing with the second question. A penetration-free model of the textile illustrated in Figure 3.8 cannot be obtained in TexGen without extremely intensive and non-generic scripting. Consequently, a simplified model necessarily contains penetrations. Penetrations mostly arise when the textile exhibits a high yarn volume fraction or when the modeling approach is too coarse. Figure 3.10 illustrates typical penetrations which can occur when dealing with a plain-weave fabric. When the yarn volume fraction f within the RVE is increased, penetrations emerge and suppressing them with maintained yarn volume fraction would require relocation of material from regions where yarns overlap to regions where there is still available open space. Such adjustments are most commonly performed via iterative geometrical considerations or FE simulations, and they become increasingly more complex as the model reaches a high level of compaction.

The hypotheses on which the contributions of this chapter are based can be summarized as follows. Textiles are coarsely modeled using TexGen, while making sure that the key parameters are compliant with respect to the real textile, such as fiber content, crimp or yarn paths. The crimp is a scalar which relates to the undulation of a yarn. It is defined as L/λ, where L is the curvilinear length of the yarn mid-line and λ its wavelength (Figure 3.11). The objective is to keep the geometrical modeling as simple as possible. To that end, the advanced functionalities of the software are not used. The yarn paths are described by sinusoidal functions or polylines. Each yarn has a constant elliptical or rectangular cross-section.

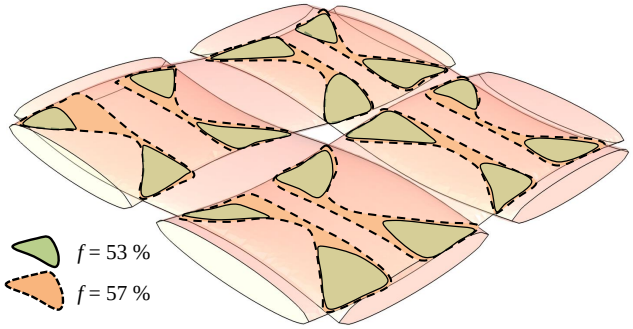


Figure 3.10: Typical textile penetrations, increasing with the yarn volume fraction f.

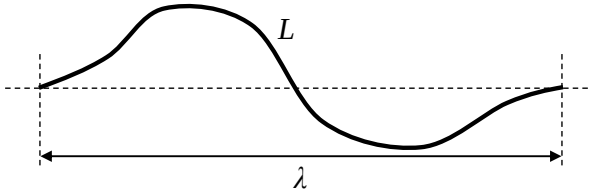


Figure 3.11: The crimp of a yarn is defined as L/λ.

The first contribution of this chapter is the development of non-conformal meshes to circumvent the penetrations within the textile, a consequence of the simplified modeling. In the intent of rationalizing the mesh size compared to classical voxels, the mesh is unstructured and is refined at the material interfaces. In a second contribution, an innovative and pragmatic adaptation of the intra-yarn fiber volume fraction is proposed to compensate for the textile penetrations. This method is generic and adapted to large penetrations. The developed methodology can be applied to any textile but is more relevant for the ones that are complex to represent geometrically, namely 3D woven textiles. Although the framework is not limited to linear elasticity, its extension to other considerations such as failure mechanisms will necessitate adjustments and particular care. It is therefore left out of the scope of this thesis, since the overall objective is to generate linear elastic material properties for curing simulations.

3.4 An unstructured non-conformal meshing approach

3.4.1 Principle

If penetrations are not mitigated, which is the case in the present work, meshing the RVE of Figure 3.10 with a conventional method would require the software to automatically detect the penetration volume and to mesh it separately from

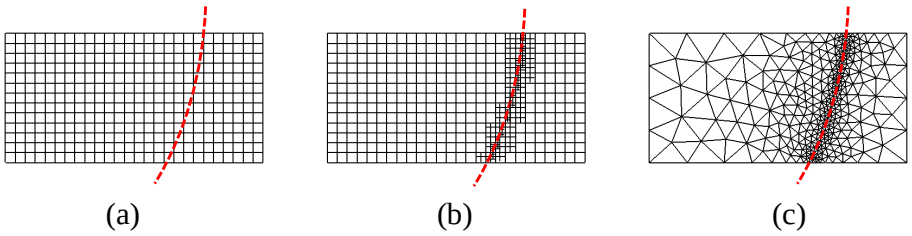


Figure 3.12: Three kinds of non-conformal meshes: (a) voxels, (b) quadtree, and (c) unstructured.

the remaining yarn volumes. In a general case of e.g. a 3D textile model, the overlapping regions can be of complex shape, which make cleaning operations complicated. Non-conformal meshing might then be a better alternative. The most classical approach would be to use a uniformly-sized voxel mesh (Figure 3.12(a)). However, it has the disadvantages of being both over-refined in the resin region and not refined enough around the yarn boundaries, leading to irregular interfaces and spurious stress concentrations. A technique to produce a voxel mesh refined at the yarn boundaries, similar to the quadtree procedure (Figure 3.12(b)), has been developed by Kim and Swan [130]. It has the additional constraint that it provides a disconnected mesh, and cumbersome post-treatment is needed in order to create suitable multi-point constraints. Here, another approach is adopted to rationalize the mesh size while keeping a classical connected mesh.

Figure 3.12 presents three different techniques for the non-conformal meshing of an interface: voxels, quadtree and unstructured. In the case of voxels, the size of the elements is, by essence, uniform. Refining the element size at the interface thus requires to refine the element size everywhere. With a quadtree approach, the elements can be refined at the interface but, as already mentioned, the mesh is disconnected. The unstructured approach consists in using tetrahedral elements, imposing a smaller mesh size near the interface. Such meshes have already been used before [139–143], including for the study of textile composites [140]. The contributions of this section are the following:

- to establish a non-conformal unstructured meshing approach suitable to the periodic meshing of RVEs containing penetrating yarns;
- to demonstrate the benefits of unstructured meshes compared to voxels, which are still widely used for homogenization purposes [111, 116, 118, 127–130].

To obtain an unstructured mesh refined around an interface, the mesh size s at point $P(x, y, z)$ is defined as a function of a scalar distance field d to the interface:

$$s(x, y, z) = \min \{M, \max[m, \beta d(x, y, z)]\}, \tag{3.11}$$

where m, M and β are user-defined parameters controlling the minimum size, the maximum size and the mesh size gradient, respectively.

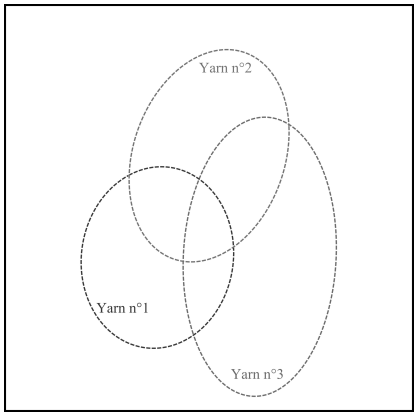


Figure 3.13: Example of three overlapping yarns in a RVE.

3.4.2 Distance computation and meshing

An appropriate distance field d in Eq. 3.11 must be defined in the case of a RVE comprising multiple yarns, possibly overlapping. For the sake of clarity, the procedure is explained in 2D with an unrealistic configuration and the distance fields are presented as filled iso-values in the different figures, but the application to the 3D case is straightforward and the real distance fields are indeed continuous. Let us consider the three overlapping yarns in Figure 3.13. As the final mesh must be periodic, the distance field must be periodic as well. To that end, the textile is first partly duplicated in all directions of space, as illustrated in Figure 3.14. Then, the signed distance field d_i to the yarn number i is computed, for each yarn. For instance, the distance field d_1 to yarn n°1 is shown in Figure 3.15. The distance field d_i is signed so that the interior of the yarn can be distinguished from its exterior based on the sign of d_i. In that sense, the distance fields used in this chapter can be considered as level-sets [144]. The chosen convention is that d_i is negative outside of yarn n°i and positive inside. After meshing, each finite element is classified within the appropriate yarn based on the value of the level-set at the centroid of the element, see Figure 3.16(b) for instance.

The combination of all level-sets d_i could be done simply by identifying the closest yarn and multiplying the distance by a sign S (+1 if the point is inside at least one yarn, -1 otherwise):

$$D_{all}(x, y, z) = S \min_i(|d_i|), \tag{3.12}$$

but the subsequent meshing with the mesh size guided by Eq. 3.11, with $d = |D_{all}|$, leads to the mesh shown in Figure 3.16(b): the mesh is not refined at the yarn-yarn interface, since D_{all} is not equal to 0 there. Instead, D_{all} is minimum at the yarn boundaries, which leads to a mesh that is uselessly fine in some locations and not refined enough at the yarn-yarn interface. In order to obtain an appropriate mesh refinement, the iso-zero of the distance field d in Eq. 3.11 must be located on the exact "yarn-yarn interface" as defined in Figure 3.17. This interface is:

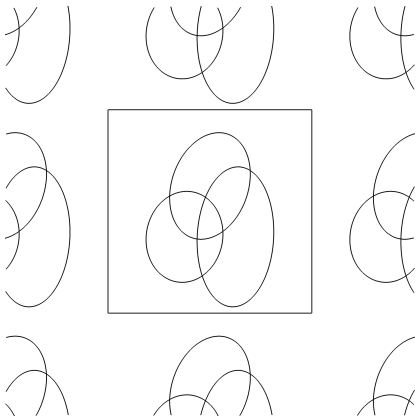


Figure 3.14: Textile duplication in all directions of periodicity.

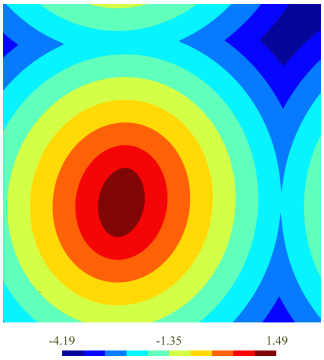


Figure 3.15: Periodic signed distance field to yarn n°1, d_1.

- aligned with the yarn boundaries at the resin-yarn interface, i.e. where there is no yarn overlap;
- equal to the iso-distance to the yarn boundaries in the overlapping regions.

Unfortunately, the location of the yarn-yarn interface is not known a priori and the true distance to this line cannot be computed directly. Sonon and Massart [145] have developed a simple signed distance definition which respects the requirements cited previously. Adapted to the current situation (d_i positive inside yarn n°i), this algorithm defines the distance as:

$$D(x,y,z) = \max_i \left\{ \min \left(d_i, d_i - \left(\max_{j \neq i} d_j \right) \right) \right\}. \tag{3.13}$$

Sonon and Massart have used their level-set in the context of the eXtended Finite Element Method (X-FEM), not for mesh adaptation. Eq. 3.13 must be

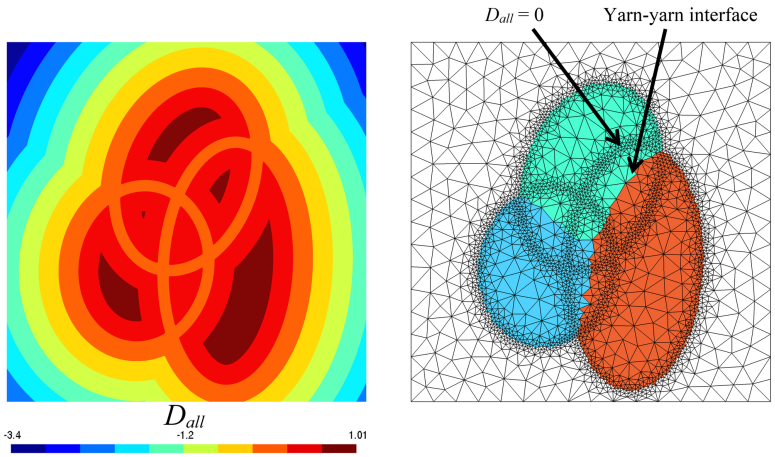


Figure 3.16: (a) Distance field D_{all} (Eq. 3.12); and (b) corresponding mesh. The iso-zero of the level-set and the yarn-yarn interface do not match.

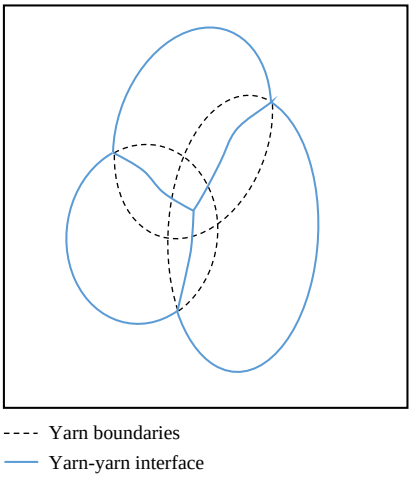


Figure 3.17: Definition of the yarn-yarn interface.

corrected as follows:

$$D_c(x,y,z) = \begin{cases} D(x,y,z) & \text{if } D \leq 0 \\ \frac{1}{2}D(x,y,z) & \text{if } D > 0 \end{cases}. \tag{3.14}$$

This discrepancy with respect to the reference definition [145] is due to the steep gradients created by Eq. 3.13 in the overlapping regions. Gradients higher than 1 in Eq. 3.11 must be avoided, since a mesh adaptation procedure cannot increase the mesh size faster than the true distance to the iso-zero of the distance field. An illustration of this phenomenon is provided in Figure 3.18

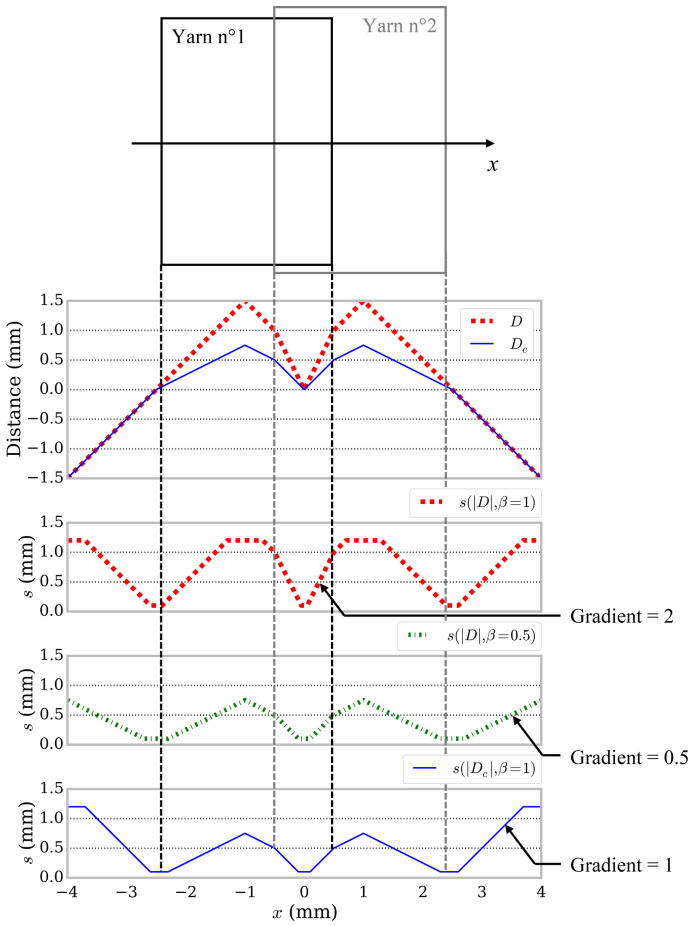


Figure 3.18: Distance to the yarn interfaces along the x axis and three different ways of computing the mesh size s: with Eq. 3.13 and $\beta = 1$, with Eq. 3.13 and $\beta = 0.5$, and with Eq. 3.14 and $\beta = 1$. Here, $M = 1.2$ and $m = 0.1$.

for a very simple case. The first graph represents the evolution of the distance to the two penetrating rectangular yarns, along the x axis, comparing both Eq. 3.13 (D) and Eq. 3.14 (D_c). The subsequent graphs represent the resulting mesh size s computed with Eq. 3.11 in three different cases. What should be understood from these graphs is that using $d = |D_c|$ and $\beta = 1$ is the best possible option, in the sense that the gradient of s:

- remains below 1. Therefore, it is compatible with the mesh adaptation algorithm;
- is equal to 1 most of the time. This allows for a faster coarsening of the mesh as we move further away from the yarn boundaries, leading to a lighter mesh compared to the other options.

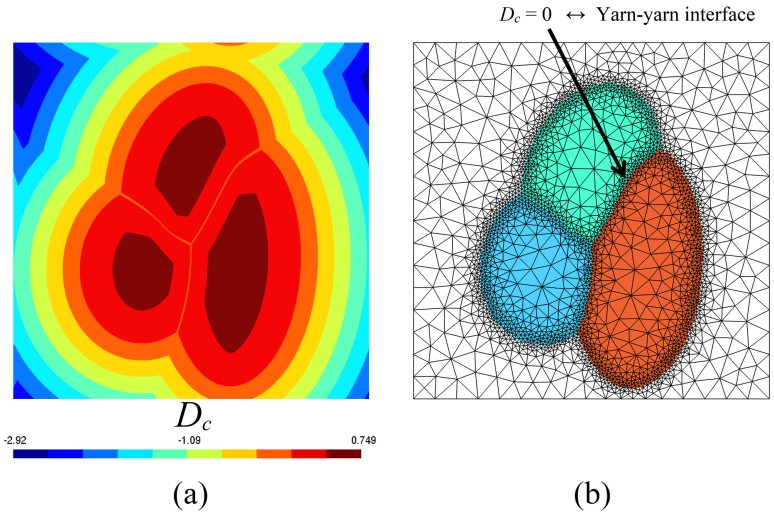


Figure 3.19: (a) Corrected distance field D_c (Eq. 3.14); and (b) corresponding mesh. The iso-zero of the level-set matches with the yarn-yarn interface.

In summary, and for the remainder of this thesis, RVEs are meshed with the open-source software GMSH [146], by imposing an isotropic spacial distribution of the mesh size s with help of Eq. 3.11, where $d = |D_c|$ and $\beta = 1$. The parameters m and M are defined based on the desired level of refinement. The mesh is strictly periodic, as GMSH meshes three faces of the RVE and copies them before meshing the volume. Since the level-set D_c must be known before meshing, it is calculated on a regular grid consisting of 1.5 million points in total. Figure 3.19 shows the result of the entire meshing procedure applied to the 3-yarn RVE. On the one hand, one can see in the distance field of Figure 3.19(a) that the iso-values are larger inside the yarns, sign of a lower gradient. This is a direct hint of the above discussion, and the resulting slower mesh size increase in those regions is the price to pay for using Eq. 3.14 for the distance calculation. On the other hand, by refining the mesh at all material interfaces, i.e. yarn-yarn and yarn-resin, it is expected that the spurious stress concentrations arising at these interfaces, due to their irregular shape, will be decreased when applying loads to the RVE, including for homogenization purposes.

3.4.3 Convergence studies and comparison to the voxel approach

In this section, an in-depth analysis of the performance of the unstructured meshing procedure is performed. This study consists in assessing the accuracy of the procedure, within the framework of linear elastic FE homogenization, and compare to the classical conformal and voxel approaches for a plain-weave textile.

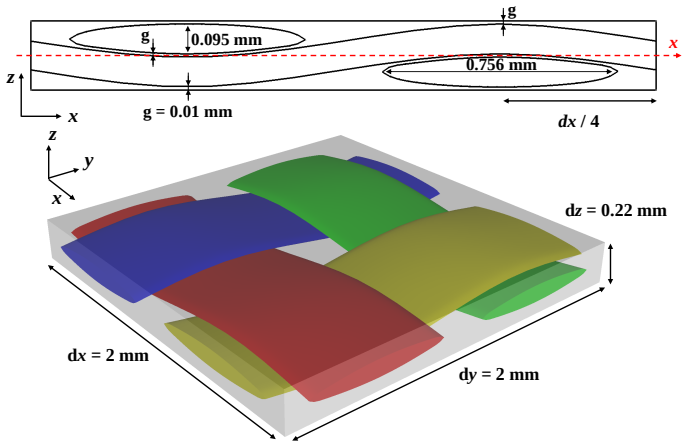


Figure 3.20: Geometrical description of the plain-weave textile used in Section 3.4.3.

Textile geometry and materials

The geometry of the textile is described in Figure 3.20. It contains no penetrations and a gap is introduced between the yarns [101, 117], to make possible the conformal meshing. The material properties of the constituents used for homogenization purposes are listed in Table 3.2. These values correspond to a typical carbon/epoxy composite. They are taken from [48] for the resin, from [147] for the mechanical properties of the carbon fibers, and from [148] for their CTE. The properties of the yarns are computed with the micromechanics-based models of Eq. 3.10, assuming a fiber volume fraction of 60 % inside the yarns. One can notice that the carbon fibers are not considered to be transversely isotropic. This is due to rounding approximations when converting from psi to MPa in [147], and to the fact that the original data [102] are given with only one or two digits and are determined from reverse analysis of testing of composite coupons. The choice to keep the orthotropic data given by [147] is motivated by Section 3.6.1, where the methodology developed in this chapter is compared to results of [147]. Comparing two methodologies demands to use the same material properties to begin with. In any case, the present section compares the homogenization predictions obtained with two meshing techniques, and the conclusions drawn do not depend on the properties of the fibers, as long as the same properties are used for all computations.

Geometrical discretization

First, it is checked that the newly-developed unstructured meshing procedure brings added value in terms of quality of the representation of the interface. One of the main drawbacks of non-conformal meshes is the artificial irregularity of the material interfaces, which leads to stress concentrations and can affect the numerical predictions. To determine an indicator of the degree of non-conformity of a mesh with respect to the interfaces between the different

Epoxy resin		
E_r	[MPa]	2600
ν_r	[-]	0.38
α_r	[/°C]	71×10^{-6}
Carbon fibers		
$E_{L,f}$	[MPa]	230 000
$E_{T,f}$	[MPa]	14 000
$\nu_{LT,f}$	[-]	0.2
$\nu_{TT,f}$	[-]	0.25
$G_{LT,f}$	[MPa]	9000
$G_{TT,f}$	[MPa]	4800
α_L, f	[/°C]	-0.6×10^{-6}
α_T, f	[/°C]	15×10^{-6}

Table 3.2: Material properties used for the convergence study. The subscripts L and T stand for the longitudinal and transverse directions of the fibers, respectively.

material phases (whether they are between two yarns or between a yarn and the resin), the nodes close to the interfaces are detected. This can be done by collecting the nodes of the element faces which cross the interfaces, as illustrated in Figure 3.21.

Let us note $\mathcal{I}$ the set of interface nodes. We can then define the "non-conformity" N from the distance between the interface nodes and the interface:

$$N(n_i) = \frac{1}{\min(dx, dy, dz)} |D(x, y, z)| \quad \forall n_i(x, y, z) \in \mathcal{I}, \tag{3.15}$$

where dx, dy, dz are the dimensions of the RVE. It can be noted that D is a better indicator of the true distance than D_c. Indeed, in the absence of penetrations within the textile, D is the exact distance to the yarn boundaries,

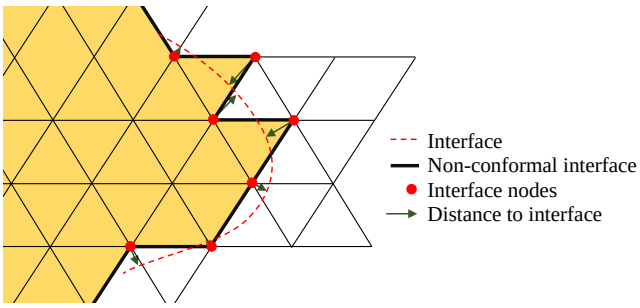


Figure 3.21: The non-conformity N of a non-conformal interface is defined from the distance of the interface nodes to the interface.

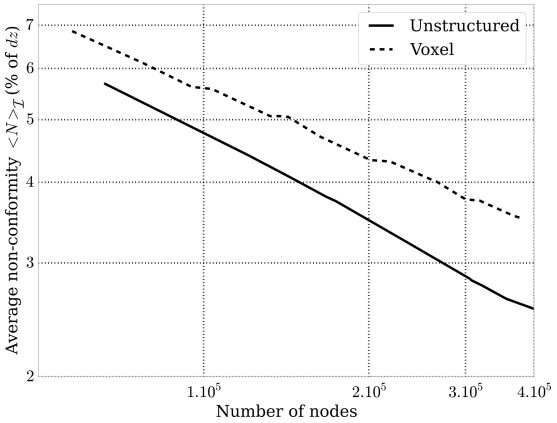


Figure 3.22: Average non-conformity: comparison between unstructured and voxel meshes.

whereas D_c is the distance divided by two inside the yarns. The latter is only useful for mesh adaptation purposes in the presence of yarn overlapping.

As indicated by Eq. 3.15, N is expressed relatively to the smallest dimension of the RVE, in this case dz. From Eq. 3.15, the average $< N >_{\mathcal{I}}$ and percentiles of the non-conformity distribution can be defined. Considering the textile of Figure 3.20, Figure 3.22 presents the average non-conformity as a function of mesh refinement, comparing the unstructured meshing strategy and the classical voxel approach. The average conformity of the unstructured mesh is consistently 1 % below that of the voxel mesh. For instance, around 250,000 nodes it is 4 % for voxels, and 3 % for the unstructured approach, i.e. one fourth less.

Homogenization: mesh convergence study

A convergence study is now performed to compare the accuracy of the unstructured meshing technique, versus voxel meshes. All meshes are made of first-order finite elements. Reference results are generated with a classical conformal mesh. Figure 3.23 presents the results of the convergence study. For each property, the relative error between the non-conformal mesh and the converged conformal results is calculated. The simple mean error, i.e. the averaged error with an equal weight for all properties, is 2.5 times less in the unstructured approach compared to voxels for the same number of nodes. At 330,000 nodes, no error is above 2.8 % in the unstructured case, while three properties are still above 5 % for voxels, with a particularly slow convergence for the in-plane Young's modulus $E_x = E_y$ and the in-plane CTE α_x. The slower convergence observed with the unstructured mesh for the out-of-plane shear modulus G_{xz} is likely due to shear locking of the tetrahedral elements [149]. However, on average, it is more beneficial to use an unstructured mesh, which is refined locally at the material interfaces, instead of being uniform for the voxel counterpart.

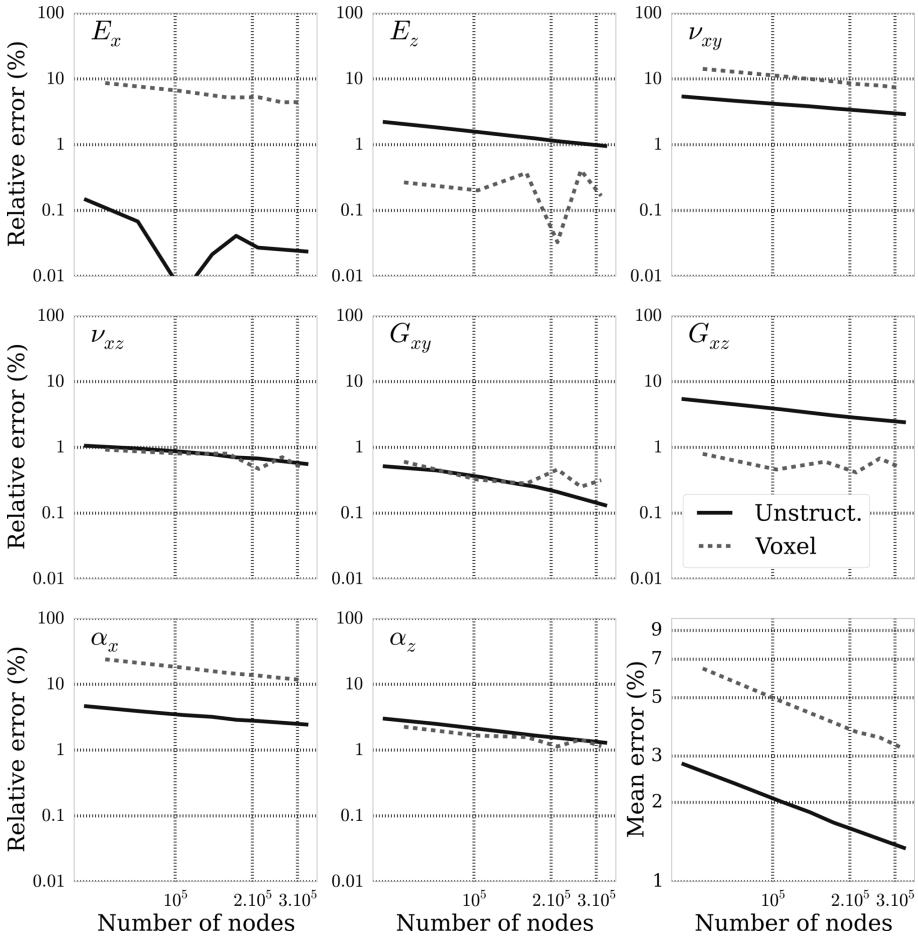


Figure 3.23: Accuracy of the homogenization of a typical plain-weave with non-conformal meshes (unstructured and voxels) compared to reference results obtained with a conformal mesh.

Detailed microscopic fields

Although it is not the primary interest in this thesis, one of the advantages of using finite elements, rather than analytical or semi-analytical approaches, is the accurate prediction of the microscopic fields within the RVE. The irregular nature of the interfaces between the different constituents in the non-conformal framework is an obstacle when it comes to predicting local stresses or strains. In the interest of remaining open, for future work, to non-linear or local phenomena, indicators of the accuracy of the presented meshing technique are provided, in particular with respect to the voxel approach, for the prediction of the microscopic fields. To this end, the following comparisons can be made:

- qualitative local comparisons, by plotting the stress field in a section plane, such as in Figure 3.26;

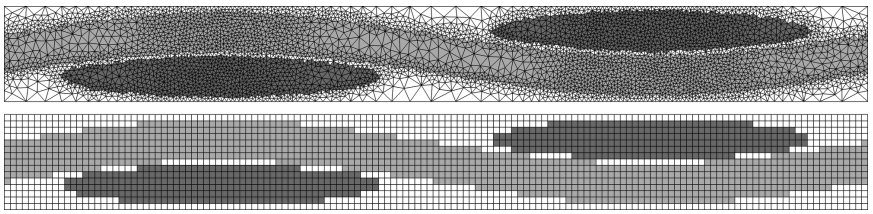


Figure 3.24: A cut view of the unstructured and voxel meshes used for the comparison of the microscopic fields. Both meshes contain about 330,000 nodes.

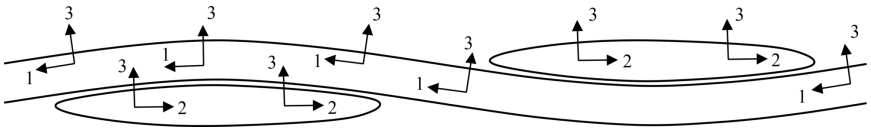


Figure 3.25: Definition of the principal directions of orthotropy within the yarns.

- quantitative local comparisons, by plotting the stress field along an axis, such as in Figure 3.27. The axis is the dashed line x in Figure 3.20;
- quantitative global comparisons, by plotting the cumulative distribution of the stress field, either in the whole RVE or within each material phase (resin, yarn n°1, etc.), as in Figure 3.28.

For a fair comparison, a similar mesh refinement, approximately 330,000 nodes, is used for the three meshing approaches. This refinement corresponds to the finest meshes studied in the convergence study of Figure 3.23. The voxel and unstructured meshes are compared in Figure 3.24, which gives an idea of the difference of quality of the representation of the interfaces.

Figures 3.26 to 3.28 provide examples of comparison of the microscopic stress fields between the different meshing techniques. In all cases, the tensor components are provided with respect to the local principal directions of orthotropy within the yarns (the direction "1" being the longitudinal direction of the fibers, see Figure 3.25). A more complete comparison can be found in Appendix B. The main conclusions are the following:

- Since the elements at the material interfaces are much smaller in the case of the unstructured mesh, the stress field is much smoother compared to the voxel mesh, for instance in Figure 3.26. However, the visualization may also be impacted by the post-processing method, which computes and displays the stresses at the centroid of the elements.
- In the detailed plots along an axis, the local stress or strain fields present oscillations, for both the unstructured and voxel meshes. In the case of Figure 3.27, the unstructured case seems more faithful to the conformal

mesh than the voxel mesh. Appendix B shows that it is not always the case, although the unstructured mesh does provide better results in most cases. A noisy microscopic field could lead to mistaken interpretations, for instance if a damage criterion needs to be computed. It becomes clear that an accurate description of the microscopic fields with non-conformal meshing techniques cannot be achieved without some kind of smoothing, or without more refined meshes. Smoothing can be considered either in the pre-processing phase, e.g. by using intermediate material properties in the interface regions rather than pure resin or pure yarn properties, or in the post-processing phase, e.g. by applying a noise reduction filter to the microscopic fields.

- Concerning the cumulative distributions of the microscopic stresses, the comparison between the unstructured approach and the voxel approach is in most cases favorable to the former. These results support observations made with Figure 3.23. For instance, Figure 3.28 shows that the longitudinal in-plane stress within a yarn under tension are much better predicted with the unstructured mesh, explaining the poor convergence observed for the in-plane Young's modulus E_1 for the voxel approach. Furthermore, Figures B.37 and B.40 confirm the fact that the in-plane strains are not well predicted with the voxel mesh, leading to a poor homogenization result of the in-plane CTE α_x.

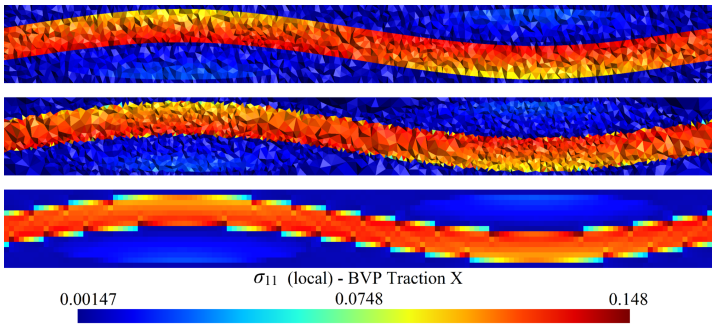


Figure 3.26: Local longitudinal stress field (σ_{11}) for a yarn under longitudinal tension. From top to bottom: conformal mesh, unstructured, voxels.

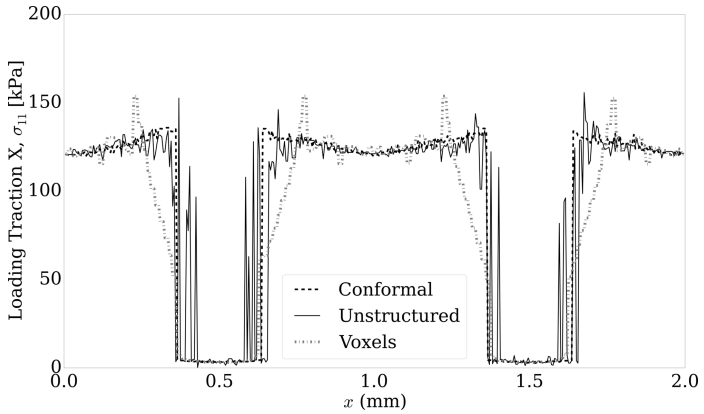


Figure 3.27: Local longitudinal stress distribution (σ_{11}) along a line (dashed line of Figure 3.20).

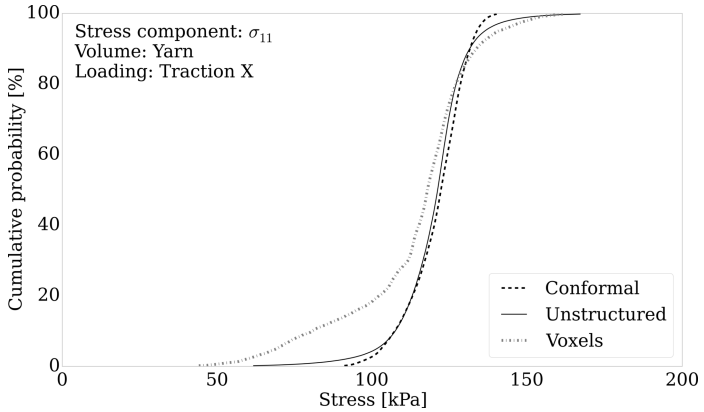


Figure 3.28: Cumulative distribution of local longitudinal (σ_{11}) within a yarn under tension.

3.5 Homogenization of penetrating textiles

3.5.1 A strategy to compensate for textile penetrations

The objective of the methodology is to compute an accurate estimation of the homogenized thermo-mechanical properties in a complex textile with a minimum effort spent on modeling. Thus, simplified models of complex textiles are generated in the open-source, user-friendly modeler TexGen. The main characteristics of the textiles, i.e. fiber content, yarn crimp and yarn volumes, are respected.

The present method assumes simple sinusoidal or piecewise linear yarn mid-lines, depending on the textile architecture. Yarn cross-sections are constant with trivial shapes, either elliptical or rectangular. They are modeled to be as representative as possible of the complex reference model. If relevant, e.g. for 3D textiles, these cross-sections are further rotated about the mid-line of the

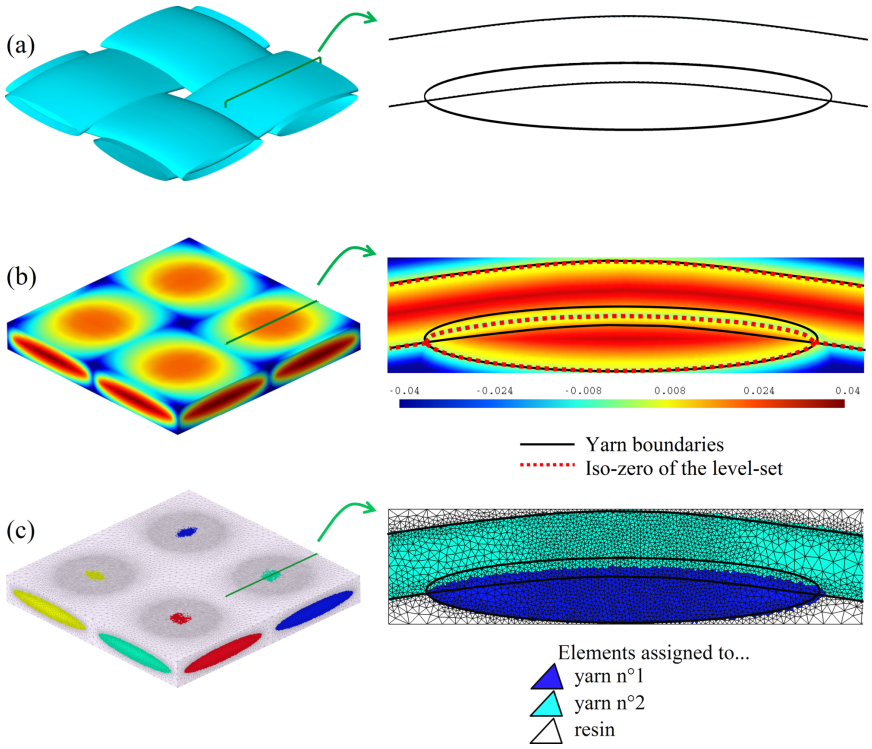


Figure 3.29: (a) Typical plain-weave textile modeled in TexGen without post-treatment. The cut view shows the penetrations due to the large volume fraction of yarns; (b) computation of the distance field (level-set) with Eq. 3.14; (c) based on the level-set, a non-conformal mesh refined at the interfaces is built and each element is classified into the relevant entity.

yarns allowing for parallel major axes of the warp and weft cross-sections at contact points. By nature, this method can induce penetrations between the yarns. In this section, a strategy is proposed to correct for the errors generated because of these penetrations. The strategy is based on the following considerations:

- Let us apply the meshing methodology described in Section 3.4, for a penetrating plain-weave textile, see Figure 3.29. It should be noted that the amount of penetrations is exaggerated for the sake of clarity.
- The volume of a yarn can be defined in three different ways, illustrated in Figure 3.30: by the nominal geometrical volume as defined in TexGen V_y, by the meshed volume of the yarn $V_{y,nc}$ as if the yarn was alone in the textile, and by the meshed volume accounting for penetrations $V_{y,p}$. The latter is the volume of the elements classified in the yarn, in the sense of Figure 3.29(c). Since a non-conformal approach is used, $V_{y,nc}$ is not necessarily equal to V_y. Moreover, $V_{y,p}$ is smaller than $V_{y,nc}$ if there are penetrations within the yarn.

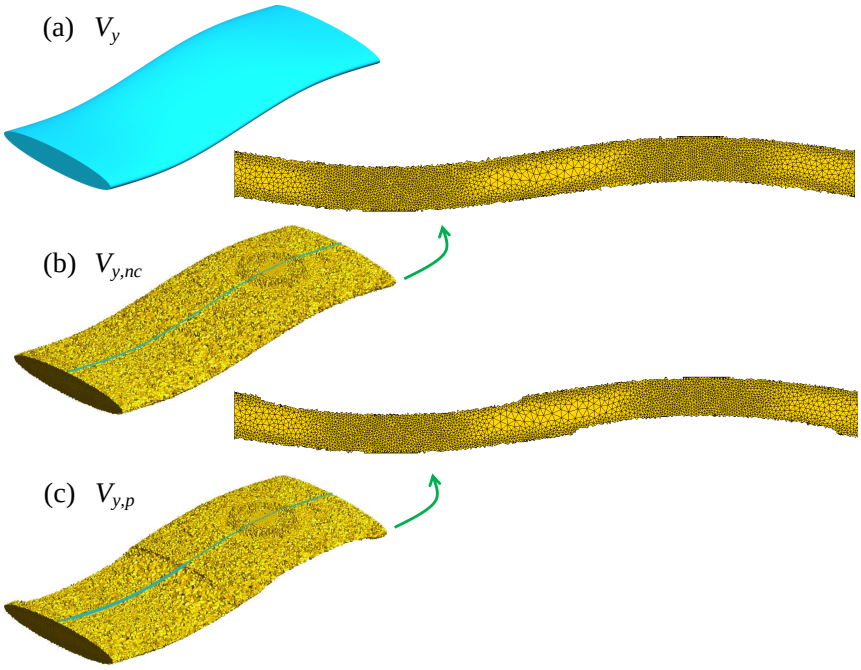


Figure 3.30: Definitions of (a) the geometrical volume V_y; (b) the meshed non-conformal volume of the yarn, as if the yarn was alone in the textile $V_{y,nc}$; (c) the volume of the elements $V_{y,p}$ that are assigned to the yarn.

- Since the homogenized properties of the textile are mainly driven by the fiber content in all directions, it is of paramount importance to guarantee a realistic representation of the fiber content in each yarn. However, since the yarn volumes differ between the geometrical and non-conformal representations, the fiber content cannot be identical unless the intra-yarn fiber volume fraction is modified.

Since $V_{y,p}$ is the yarn volume defined in the FE simulation, and V_y is the reference yarn volume, the idea is to preserve the fiber volume when transitioning from V_y to $V_{y,p}$, i.e. to find a corrected intra-yarn fiber volume fraction $k_{f,p}$ that fulfills:

$$V_{y,p}k_{f,p} = V_y k_f, \tag{3.16}$$

where k_f is the constant, reference intra-yarn fiber volume fraction in the geometrical representation. It is naturally achieved by using:

$$k_{f,p} = \frac{V_y}{V_{y,p}} k_f. \tag{3.17}$$

However, this adaptation is only based on global considerations and does not take local yarn intersections into account. An enhanced correction is proposed, accounting for local penetrations. To this end, the yarn mesh $V_{y,nc}$ is separated

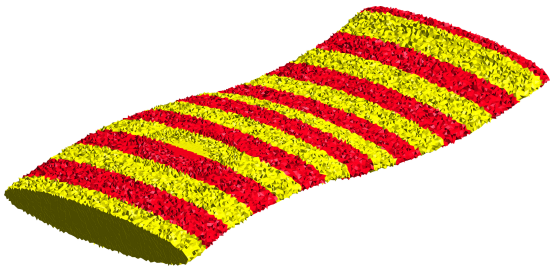


Figure 3.31: Division of a yarn into several cells for the procedure of local fiber volume fraction adaptation.

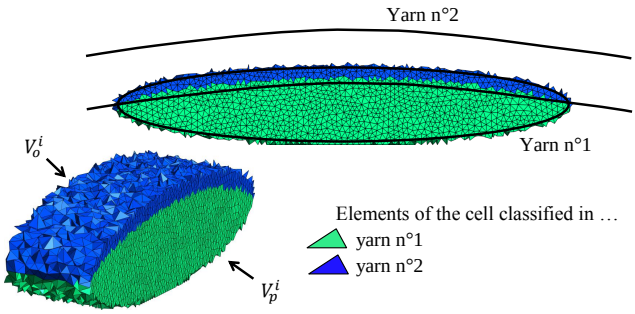


Figure 3.32: 3D and planar view of a yarn cell.

into an arbitrary number of cells, see Figure 3.31. In practice, each yarn is divided into 15-30 cells over the RVE length, depending on its geometrical complexity. While all elements lie within the yarn boundary, they are not all assigned to this particular yarn in the FE simulation. Hence, each cell i can be composed of two types of elements, see Figure 3.32. The elements that are classified in the yarn contribute to the volume V_p^i , and the elements that are assigned to other yarns contribute to the volume V_o^i . In essence, the fiber volume that is supposed to be contained in V_o^i is lost in the FE simulation and must be added to V_p^i . This transition artificially mimics the compaction of all the fibers of cell i into the FE volume V_p^i . It is achieved by adapting the intra-yarn fiber volume fraction in the cell i as,

$$k_{f,p}^i = \frac{V_y(V_p^i + V_o^i)}{V_{y,nc}V_p^i} k_f. \tag{3.18}$$

Summation over i in Eq. 3.18 fulfills the requirement expressed by Eq. 3.16. Both Eq. 3.17 and Eq. 3.18 are valid also in the absence of penetrations or if more than two yarns overlap at the same location, and compensate for the mesh-related discretization error as well as the penetration-related fiber volume loss. When the penetration volume is too large, Eq. 3.18 can lead to unrealistic values of the intra-yarn fiber volume fraction $k_{f,p}^i$. Hence, a realistic upper bound is imposed to $k_{f,p}^i$ (e.g. 0.75 [114]). If this limit is exceeded, an algorithm looks for the highest local fiber volume fraction, in the cell noted c, and for its

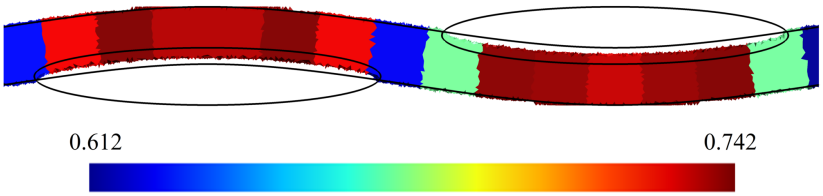


Figure 3.33: Distribution of the corrected fiber volume fraction $k^i_{f,p}$ along one yarn of the plain-weave textile. The black continuous lines represent the yarn boundaries.

two closest neighboring cells, in opposite directions along the yarn path, which do not exceed the maximum value. Then, half of the excess fiber volume in cell c is transferred to each of those two cells. The algorithm runs while there is at least one cell over the limit. It fails only if all cells exceed the upper bound, which means that the overall penetration within the yarn is too large. It can then be decided to increase the limit, understanding that this may affect the accuracy of the homogenization procedure, or to improve the geometrical representation in order to reduce penetrations.

The resulting fiber volume fraction distribution $k^i_{f,p}$ over one yarn of the plain-weave discussed previously is shown in Figure 3.33, with a nominal fiber volume fraction $k_f = 0.6$. The highest values of $k^i_{f,p}$ indeed appear where the yarn cross-section is the most compacted due to penetrations with the other yarns. In this case, none of the cells exceeds the upper bound, chosen equal to 0.75.

This method is generic and automated. It emulates changes in cross-section shapes and yarn compaction in the FE representation, while maintaining idealized and simple geometric modeling. After computing the local fiber volume fraction, using Eq. 3.18, the material properties are determined in each cell of each yarn with the micromechanics-based models given by Eq. 3.10.

3.5.2 Sensitivity analyses

A sensitivity analysis is conducted on the fictitious case in Figure 3.34. The reference configuration represents a penetration-free RVE that could have been produced by a complex textile modeling technique. The idealized configuration in Figure 3.34 represents the simplified textile in accordance to the present method. It respects the main characteristics of the reference configuration, such as the position of the mid-lines of the yarns, and the yarn volumes. The purpose of the sensitivity study is to assess the accuracy of the method, the influence of the yarn aspect ratios and the adequacy of Eq. 3.18, which corrects the intra-yarn fiber volume fraction to compensate for the penetrations.

First, the sensitivity of the homogenization results with respect to the aspect ratio of the yarn cross-section is studied. This is important, since the geometrical simplification imposed in the present method often leads to differences in the aspect ratio compared to more complex modeling approaches. The aspect ratio r of the idealized configuration is defined by the ratio between the

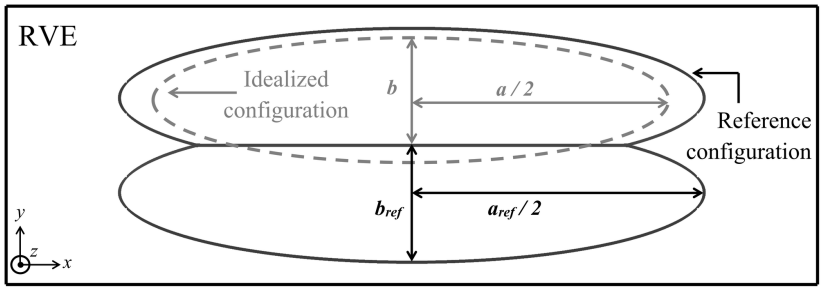


Figure 3.34: The reference configuration without penetration, versus the idealized configuration keeping yarn mid-lines and volumes. For clarity, only one yarn is illustrated in the idealized configuration.

minor axis, b, and the major axis, a, of the yarn cross-section after meshing and element classification, illustrated in Figure 3.34 as $r = b/a$. The term r_{ref} refers to the aspect ratio in the reference configuration, computed as b_{ref}/a_{ref}. Figure 3.34 depicts the situation $r = r_{ref} = 0.2$. Even when $r = r_{ref}$, the reference and idealized configurations are not equal because the areas of the ellipses in the idealized textile are equal to the cross-section areas of the reference yarns, which are not ellipses. The sensitivity study consists in performing homogenization analyses when r varies within $r_{ref} \pm 10$ %, and comparing to the reference results without any penetrations.

Then, it is checked that Eq. 3.18 is a suitable way to compensate for textile penetrations. This is evaluated by multiplying the result of Eq. 3.18 by a factor of 1 ± 0.1, which is equivalent to changing k_f by $\pm$ 10 % with respect to the reference value $k_{f,ref}$. In this case, $k_{f,ref} = 0.7$ is chosen. Since the yarns are here straight, the global and local corrections by Eq. 3.17 and Eq. 3.18, respectively, give equivalent results.

The results are presented in Figures 3.35 and 3.36 for the sensitivity with respect to the aspect ratio of the cross-section and to the correction for the fiber content Eq. 3.18, respectively. In each figure, one graph for each of the 12 orthotropic properties shows the value obtained by the idealized model normalized by the value of the reference configuration. Moreover, the mean error over all predicted properties (with identical weights for each property) is computed. Figure 3.35 also shows the results obtained when the aspect ratio varies and the penetrations are not corrected, i.e. $k_{f,p} = k_f$. The main findings are the following:

- Trends are conflicting, meaning that increasing or decreasing r or k_f leads to better accuracy for some properties and to reduced accuracy for others.
- When averaging the accuracy over all properties, the mean error reaches a minimum of 0.4 % for $r = r_{ref}$ and $k_f = k_{f,ref}$, which means that using the same aspect ratio as in the reference configuration and the correction of Eq. 3.18 for the fiber content is indeed the best possible choice. The associated maximum error is observed on G_{yz} and is about 2 %. Changing the aspect ratio or the fiber content slightly does not help

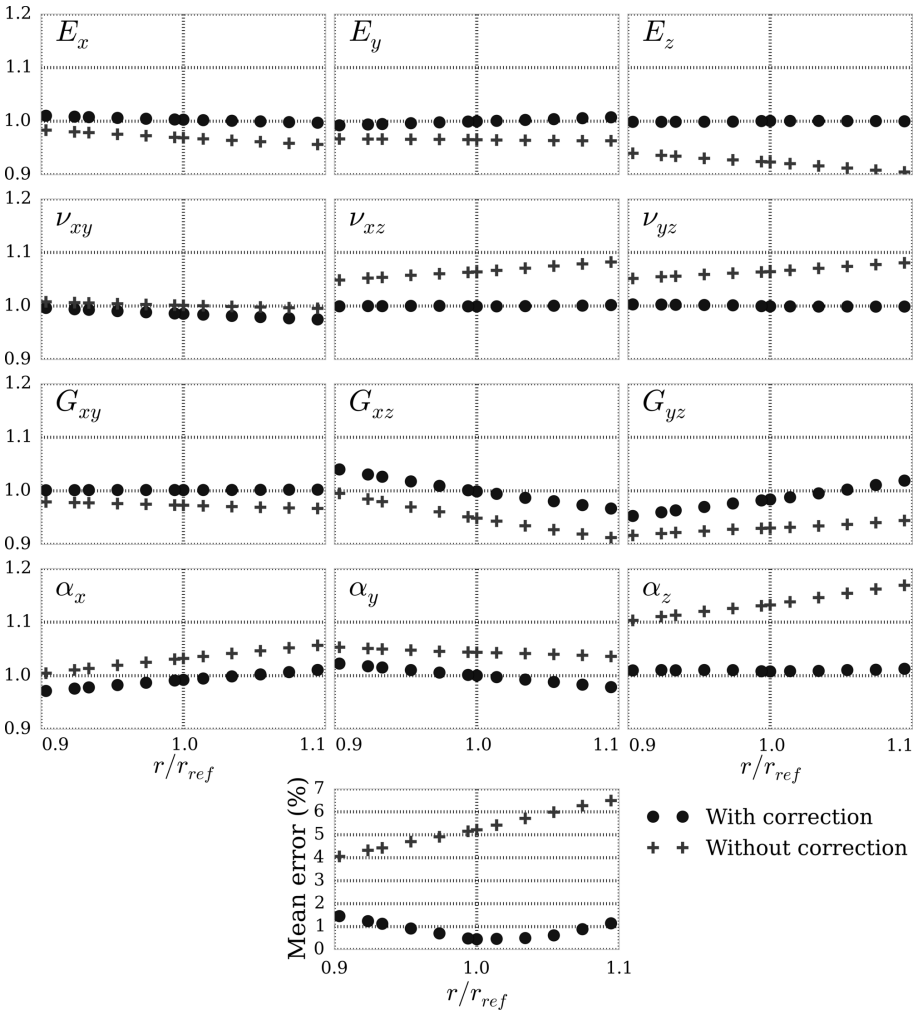


Figure 3.35: Influence of the aspect ratio r on the accuracy of the predictions of the different thermo-elastic constants and on the mean error over all these predictions.

improve the compensation for the penetrations.

- The same configuration without correcting for the penetrations leads to a mean error of 5 %, i.e. 10 times larger than when the correction is used. The maximum error reaches 13 % for the longitudinal CTE α_z. The correction also limits the sensitivity to the aspect ratio, in the sense that the mean error varies by 3 % (from 4 to 7 %) without correction, as opposed to only 1.1 % with correction, in the range $r_{ref} \pm 10$ %;
- The mean error stays below 1.5 % in the range $r_{ref} \pm 10$ %, and below 6 % in the range $k_{f,ref} \pm 10$ %. This means that, for the present test case and for the evaluated elastic properties, the accuracy of the homogenization

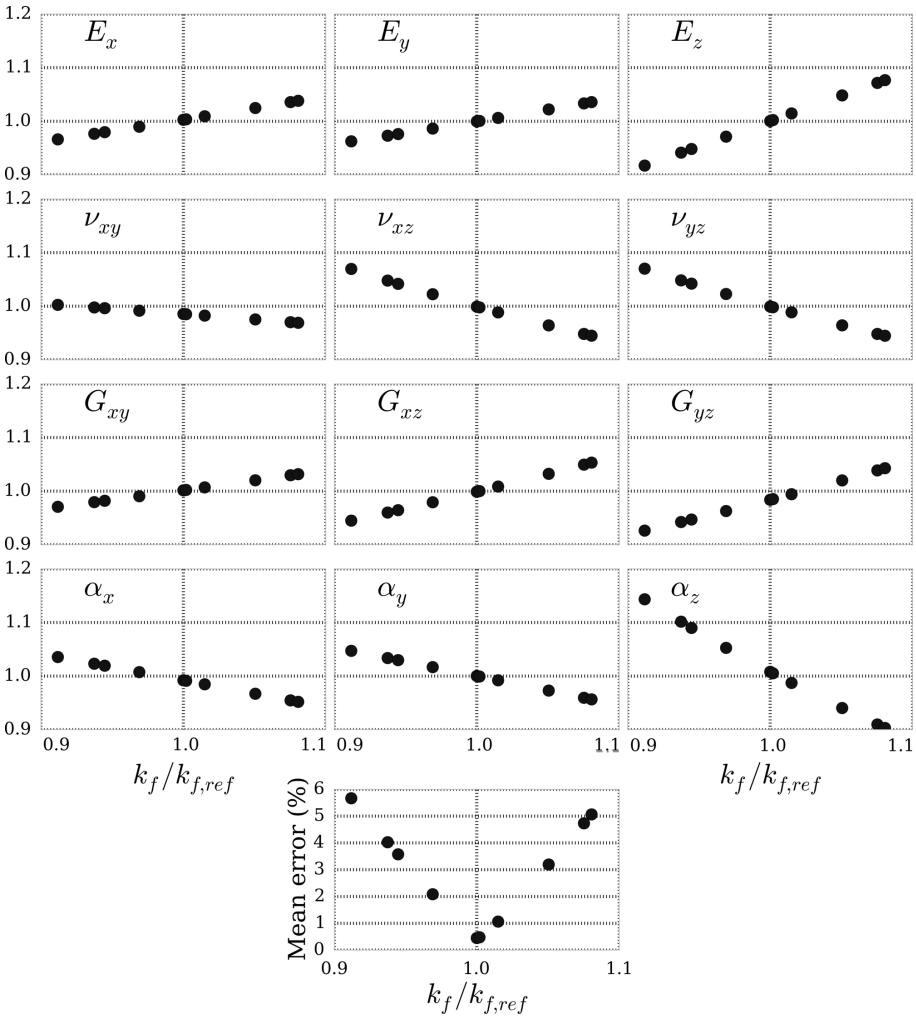


Figure 3.36: Influence of the fiber volume fraction k_f on the accuracy of the predictions of the different thermo-elastic constants and on the mean error over all these predictions.

procedure is more sensitive to variations in the fiber content than in the aspect ratio. This implies, as expected, that it is of primary importance to use a corrected fiber volume fraction in the simplified approach, with the help of Eq. 3.18. The yarn aspect ratio, on the other hand, has a subordinate effect on the accuracy.

- When applying the correction, the shear moduli G_{yz} and G_{xz}, the transverse CTE α_y and the Poisson's ratio ν_{xy} are the most sensitive to the yarn aspect ratio, with errors up to 5, 4.5, 3 and 2.5 %, respectively, when $r = r_{ref} \pm 10$ %. Without correction, the error reaches 18 % for the transverse CTE α_z.

In the aspect ratio sensitivity study, the penetration volume varies from 3 to 5 % of the total volume of the RVE, increasing with r.

3.6 Comparison to textiles studied in the literature

In this section, the new non-conformal methodology is compared to experimental and numerical results published in the literature for 3D textiles. For details about the modeling approaches used by the respective authors, the reader is referred to the referenced papers. Details necessary to reproduce the results obtained by the simplified approach, such as the geometrical information or material properties, can be found in Appendix C.

3.6.1 Case 1: A 3D-woven textile with high penetrations

A typical application of the proposed methodology is the modeling of complex, highly-compacted 3D textiles. Stig and Hallström [117, 147] developed a modeling framework suited to such textiles. Yarns are modeled as hollow tubes with shell elements and are inflated with contact conditions by running an explicit FE analysis until a desired yarn volume fraction is reached (see Figure 3.8). For the cases addressed here, the geometrical fidelity obtained with this technique with respect to the manufactured textile is remarkable [117]. The yarns occupy up to 85 % of the volume of the RVE [147]. Such compaction without yarn penetrations is out of reach with built-in functionalities of TexGen since the yarn cross-section varies significantly both in size and shape along its length. The simplified modeling strategy suggested here is applied to some of the test cases presented in [147] using the following parameters:

- identical dimensions of the RVE as in the reference case;
- similar yarn paths and yarn interlacing, from a topological point of view, as in the reference case. The yarn-path topology is illustrated in Figure 3.37(a), defined by simple sinusoidal functions, with amplitudes set to represent, on average, the prescribed crimp of the reference case, given in [147];
- constant and elliptical yarn cross-sections. The area of the cross-sections are given by the fiber count (12k for warp yarns, 6k for weft yarns) and by the assumption that the average intra-yarn fiber volume fraction is the same for all yarns [147]. The amplitudes of the yarn paths are calculated so that warp and weft yarns are tangent at contact points. A simple algorithm, implemented in the user programming interface of TexGen, selects the aspect ratio of the ellipses in order to minimize the overall amount of penetration in the RVE. The cross-section of warp yarns is progressively rotated along the yarn path so that the major axes of the yarns are parallel at the contact points.

No further hypothesis is needed to model the textile. Three textiles are reproduced from [147], referred to as “S”,“B” and “D”, in agreement with

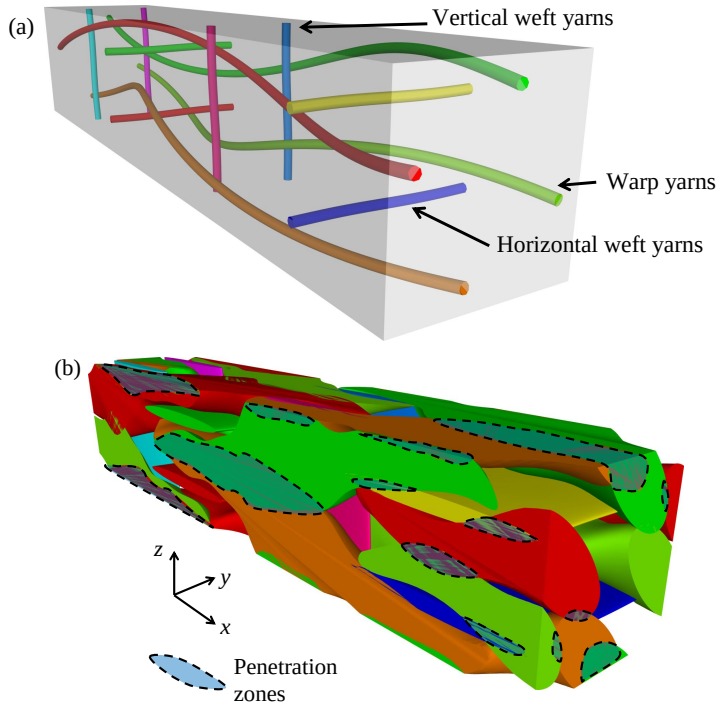


Figure 3.37: Case 1 (a) sinusoidal yarn paths of the 3D-woven textile; (b) 3D-woven textile B modeled in TexGen. Penetrations occupy 9.7 % of the RVE volume.

the notation used in the reference paper. These three textiles have the same type of architecture, but different characteristics such as RVE dimensions, fiber content or yarn crimp. For instance, the simplified model of textile B is shown in Figure 3.37(b). In this case, the penetration volume, i.e. the volume that is occupied by more than one yarn, is 9.7 % of the total volume of the RVE.

The methodology described above, including the algorithm which optimizes the aspect ratios, has been set up in a few hours and takes about five minutes to run. Although Stig and Hallström do not provide indications on the effort and computational times required to generate textiles with their approach, reading their papers [117, 147] gives an idea of the significant developments which have been needed to set up their strategy. Moreover, modeling one textile with their approach involves an explicit FE computation with a lot of contact. The approach developed in this thesis is thus much simpler. Of course, the geometrical fidelity with respect to the real textile is much better with their technique. It is nonetheless interesting to show that highly compacted textiles can indeed be modeled with TexGen, in a fast and generic manner, provided that the penetrations can be accommodated in the subsequent homogenization procedure.

All homogenization results are presented in Table 3.3. The columns “global correction” and “local correction” refer to the results obtained using Eqs. 3.17

	Present, local correction	Present, global correction	Reference, numerical	Reference, experimental [147]	Relative difference[2]
Case 1, Textile S					
E_x [GPa]	74.7	77.1	83.2	74.6 ± 0.3	+0.1 %
E_y [GPa]	11.7	11.7	12.0		
ν_{xy} [-]	0.26	0.26	0.31		
ν_{yz} [-]	0.27	0.25	0.31		
G_{xy} [GPa]	3.26	3.29	3.76		
G_{yz} [GPa]	1.93	2.27	1.93		
Case 1, Textile B					
E_x [GPa]	59.0	60.7	65.8	58.8 ± 3.7	+0.3 %
E_y [GPa]	13.3	13.2	12.5		
ν_{xy} [-]	0.27	0.27	0.36		
ν_{yz} [-]	0.23	0.22	0.28		
G_{xy} [GPa]	3.35	3.35	3.94		
G_{yz} [GPa]	1.94	2.25	1.99		
Case 1, Textile D					
E_x [GPa]	36.2	36.4	36.2	31.9 ± 2.1	+13.5 %
E_y [GPa]	15.0	14.9	11.5		
ν_{xy} [-]	0.26	0.26	0.41		
ν_{yz} [-]	0.18	0.17	0.27		
G_{xy} [GPa]	3.08	3.12	3.84		
G_{yz} [GPa]	1.95	2.23	2.19		

Table 3.3: Comparison of homogenization results for Case 1 (Stig and Hallström).

and 3.18, respectively. The comparison between the results obtained with the local correction and the reference finite element predictions demonstrates an average difference of 10 % for the elastic modulus (6 % if the worst of the six predictions is discarded) and for the shear modulus. However, the Poisson's ratios are systematically underestimated, by 15 to 35 %. This deviation is however not surprising since the predicted transverse contraction is likely to be more sensitive to the geometrical assumptions that have been made, in particular the constant yarn cross-sections. The present methodology complies very well with the experimental data presented in [147] for the modulus in the warp direction, in fact equally well or better than the reference FE results. However, as stated in [117, 147], the models are perfectly regular and periodic while the material in the experiments is not, due to semi-manual manufactur-

[2]The relative difference is calculated between the results obtained with the presented local correction and the experimental results.

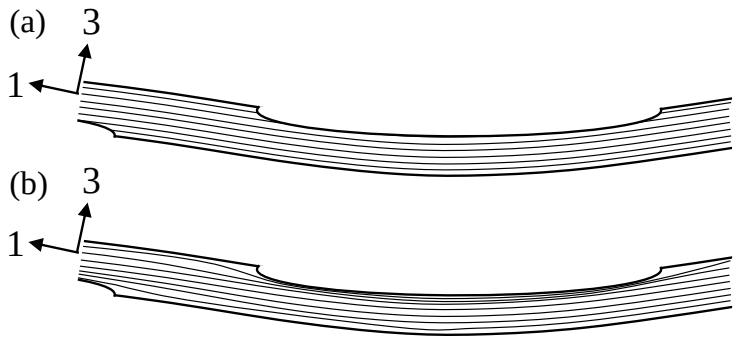


Figure 3.38: (a) Current hypothesis: the directions of orthotropy follow the yarn mid-line, even in the presence of penetrations; (b) Possible improvement.

ing, and the experimental data are based on only a few samples. As far as the Poisson's ratios are concerned, experimental data would be needed to make further conclusions.

The difference between the results obtained with the local and the global corrections is small. The shear modulus G_{yz} is affected most, with the local correction providing the lower discrepancy with respect to the reference results for two out of three cases. Therefore, it cannot be stated from these test cases that the local correction yields better homogenization predictions, although its physical interpretation seems to be more realistic. Intuitive and simpler to implement, the global correction delivers satisfactory predictions, but it probably cancels out part of the stress and strain fields heterogeneity associated with local compaction. Of apparently limited importance for the computation of homogenized properties, this difference might become relevant when addressing failure criteria within the yarns. However, more in-depth investigations are needed to demonstrate the benefits of the local approach. It should be noted that the principal directions of orthotropy are always assumed to follow the yarn mid-line, as illustrated in Figure 3.38. This could be improved by using the yarn compaction zones to guide the orientations, though this has not been implemented yet. From the perspective of computational efficiency, the local correction induces a negligible pre-treatment computational cost, typically a few seconds.

3.6.2 Cases 2 to 6: 3D-woven textiles without penetrations

Other results haven been published regarding the production and the mechanical response of 3D textiles. Five examples are addressed here. The textiles are replicated in TexGen using built-in functionalities only, i.e. in a few minutes. The result of this modeling is shown in Figure 3.39. The elastic properties are then predicted by the homogenization procedure developed earlier in this chapter. The presented textiles are 3D non-crimp fabrics based on the following references:

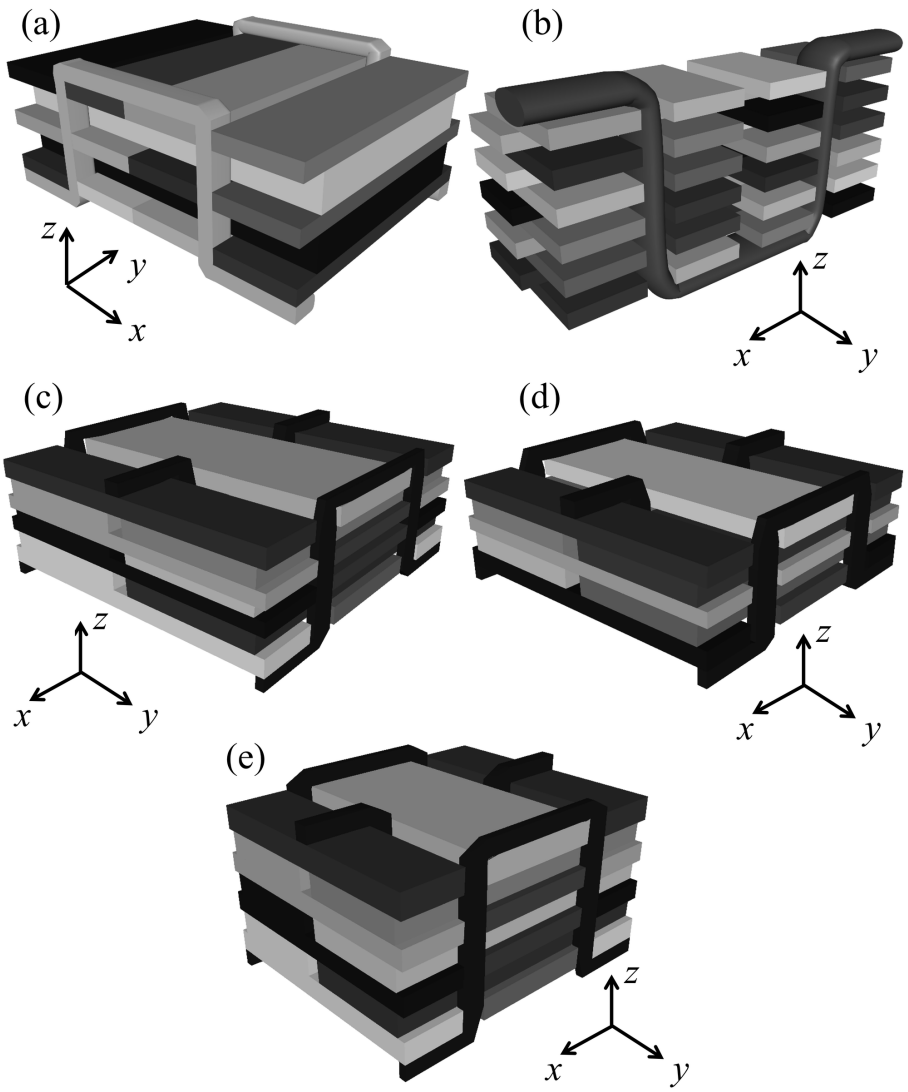


Figure 3.39: TexGen models of the 3D-woven textiles. Figures (a) to (e) correspond to cases 2 to 6, respectively.

- Case 2: S-2 glass/epoxy composite by Bogdanovich [150]. The model is based on the simplified representation by Rao et al. [151];
- Case 3: carbon/epoxy composite by Tan et al. [152, 153];
- Case 4: E-glass/epoxy composite referenced 3D-96 by Lomov et al. [154]. The geometrical model is based on measurements from [155];
- Case 5: E-glass/epoxy composite referenced 3D-78 by Lomov et al. [154]. The geometrical model is based on measurements from [155];
- Case 6: carbon/epoxy composite by Bogdanovich et al. [156]. The geo-

metrical model is based on measurements by Karahan et al. [157].

The reference models are already simplified versions of the real textile, which implies that:

- The models generated in TexGen in the present work are very similar to the reference models set up by the respective authors;
- The penetrations are solely located at the corner of the vertical yarns, occupying less than 0.05 % of the total volume. It has been checked for case 3 that the local correction leads to similar results as the corresponding analysis without correction.

Therefore, these cases validate the simplified geometrical representation combined with the non-conformal meshing approach. The penetration correction method is not addressed by these test cases. The results of the comparison are presented in Table 3.4. The symbol E_{45} designates the apparent Young's modulus measured when applying a traction oriented at 45 degrees with respect to the principal in-plane directions of orthotropy of the textile. In the simulations, this value is given by [155],

$$\frac{1}{E_{45}} = \frac{1}{4E_x} + \frac{1}{4E_y} + \frac{1}{4G_{xy}} - \frac{\nu_{xy}}{2E_x}. \tag{3.19}$$

By measuring E_{45}, one can assess the accuracy of the homogenization in predicting the shear modulus, which is more complicated to measure directly [155]. As a matter of fact, the worst prediction in Table 3.4 (difference of 18 %) is observed between the predicted shear modulus and the direct measurement of the latter for case 2. Unfortunately, the author does not give indications regarding the experimental variability, and the error of 18 % should not convey the idea that the methodology is ill-suited to predict the shear modulus. The indirect comparison of the shear modulus via E_{45} is much better for the other cases. It can be noted that, given the typical orders of magnitude at stake ($E_x \approx E_y \approx 5G_{xy}$; $\nu_{xy} \approx 0.1$), G_{xy} is by far the most influential parameter in the right-hand side of Eq. 3.19, and a small error for E_{45} likely implies a small error for G_{xy}.

The error on the principal Young's moduli, E_x and E_y, is well within the standard deviations, with an error of typically 1 to 4 %. Regarding the Poisson's ratio, which is also complicated to measure reliably [150], the error reaches 10 % but it also remains within the standard deviation of the experimental measurements. In conclusion, the overall correlation is very good.

3.7 Discussion about computational times

Since very few authors mention the computational (CPU) times required by their methodologies (either for textile modeling or homogenization), this point has not been mentioned yet in this chapter, for lack of data to compare to. For the sake of completeness, the approximate times necessary to homogenize a textile with the presented methodology are listed below. Apart from the use

	Present, numerical	Reference, numerical	Reference, experimental	Relative difference[3]
Case 2 (Bogdanovich) [150]				
E_x [GPa]	24.95	27.31	24.68	+1.1 %
E_y [GPa]	20.44	25.70	20.75	-1.5 %
ν_{xy} [-]	0.119	0.125	0.11	+8.2 %
G_{xy} [GPa]	3.15	3.58	3.86	-18.4 %
Case 3 (Tan et al.) [153]				
E_x [GPa]	41.88	39.70	40.97 ± 2.00	+2.2 %
E_y [GPa]	48.64	51.09	47.30 ± 4.02	+2.8 %
ν_{xy} [-]	0.031	0.033	0.0346 ± 0.01	-10.4 %
Case 4 (Lomov et al., textile 3D-96)[4] [154]				
E_x [GPa]	23.3	-	24.3 ± 1.2	-4.1 %
E_y [GPa]	24.4	-	25.1 ± 2.3	-2.8 %
E_{45} [GPa]	13.0	-	12.9 ± 0.5	+0.8 %
Case 5 (Lomov et al., textile 3D-78) [154]				
E_x [GPa]	23.1	-	23.0 ± 2.5	+0.4 %
E_y [GPa]	23.5	-	23.0 ± 2.5	+2.2 %
E_{45} [GPa]	13.2	-	13.4 ± 0.8	-1.5 %
ν_{xy} [-]	0.107	-	0.115 ± 0.031	-7.0 %
Case 6 (Bogdanovich et al.)[4] [156]				
E_x [GPa]	61.0	-	59.8 ± 3[5]	+2.0 %
E_y [GPa]	66.6	-	63.6 ± 3[5]	+4.7 %
E_{45} [GPa]	10.4	-	9.83 ± 0.29	+5.8 %

Table 3.4: Comparison of homogenization results for Cases 2 to to 6.

of TexGen, which is a manual operation performed on a desktop computer, the CPU times correspond to those obtained on a high performance computing center consisting of Intel E5-2967v2 (2.7 GHz) processors:

- The generation time of the textile geometry in TexGen is variable and highly depends on the complexity of the textile. Very simple textiles such as 2D-woven textiles can be modeled in a few seconds. 3D-woven textiles which do not require the use of advanced features usually require a few minutes. As mentioned previously, a slightly more complex procedure had to be set up to mimic the textiles of Stig and Hallström (Section 3.6.1), still much simpler than the original work.

[3]The relative difference is calculated between the results obtained with the presented local correction and the experimental results.

[4]The Poisson's ratio is not listed here due to a very high experimental variability (standard deviation of about 100 %) and/or inconsistent values.

[5]Several values for the Young's moduli are derived from the experiments in [156], due

- Before meshing, the level-set D_c must be computed on a regular grid. The chosen grid density is 1.5 million points, which provides a very satisfactory resolution, even for complex textiles. The resulting CPU time is about 45 minutes. This is largely over-estimated, for two reasons. Firstly, this task can be parallelized. Secondly, the distance computation has been implemented in Python, which is very slow compared to C or other programming languages, and the algorithm has not been optimized. More representative CPU times are probably those obtained by Sonon and Massart [158], ranging from a few seconds to a few minutes.
- Then, the adaptive mesh generation step in GMSH lasts a few seconds.
- On the final mesh, the level-set D_c is computed once again to classify the elements in the appropriate material. Since the distance is computed at the centroid of the elements, the CPU time is proportional to the number of elements and it is the same as mentioned previously: about 30 minutes per million elements. The mesh density which has been used for the cases presented in Section 3.6 is approximately 2 million elements. Once again, this performance could be drastically improved with optimized programming.
- A few minutes (less than 10 minutes for the heaviest meshes) are necessary to prepare the input file for the FE simulations, using a Python script. The most demanding task is the creation of the node-to-node multi-point constraints for the periodic boundary conditions (details in Appendix A).
- The CPU times used by the FE simulations are reasonable: about 5 minutes per million elements per BVP in Abaqus. This amounts to 70 minutes for the homogenization of an orthotropic RVE meshed with 2 million elements, and it can be further reduced by using parallelization. The memory usage is 8 GB per million elements.
- The post-treatment (stress or strain averaging) takes about 25 minutes per million elements, which is not negligible. It can also be parallelized. Furthermore, the CPU time could be reduced to virtually zero by taking advantage of the divergence theorem which enables to compute a surface integral instead of a volume integral [159].

3.8 Conclusion

A non-conformal meshing procedure has been proposed allowing the FE homogenization of penetrating textile geometries without FE or geometrical pre-treatment. A pre-existing level-set which captures the material interfaces in the penetration regions has been adapted to make it suitable to adaptive mesh refinement localized at the interfaces. This approach proved to be more suitable than the classical voxel meshes for the prediction of homogenized properties and also localized microscopic fields.

to the stiffening of the carbon fibers. The values retained here correspond to the ISO-10618 standard (2014), and the standard deviation is taken from Table 1 of [156].

For non-negligible penetrations, a solution has been implemented to reallocate the lost fiber volume to the remaining yarn volume. The methodology is not limited by the amount or location of the penetrations, although the physical fidelity of the model diminishes in case of exaggerated penetration volumes. The main benefits of the method are:

- Very limited effort is required to generate geometrical representations of a very wide range of textiles, after which no user intervention is necessary throughout the entire homogenization process.
- Small or large yarn overlaps are not obstacles to the FE simulations, discarding the need for complex pre-treatment to remove penetrations which are bound to appear when modeling highly compacted architectures.
- Even with a penetration-free textile, the methodology has the advantage of leaving full control to the user over the mesh size and, hence, over the computational time, as opposed to conformal meshes that may require very fine elements in thin resin regions. With the non-conformal approach, fine elements at yarn interfaces lead to improved predictions, but this is not mandatory.

A sensitivity study has shown that, in the absence of correction, a penetration volume fraction of 5 % leads to significant errors: up to 7 % on average when combining all elastic properties, and up to 18 % for one CTE. These values are limited to 1.5 % on average and 5 % for one shear modulus when applying the correction.

The presented approach is a simple, pragmatic and efficient alternative for non-specialized engineers who do not need extremely sophisticated models. The obtained predictions compare very favorably to experimental results drawn from the literature, including three configurations for which the penetration volume fraction is about 10 %. The comparison to the much more complicated numerical approach is also satistactory, except for Poisson's ratio which are underestimated by 15 to 35 %. No further conclusion is drawn in the absence of experimental data. It must be understood that the geometrical simplifications necessarily have an impact on the prediction of the most sensitive properties, and of the microscopic fields within the RVE. In that sense, the use of the penetration correction methodology for the study of non-linear phenomena is not trivial and will require precautions and detailed studies. This has been left out for further work, as it is not the primary objective of the thesis. In the absence of penetrations, it has been shown that the homogenization procedure complies very well to experimental data for 3D textiles.

Chapter 4

Mold compensation strategies

4.1 Objective and literature review

Although cure-induced distortions constitute a topic of attention in the composite literature, very few attempts have been made to address in a systematic way the problem of reducing or, better, suppressing the problem. Two main approaches can be followed. A first option is to improve the manufacturing process. Teoh and Hsiao [160] observe a spring-in reduction of L-shaped parts by using the multistage curing technique and the VARTM process. Hsiao and Gangireddy [161] propose to include carbon nanofibers in a polyester resin in order to reduce the anisotropy in the thermal expansion of the material and, hence, limit the spring-in. Both of these methods drastically increase the complexity of the manufacturing process. Jain et al. [162] optimize experimentally the spring-in of a thermoplastic C-shaped aileron rib by changing the cure temperature. These three examples rely on time-consuming experimental investigations, due to the trial-and-error sequences. Brauner [41] suggests the application of a non-uniform temperature set point to the heating RTM press. In that scenario, the temperature of each zone of the press would be predicted by simulation to decrease the overall distortions of a composite part. The author shows numerically that a thermal gradient may improve the warpage of a wing panel, but the applicability of a truly optimized approach is not demonstrated. In particular, it is acknowledged that very high temperature gradients are required (more than 20°C), which create a series of unsolved problems.

A second option consists in using numerical simulations to guide towards an optimal shape of the mold so that the final part is as close as possible to the nominal geometry. This approach is called "mold compensation", and is the subject of the present chapter[1]. Dong [163] develops a simplified curing model, creates designs of experiments for several basic composite structures

[1] *Reproduced in part from:* B. Wucher, F. Lani, T. Pardoen, C. Bailly, Ph. Martiny (2014). Tooling geometry optimization for compensation of cure-induced distortions of a curved carbon/epoxy C-spar. *Composites: Part A* 56:27–35.

with only a few parameters and develops a regression-based spring-in reduction method. Dong [9] studies the effect of the curing process on a parametrized stiffener structure, without including the model in an optimization loop. Zhu and Geubelle [10] use an optimizer to alter the mold shape for L-shaped parts. Kappel et al. [164] take advantage of the morphing function of CATIA in order to compensate the warpage of flat plates made of unidirectional carbon/epoxy prepregs. Single-curvature warpage predictions for any configuration are obtained from interpolated measurements of a series of manufactured specimens of different lengths and thicknesses. The fact that the model is calibrated on experimental data diminishes the applicability of the method to other geometries and materials. Moreover, the author does not check, numerically or experimentally, that the compensated mold shape indeed produces flat panels after cure. Jung et al. [165] perform the same study for hybrid glass/carbon composite beams and have achieved satisfactory compensation. Kappel et al. [5] also compensate a straight C-profile, once again relying on experimental measurements of spring-in of a significant number of L-shaped brackets.

All the aforementioned studies remain within the single-curvature range, where the distortions can be, in a first approximation, compensated by a simple inversion. Fernlund et al. [166] develop process modeling capabilities and apply them to tool compensation involving several distortion modes of curved L-angles [167]. The compensation strategy is solely based on analytical considerations specific to this geometry. This case study has later been included in a risk assessment framework which quantifies the probability that the manufactured parts are out tolerances [168]. Hörberg et al. [6] aim to compensate a highly-integrated 9-meter stiffened upper wing cover. To this end, they simulate and compensate a 1-meter panel. Unfortunately, no indication is provided regarding the compensation methodology, and the distortions of the full-scale wing are not measured.

Therefore, the literature does not yet provide a systematic distortion compensation strategy for complex geometries. The present chapter constitutes an attempt to fill this gap. Different techniques are introduced, keeping in mind the generic target which is emphasized in this thesis. They are tested and compared for a doubly-curved C-spar. Other numerical applications are then studied. Each method has assets and disadvantages, and a discussion is provided in Section 4.4. This chapter involves only numerical proofs of concept, while the entire methodology is validated experimentally in Chapter 5. In that sense, the numerical values hereafter (such as part dimensions, material data, curing cycle, measured distortions) have only little meaning and importance. The main interest is to predict, for a given geometry, the mold shape which minimizes the cure-induced distortions.

4.2 Development of mold compensation methods

4.2.1 CAD-based versus mesh-based methods

Two types of strategies are considered for the establishment of a generic numerical compensation framework: Computer Aided Design (CAD) based strategies and mesh-based strategies. The former consist in parametrizing a CAD model of the nominal geometry and in using an optimizer, in our case the in-house code MINAMO [169, 170], to find the optimal set of parameters which reduces the cure-induced distortions as much as possible. Two CAD-based compensation techniques differ from one another by the parametrization method and/or by how the distortions are interpreted and measured.

In contrast, mesh-based methodologies do not call for the use of an optimizer, since they rely on the application of an appropriate correction to the mesh, based on the distortions observed at a previous iteration. Whereas CAD-based methods explore a design space (made of all the possible values of the optimization parameters), the mesh-based approach is a deterministic iterative process. As discussed in Section 4.4, this is one of the main distinctions between the different methods. What should be noted now is that the numerical simulation of cure-induced distortions is at the core of all approaches, and the complexity of the computational chain depends on what must be automated or not. This is summarized in Figure 4.1. On the one hand, it is clear that, if an optimizer changes the shape of the CAD geometry, this geometry must be meshed automatically, and then the input file for the simulation must be prepared automatically as well. This includes, for instance: draping, mesh manipulations, definition of boundary conditions and solver settings. It can be very cumbersome to set up such an automated chain. On the other hand, mesh-based compensation involves solely a direct modification of the input file, which is much simpler. As hinted in Figure 4.1, mesh-based methods can require an additional time-consuming CAD reconstruction step, if necessary. This point is discussed later on. The developments and applications presented in this chapter show that both methodologies complement one another.

4.2.2 CAD-based methods

Formalization

As explained previously, CAD-based methods are based on the following principle: since a compensated mold geometry must be found, it is intuitive to parametrize the geometrical model of the mold and let an optimizer find the optimal shape which reduces the distortions. With the help of Figure 4.2, let us introduce the following notations:

- the number of parameters, n;
- the design space $\mathcal{S}_n$, a finite subset of $\mathbb{R}^n$;
- the set of parameters, $\mathcal{P} = \{p_1, \ldots, p_n\} \in \mathcal{S}_n$;

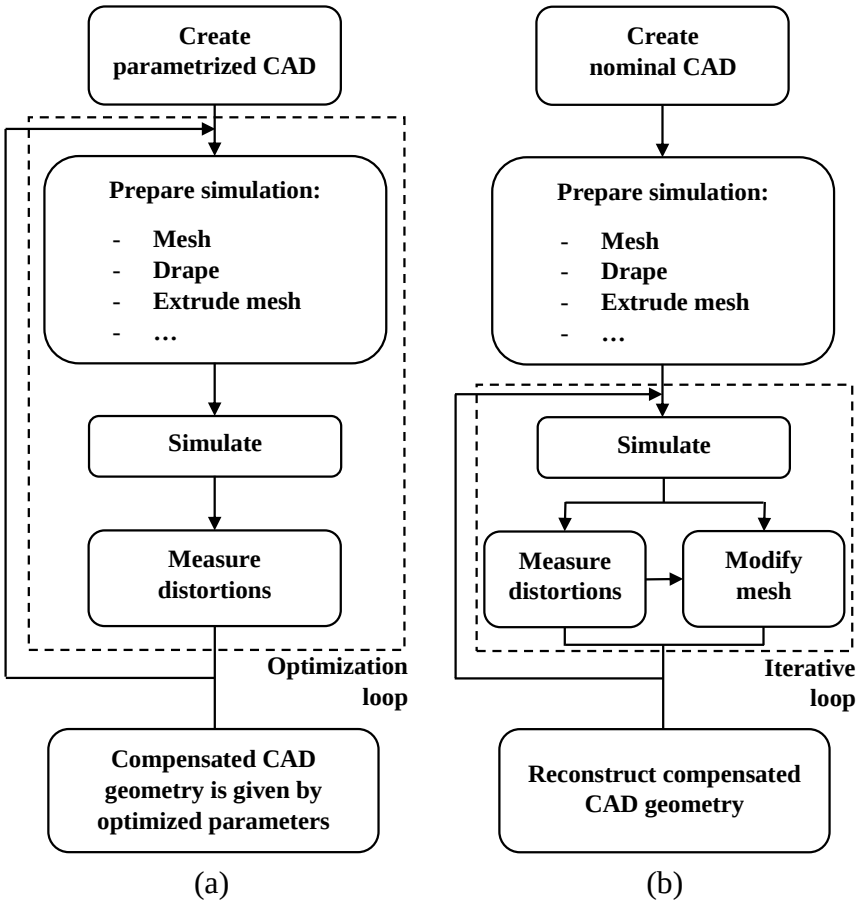


Figure 4.1: Schematics of mold compensation loops: (a) CAD-based case; (b) Mesh-based case.

- the CAD model parametrized with $\mathcal{P}$, $\mathcal{G}(\mathcal{P})$;
- the mesh of the part $\mathcal{MG}(\mathcal{P})$, which corresponds to the mold geometry $\mathcal{G}(\mathcal{P})$;
- the mesh $\mathcal{MG}(\mathcal{P})$ distorted after cure, $\mathcal{MG}_c(\mathcal{P})$.

The nominal mesh corresponds to $\mathcal{MG}(\mathcal{P}_0)$ with $\mathcal{P}_0 = \{0, \ldots, 0\} \in \mathcal{S}_n$. The objective of the optimization is to find the set of parameters $\mathcal{P}_{min}$ which minimizes the difference between the cured part $\mathcal{MG}_c(\mathcal{P}_{min})$ and the nominal part $\mathcal{MG}(\mathcal{P}_0)$.

In order to follow the progress of the compensation, a quantitative indicator is needed to measure the overall distortions of the result of the numerical simulation. In the literature, distortions are most commonly measured as spring-in angles [10] or maximum deflections [41]. Since these are explicit values, they are suitable to quantify the distortions of the specific case which is being studied. However, measuring specific quantities such as spring-in can be subjective or

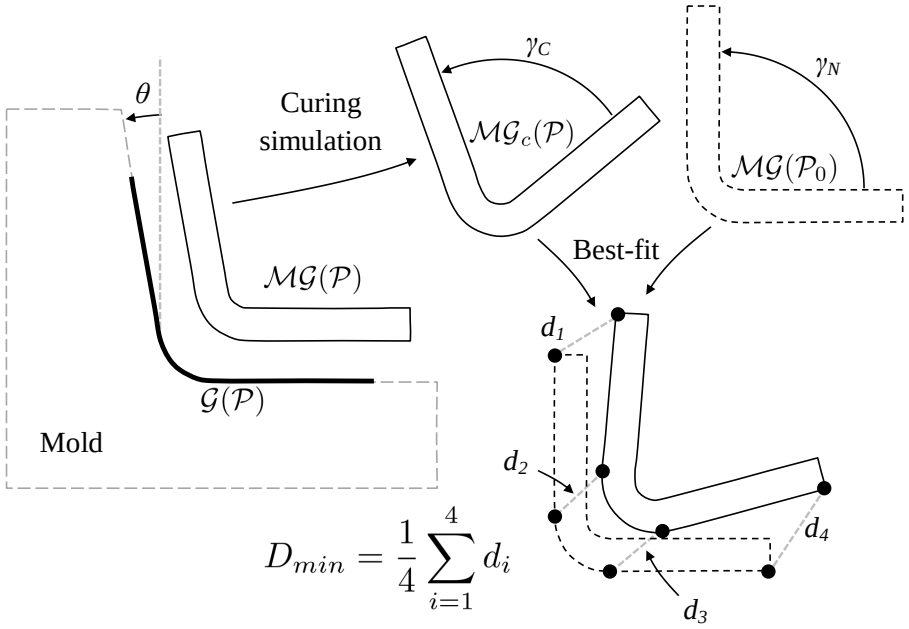


Figure 4.2: Schematic explanation of a CAD-based method and of the corresponding distortion measurement. In this example, there is only one parameter $\mathcal{P} = \{\theta\}$. For the sake of clarity, the "best-fit" position is not the real optimal position.

complex in curved regions, so much so that some researchers decompose angle measurements into spring-in and warpage components [39, 171, 172]. A more generic solution is preferable, to encompass any type of geometry and any kind of distortions. An alternative approach is to select an appropriate set of points on the distorted geometry and measure the distance between each point and its counterpart on the nominal geometry. A measure based on the displacements of the simulation would be biased, as it would highly depend on the boundary conditions imposed during the curing process. This is why a best-fit algorithm has been implemented in the frame of this thesis.

An example for the choice of the set of points is represented by the black dots in Figure 4.2. These points are supposed to be representative of the main features of the geometry, mainly of its curvature. The choice of the points remains subjective in this thesis, although it is an interesting perspective to think about potential objective methodologies for the determination of the set of points.

The best-fit algorithm finds the optimal residual distance between the cured mesh $\mathcal{MG}_c(\mathcal{P})$ and the nominal mesh $\mathcal{MG}(\mathcal{P}_0)$, as illustrated by Figure 4.2. If N is the number of points, P_i the position of the i-th point after cure, and P_i^0 its position in the nominal geometry, the purpose of the algorithm is to find the rigid body motion λ_{min} (involving three translations and three rotations) which minimizes the distance D_{quad}, which is the averaged sum of all squared

distances,

$$D_{quad}(\mathcal{MG}_c(\mathcal{P}), \mathcal{MG}(\mathcal{P}_0), \lambda) = \frac{1}{N}\sum_{i=1}^{N} \|P_i(\lambda)P_i^0\|^2 \tag{4.1}$$

where $P_i(\lambda)$ is the point P_i to which the rigid body motion λ is applied. The values λ_{min} are found by solving the non-linear equations

$$\frac{\partial D_{quad}}{\partial \lambda}(\mathcal{MG}_c(\mathcal{P}), \mathcal{MG}(\mathcal{P}_0), \lambda_{min}) = 0, \tag{4.2}$$

with the help of the Newton-Raphson method. Details about solving this equation are provided in Appendix D. Once λ_{min} is determined, the residual distance D_{min} is computed as

$$D_{min}(\mathcal{MG}_c(\mathcal{P}), \mathcal{MG}(\mathcal{P}_0)) = \frac{1}{N}\sum_{i=1}^{N} \|P_i(\lambda_{min})P_i^0\|. \tag{4.3}$$

Formally, $\mathcal{P}_{min}$ is thus defined by

$$\mathcal{P}_{min} = \underset{\mathcal{P}\in\mathcal{S}_n}{\arg\min} \left[D_{min}\Big(\mathcal{MG}_c(\mathcal{P}), \mathcal{MG}(\mathcal{P}_0)\Big)\right]. \tag{4.4}$$

The definition of D_{min} does not correspond to the true distance between two geometries. In Figure 4.2, the true distance between the cured geometry and the nominal geometry after best-fit involves projected distances, not point-to-point distances. The latter are used in Eq. 4.3 because they are much easier to compute than projected distance. In addition, D_{min} is nonetheless a relevant measure of the distortion, since $D_{min} = 0$ if, and only if, the two meshes coincide perfectly.

The classical distortion measurements may also be considered. In the case of Figure 4.2, it would be the spring-in angle $S = \gamma_N - \gamma_C$. While minimizing S or D_{min} is strictly identical for this geometry, Section 4.3.2 compares both options and proves that it is not necessarily true when there are several parameters.

Optimization procedure

The optimization problem is treated as follows by the optimizer MINAMO. In a first step, the objective function is evaluated for a collection of individuals (different sets of parameters $\mathcal{P}$) in the design space $\mathcal{S}_n$, adequately selected by a proper sampling strategy. In the present case, a latin-hypercube [173] design of experiments (DOE) is computed, in order to explore the design space and to create a database for the subsequent optimization. A surrogate model, i.e. an interpolation function, is then fitted to these results. The quality of this model is evaluated by the leave-one-out (LOO) cross-validation technique [174]. A LOO correlation coefficient equal to 1 means that the surrogate is exact and stable for the computed data. A lower value, e.g. below 0.7, means that the approximation is not accurate enough. It can be improved by an adaptive DOE technique [175] to better assess the non-linearities of the problem. In a

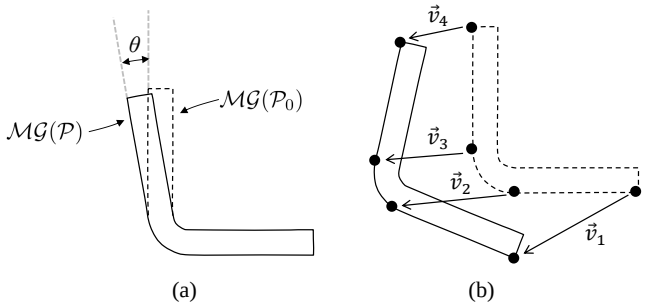


Figure 4.3: Schematic explanation (a) of the distortion modes method; and (b) of the control points method. In the former, the set of parameters is $\mathcal{P} = \{\theta\}$. In the latter, $\mathcal{P}$ is composed of the three components of each vector $\vec{v}_i$, minus 6 components to suppress the rigid body motions: there remains 6 parameters in total.

subsequent step, the optimization is launched. At each iteration, a classical evolutionary algorithm is used to minimize the value of the surrogate model. Since the latter is an approximation of the true objective function, the curing simulation of this optimum must be computed in order to obtain the real distortion value, which is then fed into the surrogate model for the following iteration. This approach is called online optimization and improves the quality of the approximation during the course of the optimization. The optimization process is stopped when the optimum of the true objective function has not improved for a significant number of iterations, at the user's discretion. The use of a surrogate-based optimizer, combined with evolutionary algorithms, allows for a much faster global optimization process compared to gradient-based methods, which lack space exploration and converge to the closest local optimum [170].

Two CAD-based methods

In this thesis, two different CAD-based compensation methods are investigated. They are designated as the "distortion modes method" (DMM) and the "control points method" (CPM). The principle of the methods is introduced very briefly, before presenting their application in Section 4.3. Figure 4.3 shows an example of both methods applied to a simple geometry.

As indicated by its name, the DMM compensates the actual deformation mechanisms which give rise to the cure-induced distortions, such as spring-in. They rely on the knowledge or on the power of observation of the user. In that sense, it is largely subjective.

On the other hand, the CPM is based on the parametrization of the position of a certain set of points, called "control points". It is consistent to choose the same set of points as in the measurement of the distortion explained in Figure 4.2. Indeed, both sets of points have the same purpose of being as representative as possible of the geometry. The term "representative" implies that if the points are linked together by splines or straight lines, the resulting

geometry is close to the nominal geometry. The choice of the control points shows that some rationale can be found, although it does remain subjective. This parametrization also offers a richer design space, since it leaves more freedom in terms of shapes which may be tested by the optimizer. As a direct consequence, the number of parameters is likely to be higher in the case of the control points. The advantages and disadvantages of both methods appear clearly when applying them to real test cases, and they are discussed in details in the conclusion of this chapter.

On a side note, the parametrization does not need to be applied to the whole geometry. The accounting for manufacturing constraints, for instance, may constrain certain zones to not be modified. In that sense, the user can keep some control on the geometry if needed.

4.2.3 A mesh-based method

A mesh-based method, called the "mirror method", is also developed. It is based on the notion that cure-induced distortions may be considered as linear in a first approximation. Under this hypothesis, the compensated geometry should thus be close to the inverted cured geometry with respect to the nominal geometry. An iterative alteration of the mesh is performed based on the explanation of Figure 4.4. A composite flat plate is represented as a 1D line, in order to simplify the figure. At iteration 0, the distortions of the nominal geometry are predicted by the numerical model. The tool geometry at iteration 1 is the inversion of this cured geometry — after a best-fit alignment. The cure-induced distortions of the part based on this tool geometry are then predicted. Logically, this cured geometry should be closer to the nominal geometry than the cured geometry at iteration 0. What is missing for the cured geometry to be equal to the nominal geometry is added to the tool geometry, resulting in the tool geometry of iteration 2. This process continues until the cured geometry converges towards the nominal geometry.

Although Figure 4.4 does not indicate it clearly, the correction of the geometry is actually performed based on the meshes. If $\mathcal{MG}_0^i$ and $\mathcal{MG}_c^i$ are the meshes of the composite part before and after the curing simulation at iteration i, respectively ($\mathcal{MG}_0^i$ can be assimilated to the tool geometry at iteration i), the corrected mesh for the next iteration is defined as

$$\mathcal{MG}_0^{i+1} = \mathcal{MG}_0^i + (\mathcal{MG}_0^0 - \mathcal{MG}_c^i), \tag{4.5}$$

where $\mathcal{MG}_0^0$ is the mesh of the nominal geometry. The correction in Eq. 4.5 is applied node by node. The material orientations (directions of orthotropy) for each finite element are determined for the corrected mesh based on vector projections from the nominal mesh to the corrected mesh, see Figure 4.5. This approach may seem like basic common sense, and the question must be raised whether or not the development of the more complicated CAD-based methods brings any advantage. The following sections of this chapter bring answers to that question.

The measurement of the distortions is the same as for CAD-based methods, except that the residual distance D_{min} covers all the nodes, and not just

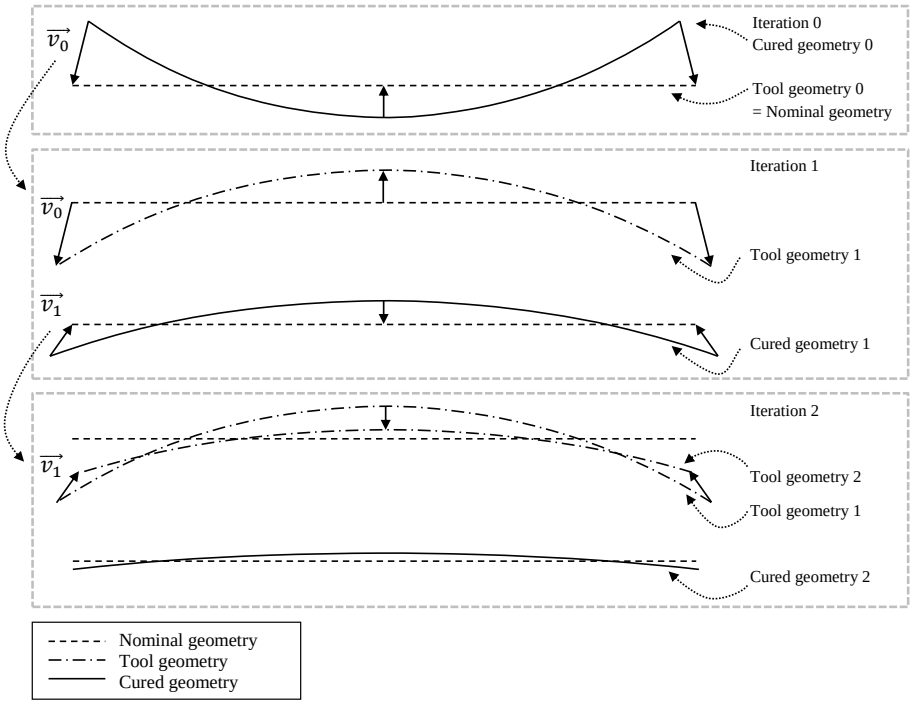


Figure 4.4: Schematic explanation of the mirror method.

selected points. This is made possible by the fact that the composite part is never remeshed, and therefore each node of the mesh has its equivalent in the nominal mesh. In that sense, the distortion measurement is more objective than for CAD-based methods, for which the points are user-selected.

4.3 Numerical applications

4.3.1 Hypotheses and numerical model

In the present study, a compensation problem always involves the following steps, either within an automated loop or directly performed by the user:

- A surface CAD model of the geometry is imported and meshed in the commercial FE package Abaqus [11].
- In order to generate realistic orientations for the curing simulation, a draping simulation is performed first with Simulayt's Composite Modeler for Abaqus [176]. Whether or not this task must be automated does not prevent the use of advanced features for complex geometries, such as seed curves or ply splits, to represent as realistically as possible the real draping process.
- The mesh is extruded by Simulayt, resulting in a volume mesh with one element per ply with the appropriate orientation for each element. If

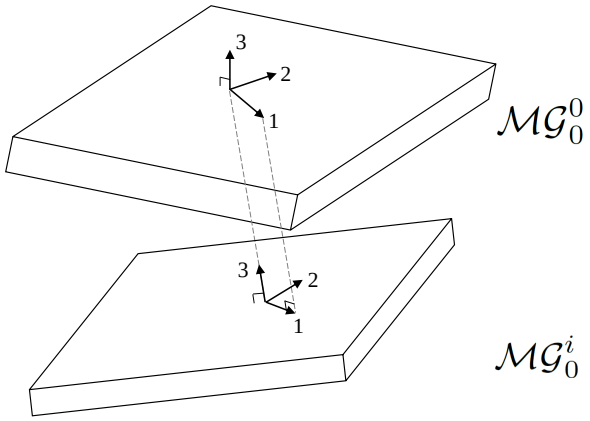


Figure 4.5: Projection of composite orientations for the mirror method. The direction 3 of the mirror mesh is normal to the element. The direction 1 is projected orthogonally from the nominal mesh. The direction 2 is computed as the cross-product of directions 3 and 1.

the geometry contains complex zones, in particular T-junctions, the extrusion function of Simulayt does not work. An in-house tool has been developed in the frame of this thesis to work around this limitation. Using one volume element per ply is the current practice at Cenaero, but this choice is not a limitation of the compensation methods. Finite elements comprising several plies can also be used.

- The mold may only be modeled as a rigid surface by extracting the mesh of the external surface of the part. More complex strategies can be put in place to be able to model the mold as a deformable body, but they have not been implemented within this thesis. The user has the choice between the following hypotheses:
  - free-standing cure: the mold is not modeled, no mechanical boundary condition is applied on the part except for the suppression of the rigid body modes;
  - fully constrained cure: the mold is not modeled, the nodes of the part's surface are fixed during the curing cycle;
  - one-sided rigid mold with a pressure on the part's free surface, mimicking the autoclave process;
  - two-sided rigid mold, mimicking the RTM process.

  Since this chapter only serves as a numerical proof of concept, the free-standing cure hypothesis is used.
- The simulation input file is prepared. This mainly consists in setting up the boundary conditions for the curing process. If the geometry comprises several parts (in particular, geometrical features such as stiffeners are considered as separate parts), they are fixed together with TIE conditions.

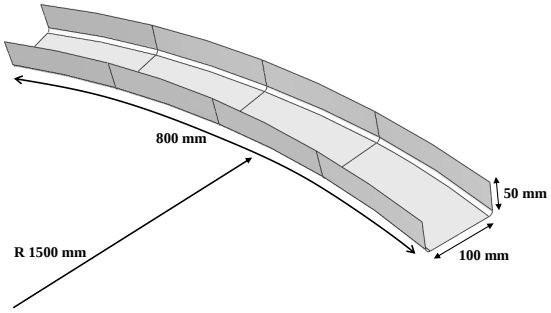


Figure 4.6: Surface geometry of the curved C-spar.

In this chapter, a uniform temperature distribution is assumed. This is not a limitation of the method, but a way to speed up the computations by suppressing the need for a transient thermal simulation. For the generic numerical applications, the following curing cycle is used: 8500 seconds at 180°C with heating and cooling ramps of 1.5°C/min.

- The simulation is launched with Abaqus/Standard [11] and with Svanberg's constitutive model described in Eq. 2.16 implemented in a user material subroutine. Besides the sound physical grounds of the model, expressed in Chapter 2, its computational efficiency is an important asset in the context of compensation, as many successive curing simulations must be completed.
- The deformed mesh is post-processed and the residual distance is evaluated by Eq. 4.2. If needed, additional measurements can be made, such as the calculation of spring-in angles or curvatures.

The three compensation methods are applied and compared for one geometry: a curved C-spar. Then, the mirror method is applied to several other test cases, in order to exhibit its simplicity but also its limitations.

4.3.2 Curved C-spar

Geometry and materials

For this proof of concept, the first selected test case is a generic curved C-spar shown in Figure 4.6. This geometry is selected because it provides an intermediate level of complexity: it is doubly-curved, and still simple enough to anticipate the distortions qualitatively. The material properties of a common carbon/epoxy UD prepreg system are used, namely AS4 fibers and 8552 resin by Hexcel, which exhibits a ply thickness of 0.2 mm [177]. The degree of cure at gelation is taken equal to 0.31 [63]. The mechanical properties are listed in Table 4.1 and are taken from [63, 178]. The relationships between the degree of cure X and the glass transition temperature T_g, the cure kinetics model and

the transverse chemical shrinkage model are given by [63],

$$T_g[^\circ C] = 164.6X^2 + 51X + 2.67, \tag{4.6a}$$

$$\frac{\mathrm{d}X}{\mathrm{d}t}[s^{-1}] = \frac{7.10^4 e^{-6.5\times10^4/RT} X^{0.5}(1-X)^{1.5}}{1+e^{30(X+1.5148-5.171\times10^{-3}T)}}, \tag{4.6b}$$

$$\varepsilon^{ch}[\%] = 2.16X^3 - 1.62X^2 - 2.7X + 0.93, \tag{4.6c}$$

where T is the temperature expressed in Kelvin and R is the universal gas constant. Chemical shrinkage in the fiber direction is assumed to be null. The physical grounds of these models and the experimental techniques to derive them have been discussed in Chapter 2. A $[0_2, 90_2]_S$ layup is used, corresponding to an uniform part thickness equal to 1.6 mm.

		Rubbery state	Glassy state
E_L	[MPa]	131 000	133 000
E_T	[MPa]	122	9130
ν_{LT}	[-]	0.33	0.27
ν_{TT}	[-]	0.64	0.47
G_{LT}	[MPa]	41.1	5210
G_{TT}	[MPa]	37.2	3210
α_L	[/°C]	0	0
α_T	[/°C]	200×10^{-6}	32.6×10^{-6}

Table 4.1: Mechanical properties of the unidirectional 8552/AS4 prepreg system during cure [63, 178]. Subscripts L and T stand for fiber and transverse directions, respectively.

Compensation with the control points method

The selected set of control points is shown in Figure 4.7. The position of each point is parametrized independently by three degrees of freedom, corresponding to its displacement in space. In the case of the C-spar, the distortions are mainly driven by the cure-induced spring-in and the control points are chosen accordingly: the C-spar is divided in five sections along its length, and the control points are taken as the four extremities of each section, for a total of 20 points. The sections are then connected together with splines to ensure a smooth transition. An exaggerated example of a deformed shape that the parametrized C-spar can take, is provided in Figure 4.8.

The control points are allowed to move around their nominal position, each component of the displacement varying between -2 mm and +2 mm. With 20 control points, there is a total of 54 optimization parameters, after fixing six degrees of freedom to suppress the rigid body motions, which therefore avoids repetitive individuals within the optimization.

First, a DOE of 150 individuals is computed, after which the LOO coefficient is equal to 0.45. This value is too low for proceeding with the optimization,

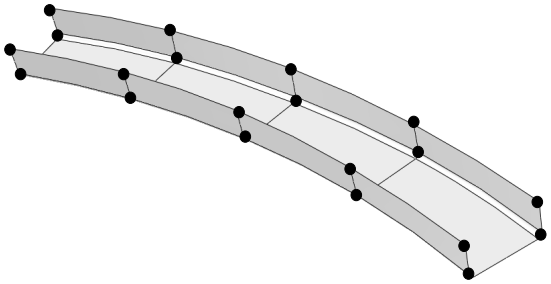


Figure 4.7: Chosen control points for the parametrization of the C-spar.

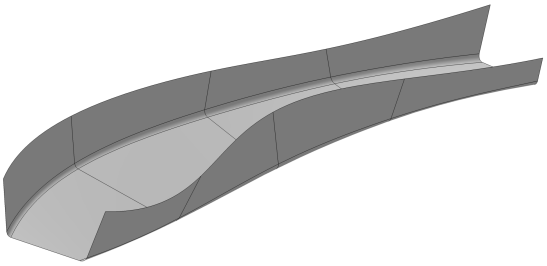


Figure 4.8: Example of the shape that the mold may take with a control points-based parametrization.

since it would lead to a coarse approximation by the surrogate model. In order to improve the quality of the model, an adaptive DOE is launched with 50 individuals. The LOO coefficient is then improved to 0.80. Next, the optimizer tries to find the optimal set of parameters in order to minimize the residual distance D_{min} given by Eq. 4.3. Since the C-spar is also compensated with the other methods, the results are provided later in this chapter, in Figure 4.14. After 300 iterations, the residual distance is reduced from 1.66 mm for the nominal geometry to 0.27 mm (average per node), which represents a reduction by 84 %. Each simulation lasts about 15 min on six cores of a double twelve-core Intel E5-2967v2 (2.7 GHz) computation node, and necessitates approximately 6 GB of RAM. In total, 500 individuals are computed sequentially, which amounts to a duration of about 6 days for the optimization process. At the end of the optimization, a few parameters are close to their upper or lower limit in the design space. An additional optimization is launched with enlarged bounds for those parameters. No improvement of D_{min} is obtained in this case. It is possible that the result may be improved by a gradient-based optimization in the vicinity of the optimum found by the surrogate-based optimization (SBO), but this has not been tested. In such a high-dimensional space, SBO tends to favor exploration of the design space over fine-tuning of the optimum in a small region.

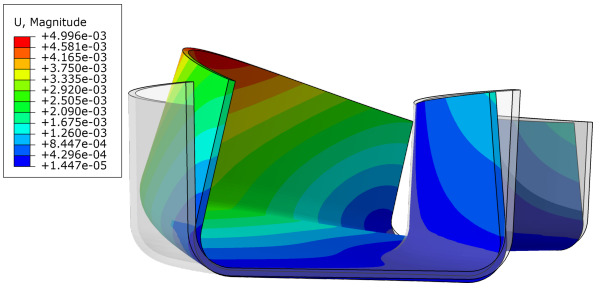


Figure 4.9: Displacement field after cure and comparison to nominal geometry (deformation factor: 10). The twist and spring-in are visible.)

Compensation with the distortion modes method

In order to setup an efficient parametrization, the cure-induced distortion modes are evaluated in a first step on the nominal geometry. The result of the curing simulation on the baseline non-compensated geometry is shown in Figure 4.9 and the observed distortion modes are schematically represented in Figure 4.10. As expected, spring-in develops in each section. Moreover, the radius of curvature of the C-spar decreases and some twist appears. The proposed parametrization is meant to compensate individually for each of these distortions (Figures 4.10 and 4.11). The walls of the C-spar are bent outwards to compensate for the spring-in. The angles θ_{ok} and θ_{ik} are introduced for each section labeled by the index k ($k = 1 \dots 5$) to control the outer and inner angles, see Figure 4.11(b). Outer and inner angles refer to the angles located in the corners in the external and internal curvature of the C-spar, which are indicated in Figure 4.10. The radius of curvature of the C-spar is slightly increased by controlling the parameter $d = D_C - D_N$ at one extremity, while leaving the other extremity fixed and keeping the curvilinear length L constant (see Figure 4.11(a)). The twist is induced in the middle of the part by the angle φ in the direction opposite to the one caused by the curing process, and linearly reduced to zero at both extremities. Each angle and length is parametrized separately, and the symbols representing these parameters are summarized in Table 4.2.

Compensated phenomenon	Symbol for compensation parameter	Symbol for post-processing value
Spring-in in section k (inner angle)	θ_{ik}	S_{ik}
Spring-in in section k (outer angle)	θ_{ok}	S_{ok}
Curvature change	$d = D_C - D_N > 0$	$D = D_N - D_A$
Twist	φ	H

Table 4.2: Nomenclature for compensation parameters and their corresponding post-processing values.

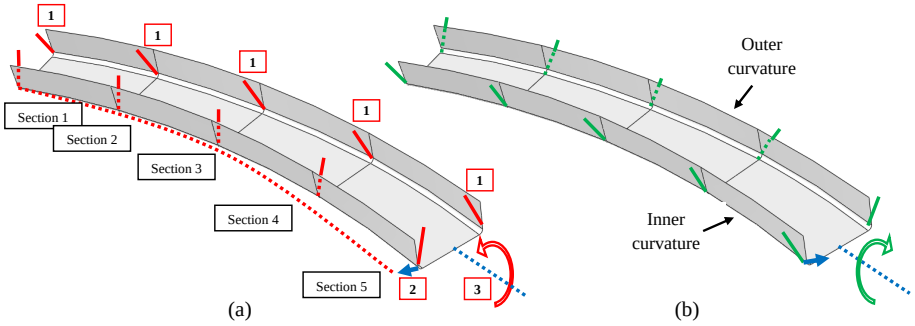


Figure 4.10: (a) distortion modes during cure: (1) spring-in, (2) decrease of the global curvature of the C-spar, (3) twist; and (b) all distortion modes are compensated individually.

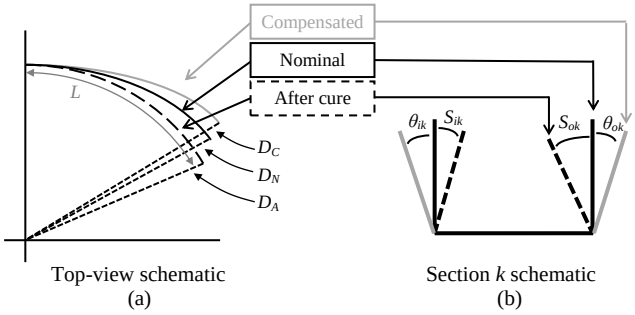


Figure 4.11: (a) schematic (top-view of the C-spar) explaining how the curvature change is parametrized and post-processed. The curvature is increased by controlling the distance $d = D_C - D_N$. The curvature reduction due to curing is measured as $D = D_N - D_A$. The curvilinear length L is kept constant; and (b) view of a cross-section and definition of the spring-in and compensation angles.

The parametrization involves 12 parameters: ten spring-in angles, one twist angle, and one curvature change. Each parameter corresponds to one distortion mode. According to what is usually done in the literature we first aim to reduce these distortion modes, and not necessarily D_{min}. These modes must be quantified in order to compute the discrepancy between the cured part and the target geometry. For this purpose, the curing simulation is post-processed as follows (see Figure 4.11):

- Each spring-in angle S_{ik} (inner angle) and S_{ok} (outer angle) is computed on the cured part ($k = 1 \dots 5$), with respect to the nominal geometry.
- The curvature change is evaluated as the difference $D = D_N - D_A$.
- The twist is evaluated as follows: the angle between the bottom of each of the five sections and the horizontal plane is calculated. Then, the variance H of these angles is computed. H equal to zero would mean that the bottom face is flat, which is the target. Therefore, H is considered as

a representative measure of the twist, and the goal of the optimization is the reduction of this value.

The purpose of the optimization is to reduce the absolute value of each mode separately. However, in order to avoid a heavy twelve-objective optimization process, all distortion values are additively combined into a single objective function. The post-processed results are transformed into adimensional data by dividing the current value by the initial value, resulting from the uncompensated cured part. To summarize the DMM, the optimization parameters are θ_{ik}, θ_{ok} $(k = 1 \dots 5)$, d and φ, and the objective is to minimize the function F_{obj} given by,

$$F_{obj} = \sum_{k=1}^{5} \left(\left| \frac{S_{ik}}{S_{ik,0}} \right| + \left| \frac{S_{ok}}{S_{ok,0}} \right| \right) + \left| \frac{D}{D_{,0}} \right| + \frac{H}{H_{,0}}, \tag{4.7}$$

where the subscript "0" means that the value is computed from the baseline uncompensated geometry after cure.

In a first approach, each distortion mode is optimized individually. That is, for each parameter, an optimization is performed with the corresponding distortion mode as the objective function, while the other parameters are kept constant. Design of experiments are performed within an interval of [0, 3°] for spring-back angles θ_{ik} and θ_{ok} $(k = 1 \dots 5)$, of [0, 5°] for the twist angle φ and of [0, 5 mm] for d. The results are summarized in Table 4.3. Column 1 presents the initial values of each distortion mode. Column 2 lists the residual values of the distortion modes after being individually optimized. Each distortion mode is reduced to a maximum of 0.9 % of its initial value, except for the flatness H, for which the optimizer could not find a better reduction than 23.6 %. The input parameters which correspond to these optima are given in Column 3. Then, a curing simulation is run using all the individually optimized parameters together, and the relative values of the distortion modes are given in Column 4. These last results emphasize the coupling between all the parameters. For instance, a value of $d = 0.50$ mm leads to $D/D_{,0} = 0.6$ % when all the other parameters have their nominal value (i.e. 0° for all angles), but the same value for d leads to $D/D_{,0} = 65.6$ % when all the optimized parameters are used. The fact that a coupling exists between the parameters highlights the irrelevance of the individual optimizations. A twelve-parameter optimization is required to simultaneously reduce all the modes.

An optimization is now launched on the fully-parametrized C-spar, with the objective function F_{obj} defined by Eq. 4.7. A DOE and an adaptive DOE of 40 and 10 individuals, respectively, are computed. The optimization itself is then launched and the optimum is obtained after 200 iterations, approximately 3 days of total computational time on six processors. The optimum is presented in Table 4.4. The distortions could not be entirely suppressed since the twist H is still equal to 22 % of its initial value (which means it has been reduced by 78 %). However, this solution is better than the one obtained with individual optimizations (Table 4.3), with an average distortion of 2.1 % compared to 8.1 % with the individual optimizations. Therefore, the discrepancy between the cured part and the nominal geometry is reduced by 97.9 %, on average,

which proves that the developed strategy fills its purpose. The convergence history of this optimization is given in Figure 4.12, which also shows that minimizing the distortion modes does not necessarily reduce the residual distance D_{min}.

Nominal distortion value	Residual distortion when each mode is individually optimized	Input parameter corresponding to each optimum distortion	Residual distortion when all optimized parameters are used at the same time
$S_{o1,0} = 2.36°$	$S_{o1}/S_{o1,0} = 0.1$ % ($S_{o1} = 0.0028°$)	$\theta_{o1} = 2.28°$	$S_{o1}/S_{o1,0} = 1.2$ %
$S_{o2,0} = 2.37°$	$S_{o2}/S_{o1,0} = 0.9$ % ($S_{o2} = 0.021°$)	$\theta_{o2} = 2.33°$	$S_{o2}/S_{o2,0} = 1.2$ %
$S_{o3,0} = 2.42°$	$S_{o3}/S_{o1,0} = 0.3$ % ($S_{o3} = 0.0082°$)	$\theta_{o3} = 2.35°$	$S_{o3}/S_{o3,0} = 0.6$ %
$S_{o4,0} = 2.36°$	$S_{o4}/S_{o1,0} < 0.1$ % ($S_{o4} = 0.00026°$)	$\theta_{o4} = 2.25°$	$S_{o4}/S_{o4,0} = 2.1$ %
$S_{o5,0} = 2.39°$	$S_{o5}/S_{o1,0} < 0.1$ % ($S_{o5} = 0.0011°$)	$\theta_{o5} = 2.33°$	$S_{o5}/S_{o5,0} = 3.0$ %
$S_{i1,0} = 2.14°$	$S_{i1}/S_{i1,0} = 0.2$ % ($S_{i1} = 0.0048°$)	$\theta_{i1} = 2.10°$	$S_{i1}/S_{i1,0} = 0.8$ %
$S_{i2,0} = 2.45°$	$S_{i2}/S_{i1,0} < 0.1$ % ($S_{i2} = 0.000066°$)	$\theta_{i2} = 2.38°$	$S_{i2}/S_{i2,0} = 1.6$ %
$S_{i3,0} = 2.48°$	$S_{i3}/S_{i1,0} = 0.3$ % ($S_{i3} = 0.0065°$)	$\theta_{i3} = 2.41°$	$S_{i3}/S_{i3,0} = 0.1$ %
$S_{i4,0} = 2.43°$	$S_{i4}/S_{i1,0} < 0.1$ % ($S_{i4} = 0.0013°$)	$\theta_{i4} = 2.34°$	$S_{i4}/S_{i4,0} = 2.0$ %
$S_{i5,0} = 2.06°$	$S_{i5}/S_{i1,0} = 0.1$ % ($S_{i5} = 0.0026°$)	$\theta_{i5} = 2.01°$	$S_{i5}/S_{i5,0} = 2.3$ %
$H_{,0} = 1.23°^2$	$H/H_{,0} = 23.6$ % ($H = 0.29°^2$)	$\varphi = 2.35°$	$H/H_{,0} = 16.4$ %
$D_{,0} = 0.57$ mm	$D/D_{,0} = 0.6$ % ($D = 0.004$ mm)	$d = 0.50°$	$D/D_{,0} = 65.6$ %
Avg.	2.2 %		8.1 %

Table 4.3: Results of the individual optimizations. Each distortion mode can be reduced individually, but the combination of all optimized parameters is not as efficient, especially for D.

Residual distortion for the optimum individual		Optimal parameters
$S_{o1} = 0.0005°$	$S_{o1}/S_{o1,0} = 0.02$ %	$\theta_{o1} = 2.23°$
$S_{o2} = 0.002°$	$S_{o2}/S_{o2,0} = 0.08$ %	$\theta_{o2} = 2.27°$
$S_{o3} = 8.4 \times 10^{-5}°$	$S_{o3}/S_{o3,0} = 0.003$ %	$\theta_{o3} = 2.37°$
$S_{o4} = 0.05°$	$S_{o4}/S_{o4,0} = 2.3$ %	$\theta_{o4} = 2.26°$
$S_{o5} = 0.003°$	$S_{o5}/S_{o5,0} = 0.1$ %	$\theta_{o5} = 2.38°$
$S_{i1} = 0.014°$	$S_{i1}/S_{i1,0} = 0.7$ %	$\theta_{i1} = 2.08°$
$S_{i2} = 0.002°$	$S_{i2}/S_{i2,0} = 0.09$ %	$\theta_{i2} = 2.34°$
$S_{i3} = 0.003°$	$S_{i3}/S_{i3,0} = 0.1$ %	$\theta_{i3} = 2.40°$
$S_{i4} = 0.0007°$	$S_{i4}/S_{i4,0} = 0.03$ %	$\theta_{i4} = 2.40°$
$S_{i5} = 0.004°$	$S_{i5}/S_{i5,0} = 0.02$ %	$\theta_{i5} = 2.09°$
$H = 0.27°^2$	$H/H_{,0} = 22.0$ %	$\varphi = 3.06°$
$D = 0.002$ mm	$D/D_{,0} = 0.3$ %	$d = 0.9$ mm
Avg.	2.1 %	

Table 4.4: Optimum found by the twelve-parameter optimization.

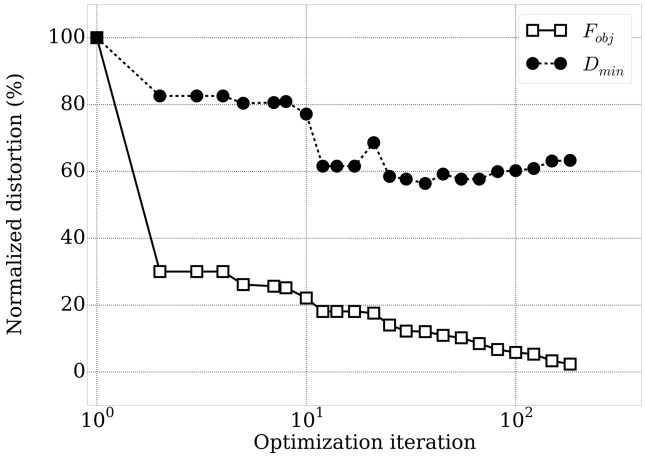


Figure 4.12: Convergence history when optimizing F_{obj} (C-spar) with the DMM.

We now consider the reduction of the residual distance D_{min}, instead of the subjectively-defined distortion modes. Based on the previous DOE, the optimization is re-run with D_{min} as the objective function. The convergence history is shown in Figure 4.14. It can be concluded that the chosen distortion modes parametrization does not perform as well as the CPM. Indeed, the residual distance is reduced by 57 %, while the CPM gives an 84 % improvement. This behavior finds its roots in the fact that the twist plays, by far, the most significant role in the value of D_{min}, as proved by the analysis of variance of

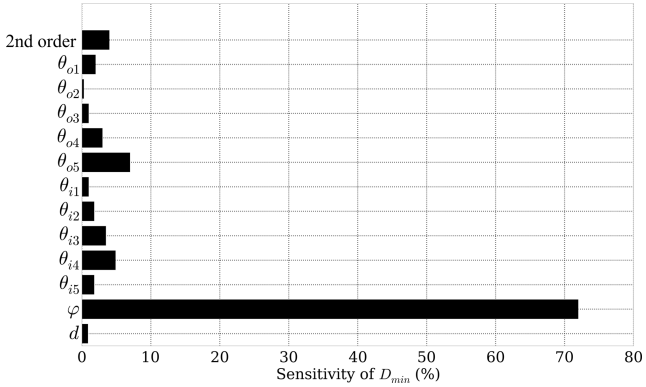


Figure 4.13: Analysis of variance (ANOVA [179]): each bar represents the sensitivity of D_{min} to a given parameter.

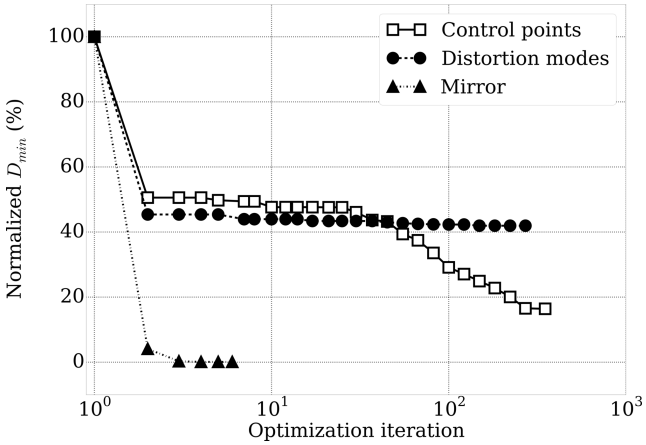


Figure 4.14: Convergence history when optimizing D_{min} (C-spar) with the three compensation methods.

the results (Figure 4.13). Given the fact that the twist is not well compensated, as seen in Table 4.4, it is unlikely that the DMM would lead to a satisfactory reduction of D_{min} with the current parametrization.

Compensation with the mirror method

Since the mirror method is deterministic by nature, no additional explanation needs to be given compared to Section 4.2.3. The method is simply applied to the case of the C-spar. The results of all three methods for this particular geometry are provided in Figure 4.14.

Discussion of the compensation methods for the C-spar application

Concerning CAD-based methods, the CPM and the DMM perform well, in different manners. On the one hand, if the objective of the compensation is

to minimize the overall distance between a cured composite part and a nominal geometry for a given set of points, then the CPM is more efficient, or the distortion modes must be chosen more adequately. On the other hand, the DMM is much faster and successful in minimizing several user-selected distortion values simultaneously. The choice of the method then depends on the specifications and objectives of the mold compensation process, and on the size of the underlying model and associated computational load. The DMM can be improved with a better parametrization. Indeed, the flatness H could not be reduced by more than 77 % with an individual optimization. This can possibly be explained by two reasons. First, the twist angle φ is imposed at the middle section (section 3) of the C-spar, while sections positioned at the extremities are not rotated (sections 1 and 5), and sections 2 and 4 are rotated by $\varphi/2$. This division by 2 is arbitrary and a possible improvement would be to add an optimization parameter for the twist of sections 2 and 4. An additional explanation is that the rotation point is arbitrarily set as the corner point of each section, on the side of the inner angles θ_{ik}. This could be improved by using optimization parameters which would move the rotation point along the width of the C-spar, in each section. Parametrizing a geometry based on intuition is clearly an iterative process and requires several trial and error optimization runs. In that respect, the CPM seems more suitable for the perspective of developing a systematic mold compensation strategy for complex geometries.

Be that as it may, both methods are superseded by the mirror method, if the objective is the reduction of D_{min}, which has been decreased by 96 % after only one iteration. After three iterations, the improvement is 99.9 %.

4.3.3 Other applications

It remains to be seen if the mirror method is always as effective as with the C-spar. This section is dedicated to a broader study of this method. The test cases are first briefly described. All the results are gathered and discussed at the end of the section.

Z-shaped brackets

Several Z-shaped brackets have been manufactured with the autoclave process in the frame of the ECOTAC project (Skywin Walloon pole of competitiveness), in collaboration with Sonaca S.A. Details about the modeling and the experimental results have been partly presented in [7], the interest in the present section is solely the performance of the compensation method. The references and the stacking sequences of the different parts are the following:

- 6.1: $[\pm 45/\overline{0-90}]_{4S}]$ (15 plies)
- 8.1: $[(\pm 45/0-90)_2/\pm 45/\pm 45/0-90/\pm 45]$ (8 plies)
- 8.2: $[G \pm 45/(\pm 45/\overline{0-90})_4]_S$ (17 plies)
- 8.3: $[R/((\pm 45/0-90)_2/\pm 45)_S]$ (11 plies)
- 8.4: $[M/((\pm 45/0-90)_2/\pm 45)_S]$ (11 plies)

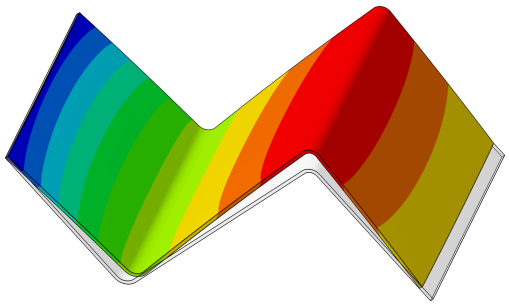


Figure 4.15: Distortions of the Z-shaped bracket 8.4 (displacement factor: 2).

- 9.1: $[45/-45/0/90]_S$ (8 UD plies)
- 9.3: $[\pm 45/\overline{0-90}]_{4S}$ (15 plies) + extra glass-fiber ply locally
- 22.1: $[\pm 45/0-90/\pm 45/0-90/\pm 45]_S$ (10 plies)
- 22.2: $[\pm 45/0-90/\overline{\pm 45}]_S$ (5 plies)
- 22.3: $[(\pm 45/0-90)_2/\pm 45/\pm 45/0-90/\pm 45]$ (8 plies)
- 22.4: $[G \pm 45/(\pm 45/\overline{0-90})_{4S}]$ (16 plies)

In the notations above, "± 45" and "$0-90$" refer to one ply of balanced textile, respectively, whereas "45" and "90" refer to unidirectional plies. The letters "G", "M"and "R" designate a glass-fiber ply, a bronze mesh impregnated in a resin layer, and a pure resin layer, respectively. The other plies are made of the aforementioned 8552/AS4 material. A bar over a ply when a symmetry is involved means that the ply is not repeated in the center of the stacking sequence.

All of these test cases provide a wide range of possibilities, with symmetric and asymmetric layups, multiple materials, and different thicknesses. Therefore, they are representative, to a large extent, of the type of distortions which may arise when manufacturing this type of composite part. The simulated distortions of part n°8.4 are shown in Figure 4.15.

One industrial application

By courtesy of Sonaca S.A., a part of an inboard flap is presented in Figure 4.16. The part is 2 meters long. The material is mainly 8552/AS4 textile prepreg. The profile of the Z is slightly curved, there are multiple drop-offs along the length, and the skin is stiffened: this part is a good candidate to study the applicability of mold compensation on a complex geometry.

A flat plate

A flat plate made of a UD material with an asymmetric layup ($[0_6/90_6]$) is also studied. As explained in Chapter 2, this kind of composite part distorts into a saddle shape (Figure 4.17), since the contraction of the 0-degree plies competes

with that of the 90-degree plies. This test case is pathological, it would not be found in a real application. Nonetheless, it is interesting considering that warpage is not the main distortion mode of the previous geometries.

A generic doubly-stiffened panel

Finally, the compensation is tested on the doubly-stiffened panel of Figure 4.18. The material is unidirectional 8552/AS4 with a $[0/45/-45/90/0/45/-45/90/0]$ layup.

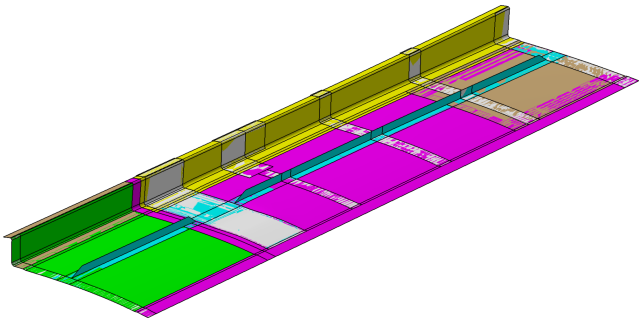


Figure 4.16: Industrial application of Sonaca S.A.

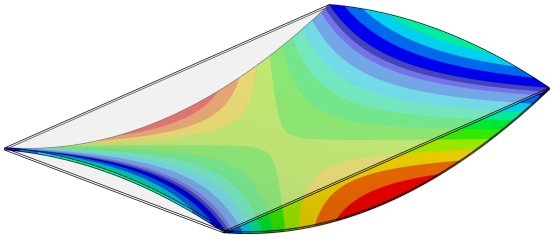


Figure 4.17: Distortions of an asymmetric flat plate.

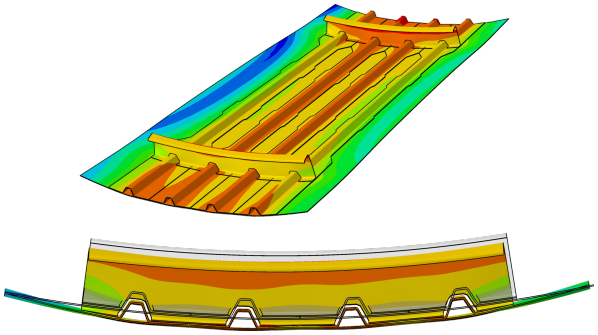


Figure 4.18: Distortions of a generic doubly-stiffened panel after cure (displacement factor: 5).

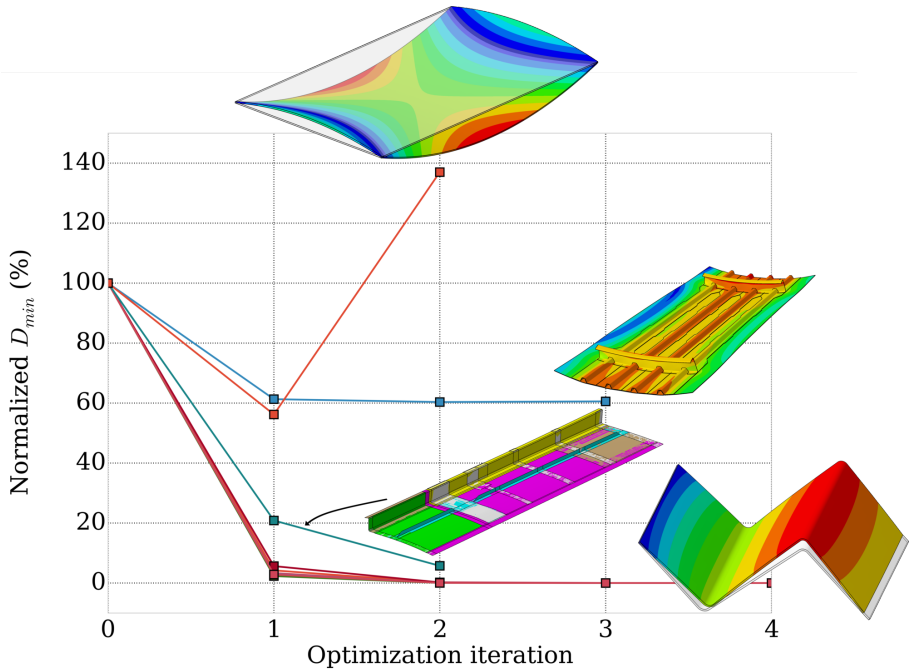


Figure 4.19: Compensation of several applications with the mirror method.

Results

The results for all these applications, in Figure 4.19, highlight a clear difference between the parts for which the main distortion mode is spring-in (Z-shaped brackets and the flap) and the other parts, when warpage prevails. The parts which exhibit spring-in converge towards a perfect compensation. For the other parts, the method stagnates or diverges. This is due to the radical change of behavior between the nominal flat plate and its reversed geometry, see Figure 4.20. In the first iteration, the initially flat plate distorts into a saddle shape. The mirror geometry is also a saddle shape, since it is reversed with respect to the nominal geometry. Figure 4.20(b) demonstrates that this saddle shape distorts much less than the flat plate. This is in contradiction with the main hypothesis of the mirror method, which is the approximately linear behavior of the structure during curing. The saddle shape distorts less since it is doubly-curved and it is much stiffer in bending than the flat plate.

The correction applied by the mirror operation must be modulated in order to adjust to the non-linearity. Basic attempts have been made during the thesis, e.g. apply only a portion of the correction, and use feedback from the previous iterations to adapt this portion. However, no improvement has been obtained, and it is likely that compensating the asymmetric flat plate with a mesh-based method requires a significant change of strategy. For now, the conclusion is that warpage-dominated parts should be compensated with CAD-based methods. This proves that iterative alteration of the mold by experimental trial-and-

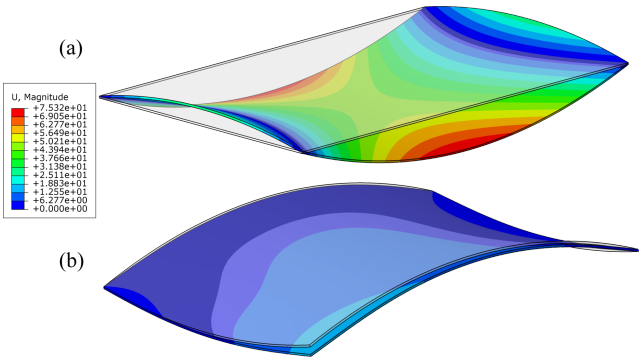


Figure 4.20: Displacement field of (a) the first iteration; and (b) the second iteration of the mirror method applied to an asymmetric flat plate. The transparent geometry is the initial geometry of the simulation (assimilated to the mold geometry)

error sequences would also fail in those cases, making numerical compensation all the more relevant.

4.4 Discussion and conclusion

In this chapter, three different methods have been explored for the compensation of composite parts by simulation. This study has highlighted advantages and weaknesses for each of those methods, which are summarized in Table 4.5.

Complexity of the computational chain: CAD-based methods require the automation of many more tasks than mesh-based methods. One must consider the particularities of each software, and also less obvious details such as license management and communication between several machines. For instance, the computational chain of the CAD-based methods which have been studied involve the following elements:

- The optimizer runs on a HPC center and generates a given set of parameters.
- The parameters are sent to a Windows machine where CATIA is launched to update the parametrized CAD model.
- This surface model is imported into Abaqus, meshed, draped with Simulayt. The layup is created and extruded in order to obtain a volume mesh with one element per ply. If needed, part of the external surface is extracted to represent the mold around the composite part.
- Still in Abaqus, the mechanical and thermal boundary conditions are created, and the model is exported.
- This file is sent back to the HPC center, where the computation is run.
- The output of the simulation is post-treated to extract the data of interest, such as the deformed mesh and spring-in angles. These data are

fed back to the optimizer, which can then decide which set of parameters should be tested next.

In addition, a robust chain must handle undesired events properly, like the unavailability of the software licenses, badly conditioned CAD models, or meshing difficulties. Mesh-based methods also involve all of those steps, but the pre-treatment steps are done only once. Therefore, they do not need to be automated, resulting in a much simpler computational chain.

Compensation time: the overall time needed for a compensation process is naturally mostly spent on curing simulations. Since CAD-based methods are based on an optimizer, they necessarily lead to a significant number of simulations, and this number grows linearly as the number of parameters increases. A minimum number of experiments is three times the number of parameters to explore the design space, plus the number of optimization iterations, which is variable. On the other hand, mesh-based methods are iterative and converge quickly, if they converge.

Current robustness: if the computational chain is properly set up, the robustness of CAD-based methods is very good. It is even excellent for the DMM, since the parametrization is based on the knowledge of the user and therefore is less likely to produce odd geometries. In that sense, the CPM is more uncertain, but failures remain occasional. It should also be noted that the optimizer is able to detect the areas of the design space where failures occur, and to avoid them for the rest of the optimization. On the contrary, in its current form, the mirror method sometimes diverges and no satisfactory solution has been found yet to improve the robustness of the method, in particular when warpage is a significant distortion mode.

Compensation success: in terms of reduction of the distortions, the three methods can be clearly ranked: the most efficient one is the mirror method, when it converges, with a residual distance reduction of almost 100 %. In the case of a C-spar, the CPM and the DMM reduced the distance by 84 % and 57 %, respectively. The DMM may certainly be improved by enriching the parametrization, at the cost of a new optimization process. However, when the optimizer targets the reduction of the distortion modes themselves instead of the residual distance, these are reduced by 98 %, on average. This means that the optimizer is able to find, in a twelve-dimensional space, an optimal configuration which reduces each distortion mode individually. One of the outcomes of our study is that the mirror method may be disappointing due to its binary success rate (either complete success or failure), whereas CAD-based methods may be less effective but will always improve the design, by a margin which depends on the quality of the parametrization.

Universality: the mirror method is, by far, the most generic method among the three presented in this chapter. It does not require more effort than setting up one curing simulation, which is unavoidable if one wants to study the cure-induced distortions of a particular geometry. The mirror method has been applied in Section 4.3.3 to several geometries of variable complexity, without any additional development. The same cannot be said about CAD-based

	Control points (CAD-based)	Distortion modes (CAD-based)	Mirror (mesh-based)
Complexity of the computational chain	+	+	+++
Compensation time	+	++	+++
Current robustness	++	+++	+
Compensation success	++	++	+++
Universality	++	+	+++
Control on final shape	+++	+++	+
CAD model of the compensated mold	+++	+++	+

Table 4.5: Strengths and weaknesses of the compensation methods. Interpretation: +: complicated; ++: good; +++: excellent

methods, which require adaptations from one geometry to another. Indeed, they involve more geometry-dependent automated tasks. That being said, the principles of the three methods are generic: it is always possible to parametrize a geometry with control points or distortion modes. The subjectivity of the CAD-based methods comes from the choice of those parameters. In that respect, the CPM is by essence more objective than the DMM: it is easier to choose the control points than the distortion modes.

Control on final shape: in an industrial context, it is likely that the designer might want to impose specific constraints on the shape of the compensated mold. For instance, it could be necessary for manufacturing reasons that a certain surface remains flat or respects a fixed curvature. Apart from the robustness, this is probably the weakest point of the mirror method. In its current form, it does not allow to include such constraints, whereas they are inherently part of the design process in CAD-based methods. In the latter, the user controls the parametrization and, therefore, controls the shape that the mold can take during the optimization. A possible workaround is to use a hybrid method, where the optimal mold shape would be generated by the mirror method, and where a CAD-based optimization would try to reproduce this shape as well as possible, taking into account the manufacturing constraints. The optimization would be very fast, since it is only based on geometrical considerations. This approach has not been tested in this thesis but, intrinsically, it should perform as well as purely CAD-based methods, and much faster.

CAD model of the compensated mold: the step which usually comes after the compensation process is the machining of the compensated mold. To that end, a CAD model of the mold should be designed. While this is tautological with CAD-based methods, a reverse engineering phase is required with mesh-based methods to transform the result of the compensation into a viable volume CAD model for the mold.

Conclusion: it can be concluded that the choice of one or the other compensation method is not obvious and it will be driven by the complexity of the geometry, by the requirements in terms of manufacturing tolerances (and hence of compensation quality), by the manufacturing constraints, and so forth. It is thus relevant to explore several compensation techniques instead of simply relying on the inversion of the cured nominal geometry, as suggested by the mirror method.

This field of research remains full of possibilities and this chapter only represents a first overview of what is possible, highlighting advantages and caveats of different methodologies. Two key points to be improved are the failure of the mirror method to compensate large warpage distortions, and the subjectivity of the CAD-based methods (choice of the distortion modes and/or of the control points). More perspectives are discussed in Chapter 6.

Chapter 5

Experimental validation

5.1 Introduction

This chapter[1] is dedicated to the experimental validation of the numerical methodologies which have been presented in the previous chapters. The homogenization and compensation procedures are applied step by step in order to predict the shape of the compensated mold for a specific application. In the final stage, the compensated parts are manufactured and measured, providing final insight into the quality and applicability of the modeling methodologies developed in this thesis. This validation involves the following steps:

1. choice of a target structural component and of the composite material;
2. manufacturing of the nominal parts, i.e. the parts produced with the mold which has not been compensated;
3. inspection of these parts to generate data relevant for the homogenization procedure (fiber volume fraction, textile geometry...);
4. application of the numerical compensation procedure;
5. machining of the compensated mold and manufacturing of the compensated parts.

Let us note right away that manufacturing the nominal parts is naturally not a necessary step. The purpose of mold compensation with the help of numerical simulation is indeed to avoid this step, and step n°3 may be performed on simple test samples instead of on full composite parts. In the context of this thesis it was found appropriate to manufacture nominal parts in order to build confidence in the numerical model, and to execute a complete compensation cycle from both numerical and experimental aspects. This also allows to measure the gap between the non-compensated geometry, the compensated geometry and the target perfect geometry.

[1] *Reproduced in part from:* B. Wucher, Ph. Martiny, F. Lani, T. Pardoen, C. Bailly, D. Dumas (2016). Simulation-driven mold compensation of composite materials: experimental validation for a doubly-curved part. *To be submitted.*

5.2 Test case definition

The C-spar geometry is once again considered to be an appropriate choice for this experimental study, since it is simple enough to be manufactured in Cenaero's lab, yet not too simple such that its compensation would be trivial. The dimensions, shown in Figure 5.1, are chosen to be as large as possible, with respect to our manufacturing capabilities, in order to reduce the manufacturing variability and the measurement error. The length of the C-spar is 1225 mm, which corresponds approximately to the maximum dimension which can be manufactured at Cenaero, keeping in mind that the mold must be somewhat larger than the part. We are also limited to the VARTM process, since the time frame of the project did not allow to produce a closed mold for RTM. Unfortunately, the use of VARTM supposedly leads to poorer part quality and higher variability. The latter is mitigated by choosing a rather thick stacking sequence, $[0, 45]_{6S}$, resulting in a 12-ply layup which is approximately 4 mm thick. Producing thicker parts tends to decrease the variability [39, 180]. The chosen materials are a carbon 5-harness satin weave for the fibers, and the aeronautical grade epoxy RTM6 by Hexcel for the matrix. The choice of this resin is driven by the following considerations:

- It is suitable for vacuum infusion.
- It is usually infused at 80°C, which makes it easier to control than cheaper resins which are processed at room temperature.
- It is often used in the aeronautics industry, which makes it more interesting to study.
- It has been widely studied in the literature and at UCL [76, 181], and its properties can be extracted and cross-checked from various sources. Most of the RTM6 properties listed in Section 5.4.2 lie between values found in other references.

5.3 Manufacturing of nominal parts

5.3.1 VARTM setup

The setup for the infusion process is described in Figure 5.2. The one-sided mold is made of aluminum. It is a male mold, which enables an easier draping operation of the carbon plies than a female one. Chemlease 1009W release agent is applied over the whole mold surface four times between each infusion (ten times before the first infusion). Airtac 2 is lightly sprayed on the top surface of the mold, so that the fibers can stay in place once they are draped. Next, the carbon plies are carefully laid by hand, starting from the center of the C-spar and progressing in a symmetric manner to the sides. A peel ply is placed on top in order to ease the removal of the other materials after demolding. Then, a flow medium covers two thirds of the surface. It has a higher permeability than the fibers and thus helps increasing the speed of the infusion by allowing the resin to flow above the fibers and then through the thickness. The flow

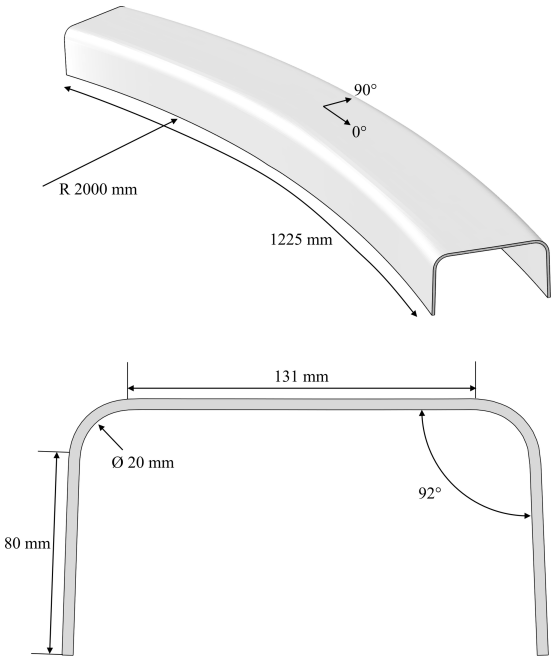


Figure 5.1: Nominal geometry of the C-spar for the experimental validation.

medium does not cover the entire surface and stops slightly before the vacuum line, so that the resin has time to permeate through the thickness everywhere.

An issue with the VARTM process when manufacturing thick composites is the need for debulking steps, i.e. pre-compacting by small groups of carbon plies. If this is not done, the vacuum bag is likely to pinch the fibers, creating folds in the corner areas which are detrimental to the spring-in behavior [182]. Here, the time-consuming debulking steps are avoided by adding a silicon sheet on top of the layup.

The whole set up presents more or less a rotational symmetry, and Figure 5.2 should be understood as a cross-section view. In particular, the resin inlet and outlet are evenly distributed along the length of the C-spar, with help of spiral tubes. This ensures a regular flow front and reduces the risk of appearance of dry spots. In practice, such problems have not been encountered. The air tightness of the whole setup is checked by isolating it from the vacuum pump before the infusion, allowing a vacuum drop of less than 1 mbar/min.

5.3.2 Processing conditions

The infusion follows the manufacturer recommended processing conditions for the RTM6 [26]. The mold is pre-heated to 120°C for one night. During that time, and after storage at -26°C, 2 kilograms of RTM6 resin are heated to room temperature. They are then poured into a 10-liter injection piston, which is slowly heated up to 80°C. Once this temperature is reached, vacuum is switched

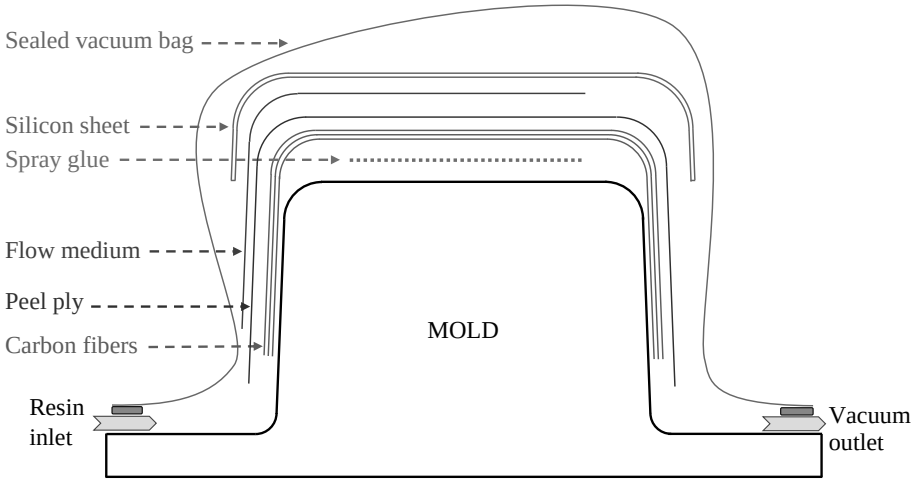


Figure 5.2: Setup for the VARTM process.

on and kept for 2 hours to remove the air entrapped inside the resin. Calculations with the cure kinetics model of the resin given in Eq. 5.5 show that the degree of cure reached during this time is negligible, since the RTM6 is intended to cure at 180°C. Once the resin is degassed, the infusion is engaged. It takes approximately 15 minutes for the resin to reach the vacuum outlet. When the infusion is complete, the outlet and inlet are closed and the curing cycle begins. The latter consists in a heating ramp of 1.5°C/min up to 180°C, followed by a two-hour dwell. Since the oven has no cooling regulation, its door is simply opened at the end of the dwell. A heat survey showed that this leads to a cooling rate of about 1°C/min, which is therefore the value that is used for the simulations conducted in the rest of this chapter.

5.3.3 Measurements

The mold-facing surface of the manufactured parts is digitized with a Nikon MMDx 100 laser scanner, mounted on a MCA II 7-axis articulated arm of a diameter of 1.8 m. The declared accuracy is 54 µm, although calibration tests show that it is in fact around 30 µm. This leads to a conservative estimation of the measurement error for the spring-in angles of $\pm 0.05°$. The obtained point clouds allow tailored post-treatment and measurements of the quantities of interest, which are detailed later. The important point for now is that this method allows to post-treat the manufactured parts and the simulations with exactly the same technique. The results are provided in Section 5.6.1, where they are compared to the results of the process simulation. Figure 5.3 presents pictures of a manufactured C-spar.



Figure 5.3: Pictures of a C-spar, manufactured by vacuum infusion, after trimming of the edges.

5.4 Curing model and material properties

5.4.1 Constitutive model

The constitutive model of the composite during the curing process is:

$$\begin{cases} \sigma_{ij} = C_{ijkl}\varepsilon^{el}_{kl} & T \geq T_g(X), \\ \dot{\sigma}_{ij} = C_{ijkl}\dot{\varepsilon}^{el}_{kl} & T < T_g(X), \end{cases} \tag{5.1}$$

$$\varepsilon^{el} = \varepsilon - \varepsilon^{E}, \tag{5.2}$$

$$\dot{\varepsilon}^{E}_{kl} = \begin{cases} \beta^{r}_{kl}\dot{X} + \alpha^{r}_{kl}\dot{T} & T \geq T_g(X), \\ \beta^{g}_{kl}\dot{X} + \alpha^{g}_{kl}\dot{T} & T < T_g(X), \end{cases} \tag{5.3}$$

where the superscripts r and g denote the rubbery and glassy states, respectively. This is equivalent to Svanberg's model discussed in Chapter 2, see Eq. 2.16, with the following adjustment: in Eq. 5.1, the elastic tensor C shifts gradually between the rubbery (C^r) and the glassy (C^g) states, whereas Svanberg uses an abrupt transition. This smooth transition is implemented as follows:

$$C = \begin{cases} C^r & T^* \geq T^*_C, \\ C^r + \frac{T^* - T^*_C}{2T^*_C}(C^r - C^g) & -T^*_C < T^* < T^*_C, \\ C^g & T^* \leq -T^*_C, \end{cases} \tag{5.4}$$

$$\text{with} \quad T^* = \frac{T - T_g}{T_g}.$$

In summary, Eq. 5.4 implies that the stiffness of the composite is linearly interpolated between that of the rubbery and the glassy states when the temperature T is close to the glass transition temperature T_g. A value of 0.01 for the dimensionless quantity T_C^* has been determined from mechanical tests in another project [7]. The stiffness tensors of the composite C^r and C^g, as well as the anisotropic CTE and coefficients of chemical shrinkage α and β, are determined by homogenization in Section 5.5, from the properties of the constituents listed in Sections 5.4.2 and 5.4.3.

5.4.2 Properties of the epoxy resin RTM6

Cure kinetics

The degree of cure X of the resin is determined depending on the temperature by integrating the following equation [183]:

$$\begin{aligned}
\frac{\mathrm{d}X}{\mathrm{d}t} &= k_1(1-X)^{n_1} + k_2 X^m (1-X)^{n_2}, \qquad (5.5)\\
\text{with } k_i &= A_i \exp\big(-\frac{E_i}{RT}\big),\\
A_1 &= 2.6 \times 10^4 \text{ s}^{-1},\\
E_1 &= 74.69 \times 10^3 \text{ J.mol}^{-1},\\
A_2 &= 5.78 \times 10^4 \text{ s}^{-1},\\
E_2 &= 58.37 \times 10^3 \text{ J.mol}^{-1},\\
m &= 1.217,\\
n_1 &= 0.449,\\
n_2 &= 1.786.
\end{aligned}$$

Glass transition temperature

The glass transition temperature T_g is computed with the DiBenedetto equation [184]:

$$\begin{aligned}
T_g(X) &= T_{g0} + (T_{g\infty} - T_{g0})\frac{\lambda X}{1-(1-\lambda)X}, \qquad (5.6)\\
\text{with } T_{g0} &= -11°C,\\
T_{g\infty} &= 206°C,\\
\lambda &= 0.435.
\end{aligned}$$

Coefficient of thermal expansion

The isotropic CTE of the resin is taken from [185]:

$$\alpha_r\ [/°\text{C}] = \begin{cases} 136 \times 10^{-6} & T \geq T_g(X), \\ 54 \times 10^{-6} + 0.16 \times 10^{-6} T\ [°\text{C}] & T < T_g(X). \end{cases} \qquad (5.7)$$

Coefficient of chemical shrinkage

The density difference between the uncured and the cured states is $\Delta V/V = -0.046$ [185]. As no information is provided regarding the evolution of the chemical shrinkage during the curing cycle, a constant linear isotropic coefficient of chemical shrinkage $\beta_r = (\Delta V/V)/3 = -0.015$ is assumed.

Mechanical properties

In the glassy state, the Poisson's ratio is considered to be constant and equal to 0.38 [65], and the elastic modulus is deduced from [65] between 25°C and 180°C:

$$E_r \text{ [MPa]} = -5.93T \text{ [K]} + 4470. \tag{5.8}$$

In the rubbery state, the resin is assumed to be incompressible [178, 186], i.e. the Poisson's ratio ν_r is equal to 0.5, and the Young's modulus is derived from the procedure proposed by Svanberg et al. [186], which mainly consists in assuming that the shear modulus of the resin is divided by 100 compared to the glassy state. The resulting value for the Young's modulus is $E_r = 29$ MPa. An alternative assumption [32] is a ratio of 1000 between the Young's modulus in the glassy state and in the rubbery state. This would lead to $E_r \approx 4$ MPa in the rubbery state. In practice, both values are sufficiently low so that choosing one or the other value has no impact on the predicted distortions.

Gel point

The gel point X_{gel} of the RTM6 resin is taken equal to 0.59 [187]. As explained in Chapter 2, an assumption of the model is that the thermal expansion of the resin does not create stresses nor distortions in the liquid state, i.e. when $X \leq X_{gel}$. The dilatational strain is set to zero below the gel point [62].

5.4.3 Properties of the carbon fibers

The carbon textile manufactured by Porcher is a balanced 6k 5-harness satin with a surface density of 375 g/m^2 and 4.6 yarns/cm. Without further information on the type of carbon fibers, these are assumed to have the same properties as T300 fibers, listed in Table 5.1. This assumption should have a limited impact on the numerical prediction of cure-induced distortions, since these are mainly driven by the properties of the resin in the glassy state [8].

5.5 Homogenization

5.5.1 Fiber volume fraction measurement

The fiber content inside the parts must be determined, in order to obtain by homogenization the thermo-mechanical properties of the textile. One of the drawbacks of using VARTM is that the thickness of the components is not controlled and thus it cannot be precisely known a priori. In the present work, the fiber volume fraction is measured from the five nominal parts which have

Carbon fibers		
$E_{L,f}$	[MPa]	230 000
$E_{T,f}$	[MPa]	40 000
$\nu_{LT,f}$	[-]	0.26
$G_{LT,f}$	[MPa]	24 000
$G_{TT,f}$	[MPa]	14 300
$\alpha_{L,f}$	[/°C]	-0.7×10^{-6}
$\alpha_{T,f}$	[/°C]	10×10^{-6}

Table 5.1: Transversely isotropic properties of T300 carbon fibers [188].

been manufactured. However, since the purpose of numerical compensation is to avoid the manufacturing step of those nominal parts, it must be noted that the measurements can also be performed on simple test samples, e.g. flat plates with the same stacking sequence and processing conditions as the real part. This remark is also valid for the measurement of the textile architecture in Section 5.5.2.

Assuming that the fiber volume fraction k_f is uniform throughout the part, and that the void content can be neglected, k_f is measured herein by two simple and independent methods. The first method is based on the thickness of the manufactured composite parts:

$$k_{f1} = \frac{AV_{f/s}}{At_{part}} = \frac{n\sigma_S}{\rho_f t_{part}}, \tag{5.9}$$

where A is the area of the part geometry, $V_{f/s}$ is the volume of fibers per unit surface, n is the number of layers, σ_S the surface density of the textile, ρ_f the volume density of carbon fibers and t_{part} the thickness of the part. The second method is based on the total mass of the parts:

$$k_{f2} = \frac{V_f}{V_f + V_r} = \frac{m_f}{\rho_f}\left(\frac{m_f}{\rho_f} + \frac{m_p - m_f}{\rho_r}\right)^{-1}, \tag{5.10}$$

where V_f is the volume of fibers, V_r is the volume of resin, $m_f = nA\sigma_S$ the mass of fibers inside the part, m_p the total mass of the part, and ρ_r the cured density of the resin. The numerical values used in Eqs. 5.9 and 5.10 are:

- $A = 0.451$ m^2 (measured in a CAD software), $n = 12$, $\rho_f = 1760$ kg.m^{-3} [188], and $\rho_r = 1140$ kg.m^{-3} [26].
- The theoretical value from the manufacturer for σ_S is 0.375 kg.m^{-2}, but it has been measured equal to 0.395 kg.m^{-2} by weighing five plies (equivalent to approximately 2.3 m^2). Since it has been measured only once, and since this higher value tends to increase the fiber volume fraction k_f, which is already quite high, the average of those two values is taken: $\sigma_S = 0.385$ kg.m^{-2}.

- The part thickness t_{part} and the part mass m_p are measured on the five manufactured parts. The obtained values are listed in Table 5.2: $t_{part} = 4.23 \pm 0.13$ mm and $m_p = 3.025 \pm 0.062$ kg. t_{part} is measured for each C-spar in at least 50 different locations along the length of the part, away from the edges. The average thickness of one ply is then deduced: $t_{ply} = t_{part}/n = 0.353 \pm 0.011$ mm.

	Part weight (kg)	Part thickness (mm)	Ply thickness (mm)
C-spar 1	2.945	4.10 ± 0.08	0.342 ± 0.006
C-spar 2	3.044	4.31 ± 0.10	0.359 ± 0.008
C-spar 3	3.094	4.41 ± 0.07	0.367 ± 0.005
C-spar 4	2.978	4.15 ± 0.10	0.346 ± 0.008
C-spar 5	3.065	4.31 ± 0.07	0.359 ± 0.006
Avg.	**3.025 ± 0.062**	**4.23 ± 0.13**	**0.353 ± 0.011**

Table 5.2: Part weight and thickness measurements.

The results for the calculations of k_f with Eqs. 5.9 and 5.10 are given in Table 5.3. The fiber volume fraction is systematically higher by about 3 % with the thickness measurements compared to the mass measurements. In any case, the values are around 60 %, which is quite high for vacuum infusion. The retained value is the average over all the measurements: 60 %. This is motivated by two factors:

- The high values are predicted by both measuring methods. These methods are considered to be independent, since the only common parameters in both equations are ρ_f, n and σ_S;
- There is no reason to believe that one method is more accurate than the other.

	k_{f1}	k_{f2}	Avg.
C-spar 1	0.64	0.61	0.63
C-spar 2	0.61	0.58	0.60
C-spar 3	0.60	0.57	0.58
C-spar 4	0.63	0.60	0.62
C-spar 5	0.61	0.58	0.59
Avg.	0.62 ± 0.02	0.59 ± 0.02	**0.60 ± 0.02**

Table 5.3: Results of fiber volume fraction calculations.

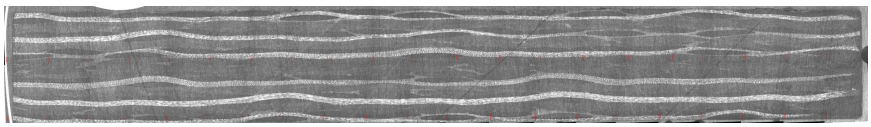


Figure 5.4: Microscopic image of a sample from a manufactured C-spar.

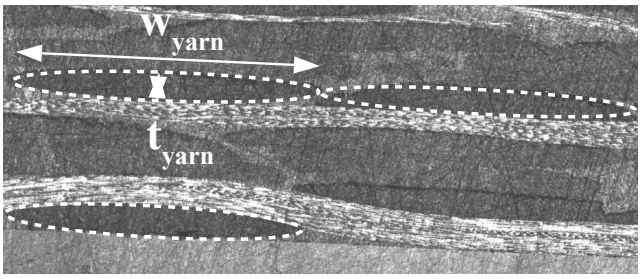


Figure 5.5: Yarn dimensions measurement and notations.

5.5.2 Yarn arrangement measurement

The geometrical data of the satin weave are now determined by microscopic measurements. These data will serve as input in the software TexGen for the geometrical representation of the textile. Square samples are cut out of two different manufactured nominal C-spars. One sample is cut from each face of each of these C-spars (the top face and the two vertical faces). This amounts to a total of six samples. Their width is about three periods of the satin weave— approximately 30 mm. One of their lateral face is sanded and scrutinized with help of an Olympus Provis AX-70 microscope. Images like Figure 5.4 are obtained for the six samples. These images are analyzed with a software allowing precise measurement of the cross-section of the yarns, considered to be ellipses, as illustrated in Figure 5.5. Only the yarns of the 0-degree plies are measured, since they are perpendicular to the plane of the figure.

Over the six samples, a total of 145 measurements of the cross-sections are gathered, summarized in Figure 5.6. The major and minor axes of the yarns are measured equal to $w_{yarn} = 2.18 \pm 0.11$ mm and $t_{yarn} = 0.204 \pm 0.017$ mm, respectively. An apparent incongruity is the fact that $2t_{yarn}$ is higher than t_{ply} by about 16 %. Figure 5.7 explains why this might seem illogical, as a ply is supposed to contain two yarns throughout its thickness. This may be discarded by two comments:

- As a matter of fact, it can be justified that $2t_{yarn} > t_{ply}$. The ply thickness t_{ply} is deduced from the total thickness of the layup t_{part}, though a layup is not a perfect superposition of separated plies. Adjacent plies are nested together, and yarns from one ply can fill gaps left between yarns of another ply. This idea is clarified by Figure 5.8 for a plain-weave textile with two plies, but the reasoning is identical in our case.
- An accurate description of a representative unit cell of the satin weave can therefore only be obtained by simulating the compaction and nesting

of at least two plies [113], or by optimizing the yarn spacing [189]. This kind of complex and costly modeling is exactly what the homogenization technique developed in Chapter 3 aims to avoid. It is readily capable of generating results for the penetrating textile represented in Figure 5.7. The impact of the absence of nesting on the elastic properties should be limited, as long as the overall fiber volume fraction is correct [190, 191].

In addition, the length w_{period} of the period of the textile, comprising 5 yarns for a 5-harness satin, is obtained by measuring 50 periods in the first ply of all C-spars (the ply in contact with the mold, for which the texture is visible). The result is $w_{period} = 10.9 \pm 0.05$ mm, which is coherent with the yarn measurements, since $5w_{yarn} = 10.9$ mm, and with the theoretical yarn count, since 4.6 yarns/cm is equivalent to 10.87 mm per period of 5 yarns.

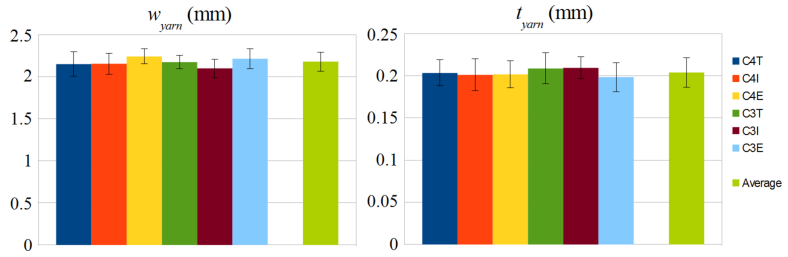


Figure 5.6: Yarn dimensions: results. Each bar corresponds to a different sample.

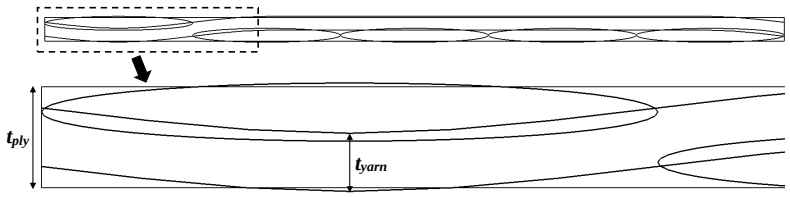


Figure 5.7: Satin weave modeled based on the measurements of the ply thickness and of the yarn dimensions.

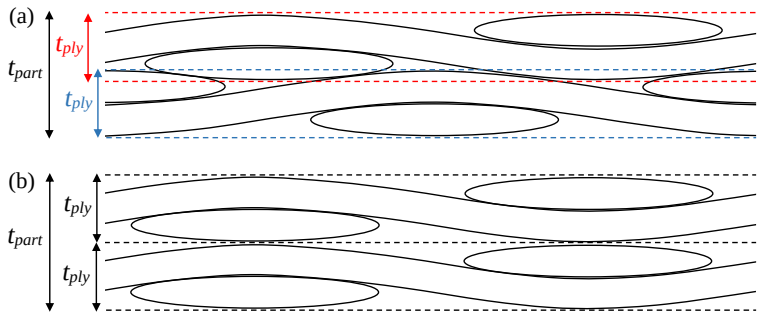


Figure 5.8: (a) realistic ply stacking: $t_{part} < nt_{ply}$; (b) idealized ply stacking: $t_{part} = nt_{ply}$.

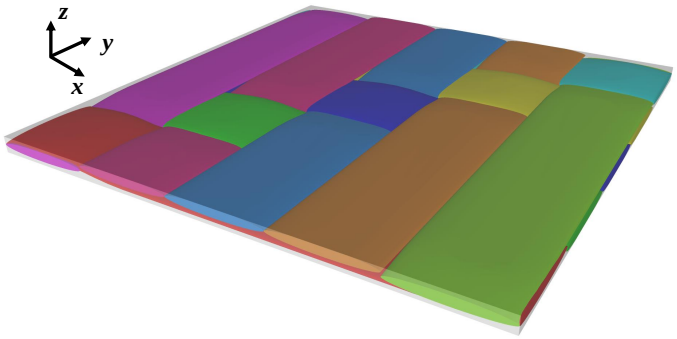


Figure 5.9: Model of the satin textile used for the homogenization procedure.

5.5.3 Homogenized properties

Taking into account all the aforementioned measurements, the model of the textile is created in TexGen. The result is shown in Figure 5.9, while Figure 5.7 represents a cut view of the model. The yarn volume fraction inside the RVE is 90.6 %, which leads to the nominal fiber volume fraction inside the yarns $k_f = 0.60/0.906 = 66.2$ %. The homogenization procedure described in Chapter 3 is applied. Since the Young's modulus and the CTE of the resin depend on the temperature in the glassy state, the homogenization procedure is performed at 4 different temperatures. An additional computation is needed for the properties in the rubbery state. The homogenized thermo-mechanical properties of the textile are summarized in Table 5.4, presented either in the form of a linear dependency with respect to the temperature, or as a constant value if this dependency is negligible.

5.6 Simulation of nominal parts and compensation

5.6.1 Comparison simulation/experiments for the nominal parts

The numerical modeling of the curing process is now undertaken for the nominal geometry, and the results are compared to the manufactured parts. The FE model is built in a similar way as in Chapter 4: the external surface of the CAD model of the nominal mold is used as a base surface for the draping simulation in Simulayt [176]. Then, a volume mesh is extruded in the upward direction, with the proper orientation for each element of each ply. The material properties in the local coordinate system of the element are the properties determined by homogenization in Table 5.4. Several types of boundary conditions are tested, ranging from very simple (uniform temperature, the mold is not modeled) to the most realistic a priori (convective heat exchange on the external surface, the mold is modeled as a volumetric deformable body,

Rubbery state		
$E_x = E_y$	[MPa]	23 512
E_z	[MPa]	393
ν_{xy}	[-]	0.54
$\nu_{xz} = \nu_{yz}$	[-]	0.55
G_{xy}	[MPa]	57
$G_{xz} = G_{yz}$	[MPa]	42
$\alpha_x = \alpha_y$	[/°C]	-1.1×10^{-6}
α_z	[/°C]	183×10^{-6}
$\beta_x = \beta_y$	[-]	4.2×10^{-5}
β_z	[-]	-1.9×10^{-2}

Glassy state		
$E_x = E_y$	[MPa]	71 964 - 19.2T
E_z	[MPa]	13 451 - 22.3T
ν_{xy}	[-]	0.073
$\nu_{xz} = \nu_{yz}$	[-]	0.459
G_{xy}	[MPa]	4701 - 8.5T
$G_{xz} = G_{yz}$	[MPa]	3287 - 6.1T
$\alpha_x = \alpha_y$	[/°C]	2.8×10^{-6}
α_z	[/°C]	$47.1 \times 10^{-6} + 0.12 \times 10^{-6} T$
$\beta_x = \beta_y$	[-]	-6.4×10^{-4}
β_z	[-]	-1.1×10^{-2}

Table 5.4: Homogenized properties of the satin + RTM6 composite. The temperature T is in degrees Celsius.

the mold/part interaction involves a stick-slip condition). As expected from a previous modeling campaign [7], the best compromise between computational time and accuracy (in terms of convergence towards the results of the most detailed boundary conditions) involves the following hypotheses:

- The temperature is uniform throughout the part, and follows the curing cycle. The convective exchange hypothesis has a significant influence on the temperature profile within the part, but not on the final part distortion.
- The mold is modeled as a rigid surface. The stick-slip condition of Khoun and Hubert [192] is used for the interaction between the part and the mold. For an aluminum tooling, this condition implies that the contact is sticking while the shear stress at the interface remains below the threshold $\tau_{max} = 126$ kPa, above which the contact is sliding with a coefficient of friction of 0.3.

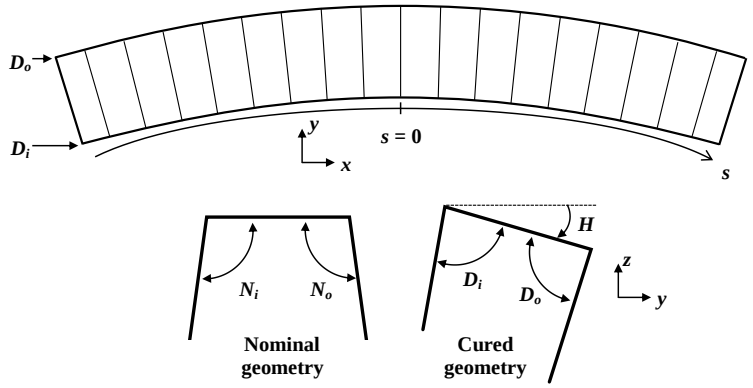


Figure 5.10: C-spar spring-in and twist measurement: notations. The spring-in angles are calculated as $S_o = N_o - D_o$ and $S_i = N_i - D_i$

The spring-in is computed by creating sections, as in Figure 5.10. $S_o = N_o - D_o$ and $S_i = N_i - D_i$ designate the spring-in in the corner located in the outer and inner curvatures, respectively. s is the curvilinear abscissa along the length of the C-spar. As in Chapter 4, the twist of the part is also considered, by measuring the angle H between the base line and the horizontal plane. It should be pointed out that, since the measurements are performed after a best-fit operation, the angle H is actually an objective measure of the twist. The comparison between the experimental measurements and the simulation is provided in Figures 5.11 and 5.12 for S_i and S_o, respectively. The error bars represent the standard deviations over all the experiments. The raw results for all the different parts can be found in Appendix E. Table 5.5 provides the numerical values based on the average of the experimental data, from which a more in-depth analysis can be conducted. First, let us recall that the measurement uncertainty is estimated to be less than $\pm 0.05°$. It can be observed in Table 5.5 that the simulation underestimates slightly but systematically the spring-in angle by approximately 0.10-0.15° with respect to the averaged experimental results. The experimental variability lies in general between 0.07° and 0.15°, which is not negligible compared to the absolute value of the spring-in (around 1°). It is however reasonable, considering the use of the VARTM process and the fact that the parts are produced in a non-industrial framework. There is no doubt that a high-pressure process with better quality control (ply cutting and draping, temperature homogeneity, predictable injection path) would result in a much better repeatability. The fact that the simulation underestimates the spring-in may be partly due to the underestimation of the out-of-plane CTE. Figure 3.23 shows for a plain-weave textile that the prediction with an unstructured mesh deviates by a few percent, depending on the mesh refinement, with respect to a conformal mesh. This deviation is in fact an underestimation, and there is no reason to believe that it would be different for the present satin textile. All things considered, the correlation between the experiments and the simulation is quite satisfactory in terms of spring-in angle. An important fact is that the trends in the simulation are

similar to those of the experiments: the spring-in is more or less constant in the middle of the part, with a decrease (resp. increase) at the free edges for the angle in the inner (resp. outer) curvature.

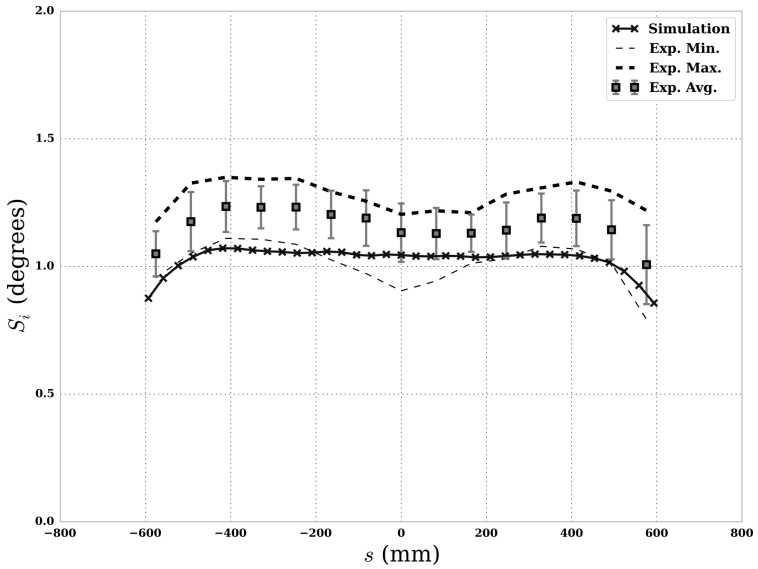


Figure 5.11: Comparison between experiments and simulation for the nominal C-spars: internal spring-in S_i.

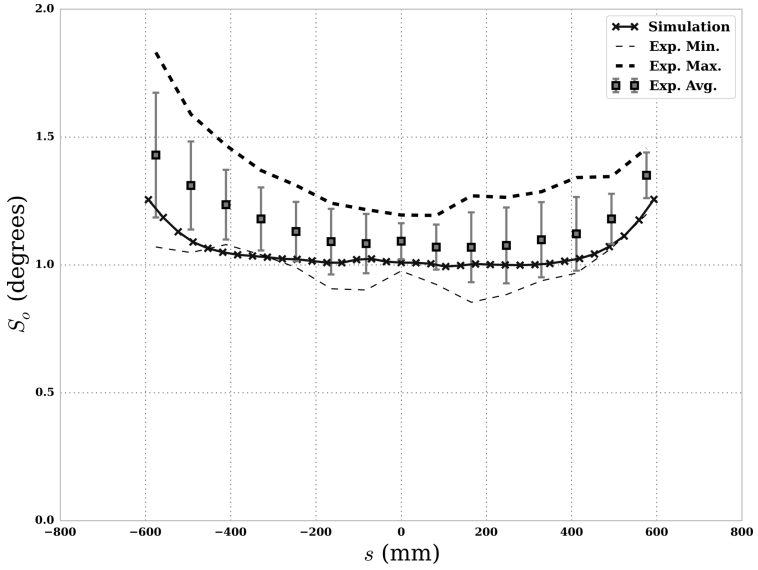


Figure 5.12: Comparison between experiments and simulation for the nominal C-spars: external spring-in S_o.

Internal spring-in S_i						
s (mm)	Simulation	Exp. Avg.	Exp. Std. Dev.	Difference		
-576	0.92°	1.05°	0.09°	-0.13°	/	-12.4 %
-494	1.04°	1.18°	0.12°	-0.14°	/	-11.9 %
-411	1.07°	1.23°	0.10°	-0.16°	/	-13.0 %
-329	1.06°	1.23°	0.08°	-0.17°	/	-13.8 %
-247	1.05°	1.23°	0.09°	-0.18°	/	-14.6 %
-165	1.06°	1.20°	0.09°	-0.14°	/	-11.7 %
-82	1.04°	1.19°	0.11°	-0.15°	/	-12.6 %
0	1.05°	1.13°	0.11°	-0.08°	/	-7.1 %
82	1.04°	1.13°	0.10°	-0.09°	/	-8.0 %
165	1.04°	1.13°	0.07°	-0.09°	/	-8.0 %
247	1.04°	1.14°	0.11°	-0.10°	/	-8.8 %
329	1.05°	1.19°	0.10°	-0.14°	/	-11.8 %
411	1.04°	1.19°	0.11°	-0.15°	/	-12.6 %
494	1.02°	1.14°	0.12°	-0.12°	/	-10.5 %
576	0.89°	1.01°	0.15°	-0.12°	/	-11.9 %
Avg.	1.03°	1.16°	0.10°	-0.13°	/	-11.2 %

External spring-in S_o						
s (mm)	Simulation	Exp. Avg.	Exp. Std. Dev.	Difference		
-576	1.22°	1.43°	0.24°	-0.21°	/	-14.7 %
-494	1.09°	1.31°	0.17°	-0.22°	/	-16.8 %
-411	1.04°	1.24°	0.14°	-0.20°	/	-16.1 %
-329	1.03°	1.18°	0.12°	-0.15°	/	-12.7 %
-247	1.02°	1.13°	0.12°	-0.11°	/	-9.7 %
-165	1.01°	1.09°	0.13°	-0.08°	/	-7.3 %
-82	1.02°	1.08°	0.12°	-0.06°	/	-5.6 %
0	1.01°	1.09°	0.07°	-0.08°	/	-7.3 %
82	1.00°	1.07°	0.09°	-0.07°	/	-6.5 %
165	1.00°	1.07°	0.14°	-0.07°	/	-6.5 %
247	1.00°	1.08°	0.15°	-0.08°	/	-7.4 %
329	1.01°	1.10°	0.15°	-0.09°	/	-8.2 %
411	1.02°	1.12°	0.14°	-0.10°	/	-8.9 %
494	1.08°	1.18°	0.10°	-0.10°	/	-8.5 %
576	1.22°	1.35°	0.09°	-0.13°	/	-9.6 %
Avg.	1.05°	1.17°	0.13°	-0.12°	/	-9.7 %

Table 5.5: Nominal parts: comparison between the averaged experimental results and the simulation.

Regarding the twist H, the comparison is less satisfactory, see Figure 5.13. A strong and repeatable asymmetry can be observed for the manufactured parts. This is clear when considering the distortion color map of Figure 5.14 (the distortion color maps of all the manufactured parts are provided in Appendix E). In this color map and more generally in all the color maps presented in this thesis, a positive deviation means that the deformed shape is above the nominal geometry. Figure 5.13 includes least-square fitted parabola for all the experiments, and it can be observed that the twist can be represented by a parabola with a very good agreement. More interestingly, Figure 5.15 presents

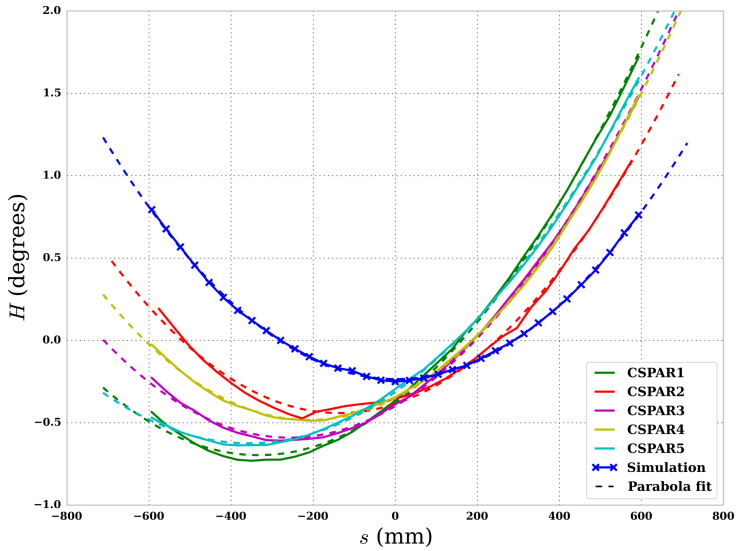


Figure 5.13: Comparison between experiments and simulation for the nominal C-spars: twist H.

the second-degree coefficient of these parabolas. It can be observed that the coefficient of the parabola is very stable over the experiments (between 86 % and 106 % of the average), and that there is less than 1 % difference between the average of the experiments and the simulation. This indicates that the parabola predicted by the simulation is simply shifted with respect to the experiments. The asymmetry may come from any deviation from the "ideal" situation: machining of the mold, deviation in the fiber orientations, non-uniformity of the infusion or the curing process, to name a few. Since the analysis of the manufacturing of the compensated parts brings additional information, these potential causes are discussed in the final results, in Section 5.7.

To conclude, even though the manufacturing of the nominal parts was not necessary to proceed to the compensation step, the results show the level of confidence that can be put in the model, before looking at the question of compensation. It quantifies the first source of error which is independent of the compensation strategy. It is clear that the spring-in is much better predicted than the other main distortion mode, i.e. the twist. If the imperfection of the manufacturing process is not related to the mold itself, and if it is not identified and resolved, there is a high probability that the twist will not be properly compensated. There is however only one way to know this for sure, and it should be pointed out that twisting is probably a less detrimental distortion than spring-in. Indeed, correcting the twist most likely requires less effort during the assembling step than correcting for spring-in.

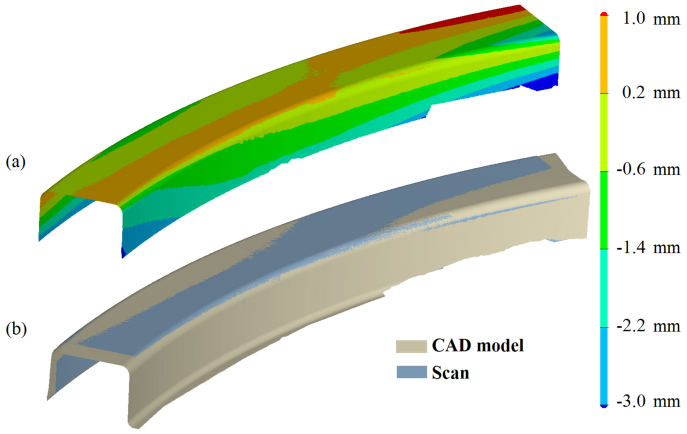


Figure 5.14: (a) Distortion map for nominal C-spar n°1; (b) Relative position of the scan with respect to the CAD model (after best-fit)

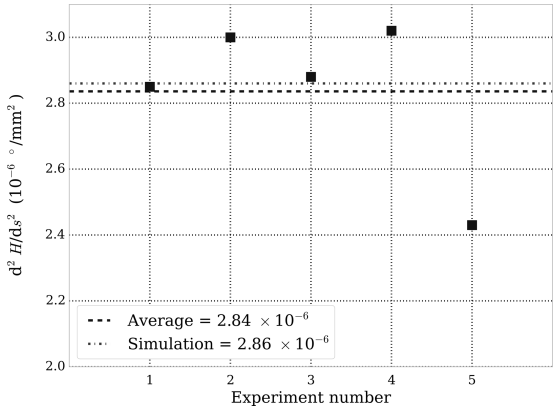


Figure 5.15: Comparison between experiments and simulation for the nominal C-spars: second derivative of the twist.

5.6.2 Sensitivity analysis: material properties

A study is conducted to assess the sensitivity of the distortions of the C-spar with respect to the material properties. This study consists in adjusting the material data within a range of ±20 % with respect to their nominal value (in Table 5.4) and in computing the difference between the distortions measured after the simulation and the distortions of the nominal simulation (Figures 5.11 to 5.13). In order to simplify the interpretation of the results, three numerical values are computed for each simulation: the average spring-in (internal S_i and external S_o) for s between -200 mm and +200 mm, since the spring-in angles exhibit a plateau in this region, and the second order coefficient $\mathrm{d}^2H/\mathrm{d}s^2$ of the parabola fitted to the twist distribution.

In Table 5.6, each property is changed by ±20 %, while all the other properties remain fixed. The properties resulting in a sensitivity of 0.2 % or less

are not listed in the table. Such a one-factor-at-a-time method hides the potential interactions between the different properties. In particular, the cure-related properties $\mathrm{d}X/\mathrm{d}t$, T_g and X_{gel} are strongly coupled to one another. Consequently, the sensitivity is also computed with a variance analysis tool (ANOVA) over a sample of 90 simulations for which all properties vary simultaneously within the continous interval [-20 %, +20 %] with respect to their nominal value. The even distribution of the experiments is ensured by the use of a latin-hypercube sampling, as explained in Chapter 4. The results of the ANOVA analysis are presented in Figure 5.16. In summary, Figure 5.16 presents the true sensitivity (first order Sobol's sensitivity indices), while Table 5.6 delivers more limited but more concrete information. These results are in agreement with previous findings [180]. In particular:

- The through-thickness CTE α_z in the glassy state is the most influencial material property.
- The cure-related properties ($\mathrm{d}X/\mathrm{d}t$, T_g, X_{gel}) are grouped in second place. This highlights the importance of the profusion of experimental data for the RTM6, e.g. [61, 184, 187, 193, 194] for the glass transition temperature, [56, 183, 194, 195] for the cure kinetics and [187, 193, 196] for the gel point.
- The through-thickness elastic modulus E_z and most of the Poisson's ratios and shear moduli have a negligible influence on the cure-induced distortions. Approximations of these properties are sufficient for predicting the cure-induced distortions of the C-spar. The same can be said about the in-plane expansion coefficient parameters $\alpha_x = \alpha_y$ and $\beta_x = \beta_y$, whose nominal values are extremely low due to the presence of the fibers.

5.6.3 Numerical compensation

Chapter 4 proved that the mirror method is suitable for the compensation of a curved C-spar. Therefore, this method is used to compensate the present geometry. Figure 5.17 presents the history of the residual distance reduction between the final cured geometry and the nominal geometry. In this case, the optimal compensation is achieved at the first iteration, since the subsequent iterations improve the residual distance by only 0.3 %. The final residual distance is 4.6 %, which means that the compensation is not perfect. However, Figure 5.18 shows that the residual distortions are localized effects due to the way the distortion is computed (node-to-node distance after best-fit, see Section 4.2.3), rather than to a distortion mode that could not be compensated. Moreover, Table 5.5 indicates that the numerical simulation is about 10 % off compared to the nominal experiments, and it is therefore not realistic to target a perfect compensation.

Figure 5.19 provides a direct comparison between the distortions of the cured nominal geometry, and the deviation between the final compensated mold geometry and the nominal geometry. The latter is more or less the inversion of the former, which highlights the mirror aspect of the compensation method. In particular, the spring-in of the cured nominal shape becomes a spring-back in

Rubbery state				
		Effect on...		
Property		S_i	S_o	$\mathrm{d}^2H/\mathrm{d}s^2$
$E_x = E_y$	-20 %	-2.3 %	-2.3 %	-2.2 %
	+20 %	+2.3 %	+2.3 %	+2.2 %
ν_{xy}	-20 %	-2.0 %	-1.9 %	-1.5 %
	+20 %	+2.6 %	+2.6 %	+2.5 %
α_z	-20 %	+0.3 %	+0.4 %	+0.6 %
	+20 %	-0.3 %	-0.3 %	-0.3 %
β_z	-20 %	**-6.3** %	**-6.3** %	**-5.7** %
	+20 %	**+6.3** %	**+6.3** %	**+6.2** %

Glassy state				
		Effect on...		
Property		S_i	S_o	$\mathrm{d}^2H/\mathrm{d}s^2$
$E_x = E_y$	-20 %	+2.6 %	+2.4 %	2.3 %
	+20 %	-1.8 %	-1.7 %	-1.6 %
G_{xy}	-20 %	+0.2 %	+0.5 %	+0.7 %
	+20 %	-0.2 %	-0.4 %	-0.3 %
$\alpha_x = \alpha_y$	-20 %	+0.6 %	+0.6 %	+0.6 %
	+20 %	-0.6 %	-0.6 %	+0.6 %
α_z	-20 %	**-13.9** %	**-13.8** %	**-13.7** %
	+20 %	**+13.8** %	**+13.8** %	**+13.7** %
β_z	-20 %	-0.8 %	-0.8 %	-0.8 %
	+20 %	+0.8 %	+0.8 %	+0.8 %

Other properties				
		Effect on...		
Property		S_i	S_o	$\mathrm{d}^2H/\mathrm{d}s^2$
X_{gel}	-20 %	-3.7 %	-3.7 %	-4.1 %
	+20 %	**-17.5** %	**-17.6** %	**-17.1** %
T_C^*	-20 %	-1.1 %	-1.1 %	-1.2 %
	+20 %	+0.7 %	+0.7 %	+0.7 %
T_g	-20 %	**-14.5** %	**-14.7** %	**-15.1** %
	+20 %	**-10.9** %	**-11.1** %	**-11.0** %
$\mathrm{d}X/\mathrm{d}t$	-20 %	**-11.4** %	**-11.7** %	**-11.7** %
	+20 %	-1.9 %	-1.9 %	-1.8 %

Table 5.6: Sensitivity of the spring-in and of the twist with respect to the material properties.

the compensated shape (meaning the angles of the mold are more opened than the nominal geometry, so that the cure simulation with this geometry leads to a zero angle difference with respect to the nominal geometry), and the twist is reversed.

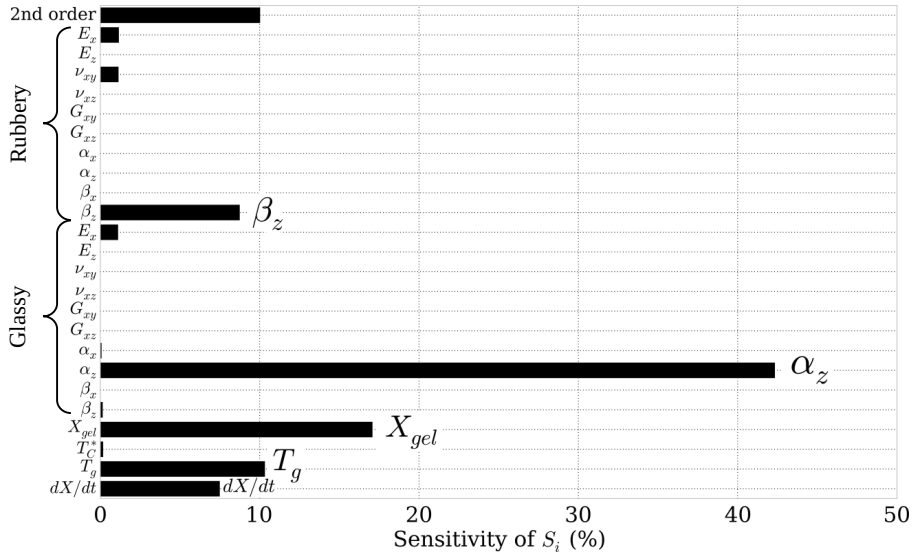


Figure 5.16: ANOVA analysis: sensitivity of the spring-in angle S_i to the material properties.

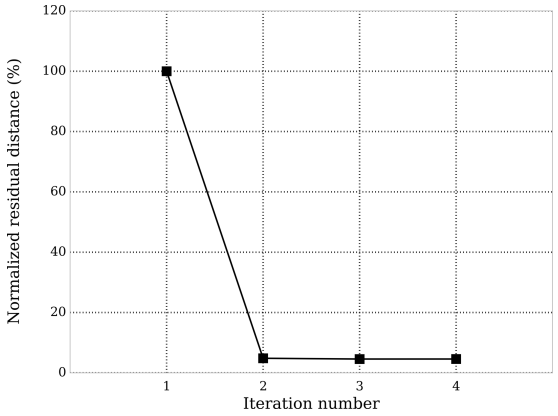


Figure 5.17: Compensation of the C-spar: application of the mirror method.

As discussed in Chapter 4, the mirror method is mesh-based and therefore requires a reverse engineering step in order to transform the compensated shape into a 3D CAD model which can be interpreted by a machining software, see Figure 5.20. The meshed compensated surface is first transformed into a CAD geometry format (e.g. IGES) with the help of a reverse engineering software. The volume of the mold and other features (for instance, for clamping or injection purposes) are then created around this surface in a CAD environment. In the present case, the model has been generated in a few hours due to the simplicity of the geometry, but it may represent a significant effort for more

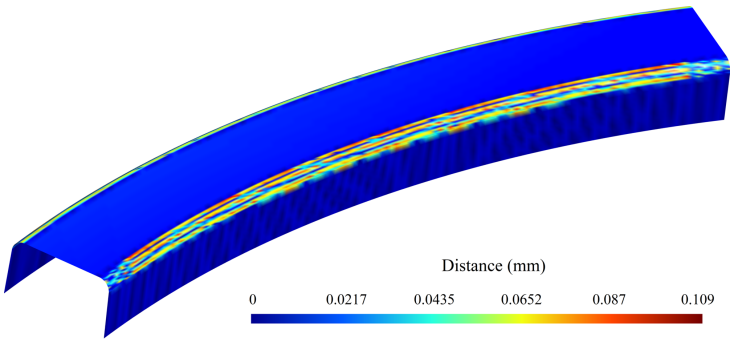


Figure 5.18: Residual distortions of the cured compensated part.

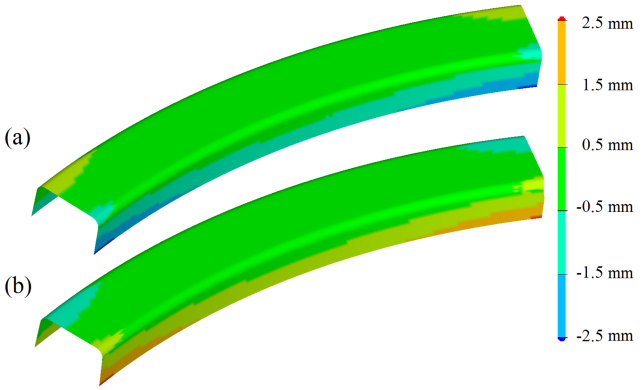


Figure 5.19: Deviations with respect to the nominal geometry: (a) cured nominal geometry; (b) compensated mold geometry.

complex industrial tests cases.

5.7 Manufacturing of the compensated parts

The compensated mold is machined at Cenaero with a CMS Antares 5-axis numerically-controlled milling machine and then sanded to obtain a smooth surface finish. The C-spars are manufactured and measured under the same conditions as previously described in Section 5.3. The measured spring-in angles are reported in Figures 5.21 and 5.22. They are also compared to the spring-in of the nominal parts, in such a way that one can see how significantly the spring-in has been reduced by the compensation procedure. These figures present averaged results, the full series of data is provided in Appendix E. The numerical values are listed in Table 5.22. The spring-in has been reduced to less than 0.1°, on average, again with a certain variability. This is less than 10 % of the original spring-in, which is a satisfactory achievement.

The twist measurements for all the parts are shown in Figure 5.23. Once again, a clear asymmetry is present. While the measured twist of the compen-

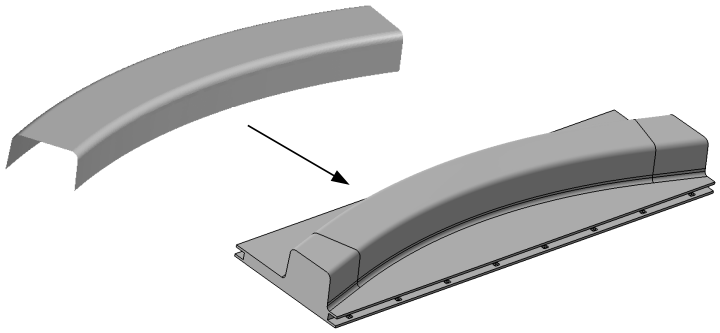


Figure 5.20: Reverse-engineering of the compensated surface into a machinable mold.

sated parts should be zero, it is instead linear. This is very interesting when considering what has been observed for the nominal parts. Indeed, the twist of the nominal parts could be well approximated by a quadratic polynomial. The numerical simulation captures well the second order coefficient, but not the linear part of the polynomial. Therefore, it can be speculated that the twist of the manufactured parts is a quadratic polynomial, plus a linear function due to an unplanned asymmetry in the manufacturing process. Since the latter is not taken into account in the simulation, the compensation procedure has suppressed only the quadratic part of the twist. In that logic, it makes sense that the twist of the compensated parts should be linear. Although this is only a conjecture, it is strongly supported by the observations of Figures 5.13, 5.15 and 5.23.

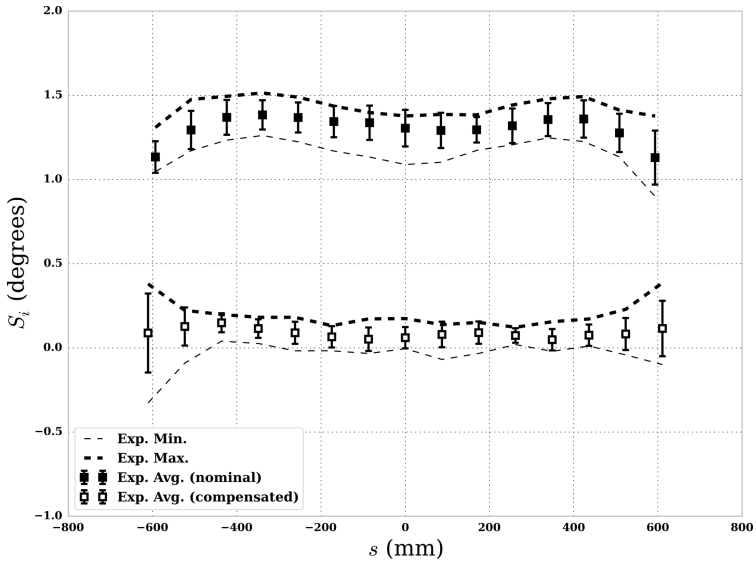


Figure 5.21: Comparison between compensated and non-compensated experiments: internal spring-in S_i.

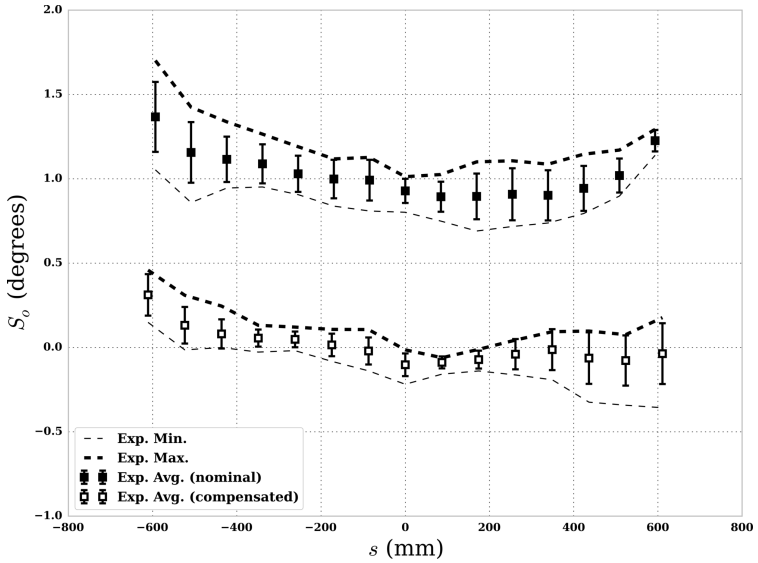


Figure 5.22: Comparison between compensated and non-compensated experiments: external spring-in S_o.

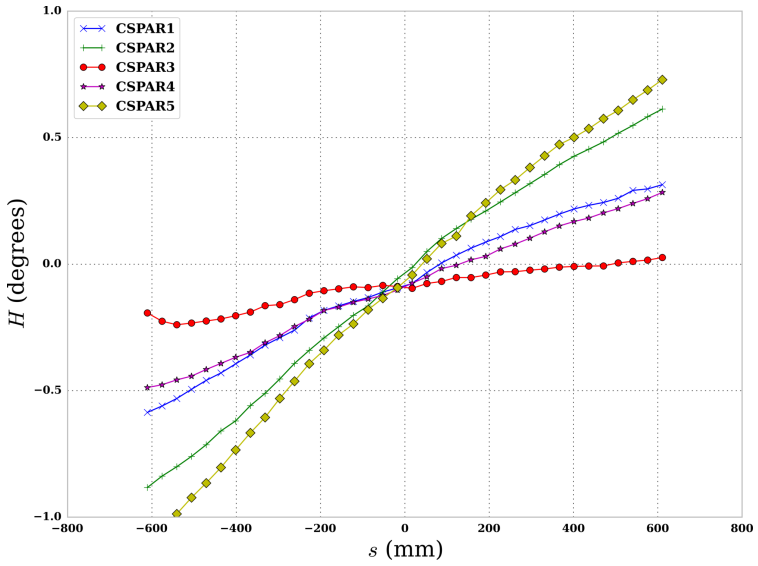


Figure 5.23: Twist H measured on the compensated parts.

Internal spring-in S_i after compensation		
s (mm)	Exp. Avg.	Exp. Std. Dev.
-576	0.09°	0.23°
-494	0.13°	0.11°
-411	0.15°	0.06°
-329	0.11°	0.06°
-247	0.09°	0.07°
-165	0.07°	0.06°
-82	0.05°	0.07°
0	0.06°	0.06°
82	0.08°	0.08°
165	0.09°	0.07°
247	0.07°	0.04°
329	0.05°	0.06°
411	0.07°	0.06°
494	0.08°	0.10°
576	0.12°	0.16°
Avg.	0.09°	0.09°

External spring-in S_o after compensation		
s (mm)	Exp. Avg.	Exp. Std. Dev.
-576	0.31°	0.12°
-494	0.13°	0.11°
-411	0.08°	0.09°
-329	0.06°	0.05°
-247	0.05°	0.05°
-165	0.02°	0.07°
-82	-0.02°	0.08°
0	-0.10°	0.07°
82	-0.09°	0.04°
165	-0.07°	0.05°
247	-0.04°	0.09°
329	-0.01°	0.12°
411	-0.06°	0.15°
494	-0.08°	0.15°
576	-0.04°	0.18°
Avg. (of absolute values)	0.08°	0.09°

Table 5.7: Compensated parts: spring-in measurements.

The distortions of the compensated parts can also be analyzed in terms of statistics of the deviations. As for nominal parts, color maps are created to represent the deviation with respect to the nominal geometry. Figure 5.24 provides an example of such a color map, and they are given for all parts in Appendix E. Each color map is made of a point cloud of about 500,000 points, which are thus a suitable basis to study the deviations from a statistical point of view. Firstly, Figure 5.25 shows the dispersion of the deviations, under the form of histograms. The dispersion is much lower for compensated parts, and the distribution of the deviations is much more condensed around zero.

The last graphs, marked "ALL", consider the point clouds of all the parts combined. Secondly, Figure 5.26 presents the cumulative distributions of the absolute deviations, for all the manufactured parts. This enables to extract percentiles of the distribution, some of which are gathered in Table 5.8. The percentiles give the number of points which are below a certain threshold. They are calculated based on the combined point clouds, i.e. considering the 5 parts together. The percentiles for each individual part are given in Appendix E. For instance, for the compensated parts, 75 % of the points deviate by less than 0.325 mm, and 98 % by less than 0.809 mm. These numbers go up to 1.098 mm and 2.616 mm, respectively, for the nominal parts. The percentiles of the compensated parts are improved by 62 % to 73 % in comparison to the nominal parts. This is a great achievement, considering that the twist has not been entirely compensated.

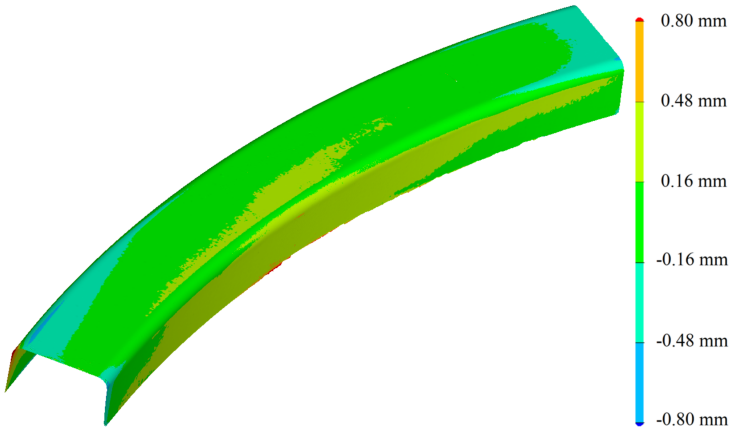


Figure 5.24: Distortion map for compensated C-spar n°3.

Percentile	Nominal parts (mm)	Compensated parts (mm)	Relative difference
5-th	0.051	0.018	-65 %
10-th	0.102	0.038	-63 %
25-th	0.253	0.097	-62 %
50-th	0.534	0.197	-63 %
75-th	1.098	0.325	-70 %
90-th	1.813	0.491	-73 %
95-th	2.240	0.633	-72 %
99-th	2.810	0.951	-66 %

Table 5.8: Absolute deviations with respect to the nominal geometry: comparison of percentiles.

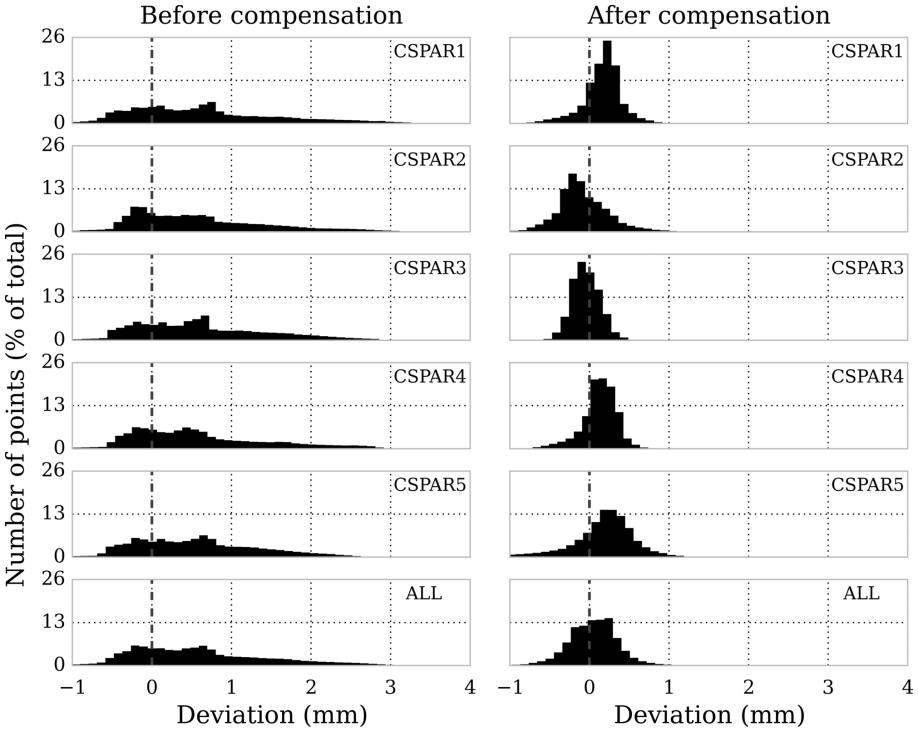


Figure 5.25: Deviations between the manufactured parts and the nominal CAD model, presented as histograms.

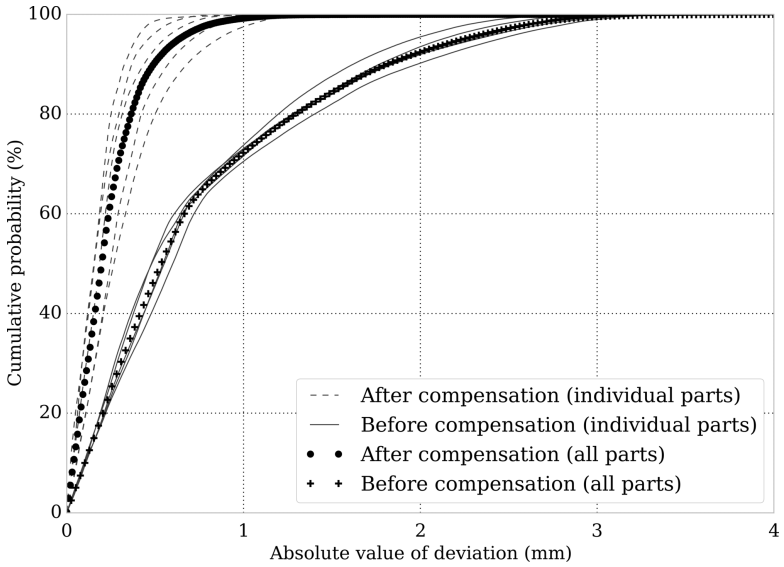


Figure 5.26: Absolute deviations between the manufactured parts and the nominal CAD model, presented as cumulative distributions.

5.8 Discussion about the twist

Let us now examine why the twist has not been compensated as well as the spring-in. The possible sources of imperfection in the manufacturing process are listed hereafter, among which those that could lead to a repeatable (at least qualitatively) asymmetry are identified:

- Non-uniform cure due to the infusion process. The infusion is not simulated numerically and the curing model therefore assumes that the part is fully infused and then starts to cure, with an initial degree of cure X equal to zero. This hypothesis misses two different ingredients of the real process. The first one is that the infusion is not instantaneous, and the second one is that the flow front may not be perfectly straight. Only the latter may create asymmetry, since the resin inlet and outlet are located on the external and internal sides, respectively (Figure 5.2). In practice, the regularity of the flow front could not be checked because of the high temperature, and because the silicon sheets under the vacuum bag obstructed the view. However, the infusion time has been measured: it takes about 15 minutes for the resin to travel through the layup before the part is fully infused, after which the real curing cycle starts. During these 15 minutes, the resin which is infused is heated to 120°C by the mold and the surrounding air, while the resin which is not infused yet is still at 80°C. It can be estimated with the kinetics model, Eq. 5.5, that the difference of initial degree of cure between any two points of the structure is less than 1 %. This is far from enough to generate the discrepancy which has been observed in the twist behavior between the experiments and the simulation.
- Non-uniform cure due to a heterogeneous temperature distribution inside the oven. If there exists a temperature gradient between the left and the right of the mold, and if the mold is always placed in the same position in the oven (which is the case), this could explain the asymmetry. A heat survey, executed twice in the same conditions, showed that there is indeed a temperature gradient. During the curing cycle, the left of the mold is hotter than the right of the mold by 1 to 3°C, and hotter than the middle of the mold by 3 to 8°C. However, a simulation carried out with these data has exhibited no significant effect on the twist.
- Fiber orientations. One of the most approximate experimental manipulations, in our context, is the cutting and the draping of the carbon plies, in particular the 45-degree plies. The latter shear easily and one must be careful when laying them onto the mold. Although this is clearly a weak point in our manufacturing chain, it is probably not the cause of the asymmetry, for two reasons: firstly, it is more a source of variability than of asymmetry; and secondly, a simulation where all ply orientations are shifted by 5 degrees demonstrated, once again, no significant effect on the twist.
- Measurement method. The parts are laid flat on a table in order to be scanned. Even though they are not mechanically clamped, since this

would influence their shape, gravity could also cause this problem. However, considering the stiffness of the C-spar and its weight, this effect is most likely negligible. Moreover, if it does lead to asymmetry, there is no reason why it would always be in the same direction. One could also point out that the best-fit operation may influence the value of the twist, which is measured relatively to the horizontal plane. This cannot be the reason for asymmetry, since performing a best-fit between a symmetric scan and a symmetric CAD keeps the symmetry. If the best-fit was somewhat uncertain, the asymmetry would not be repeatable.

- Machining accuracy. It is possible that the machining process produced imperfect molds, which could lead to imperfect part production. The deviation between the machined molds and their theoretical CAD shapes has been assessed. The results of this investigation are provided in Appendix E. The compensated mold, machined at Cenaero, is of far better quality than the nominal mold, machined by a sub-contractor. Nevertheless, no clear asymmetry has been measured for either mold and, more importantly, it is very unlikely that two completely independent molds would suffer from the same defect and produce the same trend of twist imperfection (increasing twist from left to right, see Figures 5.13 and 5.23).

Consequently, a definite answer cannot be provided, at this point, as to why all manufactured parts present the same kind of asymmetry. It is possible that some of the assumptions of the numerical simulation hide the real effect of the imperfections listed above. For instance, it is assumed in the simulations that the mold is a rigid surface because a more realistic case (deformable mold) does not have a significant influence on the spring-in; and we have seen that a thermal gradient imposed in the simulation with the rigid mold does not influence the twist. However, this does not necessarily imply that a thermal gradient with a deformable mold does not have an influence on the twist. Another sensitive hypothesis is the interaction behavior between the mold and the part, which is a research topic by itself. These are just two examples, and many more alternatives can be considered and investigated. The bottom line is that chasing perfection appears vain, especially in the context in which the C-spars have been manufactured. A very interesting topic of research would be to study the impact of these imperfections and of the variability on the reject rate in an actual industrial production line.

5.9 Conclusion

In this chapter, the homogenization-compensation computational chain has been deployed to produce C-spars with reduced distortions. Besides the geometry, only the properties of the constituents (resin and fibers) and microscopic images of the textile have been needed to complete the objective. Those images have been extracted from the nominal C-spars, but they could also have been obtained by manufacturing simple flat plates. The degree of agreement between the simulation of the curing process and the experiments has been highlighted for two types of geometry (nominal and compensated). While the

spring-in effect is qualitatively and quantitatively predicted, which results in a compensation of about 90 %, the twist distortion mode is affected by a probable imperfection in the manufacturing process which has not been identified at this stage. The 95-th percentile of the deviations has been reduced from 2.24 mm to 0.63 mm, which makes the compensated parts much more compatible to the eventual assembly step. Interestingly the twist has turned from a parabola to a linear distribution, while, in fact, the second-order coefficient of the parabola has been well-captured by the simulation. This gives the impression that, if the imperfection is identified and accounted for in the simulation, the twist will be properly compensated. The remaining twist must therefore be attributed to the manufacturing process, and not to the compensation methodology.

This experimental campaign highlights the benefits of using numerical compensation. Predicting directly the compensated shape will save the cost and time of machining a nominal mold and prevents from trying to guess the compensation based on the nominal parts. Relying on rule of thumbs, e.g. by opening the angle by 1 degree to compensate for the spring-in, would miss the fact that the spring-in is not constant, and the twist would be simply disregarded. In our case, the nominal mold costs 15,000 euros and was delivered after 6 months. This particular price bears no comparison to the cost for an industrial application.

Chapter 6

Conclusions and perspectives

6.1 Main results and conclusions

6.1.1 The global context

The aim of this project has been to fill a gap in the literature, both from the point of view of existing methodologies and experimental applications, regarding mold compensation. The experimental campaign in Chapter 5 constitutes the first complete compensation cycle, with numerical and experimental data for a non-compensated and compensated geometry. This accomplishment has been made possible by the development of pragmatic and generic methodologies. On the one hand, the homogenization procedure enhances the applicability of the prediction of cure-induced distortions, by considering the properties of the different constituents of the composite instead of mechanical tests on the said composite. This is all the more true considering the fact that industrial applications rarely consist of only one set of materials. On the other hand, numerical compensation allows for the production of parts exhibiting reduced distortions, bypassing the manufacturing of the nominal components, and without the need to make educated guesses concerning the distortion modes. Even when the compensation is not perfect, it is easier to work with parts which deviate by a maximum of 0.5 mm with respect to the target design, than trying to accommodate to 2 mm deviations. In particular, smaller distortions:

- cause fewer problems during assembling;
- make it more manageable to consider machining adjustments of a mold.

Notwithstanding that the homogenization and compensation methodologies have been developed towards a unique and coherent objective, their realization has been quite distinct in practice. Consequently, conclusions are drawn separately for each contribution.

6.1.2 Mold compensation

In Chapter 4, two main routes have been proposed to tackle the issue of mold compensation: CAD-based methods and mesh-based methods. In total, three different methods have been developed, namely the distortion modes method (DMM), the control points method (CPM) and the mirror method. They have first been tested on a curved C-spar. With an intuition-based parametrization of several distortion modes, the DMM has been able to reduce the residual distance by 57 %. This is less effective than the 84 % obtained by the CPM, where the parametrization consists of the displacement components of a certain number of points. However, the DMM necessitates fewer optimization parameters and thus results in fewer curing simulations. Interestingly, it has also been able to reduce very significantly all the distortion modes in a twelve-dimensional design space, when these modes are defined as the objective function of the optimization: a reduction of 97.9 % on average has been obtained, with a maximum of 22 % for the twist. It is likely that the parametrization could be improved, at the cost of another run of optimization. In the case of the C-spar, the mirror method has reduced the distortions by 99.9 %. This method has also been successfully applied to several other test cases, including a 2-meter long inboard flap with several materials and many variations in thickness. The final discussion of the chapter has evidenced the complementary nature of the three different techniques. While the mirror method, and mesh-based methods in general, are easier to set up and are more generic, they leave total freedom to the mold shape. This can be detrimental in case of the presence of manufacturing constraints. In its current form, the mirror method also fails for warpage-dominated structures. CAD-based methodologies provide a more robust alternative, since the user keeps the control on the geometry variations allowed to the mold.

The main conclusions of this study are as follows. Firstly, the main driver of the effectiveness of the different methods is the balance between the subjectivity of the method, the reduction of the distortions and the computational time. It is clear that a fast method which reduces only partly the distortions, thereby requiring to be launched several times, is not necessarily more relevant than a slower method which is less subjective and more efficient in the distortion reduction. In that respect, the confrontation of the DMM and the CPM is interesting. For each method, only one set of parameters, defined intuitively, has been investigated. The DMM has taken three days to achieve a 57 % improvement, while the CPM has needed six days to reach 84 %, with comparable computational resources. When observing how the twist is not as well compensated as the other modes with the DMM, one can think of changing the parametrization of the twist, and re-launch the optimization. It is the duration and effectiveness of this second optimization which can determine which parametrization performs the best.

Another outcome is that mold compensation would deserve more recognition and study in the literature. Even though the C-spar geometry is far from the complexity of the aeronautics standards, it has been shown that compensating the spring-in or the torsion, or both together, are three different things. A composite structure must be considered in its entirety. The inter-

action between the different curvatures plays an important role, and studying single-curved sub-components [5, 9, 10] is an oversimplification. Predicting the compensation of the warpage sustained by an initially flat panel [164] is not relevant if it is not checked that the compensated mold produces flat panels after cure. This is a lesson of the mirror method. In addition, the question must be raised if the mold resulting from the compensation methodology can be reasonably used in an industrial process. Most of the time, the compensation will have to adjust to the manufacturing constraints, and not the other way around. The development of several methodologies which can accommodate to the different needs of the end user is an important asset.

In Chapter 5, the mold compensation strategy has been put into practice to manufacture 1.2-meter long C-spars with reduced distortions. The spring-in has been reduced from about 1° to less than 0.1°, on average. Using a best-fit alignment with respect to the nominal geometry enables to create deviation maps and to study more finely the distribution of the deviations. These deviations have been reduced by about 70 % compared to the nominal parts. In particular, 50 % of the points deviate by less than 0.197 mm, 75 % by less than 0.325 mm, and 95 % by less than 0.633 mm. More detailed experimental results are provided in Appendix E. This is a considerable achievement for a first attempt, considering that no material characterization has been done, and that the parts have been produced in a research lab outside of the industrial standards in terms of process control. The twist of the C-spar has not been completely compensated, due to an asymmetry which has not been accounted for in the simulations. A definite answer has not been found as to where this asymmetry comes from. My conviction is that it may be a combination of fiber misalignment and heterogeneous temperature distribution inside the oven. Although the sensitivity of the distortions to these effects has been tested by simulation, it is possible that the asymmetry has not been modeled finely enough, or that other hypotheses of the curing simulation hide the true sensitivity. Interestingly, the initially quadratic shape of the twist has turned into a linear evolution after compensation, while the initial simulations have captured very well the quadratic part of the polynomial and not the linear part.

6.1.3 Homogenization

The homogenization developments in Chapter 3 had for main objective to provide a methodology for the prediction of linear elastic properties of textile composites, while remaining open to more complex non-linear aspects. The desire for the tools to be generic has led to the study of textiles which are coarsely generated in a general-purpose modeling software, in that case TexGen. The geometrical simplifications lead to penetrations, especially when trying to reproduce highly-compacted textiles. Again with the purpose of staying pragmatic and generic, it has been chosen to integrate the penetrations instead of suppressing them.

The contributions of the thesis in this regard have been twofold. Firstly, an unstructured non-conformal meshing procedure suitable to penetrating textiles has been developed. A level-set function has been used to obtain a periodic mesh refined at all material interfaces, i.e. at the yarn-resin interface but also

at the interfaces between the different yarns. This results in a more rational mesh size than with the classical voxel meshes. Consequently, the unstructured approach converges faster than voxels for the prediction of homogenized properties and also localized microscopic fields. The average error over all the elastic properties is about 2.5 times lower with the unstructured mesh compared to the voxel mesh, for a plain-weave textile.

Secondly, a solution has been implemented to compensate locally for the penetrations. After splitting the yarns in small sections, the yarn properties are modified to mimic the compaction of the fibers from the overlapping regions to the remaining yarn volume. This is done at the level of the intra-yarn fiber volume fraction, to make sure that the overall fiber volume inside the yarn is the same in the geometrical model as in the FE simulation. In theory, the procedure is not limited by the amount of penetrations, although a reasonable maximum level of compaction must be chosen to preserve the physical meaning of the method. A sensitivity analysis on a very simple case has showed the high potential of improvement brought by this correction.

While other homogenization methods are faster than the FE method, the flexibility and the accessibility of the latter to the engineers make it a relevant alternative, and the CPU times remain reasonable. The obtained predictions compare very favorably to experimental results drawn from the literature, including three configurations for which the penetration volume fraction is about 10 %. In that case, experimental data were available only for the Young's modulus in the warp direction, which is probably less sensitive to the geometrical approximations than other properties. As a matter of fact, the comparison to a much more sophisticated penetration-free numerical methodology is not as good for Poisson's ratio which are underestimated by 15 to 35 %. No further conclusion is drawn in the absence of experimental data. For textiles without penetrations, the results have shown that using a non-conformal mesh compared to predictions by other authors does not deteriorate the quality of the predictions.

In addition, the homogenization procedure has contributed to the success of the numerical compensation of the curved C-spar without composite material characterization, in Chapter 5.

6.2 Perspectives for future work

6.2.1 Mold compensation

Improvements to the existing work

As a priority, the mirror method should be made more robust when dealing with warpage-dominated structures. Instead of reversing the geometry, one can imagine a cleverly-defined modulation factor of the mirror operation, possibly non-uniformly over the structure. A possible starting point could be to apply a temperature increment to the uncured structure to evaluate its stiffness compared to the nominal geometry. If the behavior of the compensated geometry under a thermal load is significantly different than that of the nominal geometry, it probably means that the norm of the correction must be reduced. The

solution could also stem from the development of an entirely new mesh-based compensation method.

Another constraint is that the mold representation has been restricted to a rigid surface in our simulations. The experience at Cenaero is that this approach has always compared favorably to the experiments. However, we have never measured cure-induced distortions consecutive to manufacturing with a closed-mold process, such as RTM. In that case the thermal expansion of the mold may play a more critical role, which should therefore be accounted for in the simulations. To that end, the mold should be modeled as a volume body. While this is conceivable for CAD-based compensation methods (if one can create a parametrized CAD model of the composite part, a parametrized model of the mold can be set up as well), it requires some thinking and development for mesh-based approaches.

The subjectivity of CAD-based methods is another topic of improvement. The choice of the distortion modes and the choice of the control points has been user-driven until now. Part of the solution could come from modal analyses for the former, and curvature considerations for the latter.

Mold compensation would also benefit from an experimental validation at larger scale and in a more industrialized manufacturing environment. An intermediate step could be to perform another campaign at Cenaero, using an RTM press. This could not be done in the thesis for cost and timing reasons. The ultimate goal is to interact with an industrial partner in order to build compensated prototypes. Research projects are currently ongoing in this regard, and this thesis should provide a sound base for discussion.

Finally, there are probably many other compensation techniques to be found and tried. A method which would require minimal development consists in using a hybridation between CAD-based methods and mesh-based methods, where the optimal compensated shape would be predicted by the latter, and where a parametrized CAD model would be fitted to that shape. This would take advantage of the benefits of CAD-based methods, while drastically reducing the number of curing simulations.

The steps beyond

In my view, the priority long-term research path is to take a turnaround regarding what a "compensated" geometry is. In this thesis I have defined it as the shape which minimizes the distance with respect to a nominal geometry. In fact, the following definition should prevail: the compensated shape is the one which is the easier to assemble (i.e. minimal external force is required), and which respects a certain level of internal stresses after assembling. If there exists a perfect solution in terms of distance reduction (i.e. reduction of the distance to zero), then these two approaches are similar. However, if this perfect optimum is not found (for instance with the CAD-based methods), then the optimal shape in terms of distance is not necessarily the easiest to assemble. A distorted flat plate requires less effort than a distorted L-shaped bracket to return to its nominal position. This axis of research can be investigated by simulating the assembly step after cure, and retrieving the external forces and internal stresses which arise. An even further step could be to simulate

machining and the related release of the internal stresses. An attempt of assembling simulation has been made at the beginning the thesis, with inconclusive results. The major difficulty lies in the transposition of the assembling specifications into FE boundary conditions suitable to geometries which can take any form during the optimization. Ill-defined boundary conditions lead to excessive stress concentrations and do not meet the intended objective.

A second perspective is the inclusion of mold compensation in a robust design framework, which would include for instance the variability of the manufacturing process and probability of failure of the composite structures. The use by Fernlund [168] of Bayesian statistics fed by numerical and experimental data, is an inspiring first step. The reasoning is clear: since any manufacturing process has a certain variability, and since a numerical model has necessarily a few loopholes, it may not be relevant to predict in a deterministic manner the shape of the compensated mold. Instead, one could determine a range of validity corresponding to a certain probability of producing a part within given manufacturing tolerances. Fiber alignment and temperature distribution are among the sources of variability which could be taken into account.

Finally, I think that mold compensation is a perfect candidate for advanced optimization methodologies, for two different aspects. Firstly, the fact that cure-induced distortions of a composite structure may be a linear or non-linear combination of several distortion modes which are not straightforward to determine "by hand", makes compensation a relevant subject for Proper Orthogonal Decomposition. Secondly, since boundary conditions faithful to the manufacturing process are required for an accurate prediction of the distortions, and since these boundary conditions increase drastically the computational time, multi-fidelity optimization (e.g. Co-Kriging) can be considered for the compensation. The principle is to run a lot of fast low-fidelity computations, as well as some slower more accurate ones, to build the response surface within the design space of the optimization.

6.2.2 Homogenization

In the context of homogenization for the prediction of cure-induced distortion, the most interesting perspective is probably to consider the dependency of the properties on the shear angle of the textile. In this thesis, draping simulations have been used to predict the orientation of the fibers. This simulation can also provide the shear angle between the warp and weft yarns. This quantity has not been exploited in the thesis, the warp and weft yarns have been assumed to be perpendicular. However, Pautet [83] showed in a preliminary study that the dependence of the spring-in on the shear angle can reach 0.5° for a shear angle of 20° and 0.2° for a shear angle of 10°. This is far from negligible. The proposed framework for 2D-woven textiles is the following:

- model a given textile in TexGen with various shear angles γ, by steps of 5 or 10 degrees;
- apply the homogenization procedure for each shear angle;
- deduce a mathematical function of γ for each thermo-elastic property;

- launch the mold compensation optimization. In the curing simulation, use the shear angle at every point of the structure (i.e. every element), predicted by the draping simulation, to compute the corresponding material properties.

Another aspect is the use of homogenization in the context of viscoelasticity. As mentioned in Chapter 2, viscoelastic effects may be ignored during curing under various conditions. Brockman et al. [78] suggest that the presence or not of a post-curing step plays an important role in the validity of this assumption. In a student project, Bracquart [80] has developed the tools necessary to homogenize composites accounting for the viscoelastic behavior of the resin. As a proof of concept, this study has been limited to UD composites. The homogenized behavior can then be used in a curing simulation. The major contribution of this work has been the development of a material subroutine allowing anisotropy in viscoelasticity. This work can be extended towards woven textiles, though the computational cost will most probably be prohibitive. This may be the occasion to study other homogenization methods, such as mean-field approaches.

From the pure point of view of homogenization, the extension to non-linear phenomena, which require a more accurate description of the local stress concentrations, may be considered. This is however not an easy task. A first glance at the microscopic stresses in a non-penetrating plain-weave textile (Appendix B) shows that the non-conformal mesh alone (i.e. without using the penetration correction methodology) induces some noise. Ideas for potential improvements are:

- using a progressive transition between the properties of the yarn and of the resin at the interfaces. In a way, this represents the fact that the limit between the impregnated yarns and the matrix is not a clear limit;
- smoothing the stress field a posteriori, although a sound physics-based justification is needed to decide what kind of smoothing should be used;
- decreasing the irregularity of the material interfaces by using anisotropic mesh refinement [141].

Appendices

Appendix A

Periodic boundary conditions for FE homogenization

In this Appendix, the full set of multi-point constraints (MPCs) used in a finite element homogenization procedure is listed [97]. These equations are the periodic boundary conditions (PBCs) which impose that the RVE remains periodic in the three directions of space, meaning that one face is a translation of its opposite face. In the case of a mechanical loading, PBCs also create a mechanical strain within the RVE, in such a way that one component of the volume average of the strain tensor $\bar{\varepsilon}$ is equal to an imposed value μ, while the other components are zero.

Let us consider a RVE centered around the origin and of dimensions $2a_1 \times 2a_2 \times 2a_3$, see Figure A.1. The top face, for instance, is constituted by the nodes whose coordinates are $x \in [-a_1, a_1]$, $y \in [-a_2, a_2]$, and $z = +a_3$. This face is coordinated with the bottom face $x \in [-a_1, a_1]$, $y \in [-a_2, a_2]$, $z = -a_3$.

If $V_i = 2a_i e_i$ is the vector between two opposite faces ($e_i = x$, y or z), then by definition,

$$\bar{G} V_i = u^+ - u^-, \tag{A.1}$$

where $\bar{G}$ is the displacement gradient tensor, and u^+ and u^- are the displacements of two opposite nodes on the two faces (e.g. with coordinates (x, y, a_3) and $(x, y, -a_3)$, respectively). Since $\bar{G}$ is imposed, it can be imposed symmetric, in which case $\bar{\varepsilon} = \bar{G}$. Since $V_i = 2a_i e_i$, $(\bar{\varepsilon} V_i)_j = 2a_i \bar{\varepsilon}_{ji}$ (in other words, $\bar{\varepsilon} V_i$ is proportional to the i-th column of $\bar{\varepsilon}$). Finally, Eq. A.1 becomes:

$$u_j^+ - u_j^- = 2a_i \bar{\varepsilon}_{ji}. \tag{A.2}$$

In the following, Eq. A.2 is applied for all different BVPs, each loading condition corresponding to either a component of the strain tensor or to the determination of the CTE, see Table 3.1. δ_{ij} stands for the Kronecker delta. Since MPCs involve master/slave relationships, each node of the external sur-

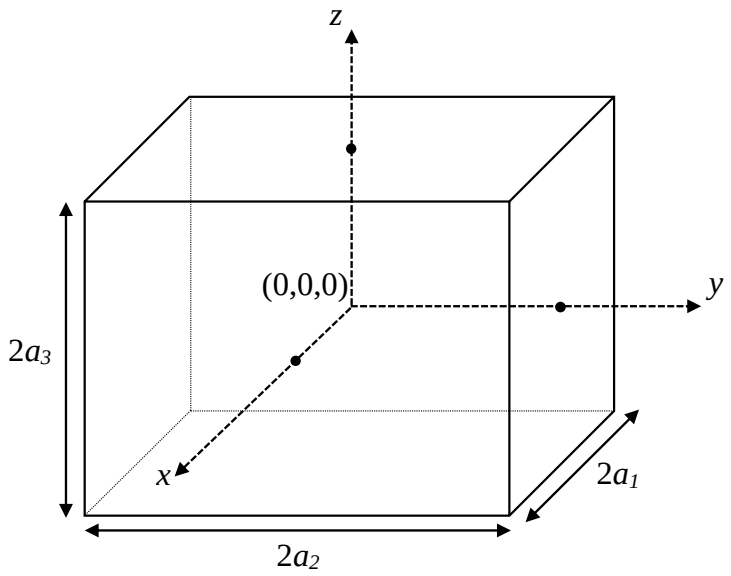


Figure A.1: Position of the RVE in the coordinate system.

face of the RVE must appear only once in the equations. To that end, each set of equations is composed of three subsets:

- the equation linking each pair of faces, without the edges (i.e. for $x \in]-a_1, a_1[$, $y \in]-a_2, a_2[$ and $z \in]-a_3, a_3[$);
- since each edge belongs to two different faces, the edges are treated separately in a second subset of equations by combining the equations of the faces;
- since each corner node belongs to three different edges, they are treated in a third subset by combining the equations of the edges.

To avoid overconstrained nodes, each node appears only once in the MPCs. Indeed, instead of coupling one edge to the three edges which are parallel (e.g. the edge $(x, y) = (-a_1, -a_2)$ with the edges $(x, y) = (-a_1, +a_2)$, $(x, y) = (+a_1, -a_2)$ and $(x, y) = (+a_1, +a_2)$), each edge is coupled to the edge which is the symmetric with respect to the origin (e.g. the edge $(x, y) = (-a_1, +a_2)$ with the edge $(x, y) = (+a_1, -a_2)$, and the edge $(x, y) = (-a_1, -a_2)$ with the edge $(x, y) = (+a_1, +a_2)$). The same remark holds for the corner nodes.

Loading "Traction X"

A macroscopic strain $\bar{\varepsilon}_{xx} = \mu$ (all the other components being equal to zero) is imposed to the RVE by the following set of equations:

$$\begin{cases} u_i(+a_1, y, z) - u_i(-a_1, y, z) = +2a_1\delta_{1i}\mu \\ u_i(x, +a_2, z) - u_i(x, -a_2, z) = 0 \\ u_i(x, y, +a_3) - u_i(x, y, -a_3) = 0 \end{cases} , \tag{A.3a}$$

$$\begin{cases} u_i(+a_1, +a_2, z) - u_i(-a_1, -a_2, z) = +2a_1\delta_{1i}\mu \\ u_i(+a_1, -a_2, z) - u_i(-a_1, +a_2, z) = +2a_1\delta_{1i}\mu \\ u_i(+a_1, y, +a_3) - u_i(-a_1, y, -a_3) = +2a_1\delta_{1i}\mu \\ u_i(+a_1, y, -a_3) - u_i(-a_1, y, +a_3) = +2a_1\delta_{1i}\mu \\ u_i(x, +a_2, +a_3) - u_i(x, -a_2, -a_3) = 0 \\ u_i(x, +a_2, -a_3) - u_i(x, -a_2, +a_3) = 0 \end{cases} , \tag{A.3b}$$

$$\begin{cases} u_i(+a_1, +a_2, +a_3) - u_i(-a_1, -a_2, -a_3) = +2a_1\delta_{1i}\mu \\ u_i(+a_1, +a_2, -a_3) - u_i(-a_1, -a_2, +a_3) = +2a_1\delta_{1i}\mu \\ u_i(-a_1, +a_2, +a_3) - u_i(+a_1, -a_2, -a_3) = -2a_1\delta_{1i}\mu \\ u_i(+a_1, -a_2, +a_3) - u_i(-a_1, +a_2, -a_3) = +2a_1\delta_{1i}\mu \end{cases} . \tag{A.3c}$$

Loading "Traction Y"

A macroscopic strain $\bar{\varepsilon}_{yy} = \mu$ (all the other components being equal to zero) is imposed to the RVE by the following set of equations:

$$\begin{cases} u_i(+a_1, y, z) - u_i(-a_1, y, z) = 0 \\ u_i(x, +a_2, z) - u_i(x, -a_2, z) = 2a_2\delta_{2i}\mu \\ u_i(x, y, +a_3) - u_i(x, y, -a_3) = 0 \end{cases}, \tag{A.4a}$$

$$\begin{cases} u_i(+a_1, +a_2, z) - u_i(-a_1, -a_2, z) = +2a_2\delta_{2i}\mu \\ u_i(+a_1, -a_2, z) - u_i(-a_1, +a_2, z) = -2a_2\delta_{2i}\mu \\ u_i(+a_1, y, +a_3) - u_i(-a_1, y, -a_3) = 0 \\ u_i(+a_1, y, -a_3) - u_i(-a_1, y, +a_3) = 0 \\ u_i(x, +a_2, +a_3) - u_i(x, -a_2, -a_3) = +2a_2\delta_{2i}\mu \\ u_i(x, +a_2, -a_3) - u_i(x, -a_2, +a_3) = +2a_2\delta_{2i}\mu \end{cases}, \tag{A.4b}$$

$$\begin{cases} u_i(+a_1, +a_2, +a_3) - u_i(-a_1, -a_2, -a_3) = +2a_2\delta_{2i}\mu \\ u_i(+a_1, +a_2, -a_3) - u_i(-a_1, -a_2, +a_3) = +2a_2\delta_{2i}\mu \\ u_i(-a_1, +a_2, +a_3) - u_i(+a_1, -a_2, -a_3) = +2a_2\delta_{2i}\mu \\ u_i(+a_1, -a_2, +a_3) - u_i(-a_1, +a_2, -a_3) = -2a_2\delta_{2i}\mu \end{cases}. \tag{A.4c}$$

Loading "Traction Z"

A macroscopic strain $\bar{\varepsilon}_{zz} = \mu$ (all the other components being equal to zero) is imposed to the RVE by the following set of equations:

$$\begin{cases} u_i(+a_1, y, z) - u_i(-a_1, y, z) = 0 \\ u_i(x, +a_2, z) - u_i(x, -a_2, z) = 0 \\ u_i(x, y, +a_3) - u_i(x, y, -a_3) = +2a_3\delta_{3i}\mu \end{cases}, \tag{A.5a}$$

$$\begin{cases} u_i(+a_1, +a_2, z) - u_i(-a_1, -a_2, z) = 0 \\ u_i(+a_1, -a_2, z) - u_i(-a_1, +a_2, z) = 0 \\ u_i(+a_1, y, +a_3) - u_i(-a_1, y, -a_3) = +2a_3\delta_{3i}\mu \\ u_i(+a_1, y, -a_3) - u_i(-a_1, y, +a_3) = -2a_3\delta_{3i}\mu \\ u_i(x, +a_2, +a_3) - u_i(x, -a_2, -a_3) = +2a_3\delta_{3i}\mu \\ u_i(x, +a_2, -a_3) - u_i(x, -a_2, +a_3) = -2a_3\delta_{3i}\mu \end{cases}, \tag{A.5b}$$

$$\begin{cases} u_i(+a_1, +a_2, +a_3) - u_i(-a_1, -a_2, -a_3) = +2a_3\delta_{3i}\mu \\ u_i(+a_1, +a_2, -a_3) - u_i(-a_1, -a_2, +a_3) = -2a_3\delta_{3i}\mu \\ u_i(-a_1, +a_2, +a_3) - u_i(+a_1, -a_2, -a_3) = +2a_3\delta_{3i}\mu \\ u_i(+a_1, -a_2, +a_3) - u_i(-a_1, +a_2, -a_3) = +2a_3\delta_{3i}\mu \end{cases}. \tag{A.5c}$$

Loading "Shear YZ"

A macroscopic strain $\bar{\varepsilon}_{yz} = \bar{\varepsilon}_{zy} = \mu/2$ (all the other components being equal to zero) is imposed to the RVE by the following set of equations:

$$\begin{cases} u_i(+a_1, y, z) - u_i(-a_1, y, z) = 0 \\ u_i(x, +a_2, z) - u_i(x, -a_2, z) = +a_2\delta_{3i}\mu \\ u_i(x, y, +a_3) - u_i(x, y, -a_3) = +a_3\delta_{2i}\mu \end{cases} , \tag{A.6a}$$

$$\begin{cases} u_i(+a_1, +a_2, z) - u_i(-a_1, -a_2, z) = +a_2\delta_{3i}\mu \\ u_i(+a_1, -a_2, z) - u_i(-a_1, +a_2, z) = -a_2\delta_{3i}\mu \\ u_i(+a_1, y, +a_3) - u_i(-a_1, y, -a_3) = +a_3\delta_{2i}\mu \\ u_i(+a_1, y, -a_3) - u_i(-a_1, y, +a_3) = -a_3\delta_{2i}\mu \\ u_i(x, +a_2, +a_3) - u_i(x, -a_2, -a_3) = +a_2\delta_{3i}\mu + a_3\delta_{2i}\mu \\ u_i(x, +a_2, -a_3) - u_i(x, -a_2, +a_3) = +a_2\delta_{3i}\mu - a_3\delta_{2i}\mu \end{cases} , \tag{A.6b}$$

$$\begin{cases} u_i(+a_1, +a_2, +a_3) - u_i(-a_1, -a_2, -a_3) = +a_2\delta_{3i}\mu + a_3\delta_{2i}\mu \\ u_i(+a_1, +a_2, -a_3) - u_i(-a_1, -a_2, +a_3) = +a_2\delta_{3i}\mu - a_3\delta_{2i}\mu \\ u_i(-a_1, +a_2, +a_3) - u_i(+a_1, -a_2, -a_3) = +a_2\delta_{3i}\mu + a_3\delta_{2i}\mu \\ u_i(+a_1, -a_2, +a_3) - u_i(-a_1, +a_2, -a_3) = -a_2\delta_{3i}\mu + a_3\delta_{2i}\mu \end{cases} . \tag{A.6c}$$

Loading "Shear XZ"

A macroscopic strain $\bar{\varepsilon}_{xz} = \bar{\varepsilon}_{zx} = \mu/2$ (all the other components being equal to zero) is imposed to the RVE by the following set of equations:

$$\begin{cases} u_i(+a_1, y, z) - u_i(-a_1, y, z) = +a_1\delta_{3i} \\ u_i(x, +a_2, z) - u_i(x, -a_2, z) = 0 \\ u_i(x, y, +a_3) - u_i(x, y, -a_3) = +a_3\delta_{1i} \end{cases}, \tag{A.7a}$$

$$\begin{cases} u_i(+a_1, +a_2, z) - u_i(-a_1, -a_2, z) = +a_1\delta_{3i}\mu \\ u_i(+a_1, -a_2, z) - u_i(-a_1, +a_2, z) = +a_1\delta_{3i}\mu \\ u_i(+a_1, y, +a_3) - u_i(-a_1, y, -a_3) = +a_1\delta_{3i}\mu + a_3\delta_{1i}\mu \\ u_i(+a_1, y, -a_3) - u_i(-a_1, y, +a_3) = +a_1\delta_{3i}\mu - a_3\delta_{1i}\mu \\ u_i(x, +a_2, +a_3) - u_i(x, -a_2, -a_3) = +a_3\delta_{1i}\mu \\ u_i(x, +a_2, -a_3) - u_i(x, -a_2, +a_3) = -a_3\delta_{1i}\mu \end{cases}, \tag{A.7b}$$

$$\begin{cases} u_i(+a_1, +a_2, +a_3) - u_i(-a_1, -a_2, -a_3) = +a_1\delta_{3i}\mu + a_3\delta_{1i}\mu \\ u_i(+a_1, +a_2, -a_3) - u_i(-a_1, -a_2, +a_3) = +a_1\delta_{3i}\mu - a_3\delta_{1i}\mu \\ u_i(-a_1, +a_2, +a_3) - u_i(+a_1, -a_2, -a_3) = -a_1\delta_{3i}\mu + a_3\delta_{1i}\mu \\ u_i(+a_1, -a_2, +a_3) - u_i(-a_1, +a_2, -a_3) = +a_1\delta_{3i}\mu + a_3\delta_{1i}\mu \end{cases}. \tag{A.7c}$$

Loading "Shear XY"

A macroscopic strain $\bar{\varepsilon}_{xy} = \bar{\varepsilon}_{yx} = \mu/2$ (all the other components being equal to zero) is imposed to the RVE by the following set of equations:

$$\begin{cases} u_i(+a_1, y, z) - u_i(-a_1, y, z) = +a_1\delta_{2i}\mu \\ u_i(x, +a_2, z) - u_i(x, -a_2, z) = +a_2\delta_{1i}\mu \\ u_i(x, y, +a_3) - u_i(x, y, -a_3) = 0 \end{cases} , \tag{A.8a}$$

$$\begin{cases} u_i(+a_1, +a_2, z) - u_i(-a_1, -a_2, z) = +a_1\delta_{2i}\mu + a_2\delta_{1i}\mu \\ u_i(+a_1, -a_2, z) - u_i(-a_1, +a_2, z) = +a_1\delta_{2i}\mu - a_2\delta_{1i}\mu \\ u_i(+a_1, y, +a_3) - u_i(-a_1, y, -a_3) = +a_1\delta_{2i}\mu \\ u_i(+a_1, y, -a_3) - u_i(-a_1, y, +a_3) = +a_1\delta_{2i}\mu \\ u_i(x, +a_2, +a_3) - u_i(x, -a_2, -a_3) = +a_2\delta_{1i}\mu \\ u_i(x, +a_2, -a_3) - u_i(x, -a_2, +a_3) = +a_2\delta_{1i}\mu \end{cases} , \tag{A.8b}$$

$$\begin{cases} u_i(+a_1, +a_2, +a_3) - u_i(-a_1, -a_2, -a_3) = +a_1\delta_{2i}\mu + a_2\delta_{1i}\mu \\ u_i(+a_1, +a_2, -a_3) - u_i(-a_1, -a_2, +a_3) = +a_1\delta_{2i}\mu + a_2\delta_{1i}\mu \\ u_i(-a_1, +a_2, +a_3) - u_i(+a_1, -a_2, -a_3) = -a_1\delta_{2i}\mu + a_2\delta_{1i}\mu \\ u_i(+a_1, -a_2, +a_3) - u_i(-a_1, +a_2, -a_3) = +a_1\delta_{2i}\mu - a_2\delta_{1i}\mu \end{cases} . \tag{A.8c}$$

Loading "Thermal"

The thermal loading does not consist in applying a mechanical strain through multi-point constraints. The loading is an increment of temperature. The multi-point constraints only ensure that opposite faces remain periodic. This is achieved by the following equations, where U^1, U^2 and U^3 are dummy nodes disconnected from the structure, and U_i^k their degrees of freedom ($i = 1 \dots 3$).

$$\begin{cases} u_i(+a_1, y, z) - u_i(-a_1, y, z) = U_i^1 \\ u_i(x, +a_2, z) - u_i(x, -a_2, z) = U_i^2 \\ u_i(x, y, +a_3) - u_i(x, y, -a_3) = U_i^3 \end{cases}, \tag{A.9a}$$

$$\begin{cases} u_i(+a_1, +a_2, z) - u_i(-a_1, -a_2, z) = U_i^1 + U_i^2 \\ u_i(+a_1, -a_2, z) - u_i(-a_1, +a_2, z) = U_i^1 + U_i^2 \\ u_i(+a_1, y, +a_3) - u_i(-a_1, y, -a_3) = U_i^1 + U_i^3 \\ u_i(+a_1, y, -a_3) - u_i(-a_1, y, +a_3) = U_i^1 + U_i^3 \\ u_i(x, +a_2, +a_3) - u_i(x, -a_2, -a_3) = U_i^2 + U_i^3 \\ u_i(x, +a_2, -a_3) - u_i(x, -a_2, +a_3) = U_i^2 + U_i^3 \end{cases}, \tag{A.9b}$$

$$\begin{cases} u_i(+a_1, +a_2, +a_3) - u_i(-a_1, -a_2, -a_3) = U_i^1 + U_i^2 + U_i^3 \\ u_i(+a_1, +a_2, -a_3) - u_i(-a_1, -a_2, +a_3) = U_i^1 + U_i^2 - U_i^3 \\ u_i(-a_1, +a_2, +a_3) - u_i(+a_1, -a_2, -a_3) = -U_i^1 + U_i^2 + U_i^3 \\ u_i(+a_1, -a_2, +a_3) - u_i(-a_1, +a_2, -a_3) = U_i^1 - U_i^2 + U_i^3 \end{cases}. \tag{A.9c}$$

Appendix B

Detailed comparison unstructured/voxel meshing

In this section, selected results are provided regarding the comparison between the voxel and the unstructured approaches, applied to the penetration-free plain-weave textile studied in Section 3.4.3. All meshes have similar number of nodes, approximately 330,000.

Visual comparison of microscopic stress fields

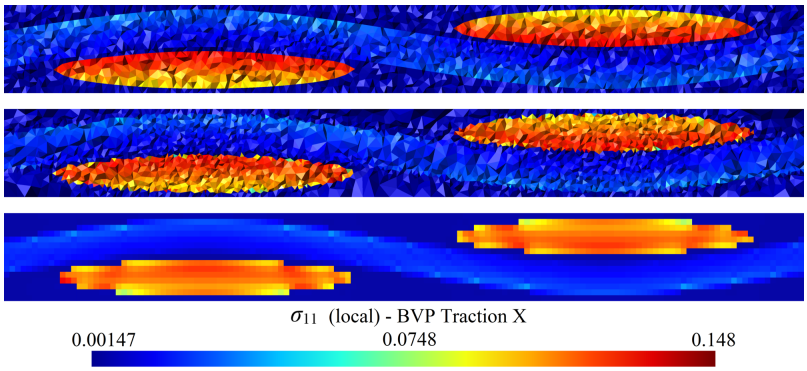


Figure B.1: Transverse view of the local longitudinal stress field (σ_{11}) for a yarn under longitudinal tension. From top to bottom: conformal mesh, unstructured, voxels.

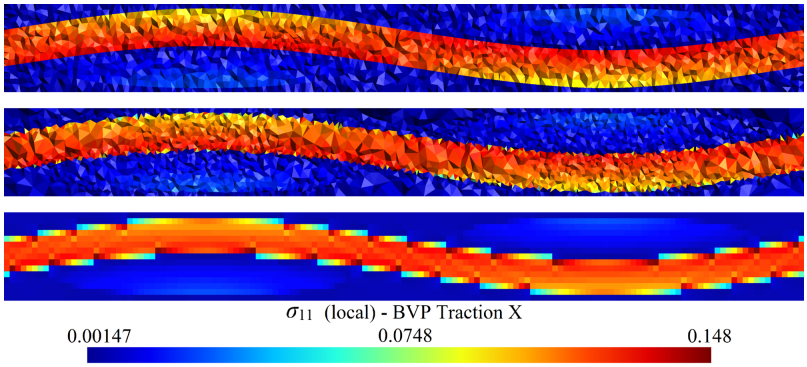


Figure B.2: Longitudinal view of the local longitudinal stress field (σ_{11}) for a yarn under longitudinal tension. From top to bottom: conformal mesh, unstructured, voxels.

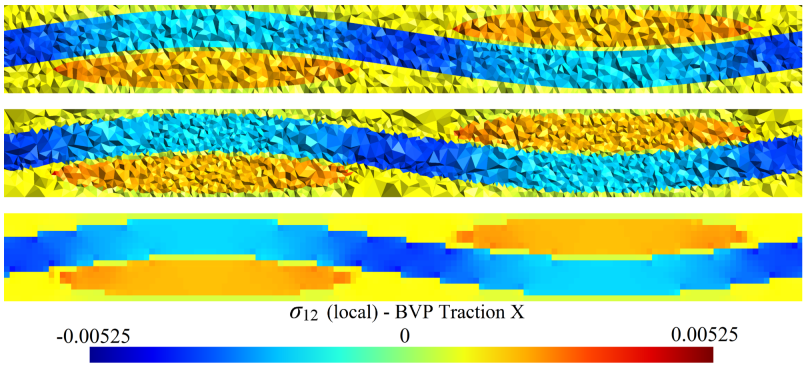


Figure B.3: Local shear stress field (σ_{12}) for a yarn under in-plane shear. From top to bottom: conformal mesh, unstructured, voxels.

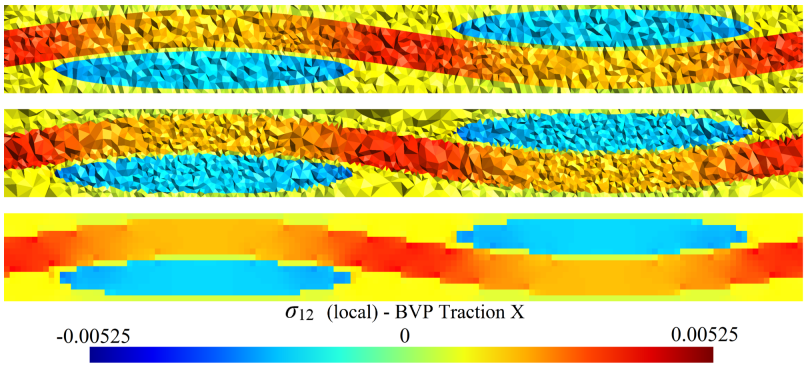


Figure B.4: Local shear stress field (σ_{12}) for a yarn under in-plane shear (other section plane). From top to bottom: conformal mesh, unstructured, voxels.

Microscopic fields distribution along a line

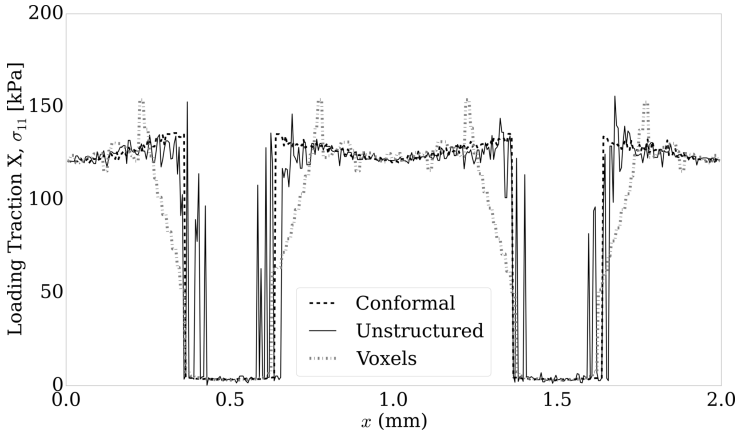


Figure B.5: σ_{11} along a line for macroscopic Traction X.

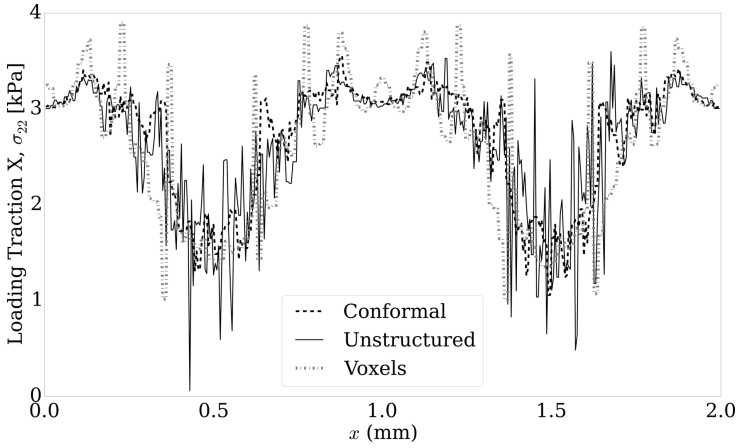


Figure B.6: σ_{22} along a line for macroscopic Traction X.

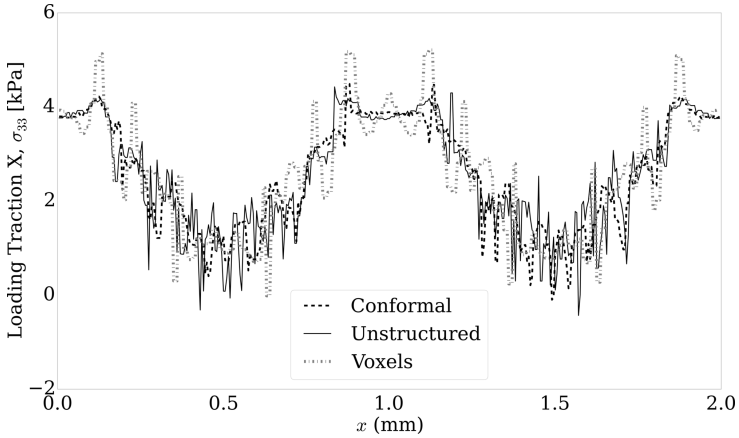


Figure B.7: σ_{33} along a line for macroscopic Traction X.

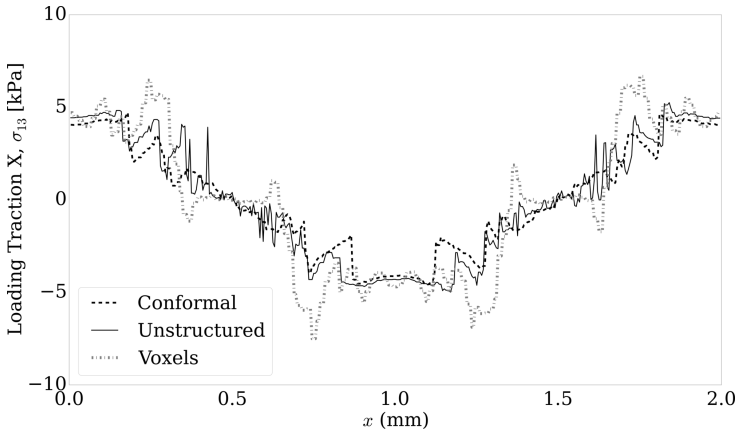


Figure B.8: σ_{23} along a line for macroscopic Traction X.

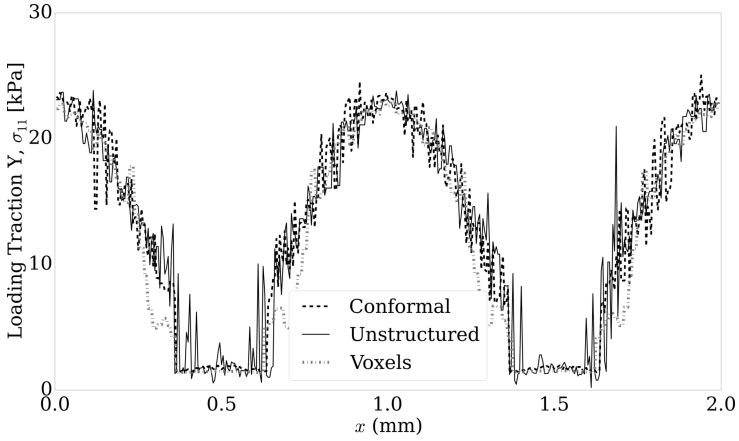


Figure B.9: σ_{11} along a line for macroscopic Traction Y.

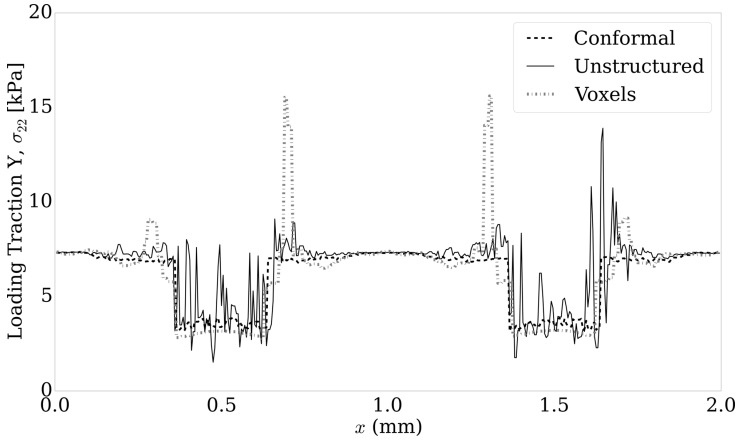


Figure B.10: σ_{22} along a line for macroscopic Traction Y.

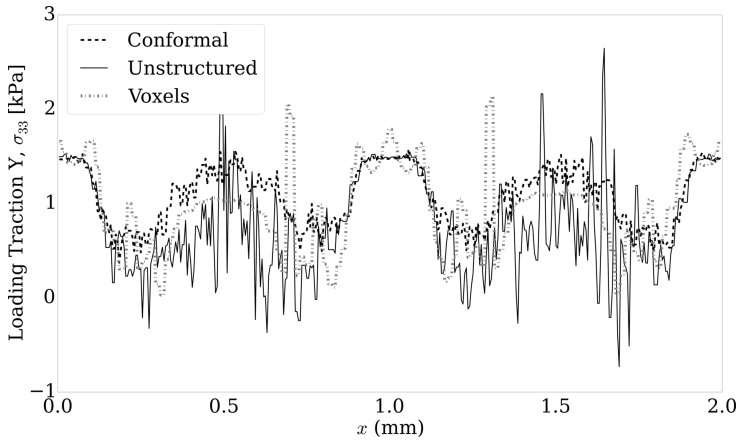


Figure B.11: σ_{33} along a line for macroscopic Traction Y.

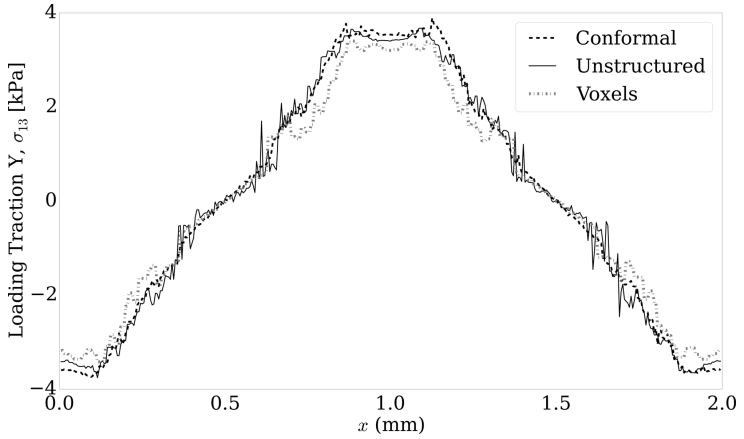


Figure B.12: σ_{23} along a line for macroscopic Traction Y.

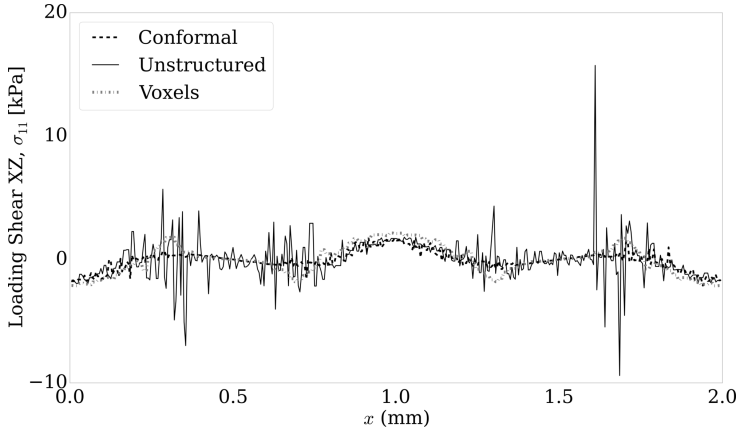


Figure B.13: σ_{11} along a line for macroscopic Shear XZ.

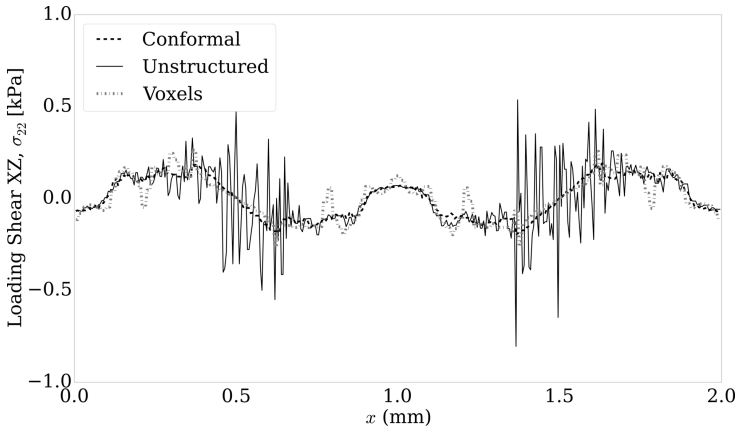


Figure B.14: σ_{22} along a line for macroscopic Shear XZ.

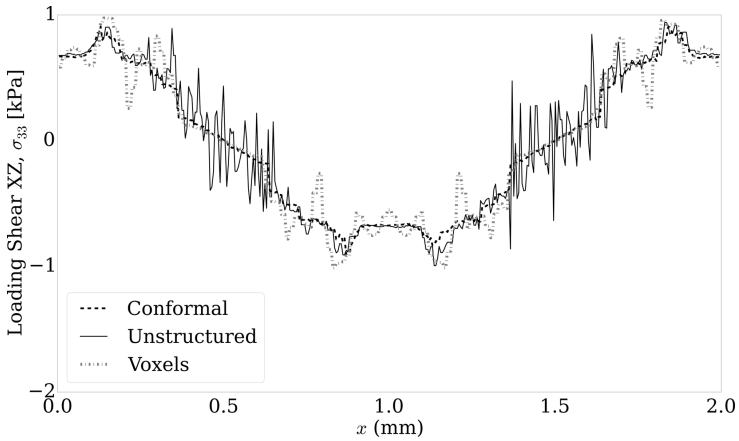


Figure B.15: σ_{33} along a line for macroscopic Shear XZ.

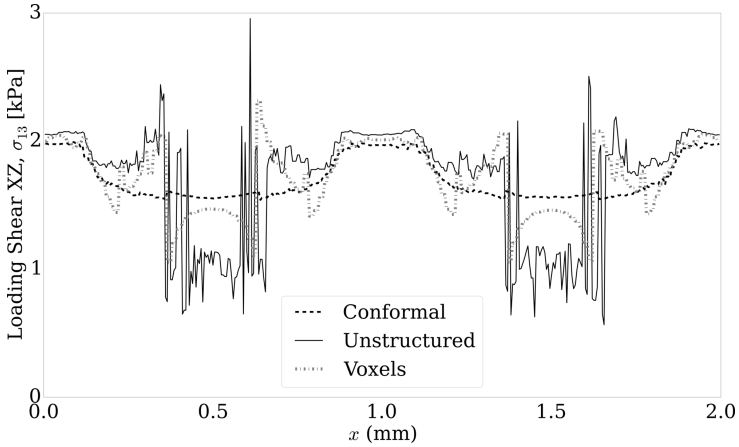


Figure B.16: σ_{23} along a line for macroscopic Shear XZ.

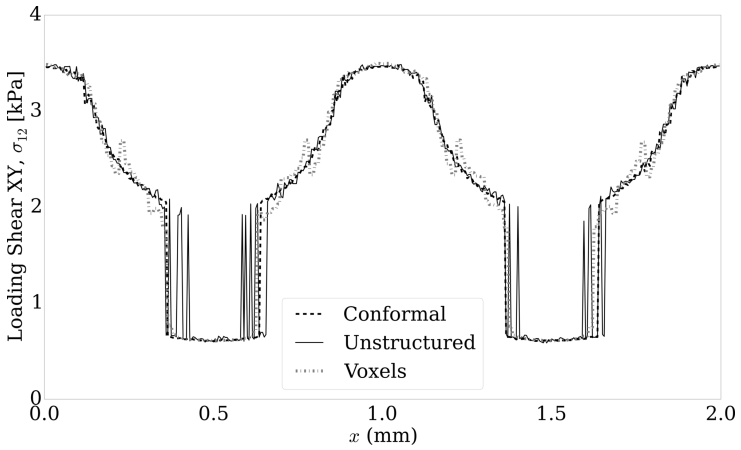


Figure B.17: σ_{12} along a line for macroscopic Shear XY.

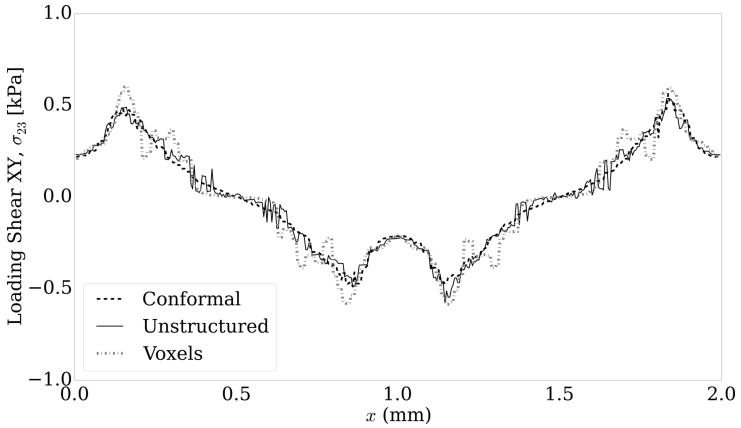


Figure B.18: σ_{23} along a line for macroscopic Shear XY.

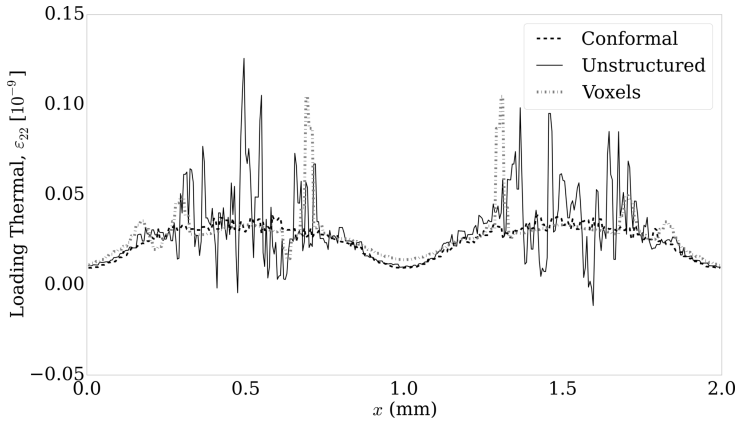


Figure B.19: ε_{22} along a line for macroscopic Thermal.

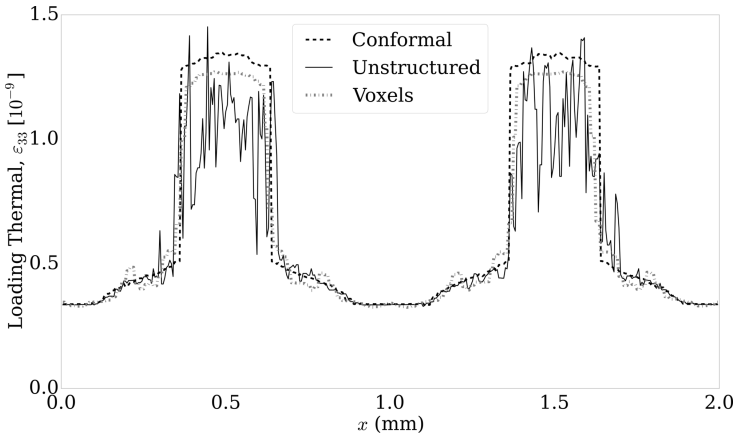


Figure B.20: ε_{33} along a line for macroscopic Thermal.

Cumulative distributions of microscopic fields

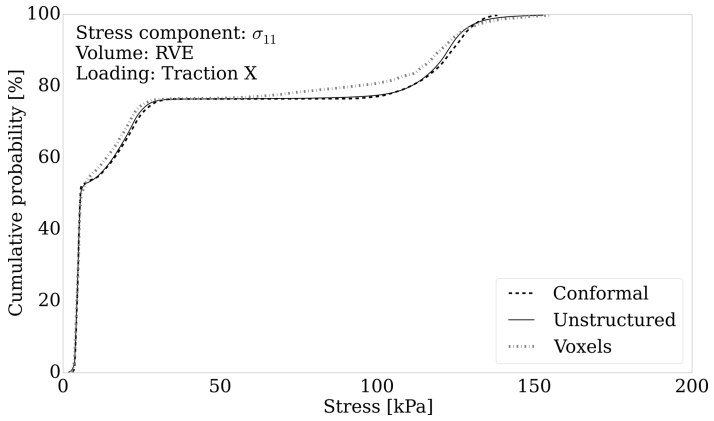


Figure B.21: Cumulative distribution of σ_{11} (RVE, Traction X).

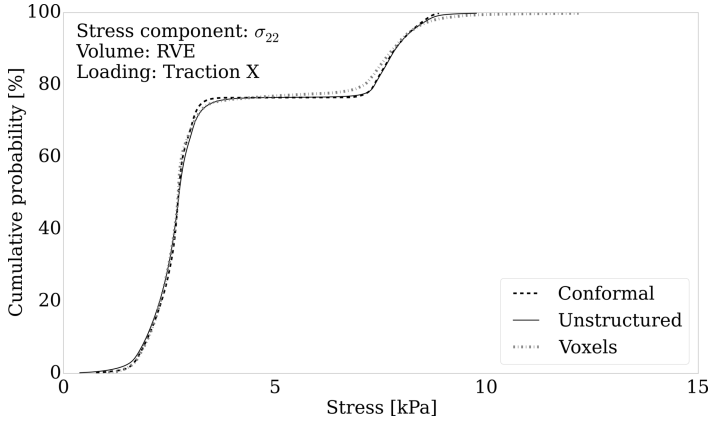


Figure B.22: Cumulative distribution of σ_{22} (RVE, Traction X).

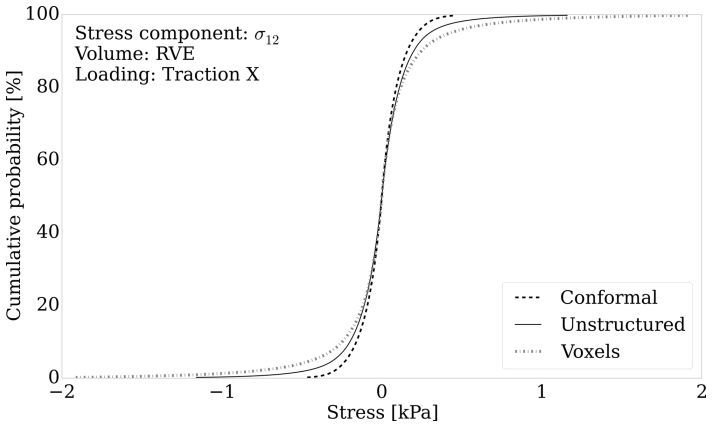


Figure B.23: Cumulative distribution of σ_{12} (RVE, Traction X).

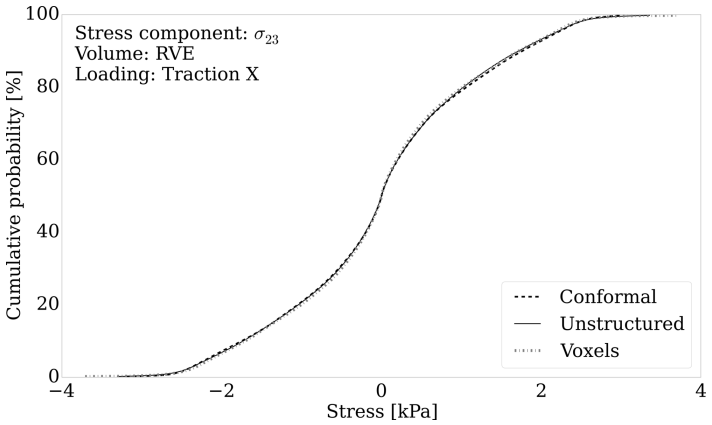


Figure B.24: Cumulative distribution of σ_{23} (RVE, Traction X).

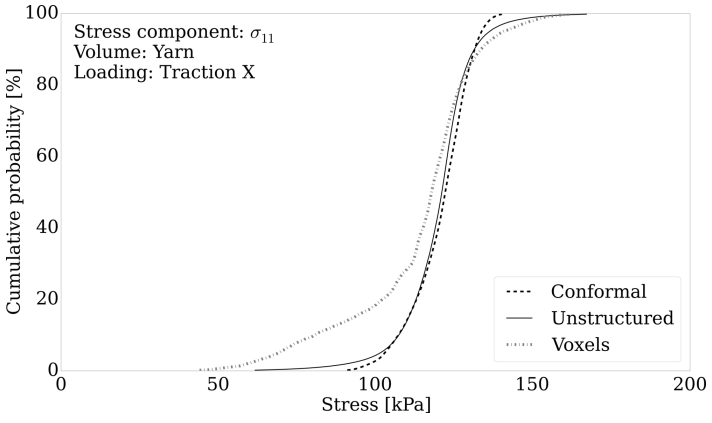


Figure B.25: Cumulative distribution of σ_{11} (yarn, Traction X).

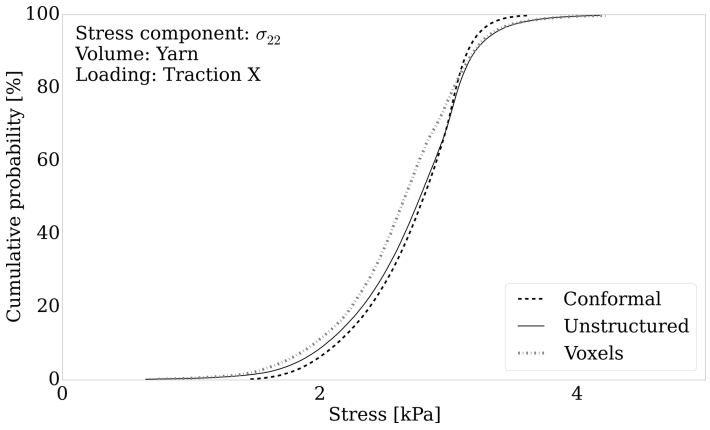


Figure B.26: Cumulative distribution of σ_{22} (yarn, Traction X).

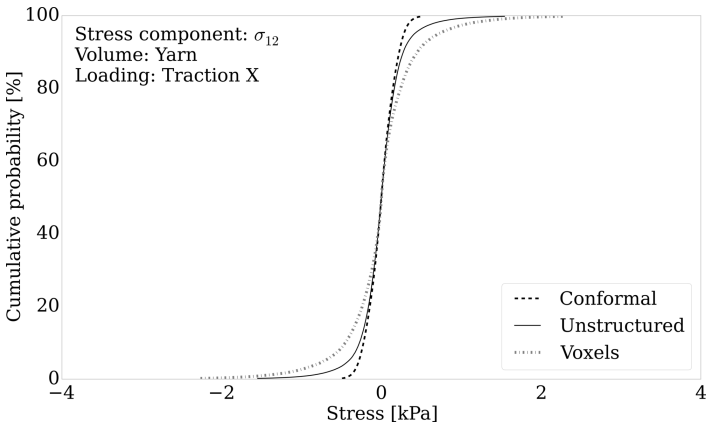


Figure B.27: Cumulative distribution of σ_{12} (yarn, Traction X).

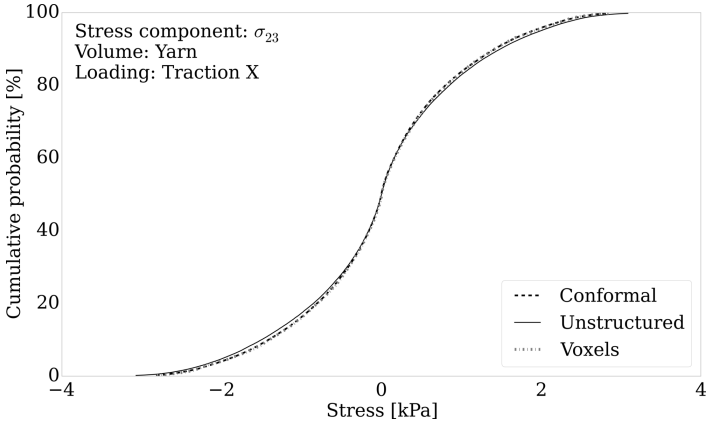


Figure B.28: Cumulative distribution of σ_{23} (yarn, Traction X).

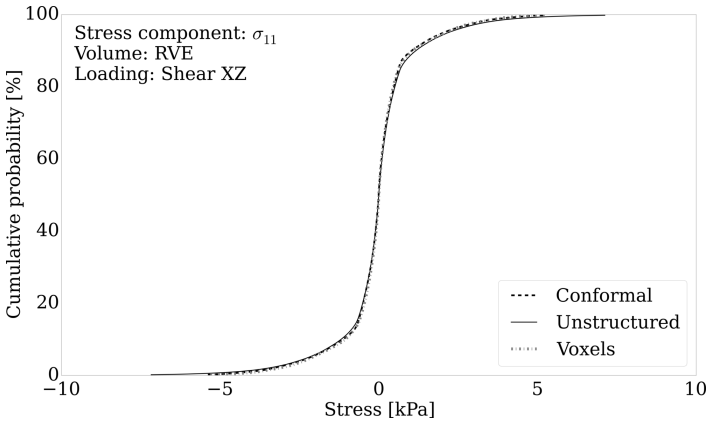


Figure B.29: Cumulative distribution of σ_{11} (RVE, Shear XZ).

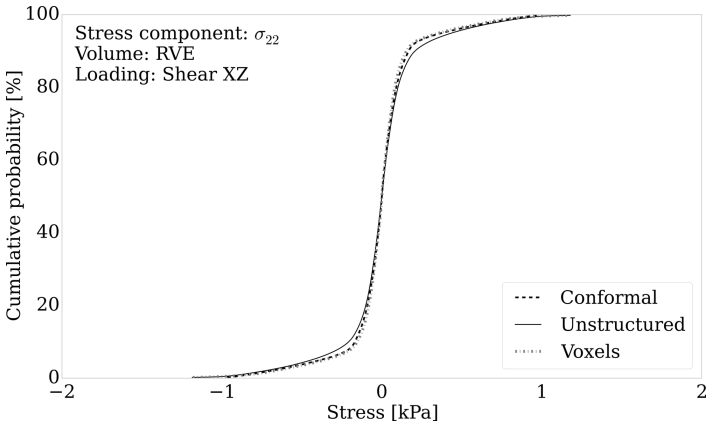


Figure B.30: Cumulative distribution of σ_{22} (RVE, Shear XZ).

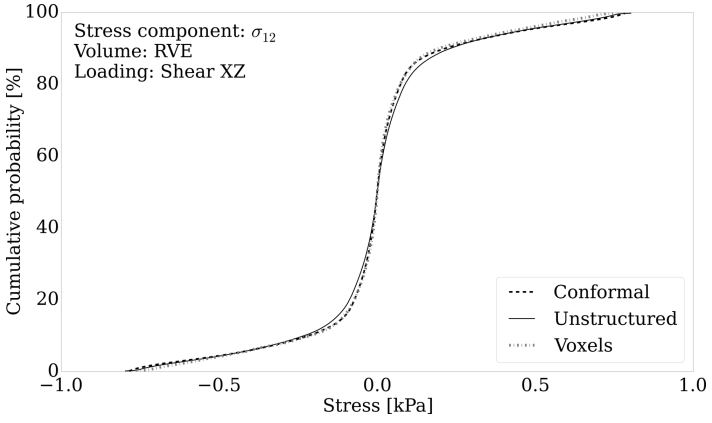


Figure B.31: Cumulative distribution of σ_{12} (RVE, Shear XZ).

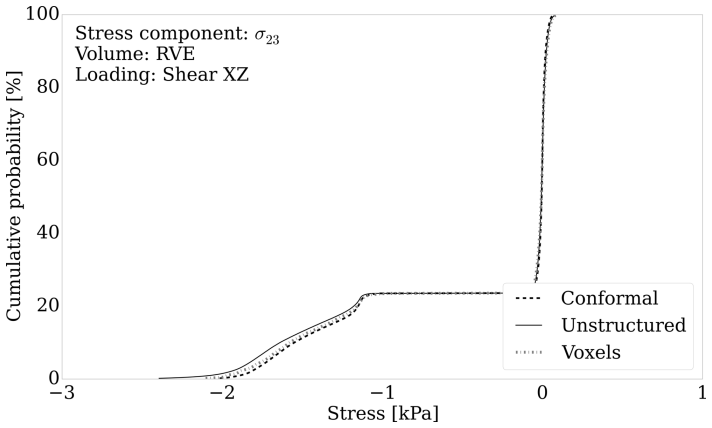


Figure B.32: Cumulative distribution of σ_{23} (RVE, Shear XZ).

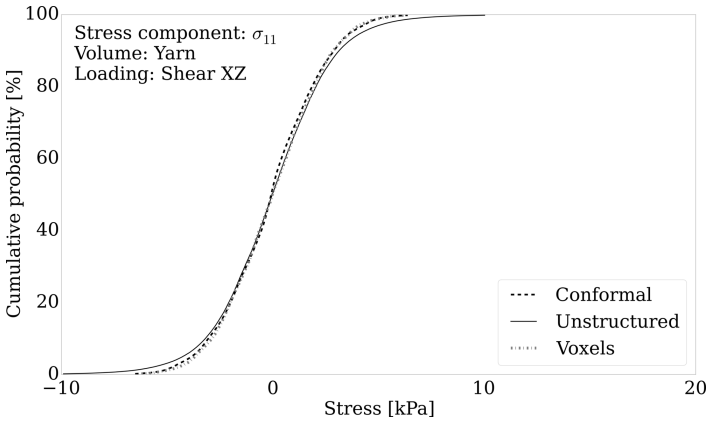


Figure B.33: Cumulative distribution of σ_{11} (yarn, Shear XZ).

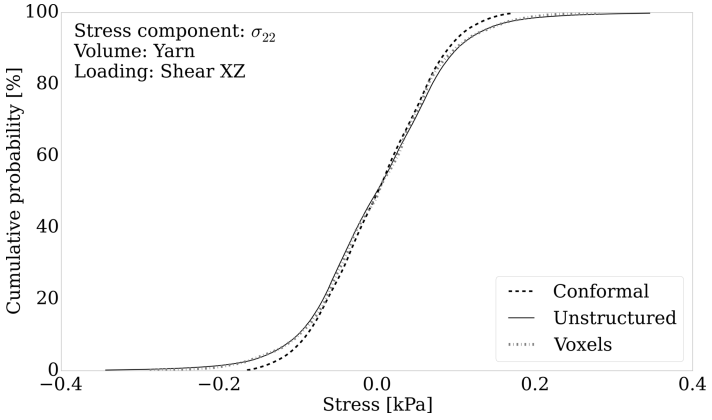


Figure B.34: Cumulative distribution of σ_{22} (yarn, Shear XZ).

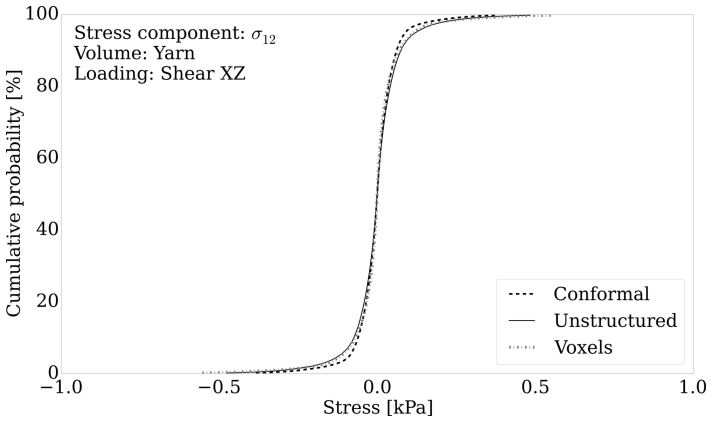


Figure B.35: Cumulative distribution of σ_{12} (yarn, Shear XZ).

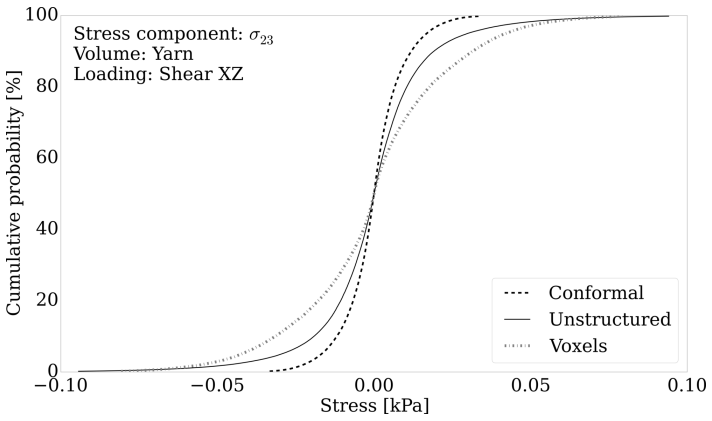


Figure B.36: Cumulative distribution of σ_{23} (yarn, Shear XZ).

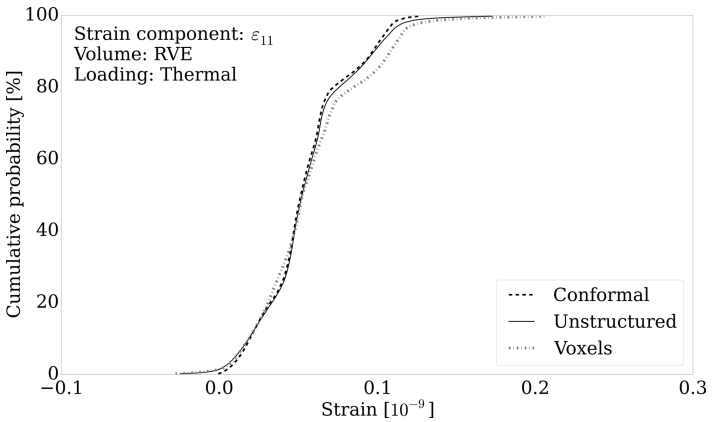


Figure B.37: Cumulative distribution of ε_{11} (RVE, Thermal).

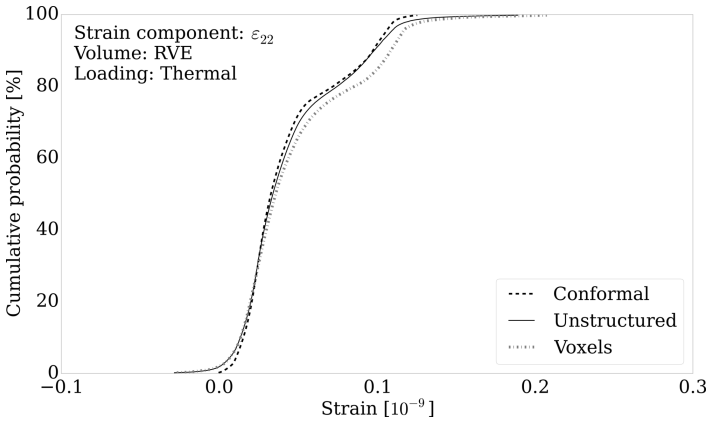


Figure B.38: Cumulative distribution of ε_{22} (RVE, Thermal).

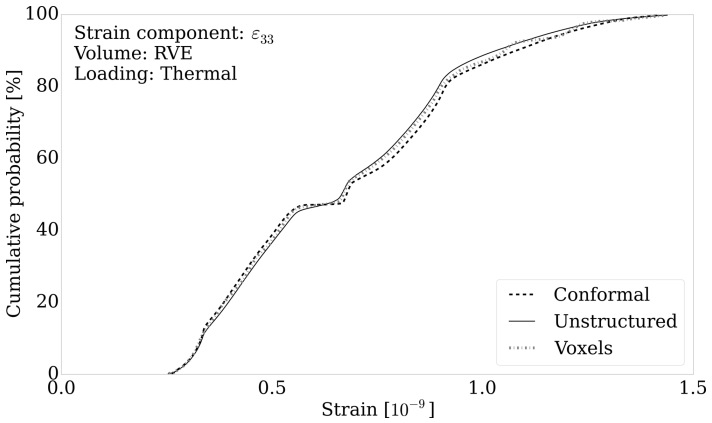


Figure B.39: Cumulative distribution of ε_{33} (RVE, Thermal).

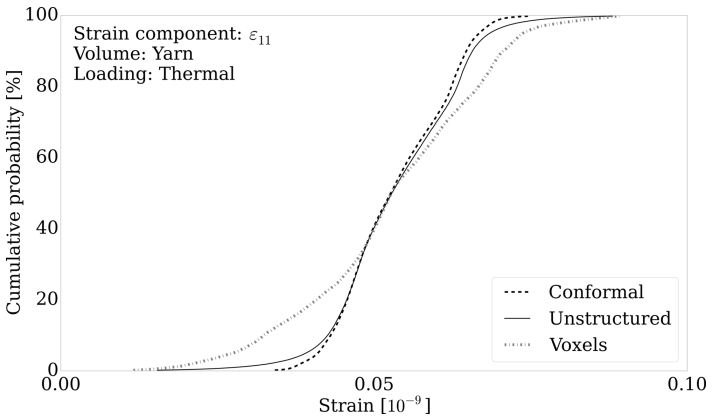


Figure B.40: Cumulative distribution of ε_{11} (yarn, Thermal).

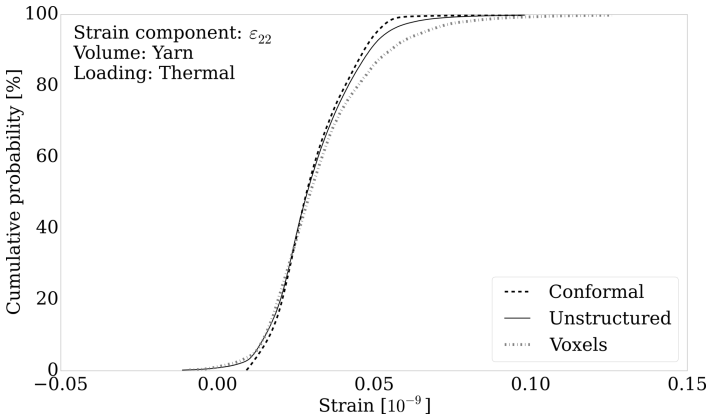


Figure B.41: Cumulative distribution of ε_{22} (yarn, Thermal).

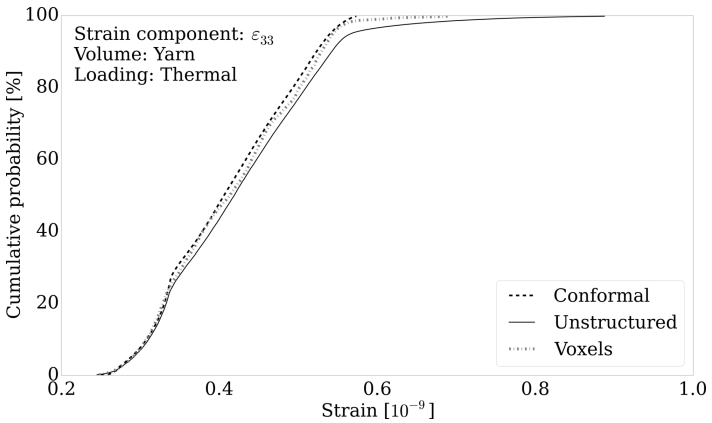


Figure B.42: Cumulative distribution of ε_{33} (yarn, Thermal).

Appendix C

Textile geometrical description

Tables C.1 to C.3 give all details necessary to reproduce in TexGen the test cases studied in Section 3.6. All the values inside the tables are derived, directly or indirectly, from the referenced papers, except:

- For cases 4 to 6 (Table C.3), the total thickness of the composite is adjusted to be as large as the total thickness of the warp and weft yarns, plus an additional margin for the vertical yarn. This margin is smaller than the thickness of the vertical yarn, which leads to part of the yarn being out of the RVE. This is by essence mitigated by the homogenization procedure which adapts the intra-yarn fiber volume fraction, since the geometrical volume declared by TexGen is larger than the final meshed volume.
- The intra-yarn fiber volume fraction is derived from the yarn volumes in TexGen and the target total fiber volume fraction, as well as the fiber distribution in the different directions of the composite. In particular, the intra-yarn fiber volume fractions for Case 6 have been determined by scaling yarn-per-yarn values given in [157] in order to achieve the target total value.

The properties of the vinyl ester resin Dow Derakane 8084 are not identical in Tables C.2 and C.3. They are chosen consistently with the respective reference papers.

	Case 1 Textile S	Case 1 Textile B	Case 1 Textile D
RVE dimensions $X \times Y \times Z$ [mm^3] [147]	17.72 $\times$ 2.12 $\times$ 2.12	11.74 $\times$ 2.18 $\times$ 2.18	7.47 $\times$ 2.33 $\times$ 2.33
Warp yarns cross-section [mm^2]	Elliptical (1.57 $\times$ 0.71)	Elliptical (1.63 $\times$ 0.66)	Elliptical (1.68 $\times$ 0.58)
Weft yarns cross-section [mm^2]	Elliptical (2.94 $\times$ 0.19)	Elliptical (2.73 $\times$ 0.20)	Elliptical (2.01 $\times$ 0.24)
Vertical yarns cross-section [mm^2]	Elliptical (2.94 $\times$ 0.19)	Elliptical (2.73 $\times$ 0.20)	Elliptical (2.01 $\times$ 0.24)
Warp yarns mid-line	Helicoidal, ampl. 0.44 mm	Helicoidal, ampl. 0.42 mm	Helicoidal, ampl. 0.40 mm
Weft/vertical yarns mid-line	Sinusoidal, ampl. 0.0095 mm	Sinusoidal, ampl. 0.0098 mm	Sinusoidal, ampl. 0.0105 mm
Yarn volume fraction [147]	83 %	81 %	74 %
Intra-yarn fiber volume fraction k_f [147]	54 %	54 %	57 %
Total fiber volume fraction	45 %	44 %	42 %
Penetration volume fraction	10.5 %	9.7 %	7.7 %
Resin properties	Reichhold Dion 9500 [147] $E = 3.1$ GPa $\nu = 0.35$		
Fiber properties	T700 carbon fibers [147] $E_L = 230$ GPa, $E_T = 14$ GPa $\nu_{LT} = 0.2$, $\nu_{TT} = 0.25$ $G_{LT} = 9$ GPa, $G_{TT} = 4.8$ GPa		
Yarn properties	Micromechanics (Eq. 3.10)		

Table C.1: Geometrical details and materials used for Case 1 (Stig and Hallström [147])

	Case 2	Case 3
RVE dimensions $X \times Y \times Z$ [mm^3]	6.64 × 5.03 × 2.7632	5.44 × 1.57 × 2.79
Warp yarns cross-section [mm^2]	Rectangular (4.12 × 0.637)	Rectangular (0.90 × 0.19)
Weft yarns cross-section [mm^2]	Rectangular (1.514 × 0.292)	Rectangular (0.96 × 0.22)
Vertical yarns cross-section [mm^2]	Rectangular (0.910 × 0.292)	Elliptical (0.67 × 0.32)
Yarns mid-line	Piecewise linear	
Yarn volume fraction	69.8 %	57.1 %
Intra-yarn fiber volume fraction k_f	70.2 %	Warp: 92.0 % Weft: 70.2 % Vertical: 51.0 %
Total fiber volume fraction	49 %	43 %
Fiber volume distribution	Warp: 50.8 % Weft: 45.6 % Vertical: 3.6 %	Warp: 41.7 % Weft: 50 % Vertical: 8.3 %
Penetration volume fraction	0.03 %	0.001 %
Resin properties	Dow Derakane 8084 [150] $E = 3.53$ GPa $\nu = 0.35$	Epicote 828 [153] $E = 2.2$ GPa $\nu = 0.35$
Fiber properties	S-2 glass fibers [150] $E = 86.9$ GPa $\nu = 0.22$	T300 carbon fibers [153] $E_L = 220$ GPa $E_T = 13.8$ GPa $\nu_{LT} = 0.2$ $\nu_{TT} = 0.25$ $G_{LT} = 11.35$ GPa
Yarn properties	From [150]	Micromechanics (Eq. 3.10)

Table C.2: Geometrical details and materials used for Cases 2 (Bogdanovich [150]) and 3 (Tan et al. [153])

	Case 4	Case 5	Case 6
RVE dimensions $X \times Y \times Z$ [mm^3]	7.46 × 7.34 × 3.10	7.38 × 7.42 × 2.90	5.10 × 4.16 × 3.10
Warp yarns cross-section [mm^2]	Rectangular L1&3: 3.29 × 0.42 L2: 3.23 × 0.22	Rectangular (3.26 × 0.47)	Rectangular L1&3: 1.83 × 0.39 L2: 1.83 × 0.37
Weft yarns cross-section [mm^2]	Rectangular L1&4: 2.90 × 0.41 L2&3: 3.16 × 0.32	Rectangular L1&3: 2.68 × 0.43 L2: 2.72 × 0.34	Rectangular L1: 2.14 × 0.39 L2&3: 2.14 × 0.32 L4: 2.14 × 0.37
Vertical yarns cross-section [mm^2]	Rectangular (0.57 × 0.38)	Rectangular (0.67 × 0.45)	Rectangular (0.41 × 0.25)
Yarns mid-line	Piecewise linear		
Yarn volume fraction	71.7 %	63.3 %	73.6 %
Intra-yarn fiber volume fraction k_f	Warp: 79.2 % Weft: 63.2 % Vertical: 24.5 %	Warp: 79.8 % Weft: 75.6 % Vertical: 45.5 %	Warp L1: 76.2 % Warp L2: 66.8 % Warp L3: 74.1 % Weft L1: 71.1 Weft L2: 64.8 Weft L3: 65.8 Weft L4: 74.3 % Vertical: 40.3 %
Total fiber volume fraction	48.9 %	47.5 %	51.1 %
Fiber volume distribution	Warp: 49.3 % Weft: 49.0 % Vertical: 1.7 %	Warp: 47.6 % Weft: 47.8 % Vertical: 4.6 %	Warp: 46.12 % Weft: 51.24 % Vertical: 2.64 %
Penetration volume fraction	0 %	0 %	0 %
Resin properties	Dow Derakane 8084 [155] $E = 2.9$ GPa $\nu = 0.23$		West System 105+209 [197] $E = 2.74$ GPa $\nu = 0.35$
Fiber properties	E-glass fibers [100] $E = 73.1$ GPa $\nu = 0.22$		Toho Tenax carbon fibers [197] $E_L = 239$ GPa $E_T = 14$ GPa $\nu_{LT} = 0.23$ $\nu_{TT} = 0.15$ $G_{LT} = 8$ GPa
Yarn properties	Micromechanics (Eq. 3.10)		

Table C.3: Geometrical details and materials used for Cases 4-5 (Lomov et al. [154]) and Case 6 (Bogdanovich et al. [156]). L1 to L4 designate the number of the layer within the composite (the layers are numbered from top to bottom)

Appendix D

Best-fit algorithm

This section describes an in-house algorithm, implemented in the frame of this thesis, designed to perform a best-fit alignment of a set of points onto another set of points. Both sets must contain the same number of points N. The objective is to find the optimal rigid body motion λ that minimizes the residual distance between the two sets of points, the reference and the deformed sets of points. λ is composed of three rotations and three translations:

$$\lambda = \{\alpha, \beta, \gamma, d, e, f\}^T \tag{D.1}$$

where d, e, f are translation degrees of freedom with respect to the X, Y and Z axis, respectively, and α, β, γ are rotation degrees of freedom about the X, Y and Z axis, respectively. Let us consider a point $P_i = \{x_i, y_i, z_i\}^T$ of the deformed set of points. Its position in the reference set of points is $P_i^0 = \{x_i^0, y_i^0, z_i^0\}^T$. The rigid body motion λ applied to point P_i gives a rotated point P_i^r:

$$P_i^r(\lambda) = R_z(\gamma)R_y(\beta)R_x(\alpha)P_i + \begin{Bmatrix} d \\ e \\ f \end{Bmatrix}, \tag{D.2}$$

where R_a is the rotation matrix about axis a. If the letters "c" and "s" denote the cosinus and sinus of an angle, respectively, these matrices are given by:

$$R_x(\alpha) = \begin{bmatrix} 1 & 0 & 0 \\ 0 & c\alpha & -s\alpha \\ 0 & s\alpha & c\alpha \end{bmatrix}, \tag{D.3a}$$

$$R_y(\beta) = \begin{bmatrix} c\beta & 0 & s\beta \\ 0 & 1 & 0 \\ -s\beta & 0 & c\beta \end{bmatrix}, \tag{D.3b}$$

$$R_z(\gamma) = \begin{bmatrix} c\gamma & -s\gamma & 0 \\ s\gamma & c\gamma & 0 \\ 0 & 0 & 1 \end{bmatrix}. \tag{D.3c}$$

After calculations and by posing $P_i^r = \{A_i, B_i, C_i\}^T$,

$$P_i^r(\lambda) = \begin{Bmatrix} A_i(\lambda) \\ B_i(\lambda) \\ C_i(\lambda) \end{Bmatrix} = \begin{Bmatrix} c\gamma c\beta x_i + (c\gamma s\beta s\alpha - s\gamma c\alpha)y_i + (s\gamma s\alpha + c\gamma s\beta c\alpha)z_i + d \\ s\gamma c\beta x_i + (c\gamma c\alpha + s\gamma s\beta s\alpha)y_i + (s\gamma s\beta c\alpha)z_i + e \\ -s\beta x_i + c\beta s\alpha y_i + c\beta c\alpha z_i + f \end{Bmatrix}. \quad \text{(D.4)}$$

The distance between the rotated deformed point P_i^r and the reference point P_i^0 is then:

$$D_i(\lambda) = \big[(x_i^0 - A_i(\lambda))^2 + (y_i^0 - B_i(\lambda))^2 + (z_i^0 - C_i(\lambda))^2\big]^{1/2}. \quad \text{(D.5)}$$

The final aim is to minimize the residual distance between two sets of points, more precisely the average distance per point. However, minimizing the average of the the square of the distances is more efficient and simplifies the analytical expressions. Consequently, the objective of the algorithm is to minimize the following quantity:

$$D_{quad}(\lambda) = \frac{1}{N}\sum_{i=1}^{N} D_i^2(\lambda). \quad \text{(D.6)}$$

To this end, λ is searched so that the derivative of D_{quad} with respect to λ is null. This can be achieved by the Newton-Raphson (NR) method. Let us note f_p the derivative of D_{quad} with respect to λ_p, the p-th component of λ. We search the solution of:

$$F(\lambda) = \begin{Bmatrix} f_1(\lambda) \\ f_2(\lambda) \\ f_3(\lambda) \\ f_4(\lambda) \\ f_5(\lambda) \\ f_6(\lambda) \end{Bmatrix} = \begin{Bmatrix} \partial D_{quad}(\lambda)/\partial\alpha \\ \partial D_{quad}(\lambda)/\partial\beta \\ \partial D_{quad}(\lambda)/\partial\gamma \\ \partial D_{quad}(\lambda)/\partial d \\ \partial D_{quad}(\lambda)/\partial e \\ \partial D_{quad}(\lambda)/\partial f \end{Bmatrix} = 0. \quad \text{(D.7)}$$

The NR method searches the zero of F. If it converges, the algorithm runs while the norm of F is above a certain tolerance ε. This criterion Q is calculated as:

$$Q(\lambda) = \|F(\lambda)\| \equiv \Big[\sum_{p=1}^{6} f_{p,adim}^2(\lambda)\Big]^{1/2}, \quad \text{(D.8)}$$

where $f_{p,adim}$ is the dimensionless version of f_p. For $p \leq 3$, the dimension of f_p is a quadratic length. f_p is thus divided by G^2, where G is the length of the diagonal of the bounding box of the reference set of points, given by Eq. D.9. For $p > 3$, f_p is a length and is therefore divided by G.

$$G = \big[(\max_i x_i^0 - \min_i x_i^0)^2 + (\max_i y_i^0 - \min_i y_i^0)^2 + (\max_i z_i^0 - \min_i z_i^0)^2\big]^{1/2}. \quad \text{(D.9)}$$

The NR method also necessitates the definition of the Jacobian matrix of F:

$$J_{pq}(\lambda) = \frac{\partial f_p(\lambda)}{\partial \lambda_q} \text{ with } p, q = 1 \dots 6. \tag{D.10}$$

Expression of $F(\lambda)$

From Eq. D.6, the p-th component of F is:

$$f_p(\lambda) = \frac{\partial D_{quad}(\lambda)}{\partial \lambda_p} = \frac{1}{N} \sum_{i=1}^{N} \frac{\partial}{\partial \lambda_p} D_i^2(\lambda). \tag{D.11}$$

Differentiating Eq. D.5 gives:

$$\begin{aligned} \frac{\partial}{\partial \lambda_p} D_i^2(\lambda) =& 2(A_i(\lambda) - x_i^0) \frac{\partial A_i(\lambda)}{\partial \lambda_p} \\ &+ 2(B_i(\lambda) - y_i^0) \frac{\partial B_i(\lambda)}{\partial \lambda_p} \\ &+ 2(C_i(\lambda) - z_i^0) \frac{\partial C_i(\lambda)}{\partial \lambda_p}. \end{aligned} \tag{D.12}$$

Expression of $J(\lambda)$

Accounting for Eqs. D.10 and D.11 leads to:

$$J_{pq}(\lambda) = \frac{\partial f_p(\lambda)}{\partial \lambda_q} = \frac{1}{N} \sum_{i=1}^{N} \frac{\partial^2}{\partial \lambda_p \partial \lambda_q} D_i^2(\lambda). \tag{D.13}$$

Moreover, by differentiating Eq. D.12:

$$\begin{aligned} \frac{\partial^2}{\partial \lambda_p \partial \lambda_q} D_i^2(\lambda) =& 2 \frac{\partial A_i(\lambda)}{\partial \lambda_p} \frac{\partial A_i(\lambda)}{\partial \lambda_q} + 2(A_i(\lambda) - x_i^0) \frac{\partial^2 A_i(\lambda)}{\partial \lambda_p \partial \lambda_q} \\ &+ 2 \frac{\partial B_i(\lambda)}{\partial \lambda_p} \frac{\partial B_i(\lambda)}{\partial \lambda_q} + 2(B_i(\lambda) - y_i^0) \frac{\partial^2 B_i(\lambda)}{\partial \lambda_p \partial \lambda_q} \\ &+ 2 \frac{\partial C_i(\lambda)}{\partial \lambda_p} \frac{\partial C_i(\lambda)}{\partial \lambda_q} + 2(C_i(\lambda) - z_i^0) \frac{\partial^2 C_i(\lambda)}{\partial \lambda_p \partial \lambda_q}. \end{aligned} \tag{D.14}$$

First derivatives

To compute J and F, the first derivatives of A_i, B_i and C_i with respect to the degrees of freedom are needed. These derivatives are obtained by differentiation of Eq. D.4 (missing derivatives are equal to zero):

$$\begin{cases} \frac{\partial A_i(\lambda)}{\partial \alpha} = (c\gamma s\beta c\alpha + s\gamma s\alpha)y_i + (s\gamma c\alpha - c\gamma s\beta s\alpha)z_i \\ \frac{\partial A_i(\lambda)}{\partial \beta} = -c\gamma s\beta x_i + c\gamma c\beta s\alpha y_i + c\gamma c\beta c\alpha z_i \\ \frac{\partial A_i(\lambda)}{\partial \gamma} = -s\gamma c\beta x_i + (-s\gamma s\beta s\alpha - c\gamma c\alpha)y_i + (c\gamma s\alpha - s\gamma s\beta c\alpha)z_i \\ \frac{\partial A_i(\lambda)}{\partial d} = 1 \end{cases}, \tag{D.15a}$$

$$\begin{cases} \frac{\partial B_i(\lambda)}{\partial \alpha} = (-c\gamma s\alpha + s\gamma s\beta c\alpha)y_i + (-s\gamma s\beta s\alpha - c\gamma c\alpha)z_i \\ \frac{\partial B_i(\lambda)}{\partial \beta} = -s\gamma s\beta x_i + s\gamma c\beta s\alpha y_i + s\gamma c\beta c\alpha z_i \\ \frac{\partial B_i(\lambda)}{\partial \gamma} = c\gamma c\beta x_i + (-s\gamma c\alpha + c\gamma s\beta s\alpha)y_i + (c\gamma s\beta c\alpha + s\gamma s\alpha)z_i \\ \frac{\partial B_i(\lambda)}{\partial e} = 1 \end{cases}, \tag{D.15b}$$

$$\begin{cases} \frac{\partial C_i(\lambda)}{\partial \alpha} = c\beta c\alpha y_i - c\beta s\alpha z_i \\ \frac{\partial C_i(\lambda)}{\partial \beta} = -c\beta x_i - s\beta s\alpha y_i - s\beta c\alpha z_i \\ \frac{\partial C_i(\lambda)}{\partial f} = 1 \end{cases}. \tag{D.15c}$$

Second derivatives

In order to compute J, the second derivatives of A_i, B_i and C_i with respect to the degrees of freedom are needed. These derivatives are obtained by differentiation of Eq. D.15 (missing derivatives are equal to zero):

$$\begin{cases} \frac{\partial^2 A_i(\lambda)}{\partial \alpha^2} = (-c\gamma s\beta s\alpha + s\gamma c\alpha)y_i + (-s\gamma s\alpha - c\gamma s\beta c\alpha)z_i \\ \frac{\partial^2 A_i(\lambda)}{\partial \beta^2} = -c\gamma c\beta x_i - c\gamma s\beta s\alpha y_i - c\gamma s\beta c\alpha z_i \\ \frac{\partial^2 A_i(\lambda)}{\partial \gamma^2} = -c\gamma c\beta x_i + (-c\gamma s\beta s\alpha + s\gamma c\alpha)y_i + (-s\gamma s\alpha - c\gamma s\beta c\alpha)z_i \\ \frac{\partial^2 A_i(\lambda)}{\partial \alpha \partial \beta} = c\gamma c\beta c\alpha y_i - c\gamma c\beta s\alpha z_i \\ \frac{\partial^2 A_i(\lambda)}{\partial \alpha \partial \gamma} = (-s\gamma s\beta c\alpha + c\gamma s\alpha)y_i + (c\gamma c\alpha + s\gamma s\beta s\alpha)z_i \\ \frac{\partial^2 A_i(\lambda)}{\partial \beta \partial \gamma} = s\gamma s\beta x_i - s\gamma c\beta s\alpha y_i - s\gamma c\beta c\alpha z_i \end{cases}, \tag{D.16a}$$

$$\begin{cases} \frac{\partial^2 B_i(\lambda)}{\partial \alpha^2} = (-c\gamma c\alpha - s\gamma s\beta s\alpha)y_i + (-s\gamma s\beta c\alpha + c\gamma s\alpha)z_i \\ \frac{\partial^2 B_i(\lambda)}{\partial \beta^2} = -s\gamma c\beta x_i - s\gamma s\beta s\alpha y_i - s\gamma s\beta c\alpha z_i \\ \frac{\partial^2 B_i(\lambda)}{\partial \gamma^2} = -s\gamma c\beta x_i(-c\gamma c\alpha - s\gamma s\beta s\alpha)y_i + (-s\gamma s\beta c\alpha + c\gamma s\alpha)z_i \\ \frac{\partial^2 B_i(\lambda)}{\partial \alpha \partial \beta} = s\gamma c\beta c\alpha y_i - s\gamma c\beta s\alpha z_i \\ \frac{\partial^2 B_i(\lambda)}{\partial \alpha \partial \gamma} = (s\gamma s\alpha + c\gamma s\beta c\alpha)y_i + (-c\gamma s\beta s\alpha + s\gamma c\alpha)z_i \\ \frac{\partial^2 B_i(\lambda)}{\partial \beta \partial \gamma} = -c\gamma s\beta x_i + c\gamma c\beta s\alpha y_i + c\gamma c\beta c\alpha z_i \end{cases}, \tag{D.16b}$$

$$\begin{cases} \frac{\partial^2 C_i(\lambda)}{\partial \alpha^2} = -c\beta s\alpha y_i - c\beta c\alpha e_i \\ \frac{\partial^2 C_i(\lambda)}{\partial \beta^2} = s\beta x_i - c\beta s\alpha y_i - c\beta c\alpha z_i \\ \frac{\partial^2 C_i(\lambda)}{\partial \alpha \partial \beta} = -s\beta c\alpha y_i + s\beta s\alpha z_i \end{cases}. \tag{D.16c}$$

Algorithm

Eq. D.7 is solved by the following Newton-Raphson algorithm:

$\lambda \leftarrow \lambda_0$;
$Q \leftarrow 10^{30}$;
$\varepsilon \leftarrow 10^{-4}$;
$D_{quad,min} \leftarrow 10^{30}$;

while $Q > \varepsilon$ **do**
  for $i = 1 \dots N$ **do**
    Compute $A_i(\lambda)$, $B_i(\lambda)$, $C_i(\lambda)$ (Eq. D.4);
    Compute their derivatives (Eqs. D.15–D.16);
  end

  Compute $F(\lambda)$ (Eqs. D.11–D.12);
  Compute $J(\lambda)$ (Eqs. D.13–D.14);
  Compute $Q(\lambda)$ (Eq. D.8);
  Compute $D_{quad}(\lambda)$ (Eqs. D.5–D.6);

  if $D_{quad} < D_{quad,min}$ **then**
    $\lambda_{min} \leftarrow \lambda$;
    $D_{quad,min} \leftarrow D_{quad}$;
  end

  Compute $\delta\lambda = -J^{-1}(\lambda)F(\lambda)$;
  $\lambda \leftarrow \lambda + \delta\lambda$;
end

Algorithm 1: Newton-Raphson algorithm

If the algorithm converges, $D_{quad,min}$ provides the closest local minimum to λ_0 of the quadratic residual distance between the two sets of points, and it is obtained with the rigid body motion λ_{min}. A choice needs to be made regarding the starting point of the algorithm λ_0, since several local minima could exist. Consequently, the algorithm is always executed for several values of λ_0. In practice, $\lambda_0 = 0$ always provides a $D_{quad,min}$ very close to the best result obtained with other λ_0 values (less than 1 % of difference). Attempts have been made to provide a "smart guess" for λ_0 but failed to improve the convergence speed. The tolerance ε is set to 10^{-4}. Potential symmetries of the geometry (e.g. if only a quarter of the geometry is simulated) are easily accounted for by deactivating the corresponding degrees of freedom. The algorithm is implemented in C++ and runs in a few seconds.

Appendix E

Detailed experimental results

In this section, more exhaustive experimental results are provided regarding the C-spars manufactured in Chapter 5. More particularly, the full set of results is presented for the spring-in measurements, which are averaged in Chapter 5. The distortion maps of all the manufactured parts are also included. For the sake of clarity, the color maps of the nominal parts present the same color scale. The same remark holds for the compensated parts. The main conclusions which can be drawn when observing these pictures are:

- All the parts distort in an asymmetric manner, and the twist is always in the same direction, even for the compensated parts: the top right corner and the bottom left corner are above the reference geometry, and the other two corners are below the reference.
- The color scales are chosen in order to be representative of all the parts. The resulting distortion range (difference between the maximum and minimum values) is 4 mm for the nominal parts, and 1.6 mm for the compensated parts. These extrema are exceeded in the red and dark blue zones, which means that a part which presents a large red or dark blue zone presents more distortions. To the contrary, the absence of red or dark blue zone indicates that the extrema are not reached, meaning that the distortion range is less than the aforementioned values. This is typically the case for compensated parts n°3 and 4, see Figures E.6(c) and (d).

Table E.1 provides the detailed percentiles and averages of the distribution of the absolute deviations, for the nominal parts and the compensated parts. It appears, for instance, that the compensation procedure has allowed the reduction of the average deviation from 0.762 ± 0.686 mm to 0.240 ± 0.199 mm, of the 50-th percentile from 0.534 mm to 0.197 mm, and of the 98-th percentile from 2.616 mm to 0.809 mm.

Detailed spring-in results for nominal parts

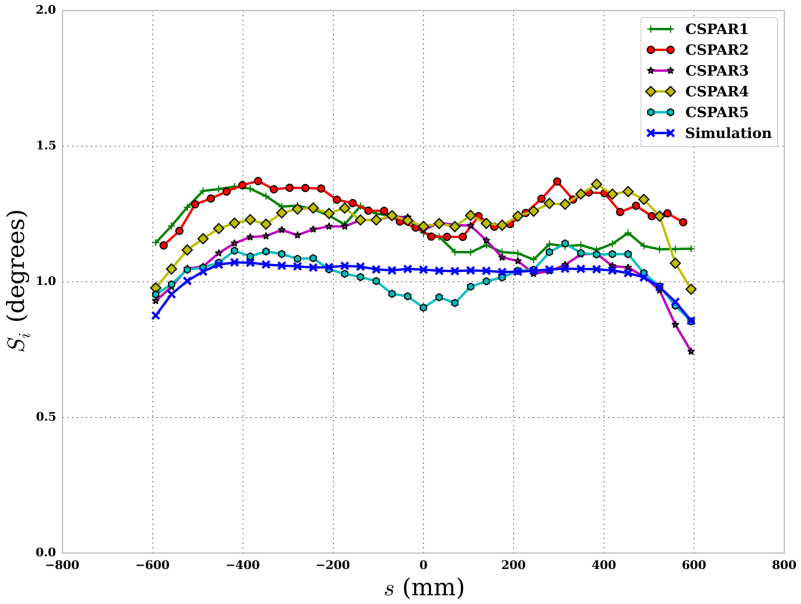


Figure E.1: Spring-in results for nominal parts: internal spring-in.

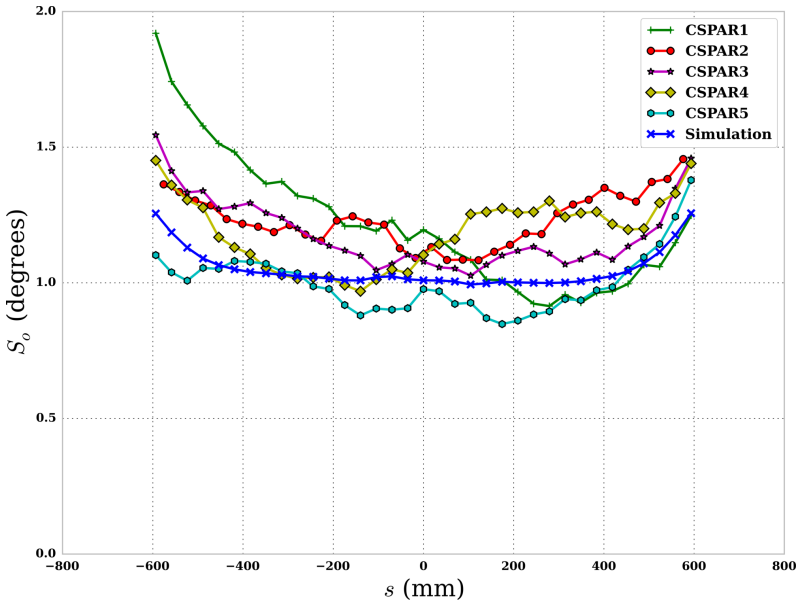


Figure E.2: Spring-in results for nominal parts: external spring-in.

Detailed spring-in results for compensated parts

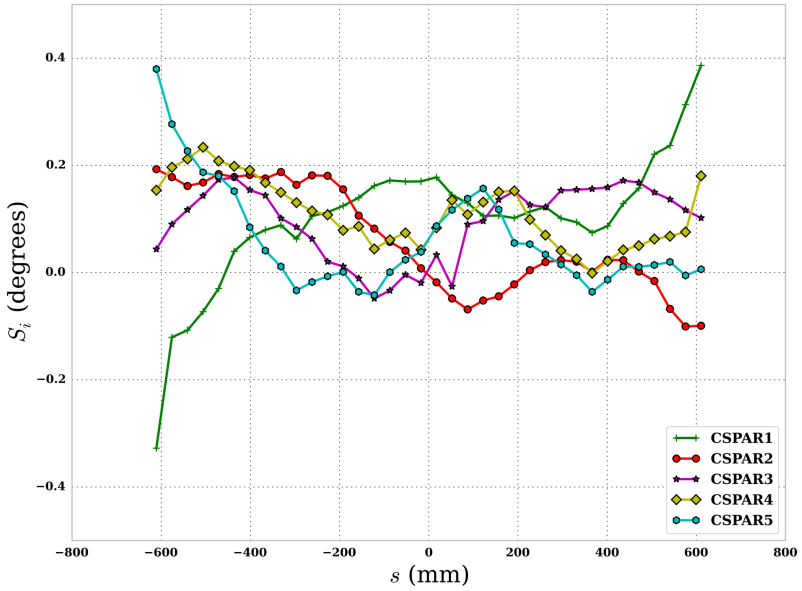


Figure E.3: Spring-in results for compensated parts: internal spring-in.

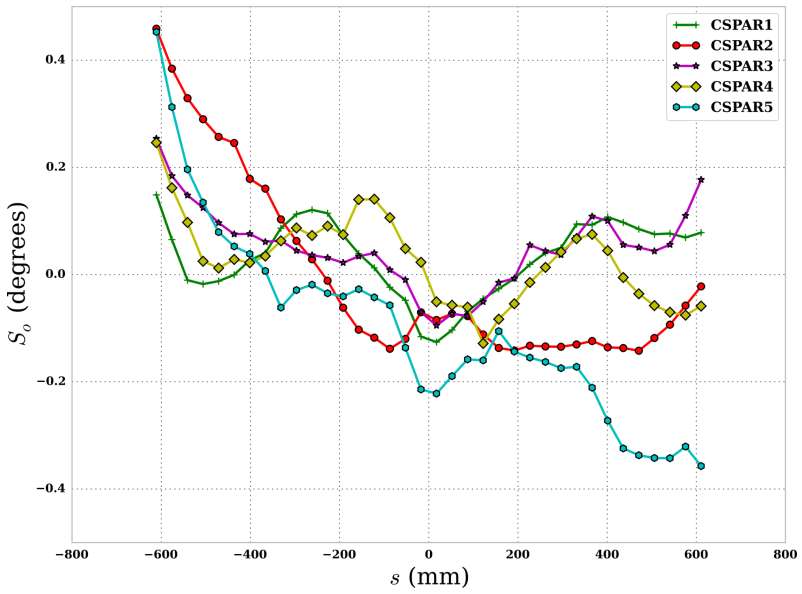


Figure E.4: Spring-in results for compensated parts: external spring-in.

Distortions of nominal parts

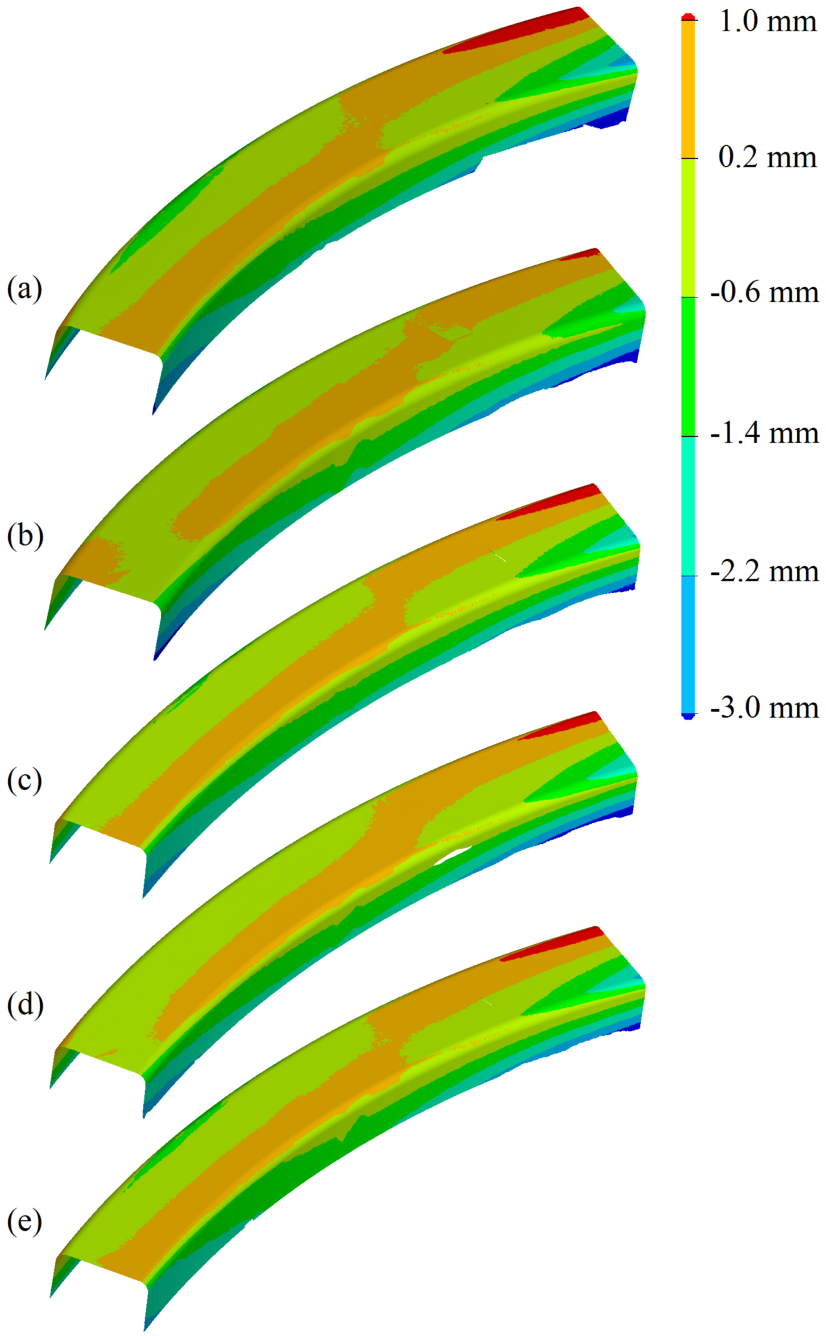


Figure E.5: Distortion map of nominal C-spars: n°1 (a) to n°5 (e).

Distortions of compensated parts

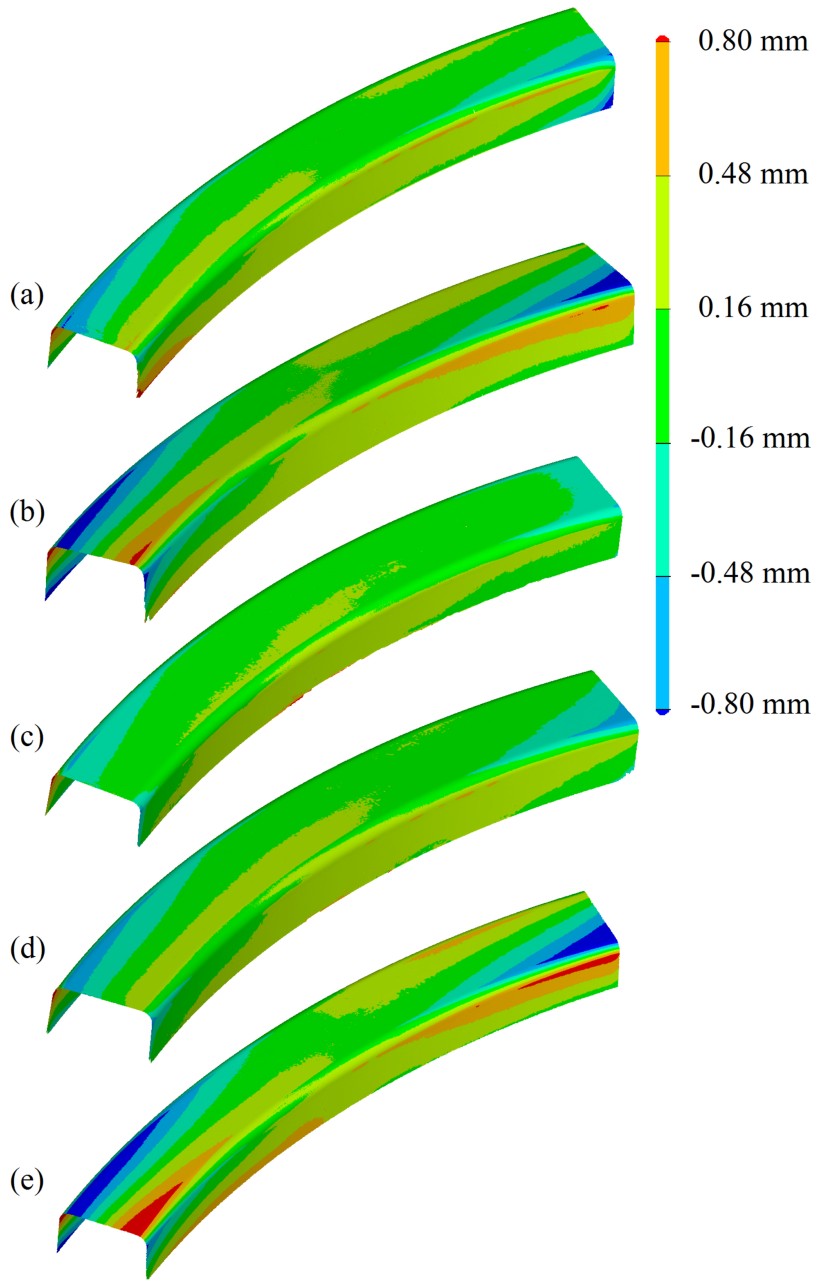


Figure E.6: Distortion map of compensated C-spars: n°1 (a) to n°5 (e).

Part distortions: detailed percentiles

Nominal parts						
Percentile of distribution	CSPAR1 (mm)	CSPAR2 (mm)	CSPAR3 (mm)	CSPAR4 (mm)	CSPAR5 (mm)	All (mm)
5-th	0.048	0.051	0.056	0.048	0.055	0.051
10-th	0.102	0.102	0.108	0.097	0.106	0.102
25-th	0.279	0.231	0.269	0.240	0.259	0.253
50-th	0.600	0.481	0.544	0.479	0.551	0.534
75-th	1.182	1.075	1.113	1.075	1.038	1.098
90-th	1.982	1.834	1.768	1.845	1.620	1.813
95-th	2.441	2.313	2.120	2.290	1.959	2.240
99-th	3.007	2.917	2.631	2.745	2.447	2.810
Avgerage of distribution	0.818	0.747	0.756	0.743	0.7416	0.762
Standard deviation of distribution	0.741	0.709	0.647	0.698	0.596	0.686

Compensated parts						
Percentile of distribution	CSPAR1 (mm)	CSPAR2 (mm)	CSPAR3 (mm)	CSPAR4 (mm)	CSPAR5 (mm)	All (mm)
5-th	0.017	0.029	0.017	0.010	0.028	0.018
10-th	0.035	0.056	0.033	0.021	0.055	0.038
25-th	0.090	0.133	0.073	0.068	0.133	0.097
50-th	0.186	0.248	0.154	0.156	0.267	0.197
75-th	0.279	0.388	0.230	0.260	0.446	0.325
90-th	0.437	0.574	0.327	0.368	0.680	0.491
95-th	0.551	0.710	0.392	0.460	0.853	0.633
99-th	0.757	0.999	0.532	0.642	1.137	0.951
Avgerage of distribution	0.213	0.288	0.169	0.182	0.325	0.240
Standard deviation of distribution	0.166	0.216	0.127	0.144	0.254	0.199

Table E.1: Absolute deviations with respect to the nominal geometry: comparison of percentiles.

Quality of the machined molds

Figures E.7 to E.11 provide comparisons between scans of the machined molds and their respective CAD models. The scan of the nominal mold is compared to the nominal CAD model, the scan of the compensated mold is compared to the compensated CAD model. This gives useful information about the quality of the machining process.

The nominal mold was machined by a subcontractor. Figure E.10 shows that the machining accuracy is much lower than that of the compensated mold, which was machined at Cenaero, see Figure E.11. These deviations are visible mainly on the vertical sides, as shown by Figures E.7 to E.9, which measure the angle deviation of the horizontal side of the molds compared to the CAD models in Figure E.7, and the angle deviation of the vertical sides, see Figures E.8 and E.9. It appears that the top sides are very close to the CAD models, while the vertical sides exhibit an error up to 0.2° for the nominal mold. This deviation had to be taken into account when measuring the spring-in of the manufactured nominal parts in Chapter 5. Comparing to the CAD model would have led to biased conclusions, since 0.2° represents almost 20 % of the cure-induced spring-in of the nominal parts.

The quality of the machined molds has been investigated when looking for possible explanations of the asymmetry of the twist exhibited by the manufactured parts, see Section 5.8. However, the angle deviation of the nominal mold does not explain the asymmetry. This has been confirmed by curing simulations using the scanned mold instead of the CAD model.

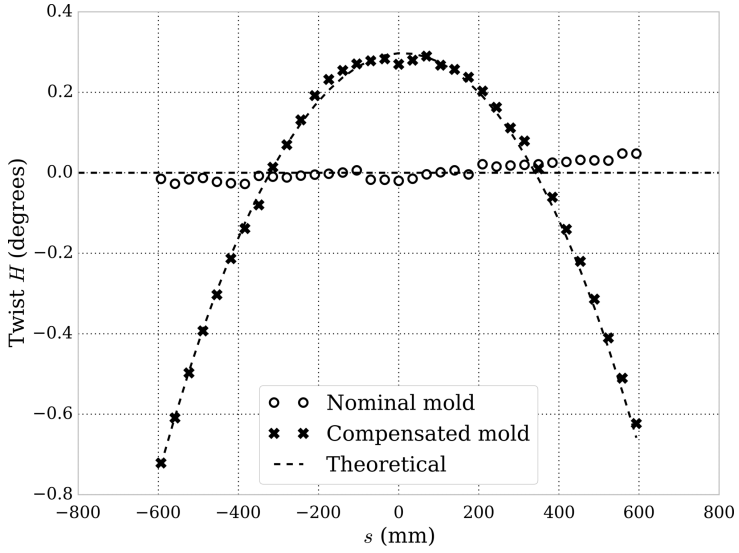


Figure E.7: Comparison of horizontality between the scanned molds and their CAD counterparts.

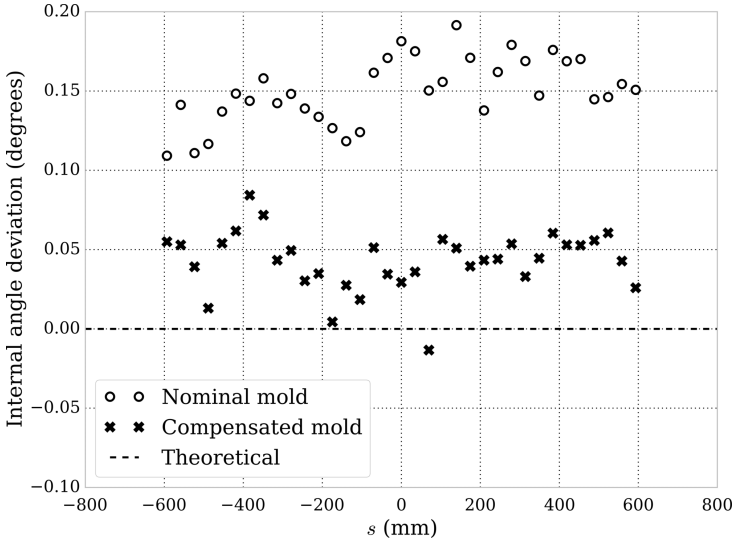


Figure E.8: Angle deviation between the scanned molds and their CAD counterparts (internal angle).

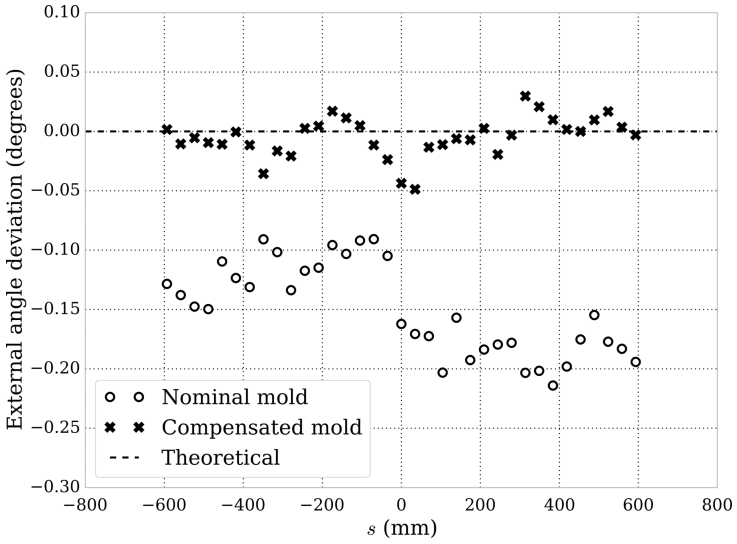


Figure E.9: Angle deviation between the scanned molds and their CAD counterparts (external angle).

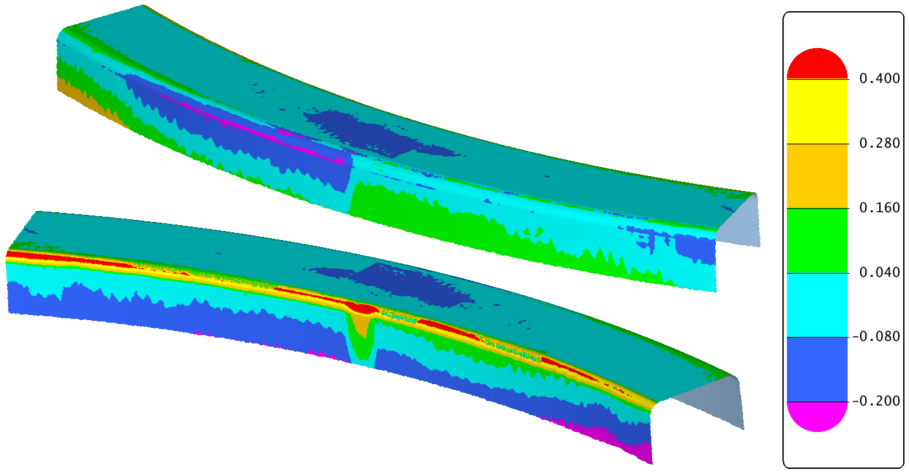


Figure E.10: Deviations between the scanned nominal mold (machined by a sub-contractor) and the corresponding CAD model. The deviations are in millimeters.

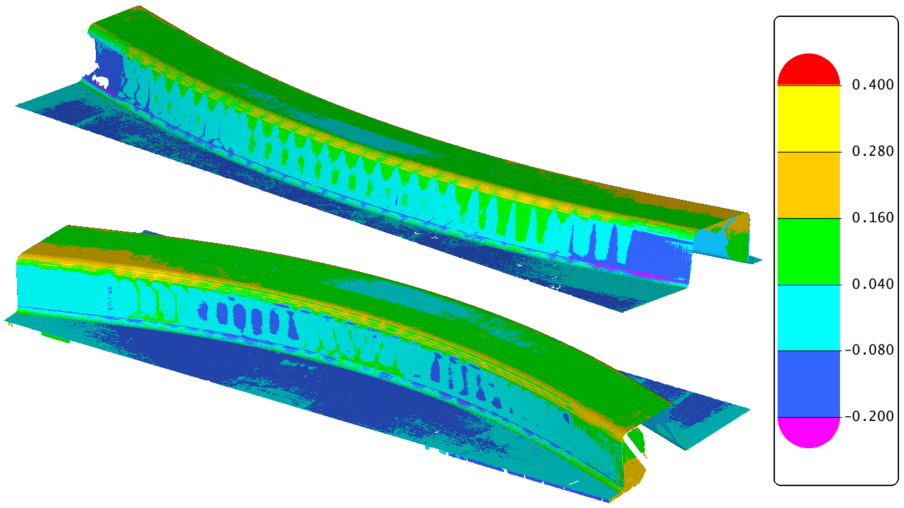


Figure E.11: Deviations between the scanned compensated mold (machined at Cenaero) and the corresponding CAD model. The deviations are in millimeters.

List of publications

Scientific papers related to the thesis

Wucher B, Lani F, Pardoen T, Bailly C, and Martiny Ph. Tooling geometry optimization for compensation of cure-induced distortions of a curved carbon/epoxy C-spar. *Composites: Part A*, 56:27–35, 2014.

Wucher B, Hallström S, Dumas D, Pardoen T, Bailly C, Martiny Ph, and Lani F. Nonconformal mesh-based finite element strategy for 3D textile composites. *Journal of Composite Materials*, first published on September 20, 2016, *doi:10 .1177/0021998316669875*.

Wucher B, Martiny Ph, Lani F, Pardoen T, Bailly C, and Dumas D. Simulation-driven mold compensation of composite materials: experimental validation for a doubly-curved part. *To be submitted*.

Oral communications in conferences related to the thesis

Wucher B, Lani F, Martiny Ph, Pardoen T, and Bailly C. An example of mold compensation by means of numerical simulation on a generic curved CFRP C-spar. *15-th European Conference on Composite Materials (ECCM15)*, Venice, Italy, June 24-28 2012.

Wucher B, Lani F, Martiny Ph, Pardoen T, and Bailly C. Numerical prediction of the cure-induced deformation in composites and its application to mold compensation. *2012 Benelux Regional User Meeting*, Turnhout, Belgium, November 8-9 2012.

Wucher B, Lani F, Martiny Ph, Pardoen T, and Bailly C. Identification of the material properties needed in cure simulations from inverse analysis and finite element homogenization. *17-th International Conference on Composite Structures (ICCS17)*, University of Porto, Porto, Portugal, June 17-21 2013.

Wucher B, Lani F, Pardoen T, Bailly C, and Martiny Ph. Simulation-driven tooling shape optimization for an easier assembling process of composite parts. *16-th European Conference on Composite Materials (ECCM16)*, Sevilla, Spain, June 22-26 2014.

Wucher B, Hallström S, Dumas D, Pardoen T, Bailly C, Martiny Ph, and Lani F. A non-conformal finite element approach to determine the elastic properties of complex woven composites with simple geometrical modeling. *12-th International Conference on Textile Composites (TEXCOMP-12)*, Raleigh, NC, USA, May 26-29 2015.

Wucher B, Hallström S, Dumas D, Pardoen T, Bailly C, Martiny Ph, and Lani F. Non-conformal finite element homogenization applied to woven composites with complex textile architectures. *20-th International Conference on Composite Materials (ICCM20)*, Copenhagen, Denmark, July 19-24 2015.

Wucher B, Dumas D, Pardoen T, Bailly C, Martiny Ph, and Lani F. Generic tooling compensation strategy to minimize cure-induced distortions. *International conference on Computational Methods in Manufacturing Processes (ICOMP)*, Liège, Belgium, May 18-20 2016.

Bibliography

[1] Tropis A. Composite structure: evolution and future challenges. GdR Mise en oeuvre des composites, Roubaix (France), November 2015.

[2] Groh F, Kappel E, Hühne C, and Brymerski W. Experimental investigation of process induced deformations of automotive composites with focus on fast curing epoxy resins. In *Proceedings of the ICCM20 conference*, Copenhagen, Denmark, July 2015.

[3] Gersborg AR, Jørgensen JE, Gaarde R, Alkemade H, Vanaparthi SK, and Patil S. Permeability measurements and process simulation of large sandwich structures for industrial wind turbine blades. In *Proceedings of the ICCM20 conference*, Copenhagen, Denmark, July 2015.

[4] Wijskamp S. *Shape distortions in composites forming.* PhD thesis, University of Twente, 2005.

[5] Kappel E, Stefaniak D, and Hühne C. Semi-analytical spring-in analysis to counteract CFRP manufacturing deformations by tool compensation. In *Proceedings of the 28-th international congress of the aeronautical sciences*, Brisbane, Australia, September 2012.

[6] Hörberg E, Nyman T, Hellström T, Rudlund M, Bohlin J, and Berg R. Shape distortion analysis of a complex shaped wing skin section. In *Proceedings of the ICCM20 conference*, Copenhagen, Denmark, July 2015.

[7] Parmentier A, Wucher B, and Dumas D. Determination of the model complexity level required to predict the cure-induced deformations in thermoset-based composite parts. In *Proceedings of the ECCM16 conference*, Sevilla, Spain, June 2014.

[8] Parmentier A, Wucher B, and Dumas D. Influence of the thermomechanical properties on the predictions of the cure-induced deformations in thermoset-based composite parts. In *Proceedings of the ICCM20 conference*, Copenhagen, Denmark, July 2015.

[9] Dong C. Process-induced deformation of composite T-stiffener structures. *Compos Struct*, 92(7):1614–1619, 2010.

[10] Zhu Q and Geubelle PH. Dimensional accuracy of thermoset composites: shape optimization. *J Compos Mater*, 36(6):647–672, 2002.

[11] Dassault Systèmes Simulia, Abaqus V6.12. General purpose finite element software. Web page: www.3ds.com.

[12] Siemens PLM Software, Samcef V16.1. General purpose finite element software. Web page: www.plm.automation.siemens.com.

[13] Mazumdar S. *Composites Manufacturing: Materials, Product, and Process Engineering*. CRC Press, 2001.

[14] Advani SG and Sozer EM. *Process Modeling in Composites Manufacturing*. Manufacturing engineering and materials processing. CRC Press, 2002.

[15] Xin CB, Gu YZ, Li M, Luo J, Li YX, and Zhang ZG. Experimental and numerical study on the effect of rubber mold configuration on the compaction of composite angle laminates during autoclave processing. *Compos Part A-Appl S*, 42(10):1353–1360, 2011.

[16] Newsom CM. Tubular autoclave for curing composite parts, March 5 1991. US Patent 4,997,511.

[17] Kourkoutsakia T, Comas-Cardona S, Binetruy C, Upadhyay RK, and Hinterhoelzl R. The impact of air evacuation on the impregnation time of Out-of-Autoclave prepregs. *Compos Part A-Appl S*, 79:30–42, 2015.

[18] Centea T, Grunenfelder LK, and Nutt SR. A review of out-of-autoclave prepregs – Material properties, process phenomena, and manufacturing considerations. *Compos Part A-Appl S*, 70:132–154, 2015.

[19] Helmus R, Hinterhölzl R, and Hubert P. A stochastic approach to model material variation determining tow impregnation in out-of-autoclave prepreg consolidation. *Compos Part A-Appl S*, 77:293–300, 2015.

[20] Hayashi N, Mizuno H, Hasegawa K, and Ota K. RTM molding method, August 31 2010. US Patent 7,785,525.

[21] Bodaghi M, Cristóvão C, Gomes R, and Correia NC. Experimental characterization of voids in high fibre volume fraction composites processed by high injection pressure RTM. *Compos Part A-Appl S*, 82:88–99, 2016.

[22] Carlier V, Bertin A, and Vandeuren M. Method and apparatus for moulding parts made from composite materials, October 20 2011. WO Patent App. PCT/EP2011/056,063.

[23] Naik NK, Sirisha M, and Inani A. Permeability characterization of polymer matrix composites by RTM/VARTM. *Prog Aerosp Sci*, 65:22–40, 2014.

[24] Hou TH and Jensen BJ. Double-vacuum-bag technology for volatile management in composite fabrication. *Polym Compos*, 29(8):906–914, 2008.

[25] Nalla AR, Fuqua M, Glancey J, and Lelievre B. A multi-segment injection line and real-time adaptive, model-based controller for vacuum assisted resin transfer molding. *Compos Part A-Appl S*, 38(3):1058–1069, 2007.

[26] Hexcel. Hexflow®RTM6. Product datasheet, December 2014.

[27] Hexcel. Hexply®8552 Epoxy Matrix. Product datasheet, February 2014.

[28] Svanberg JM. *Predictions of manufacturing induced shape distortions – high performance thermoset composites*. PhD thesis, Luleå University of Technology, 2002.

[29] Javdanitehran M, Berg DC, Duemichen E, and Ziegmann G. An iterative approach for isothermal curing kinetics modelling of an epoxy resin system. *Thermochim Acta*, 623:72–79, 2016.

[30] Al-Safy R, Al-Mahaidi R, and Simon GP. A study of the practicality and performance of CFRP applications using post-curing at moderately elevated temperatures. *Compos Part B-Eng*, 48:140–157, 2013.

[31] Ruiz E and Trochu F. Multi-criteria thermal optimization in liquid composite molding to reduce processing stresses and cycle time. *Compos Part A-Appl S*, 37(6):913–924, 2006.

[32] Johnston AA. *An integrated model of the development of process-induced deformation in autoclave processing of composite structures*. PhD thesis, The University of British Columbia, 1997.

[33] Boriek AM, Akin JE, and Armeniades CD. Setting stress distribution in particle reinforced polymer composites. *J Compos Mater*, 22(10):986–1002, 1988.

[34] Skordos AA and Partridge IK. Effects of tool-embedded dielectric sensors on heat transfer phenomena during composite cure. *Polym Compos*, 28(2):139–152, 2007.

[35] Li C, Potter K, Wisnom MR, and Stringer G. In-situ measurement of chemical shrinkage of MY750 epoxy resin by a novel gravimetric method. *Compos Sci Technol*, 64(1):55–64, 2004.

[36] White SR and Hahn HT. Process modeling of composite materials: Residual stress development during cure. Part II. Experimental validation. *J Compos Mater*, 26(16):2423–2453, 1992.

[37] Ochi M, Yamashita K, and Shimbo M. The mechanism for occurrence of internal stress during curing epoxide resins. *J Appl Polym Sci*, 43(11):2013–2019, 1991.

[38] White SR and Hahn HT. Cure cycle optimization for the reduction of processing-induced residual stresses in composite materials. *J Compos Mater*, 27(14):1352–1378, 1993.

[39] Albert C and Fernlund G. Spring-in and warpage of angled composite laminates. *Compos Sci Technol*, 62(14):1895–1912, 2002.

[40] Sarrazin H, Kim B, Ahn SH, and Springer GS. Effects of processing temperature and layup on springback. *J Compos Mater*, 29(10):1278–1294, 1995.

[41] Brauner C. *Analysis of process-induced distortions and residual stresses of composite structures*. PhD thesis, Universität Bremen, 2014.

[42] Ersoy N, Garstka T, Potter K, Wisnom MR, Porter D, and Stringer G. Modelling of the spring-in phenomenon in curved parts made of a thermosetting composite. *Compos Part A-Appl S*, 41(3):410–418, 2010.

[43] Wang X, Su H, Jia Y, and Li P. Integrated analysis on cure-microstructure-property-deformation correlation of carbon fiber reinforced resin composites. *Comp Mater Sci*, 109:7–13, 2015.

[44] Zeng X and Raghavan J. Role of tool-part interaction in process-induced warpage of autoclave-manufactured composite structures. *Compos Part A-Appl S*, 41(9):1174–1183, 2010.

[45] Fernlund G, Rahman N, Courdji R, Bresslauer M, Poursartip A, Willden K, and Nelson K. Experimental and numerical study of the effect of cure cycle, tool surface, geometry, and lay-up on the dimensional fidelity of autoclave-processed composite parts. *Compos Part A-Appl S*, 33(3):341–351, 2002.

[46] Twigg G, Poursartip A, and Fernlund G. Tool-part interaction in composites processing. Part I: experimental investigation and analytical model. *Compos Part A-Appl S*, 35(1):121–133, 2004.

[47] Radford DW, Fu S, and Derringer D. Measurement of manufacturing distortion in flat composite laminates. In *Proceedings of the ICCM12 conference*, Paris, France, July 1999.

[48] Svanberg JM and Holmberg JA. Prediction of shape distortions. Part II. Experimental validation and analysis of boundary conditions. *Compos Part A-Appl S*, 35(6):723–734, 2004.

[49] Potter KD. Understanding the origins of defects and variability in composites manufacture. In *Proceedings of the ICCM17 conference*, Edinburgh, UK, July 2009.

[50] Rabearison N. *Elaboration d'un outil numérique dédié à la simulation du procédé de fabrication des matériaux composites à résine thermodurcissable – prédiction des contraintes internes*. PhD thesis, Université de Bretagne Occidentale, 2009.

[51] Zvetkov VL. Mechanistic modeling of the epoxyamine reaction: Model derivations. *Thermochim Acta*, 435(1):71–84, 2005.

[52] Zhao L and Hu X. A variable reaction order model for prediction of curing kinetics of thermosetting polymers. *Polymer*, 48(20):6125–6133, 2007.

[53] Lee SN, Chiu MT, and Lin HS. Kinetic model for the curing reaction of a tetraglycidyl diamino diphenyl methane/diamino diphenyl sulfone (TGDDM/DDS) epoxy resin system. *Polym Eng Sci*, 32(15):1037–1046, 1992.

[54] Sourour S and Kamal MR. Differential scanning calorimetry of epoxy cure: isothermal cure kinetics. *Thermochim Acta*, 14(1–2):41–59, 1976.

[55] Fournier J, Williams G, Duch C, and Aldridge GA. Changes in molecular dynamics during bulk polymerization of an epoxide–amine system as studied by dielectric relaxation spectroscopy. *Macromolecules*, 29(22):7097–7107, 1996.

[56] Skordos AA and Partridge IK. Cure kinetics modeling of epoxy resins using a non-parametric numerical procedure. *Polym Eng Sci*, 41(5):793–805, 2001.

[57] DiBenedetto AT. Prediction of the glass transition temperature of polymers: A model based on the principle of corresponding states. *J Polym Sci Pol Phys*, 25(9):1949–1969, 1987.

[58] Svanberg JM. Shape distortion of non-isothermally cured composite angle bracket. *Plast Rubber Compos*, 31(9):398–404, 2002.

[59] Van Assche G, Swier S, and Van Mele B. Modeling and experimental verification of the kinetics of reacting polymer systems. *Thermochim Acta*, 388(1–2):327–341, 2002.

[60] Stark W and Jaunich M. Investigation of Ethylene/Vinyl Acetate Copolymer (EVA) by thermal analysis DSC and DMA. *Polym Test*, 30(2):236–242, 2011.

[61] Aduriz XA, Lupi C, Boyard N, Bailleul JL, Leduc D, Sobotka V, Lefèvre N, Chapeleau X, Boisrobert C, and Delaunay D. Quantitative control of RTM6 epoxy resin polymerisation by optical index determination. *Compos Sci Technol*, 67(15–16):3196–3201, 2007.

[62] Svanberg JM and Holmberg JA. Prediction of shape distortions. Part I. FE-implementation of a path dependent constitutive model. *Compos Part A-Appl S*, 35(6):711–721, 2004.

[63] Ersoy N, Potter K, Wisnom MR, and Clegg MJ. Development of spring-in angle during cure of a thermosetting composite. *Compos Part A-Appl S*, 36(12):1700–1706, 2005.

[64] Zarrelli M, Skordos AA, and Partridge IK. Investigation of cure induced shrinkage in unreinforced epoxy resin. *Plast Rubber Compos*, 31(9):377–384, 2002.

[65] Hobbiebrunken T, Fiedler B, Hojo M, Ochiai S, and Schulte K. Microscopic yielding of CF/epoxy composites and the effect on the formation of thermal residual stresses. *Compos Sci Technol*, 65(10):1626–1635, 2005.

[66] El-Tonsy MM. Automatic measurement of the absolute CTE of thin polymer samples: I–effect of multiple processing on thermal expansion of polypropylene films. *Polym Test*, 23(3):355–360, 2004.

[67] Sadeghinia M, Jansen KMB, and Ernst LJ. Characterization and modeling the thermo-mechanical cure-dependent properties of epoxy molding compound. *Int J Adhes Adhes*, 32:82–88, 2012.

[68] Bogetti TA and Gillespie JW. Process-induced stress and deformation in thick-section thermoset composite laminates. *J Compos Mater*, 26(5):626–660, 1992.

[69] Khoun L and Hubert P. Cure shrinkage characterization of an epoxy resin system by two in situ measurement methods. *Polym Compos*, 31(9):1603–1610, 2010.

[70] Haider M, Hubert P, and Lessard L. Cure shrinkage characterization and modeling of a polyester resin containing low profile additives. *Compos Part A-Appl S*, 38(3):994–1009, 2007.

[71] Hill RR, Muzumdar SV, and Lee LJ. Analysis of volumetric changes of unsaturated polyester resins during curing. *Polym Eng Sci*, 35(10):852–859, 1995.

[72] Tai HJ and Chou HL. Chemical shrinkage and diffusion-controlled reaction of an epoxy molding compound. *Eur Polym J*, 36(10):2213–2219, 2000.

[73] Sobotka V, Lefevre N, Jarny Y, and Delaunay D. Inverse methodology to determine mold set-point temperature in resin transfer molding process. *Int J Therm Sci*, 49(11):2138–2147, 2010.

[74] Ding Y, Chiu WK, and Liu XL. Numerical investigation on thermal response of oil-heated tool for manufacture of composite products. *Compos Struct*, 47(1–4):491–495, 1999.

[75] Ding Y, Chiu WK, Liu XL, and Whittingham B. Modelling of thermal response of oil-heated tools due to different flow rates for the manufacture of composite structures. *Compos Struct*, 54(4):477–488, 2001.

[76] Morelle X. *Mechanical Characterization and Physics-Based Modeling of a Highly-Crosslinked Epoxy Resin*. PhD thesis, Université Catholique de Louvain, 2015.

[77] Simon SL, Mckenna GB, and Sindt O. Modeling the evolution of the dynamic mechanical properties of a commercial epoxy during cure after gelation. *J Appl Polym Sci*, 76(4):495–508, 2000.

[78] Brockman RA, Storage TM, Lee CW, Coomer RR, and Volk BL. Characterizing, modeling, and validating the processing of out-of-autoclave organic matrix composites as a function of cure cycle. In *Proceedings of the ICCM20 conference*, Copenhagen, Denmark, July 2015.

[79] Zobeiry N, Vaziri R, and Poursartip A. Computationally efficient pseudo-viscoelastic models for evaluation of residual stresses in thermoset polymer composites during cure. *Compos Part A-Appl S*, 41(2):247–256, 2010.

[80] Bracquart B. *Determination of the mechanical properties of composite materials as a function of the degree of cure and application to curing simulations.* Master's thesis, École Centrale de Nantes, Cenaero, Belgium, September 2013.

[81] Garstka T, Cole G, Irving D, and Lyons P. Integrated Finite Element environment for composite process simulation. In *Proceedings of the ICCM17 conference*, Edinburgh, UK, July 2009.

[82] ESI Group, PAM-Distortion software package. Web page: www.esi-group.com.

[83] Pautet N. *Campagne expérimentale et numérique sur l'influence du cisaillement textile sur les distorsions de cornières composites lors de leur cuisson.* Student project, École Centrale de Nantes, Cenaero, Belgium, August 2014.

[84] Gommers B, Verpoest I, and Van Houtte P. The Mori-Tanaka method applied to textile composite materials. *Acta Mater*, 46(6):2223–2235, 1998.

[85] Bower AF. *Applied Mechanics of Solids.* CRC Press, 2009.

[86] Doghri I. *Mechanics of Deformable Solids: Linear, Nonlinear, Analytical and Computational Aspects.* Engineering online library. Springer Berlin Heidelberg, 2000.

[87] Pierard O, Friebel C, and Doghri I. Mean-field homogenization of multi-phase thermo-elastic composites: a general framework and its validation. *Compos Sci Technol*, 64(10–11):1587–1603.

[88] Friebel C, Doghri I, and Legat V. General mean-field homogenization schemes for viscoelastic composites containing multiple phases of coated inclusions. *Int J Solids Struct*, 43(9):2513–2541, 2006.

[89] Delannay L, Lani F, Pardoen T, and Delannay F. Mean field modelling of the plastic behaviour of co-continuous dual-phase alloys with strong morphological anisotropy. *Int J Plasticity*, 22(12):2327–2345, 2006.

[90] Hassani B and Hinton E. A review of homogenization and topology optimization I–homogenization theory for media with periodic structure. *Comput Struct*, 69(6):707–717, 1998.

[91] Chung PW, Tamma KK, and Namburu RR. A micro/macro homogenization approach for viscoelastic creep analysis with dissipative correctors for heterogeneous woven-fabric layered media. *Compos Sci Technol*, 60(12–13):2233–2253, 2000.

[92] Chung PW, Tamma KK, and Namburu RR. Asymptotic expansion homogenization for heterogeneous media: computational issues and applications. *Compos Part A-Appl S*, 32(9):1291–1301, 2001.

[93] Paley M and Aboudi J. Micromechanical analysis of composites by the generalized cells model. *Mech Mater*, 14(2):127–139, 1992.

[94] Aboudi J, Pindera MJ, and Arnold SM. Linear thermoelastic higher-order theory for periodic multiphase materials. *J Appl Mech*, 68(5):697–707, 2001.

[95] Pan L, Liu K, Zhang F, Gu B, and Sun B. Finite element modeling of compressive properties of three-dimensional woven composites under various strain rates. *J Compos Mater*, 49(20):2519–2528, 2015.

[96] Labanieh AR, Legrand X, Koncar V, and Soulat D. Evaluation of the elastic behavior of multiaxis 3D-woven preforms by numerical approach. *J Compos Mater*, 48(26):3243–3252, 2014.

[97] Barbero EJ. *Finite Element Analysis of Composite Materials*. Composite Materials. Taylor & Francis, 2007.

[98] Li S and Wongsto A. Unit cells for micromechanical analyses of particle-reinforced composites. *Mech Mater*, 36(7):543–572, 2004.

[99] Kouznetsova V, Brekelmans WAM, and Baaijens FPT. An approach to micro-macro modeling of heterogeneous materials. *Comput Mech*, 27(1):37–48, 2001.

[100] Shah Mohammadi M, Komeili M, Phillion AB, and Milani AS. Toward better understanding of the effect of fiber distribution on effective elastic properties of unidirectional composite yarns. *Comput Struct*, 163(15):29–40, 2016.

[101] Lomov SV, Ivanov DS, Verpoest I, Zako M, Kurashiki T, Nakai H, and Hirosawa S. Meso-FE modelling of textile composites: Road map, data flow and algorithms. *Compos Sci Technol*, 67(9):1870–1891, 2007.

[102] Chamis CC. Simplified composite micromechanics equations for strength, fracture toughness, impact resistance and environmental effects. *SAMPE Quart*, July 1984.

[103] Schapery RA. Thermal expansion coefficients of composite materials based on energy principles. *J Compos Mater*, 2(3):380–404, 1968.

[104] Hyer MW. *Stress analysis of fiber-reinforced materials*. Destech Publications, Inc., Lancaster, PA, USA, 2nd edition, 2009.

[105] Chamis CC, Handler LM, and Manderscheid J. Composite nanomechanics: A mechanistic properties prediction. Technical report, NASA/TM–2007-214673.

[106] Sherburn M. *Geometric and Mechanical Modelling of Textiles*. PhD thesis, The University of Nottingham, 2007.

[107] Lomov SV, Gusakov AV, Huysmans G, Prodromou A, and Verpoest I. Textile geometry preprocessor for meso-mechanical models of woven composites. *Compos Sci Technol*, 60(11):2083–2095, 2000.

[108] Lomov SV, Verpoest I, Cichosz J, Hahn C, Ivanov DS, and Verleye B. Meso-level textile composites simulations: Open data exchange and scripting. *J Compos Mater*, 48(5):621–637, 2014.

[109] Verpoest I and Lomov SV. Virtual textile composites software *WiseTex*: Integration with micro-mechanical, permeability and structural analysis. *Compos Sci Technol*, 65(15–16):2563–2574, 2005.

[110] Lin H, Brown LP, and Long AC. Modelling and simulating textile structures using TexGen. *Adv Mat Res*, 331:44–47, 2011.

[111] Straumit I, Lomov SV, and Wevers M. Quantification of the internal structure and automatic generation of voxel models of textile composites from X-ray computed tomography data. *Compos Part A-Appl S*, 69:150–158, 2015.

[112] Straumit I, Hahn C, Winterstein E, Plank B, Lomov SV, and Wevers M. Computation of permeability of a non-crimp carbon textile reinforcement based on X-ray computed tomography images. *Compos Part A-Appl S*, 81:289–295, 2016.

[113] Mahadik Y and Hallett SR. Finite element modelling of tow geometry in 3D woven fabrics. *Compos Part A-Appl S*, 41(9):1192–1200, 2010.

[114] Green SD, Long AC, El Said BSF, and Hallett SR. Numerical modelling of 3D woven preform deformations. *Compos Struct*, 108:747–756, 2014.

[115] Miao Y, Zhou E, Wang Y, and Cheeseman BA. Mechanics of textile composites: Micro-geometry. *Compos Sci Technol*, 68(7–8):1671–1678, 2008.

[116] Green SD, Matveev MY, Long AC, Ivanov D, and Hallett SR. Mechanical modelling of 3D woven composites considering realistic unit cell geometry. *Compos Struct*, 118:284–293, 2014.

[117] Stig F and Hallström S. A modelling framework for composites containing 3D reinforcement. *Compos Struct*, 94(9):2895–2901, 2012.

[118] Zeng X, Brown LP, Endruweit A, Matveev M, and Long AC. Geometrical modelling of 3D woven reinforcements for polymer composites: Prediction of fabric permeability and composite mechanical properties. *Compos Part A-Appl S*, 56:150–160, 2014.

[119] Rinaldi RG, Blacklock M, Bale H, Begley MR, and Cox BN. Generating virtual textile composite specimens using statistical data from micro-computed tomography: 3D tow representations. *J Mech Phys Solids*, 60(8):1561–1581, 2012.

[120] Grail G, Hirsekorn M, Wendling A, Hivet G, and Hambli R. Consistent Finite Element mesh generation for meso-scale modeling of textile composites with preformed and compacted reinforcements. *Compos Part A-Appl S*, 55:143–151, 2013.

[121] Brown LP, Yan S, Zeng X, and Long AC. Mesoscale geometric modelling of bifurcation in 3D woven T-beam preforms. In *Proceedings of the TexComp-12 conference*, Raleigh, NC, USA, May 2015.

[122] Ishikawa T and Chou TW. Stiffness and strength behaviour of woven fabric composites. *J Mater Sci*, 17(11):3211–3220, 1982.

[123] Vandeurzen P, Ivens J, and Verpoest I. A three-dimensional micromechanical analysis of woven-fabric composites: I. Geometric analysis. *Compos Sci Technol*, 56(11):1303–1315, 1996.

[124] Vandeurzen P, Ivens J, and Verpoest I. A three-dimensional micromechanical analysis of woven-fabric composites: II. Elastic analysis. *Compos Sci Technol*, 56(11):1317–1327, 1996.

[125] Prodromou AG, Lomov SV, and Verpoest I. The method of cells and the mechanical properties of textile composites. *Compos Struct*, 93(4):1290–1299, 2011.

[126] Melchior MA, Duflot M, Gerard JS, Adam L, and Assaker R. End-to-end FE based homogenization of woven composites. In *Proceedings of the ACCE Conference*, Novi, MI, USA, September 2014.

[127] Ernst G, Vogler M, Hühne C, and Rolfes R. Multiscale progressive failure analysis of textile composites. *Compos Sci Technol*, 70(1):61–72, 2010.

[128] Hello G, Schneider J, and Aboura Z. Numerical simulations of woven composite materials with voxel-FE models. In *Proceedings of the ECCM16 conference*, Sevilla, Spain, June 2014.

[129] Potter E, Pinho ST, Robinson P, Iannucci L, and McMillan AJ. Mesh generation and geometrical modelling of 3D woven composites with variable tow cross-sections. *Comp Mater Sci*, 51(1):103–111, 2012.

[130] Kim HJ and Swan CC. Voxel-based meshing and unit-cell analysis of textile composites. *Int J Numer Meth Eng*, 56(7):977–1006, 2003.

[131] Crookston JJ, Ooi JW, Zhao LG, Sherburn MN, Long AC, Jones IA, and Warrior NA. Finite element analysis of textile composite unit cells using conventional and novel techniques. In *Proceedings of the ICCM15 conference*, Durban, South Africa, June 2005.

[132] Iarve EV, Mollenhauer DH, Zhou EG, Breitzman T, and Whitney TJ. Independent mesh method-based prediction of local and volume average fields in textile composites. *Compos Part A-Appl S*, 40(12):1880–1890, 2009.

[133] Nakai H, Kurashiki T, and Zako M. Individual modeling of composite materials with mesh superposition method under periodic boundary condition. In *Proceedings of the ICCM16 conference*, Kyoto, Japan, July 2007.

[134] Tabatabaei SA, Lomov SV, and Verpoest I. Assessment of embedded element technique in meso-FE modelling of fibre reinforced composites. *Compos Struct*, 107:436–446, 2014.

[135] Tabatabaei SA and Lomov SV. Eliminating the volume redundancy of embedded elements and yarn interpenetrations in meso-finite element modelling of textile composites. *Comput Struct*, 152:142–154, 2015.

[136] Cox BN, Carter WC, and Fleck NA. A binary model of textile composites – I. Formulation. *Acta Metall Mater*, 42(10):3463–3479, 1994.

[137] Doghri I and Tinel T. Micromechanical modeling and computation of elasto-plastic materials reinforced with distributed-orientation fibers. *Int J Plasticity*, 21(10):1919–1940, 2005.

[138] Doghri I and Tinel T. Micromechanics of inelastic composites with misaligned inclusions: Numerical treatment of orientation. *Comput Method Appl M*, 195(13–16):1387–1406, 2006.

[139] Dobrzynski C, Melchior M, Delannay L, and Remacle JF. A mesh adaptation procedure for periodic domains. *Int J Numer Meth Eng*, 86(12):1396–1412, 2011.

[140] Moës N, Cloirec M, Cartraud P, and Remacle JF. A computational approach to handle complex microstructure geometries. *Comput Method Appl M*, 192(28–30):3163–3177, 2003.

[141] Quan DL, Toulorge T, Marchandise E, Remacle JF, and Bricteux G. Anisotropic mesh adaptation with optimal convergence for finite elements using embedded geometries. *Comput Method Appl M*, 268:65–81, 2014.

[142] Zhao X, Conley R, Ray N, Mahadevan VS, and Jiao X. Conformal and non-conformal adaptive mesh refinement with hierarchical array-based half-facet data structures. *Procedia Eng*, 124:304–316, 2015.

[143] Resk H, Delannay L, Bernacki M, Coupez T, and Logé R. Adaptive mesh refinement and automatic remeshing in crystal plasticity finite element simulations. *Model Simul Mater Sc*, 17(7):075012, 2009.

[144] Osher S and Sethian JA. Fronts propagating with curvature-dependent speed: Algorithms based on Hamilton-Jacobi formulations. *J Comp Phys*, 79(1):12–49, 1988.

[145] Sonon B and Massart TJ. A level-set based representative volume element generator and XFEM simulations for textile and 3D-reinforced composites. *Materials*, 6:5568–5592, 2013.

[146] Geuzaine C and Remacle JF. Gmsh: A 3-D finite element mesh generator with built-in pre- and post-processing facilities. *Int J Numer Meth Eng*, 79(11):1309–1331, 2009.

[147] Stig F and Hallström S. Spatial modelling of 3D-woven textiles. *Compos Struct*, 94(5):1495–1502, 2012.

[148] Korb G, Koráb J, and Groboth G. Thermal expansion behaviour of unidirectional carbon-fibre-reinforced copper-matrix composites. *Compos Part A-Appl S*, 29(12):1563–1567, 1998.

[149] Totry E, González C, and LLorca J. Prediction of the failure locus of C/PEEK composites under transverse compression and longitudinal shear through computational micromechanics. *Compos Sci Technol*, 68(15–16):3128–3136, 2008.

[150] Bogdanovich AE. Multi-scale modeling, stress and failure analyses of 3-D woven composites. *J Mater Sci*, 41(20):6547–6590, 2006.

[151] Rao MP, Sankar BV, and Subhash G. Effect of Z-yarns on the stiffness and strength of three-dimensional woven composites. *Compos Part B-Eng*, 40(6):540–551, 2009.

[152] Tan P, Tong L, Steven GP, and Ishikawa T. Behavior of 3D orthogonal woven CFRP composites. Part I. Experimental investigation. *Compos Part A-Appl S*, 31(3):259–271, 2000.

[153] Tan P, Tong L, and Steven GP. Behavior of 3D orthogonal woven CFRP composites. Part II. FEA and analytical modeling approaches. *Compos Part A-Appl S*, 31(3):273–281, 2000.

[154] Lomov SV, Bogdanovich AE, Ivanov DS, Mungalov D, Karahan M, and Verpoest I. A comparative study of tensile properties of non-crimp 3D orthogonal weave and multi-layer plain weave E-glass composites. Part 1: Materials, methods and principal results. *Compos Part A-Appl S*, 40(8):1134–1143, 2009.

[155] Desplentere F, Lomov SV, Woerdeman DL, Verpoest I, Wevers M, and Bogdanovich A. Micro-CT characterization of variability in 3D textile architecture. *Compos Sci Technol*, 65(13):1920–1930, 2005.

[156] Bogdanovich AE, Karahan M, Lomov SV, and Verpoest I. Quasi-static tensile behavior and damage of carbon/epoxy composite reinforced with 3D non-crimp orthogonal woven fabric. *Mech Mater*, 62:14–31, 2013.

[157] Karahan M, Lomov SV, Bogdanovich AE, Mungalov D, and Verpoest I. Internal geometry evaluation of non-crimp 3D orthogonal woven carbon fabric composite. *Compos Part A-Appl S*, 41(9):1301–1311, 2010.

[158] Sonon B, François B, and Massart TJ. A unified level set based methodology for fast generation of complex microstructural multi-phase RVEs. *Comput Method Appl M*, 223–224:103–122, 2012.

[159] Sonon B. *On advanced techniques for generation and discretization of the microstructure of complex heterogeneous materials*. PhD thesis, Université Libre de Bruxelles, 2014.

[160] Teoh KJ and Hsiao KT. Improved dimensional infidelity of curve-shaped VARTM composite laminates using a multi-stage curing technique – Experiments and modeling. *Compos Part A-Appl S*, 42(7):762–771, 2011.

[161] Hsiao KT and Gangireddy S. Investigation on the spring-in phenomenon of carbon nanofiber glass fiber/polyester composites manufactured with vacuum assisted resin transfer molding. *Compos Part A-Appl S*, 39(5):834–842, 2008.

[162] Jain LK, Hou M, Ye L, and Mai YW. Spring-in study of the aileron rib manufactured from advanced thermoplastic composite. *Compos Part A-Appl S*, 29(8):973–979, 1998.

[163] Dong C. *Dimension variation prediction and control for composites*. PhD thesis, The Florida State University, 2003.

[164] Kappel E, Stefaniak D, Spröwitz T, and Hühne C. A semi-analytical simulation strategy and its application to warpage of autoclave-processed CFRP parts. *Compos Part A-Appl S*, 42(12):1985–1994, 2011.

[165] Jung WK, Chu WS, Ahn SH, and Won MS. Measurement and compensation of spring-back of a hybrid composite beam. *J Compos Mater*, 41(7):851–864, 2007.

[166] Fernlund G, Osooly A, Poursartip A, Vaziri R, Courdji R, Nelson K, George P, Hendrickson L, and Griffith J. Finite element based prediction of process-induced deformation of autoclaved composite structures using 2D process analysis and 3D structural analysis. *Compos Struct*, 62(2):223–234, 2003.

[167] Fernlund G and Floyd A. Process analysis and tool compensation for curved composite L-angles. In *Proceedings of The Sixth Canadian-International Composites Conference*, Winnipeg, Canada, August 2007.

[168] Fernlund G. Risk reduction in composites processing using prototype data, process simulation, and Bayesian statistics. *Compos Part A-Appl S*, 41(2):295–303, 2010.

[169] Cenaero, Minamo V1.7. Optimization software package. Web page: www.cenaero.be.

[170] Sainvitu C, Iliopoulou V, and Lepot I. *Recent Advances in Optimization and its Applications in Engineering*, chapter Global optimization with expensive functions – sample turbomachinery design application, pages 499–509. Springer, 2010.

[171] Kappel E, Stefaniak D, Holzhüter D, Hühne C, and Sinapius M. Manufacturing distortions of a CFRP box-structure – A semi-numerical prediction approach. *Compos Part A-Appl S*, 51:89–98, 2013.

[172] Causse P, Ruiz E, and Trochu F. Spring-in behavior of curved composites manufactured by Flexible Injection. *Compos Part A-Appl S*, 43(11):1901–1913, 2012.

[173] McKay MD, Beckman RJ, and Conover WJ. A comparison of three methods for selecting values of input variables in the analysis of output from a computer code. *Technometrics*, 21(2):239–245, 1979.

[174] Meckesheimer M, Booker AJ, Barton RR, and Simpson TW. Computationally inexpensive metamodel assessment strategies. *AIAA J*, 40(10):2053–2060, 2002.

[175] Jones DR, Schonlau M, and Welch WJ. Efficient global optimization of expensive black-box functions. *J Global Optim*, 13(4):455–492, 1998.

[176] Dassault Systèmes, Simulayt for V5 Release 5.25 software package. Web page: www.3ds.com.

[177] Vargas G and Mujika F. Determination of in-plane shear properties by three-point flexure test of ±45° anti-symmetric laminates. *Polym Test*, 30(2):204–215, 2011.

[178] Ersoy N, Garstka T, Potter K, Wisnom MR, Porter D, Clegg M, and Stringer G. Development of the properties of a carbon fibre reinforced thermosetting composite through cure. *Compos Part A-Appl S*, 41(3):401–409, 2010.

[179] Balesdent M, Brevaul L, Lacaze S, Missoum S, and Morio J. 8 – Methods for high-dimensional and computationally intensive models. In Morio J and Balesdent M, editors, *Estimation of Rare Event Probabilities in Complex Aerospace and Other Systems*, pages 109–136. Woodhead Publishing, 2016.

[180] Parmentier A, Wucher B, and Martiny P. Experimental and numerical study of the cure-induced deformations in composites produced by vacuum infusion. In *Proceedings of the ICCM19 conference*, Montreal, Canada, July 2013.

[181] Chevalier J, Morelle XP, Bailly C, Camanho PP, Pardoen T, and Lani F. Micro-mechanics based pressure dependent failure model for highly cross-linked epoxy resins. *Eng Fract Mech*, 158:1–12, 2016.

[182] Potter K, Khan B, Wisnom M, Bell T, and Stevens J. Variability, fibre waviness and misalignment in the determination of the properties of composite materials and structures. *Compos Part A-Appl S*, 39(9):1343–1354, 2008.

[183] Karkanas PI and Partridge IK. Cure modeling and monitoring of epoxy/amine resin systems. I. Cure kinetics modeling. *J Appl Polym Sci*, 77(7):1419–1431, 2000.

[184] Karkanas PI and Partridge IK. Cure modeling and monitoring of epoxy/amine resin systems. II. Network formation and chemoviscosity modeling. *J Appl Polym Sci*, 77(10):2178–2188, 2000.

[185] Skordos AA and Partridge IK. Monitoring and heat transfer modelling of the cure of thermoset composites processed by resin transfer moulding. In *Proceedings of the International Symposium on Polymer Composites Science and Technology*, Québec, Canada, October 1999.

[186] Svanberg JM, Altkvist C, and Nyman T. Prediction of shape distortions for a curved composite C-spar. *J Reinf Plast Comp*, 24(3):323–339, 2005.

[187] Karkanas PI. *Cure modelling and monitoring of epoxy/amine resin systems*. PhD thesis, Cranfield University, 1998.

[188] Naik NK and Ganesh VK. An analytical method for plain weave fabric composites. *Composites*, 26(4):281–289, 1995.

[189] Lomov SV, Verpoest I, Peeters T, Roose D, and Zako M. Nesting in textile laminates: geometrical modelling of the laminate. *Compos Sci Technol*, 63(7):993–1007, 2003.

[190] Sevenois RDB, Garoz D, Gilabert FA, Spronk SWF, Fonteyn S, Heyndrickx M, Pyl L, Van Hemelrijck D, Degrieck J, and Van Paepegem W. Avoiding interpenetrations and the importance of nesting in analytic geometry construction for Representative Unit Cells of woven composite laminates. *Compos Sci Technol*, 2016. In Press, Accepted Manuscript. Available online 17 October 2016.

[191] Matveev MY, Long AC, Brown LP, and Jones IA. Effects of layer shift and yarn path variability on mechanical properties of a twill weave composite. *J Compos Mater*, 2016. Published online before print June 24.

[192] Khoun L and Hubert P. Investigation of the dimensional stability of carbon epoxy cylinders manufactured by resin transfer moulding. *Compos Part A-Appl S*, 41(1):116–124, 2010.

[193] Holmberg JA. *Resin transfer moulded composite materials*. PhD thesis, Luleå University of Technology, 1997.

[194] Balvers JM, Bersee HEN, Beukers A, and Jansen KMB. Determination of cure dependent properties for curing simulation of thick-walled composites. In *Proceedings of the 49th AIAA/ASME/ASCE/AHS/ASC Structures, Structural Dynamics and Materials Conference*, Schaumburg, IL, USA, April 2008.

[195] Navabpour P, Nesbitt A, Degamber B, Fernando G, Mann T, and Day R. Comparison of the curing kinetics of the RTM6 epoxy resin system using differential scanning calorimetry and a microwave-heated calorimeter. *J Appl Polym Sci*, 99(6):3658–3668, 2006.

[196] Varley RJ. Reaction kinetics and phase transformations during cure of a thermoplastic-modified epoxy thermoset. *Macromol Mater Eng*, 292(1):46–61, 2007.

[197] Carvelli V, Pazmino J, Lomov SV, Bogdanovich AE, Mungalov DD, and Verpoest I. Quasi-static and fatigue tensile behavior of a 3D rotary braided carbon/epoxy composite. *J Compos Mater*, 47(25):3195–3209, 2013.